Measurements and Modeling of the Dynamics of Optically and Electrically Induced Dissipation in Quantum Hall Systems

Von der Fakultät für Elektrotechnik, Informationstechnik, Physik
der Technischen Universität Carolo-Wilhelmina
zu Braunschweig
zur Erlangung des Grades eines

Doktors der Naturwissenschaften
(Dr. rer. nat.)

genehmigte
Dissertation

von

Gabriel Vasile

aus Livezi-Rumänien

1. Referent:	Prof. Dr. Georg Nachtwei
2. Referent:	Prof. Dr. Rolf R. Gerhardts
Eingereicht am:	19.07.2007
Disputation am:	27.09.2007

Druckjahr: 2007

Prior publications of the thesis

Partial results from this work were published with permission of the common scientific faculty, represented by the Mentor, in the following contributions first:

Publications:

1. G. Nachtwei, C. Stellmach, G. Vasile, G. Hein, *Optically and electrically induced dissipation in quantum Hall systems*, Phys. Stat. Sol. (b), 2007*, to be published*.

2. C. Stellmach, G. Vasile, A. Hirsch, R. Bonk, Yu. B. Vasilyev, G. Hein, C. R. Becker, G. Nachtwei, *Time- and spectrally resolved terahertz photoconductivity of quantum Hall systems*, Phys. Rev. B 76, 035341 (2007).

3. G. Vasile, C. Stellmach, M. Koch, G. Hein, G. Nachtwei, *Nonequilibrium Laser Excitation of Terahertz-Quantum-Hall-Detectors*, Proceedings submitted to the 15th International Conference on Nonequilibrium Carrier Dynamics in Semiconductors (HCIS-15), Tokyo, Japan, 2007.

4. G. Vasile, C. Stellmach, R. R. Gerhardts, G. Nachtwei, *Calculations of the THz Conductivity of Quantum Hall Systems*, Proceedings of the 28th International Conference on the Physics of Semiconductors (ICPS-28), Vienna, Austria, 2006, edited by W. Jantsch and F. Schaffler, American Institute of Physics (New York 2007), Vol. 893, p. 649.

5. R. Bonk, C. Stellmach, Yu. B. Vasilyev, C. R. Becker, G. Hein, G. Vasile, G. Nachtwei, *Fast and Tunnable Photodetectors for Terahertz Radiation based on Landau Quantization at HgTe/HgCdTe Heterojunctions*, Proceedings of the 28th International Conference on the Physics of Semiconductors (ICPS-28), Vienna, Austria, 2006, edited by W. Jantsch and F. Schaffler, American Institute of Physics (New York 2007), Vol. 893, p. 491.

6. G. Vasile, C. Stellmach, G. Hein, G. Nachtwei, *Measurements of the electrical excitation of quantum Hall devices in the real-time domain*, Semicond. Sci. Technol. 21, 1714 (2006).

7. G. Vasile, C. Stellmach, G. Hein, G. Nachtwei, *Measurements of the electrical excitation of QH-devices in the real-time domain*, Proceedings of the 14th International Conference on Nonequilibrium Carrier Dynamics in Semiconductors (HCIS-14), Chicago, U.S.A., 2005, edited by M. Saraniti and U. Ravaioli, Springer Proceedings in Physics (Springer, Berlin-Heidelberg 2006), Vol. 110, p. 95.

Posters:

1. G. Vasile, C. Stellmach, Yu. B. Vasilyev, A. Hirsch, G. Hein, R. R. Gerhardts, G. Nachtwei, *Experimental and Numerical Investigations of the THz Photoconductivity of QH Systems with Corbino geometry*, Conference on Precision Electromagnetic Measurements (CPEM-2006), Turin, Italy, 2006, Poster WeP-26.
2. G. Vasile, C. Stellmach, Yu. B. Vasilyev, A. Hirsch, G. Hein, R. R. Gerhardts, G. Nachtwei, *Experimental and Numerical Investigations of the Terahertz Conductivity of QH Systems*, DPG-Frühjahrstagung Dresden, Germany, 2006, Poster HL 9.100.
3. G. Vasile, C. Stellmach, G. Nachtwei, G. Hein, *Electrical and optical exciation of Quantum Hall Systems: New Experiments and Model*, DFG-Schwerpunkt Quanten-Hall-Systeme, DFG-Koloquium, Bad Honnef, Germany, 2005, Poster 015.
4. G. Vasile, C. Stellmach, G. Hein, G. Nachtwei, *Two-level model for electrical and optical excitation and relaxation in QH Systems*, International Symposium on Quantum Hall Systems and Quantum Materials (QHSQM-2004), Hamburg, Germany, 2004, Poster 022.

Contents

Chapter 1

Introduction

It is well known that one “key” to gain insight about the internal (electronic) properties of the conducting materials is achieved by the transport measurements. When an electric current passes through a metal strip there is a voltage drop along the strip, which can be measured. In 1879, E. H. Hall discovered that by applying a perpendicular magnetic field to a gold leaf mounted on a glass plate (perpendicular to the direction of a current flowing through the metal) a voltage V_{H}, so called the *Hall voltage*, is produced across the metal strip[1]. The appearance of the Hall voltage V_{H} is known as the *classic Hall effect* (CHE) [1]. The occurrence of the classic Hall effect is due to the deflection[2] of the charge carriers by the Lorentz force to the edge of the sample. The equilibrium is achieved when the Lorentz force $\vec{F}_L = q\vec{v} \times \vec{B}$ is balanced by the electrostatic force $\vec{E} = qV_{\mathrm{H}}/w$ from the build up of charge at the edge (q is the charge of the carrier, v is the drift velocity of the charged carrier, B is the perpendicular magnetic field, E is the electric field, and V_{H} is the Hall voltage). The Hall effect has been thoroughly investigated and well understood in metals and semiconductors. The study of the Hall effect in the two-dimensional electron systems[3] (2DES) showed new and interesting quantum effects. The pioneering work of Fowler *et al*. [2] has opened the field of transport studies at 2DES. Further experimental [3,4] or theoretical works [5–9] show that at high magnetic fields and low temperatures the conductivity shows deep minima which tend to zero for integer filling factors.

24 years after the first Nobel prize awarded in the field of semiconductor physics[4], in 1980 K. von Klitzing discovered a special Hall effect, so called the *integer quantum Hall effect* (IQHE). The IQHE was discovered in a 2DES occurring in the inversion layer of a Silicon

---

[1] The Hall voltage appears in the perpendicular direction to the plane made by the current flow direction and the magnetic field.

[2] The moving charged carriers in the presence of a magnetic fields are deflected to the edge by the action of Lorentz force.

[3] In the 2DES the electrons are restricted to move quasi-free in two spatial directions while in the other spatial direction the motion of electrons is quantized.

[4] In 1956 W. B. Shockley, J. Bardeen and W. H. Brattain were awarded with the Nobel prize in Physics for the discovery of the transistor effect.

metal-oxide-semiconductor field-effect transistor (*Si*-MOSFET) at strong magnetic fields $B = 18\mathrm{T}$ and low temperatures $T = 1.5\mathrm{K}$ [10]. The most striking difference between the IQHE and the CHE is that the Hall resistance, instead of increasing linearly with increasing the magnetic field as in CHE for constant electron density, it develops a series of plateaus. In the same intervals of magnetic fields where the Hall resistance exhibits plateaus, the longitudinal resistance vanishes[5]. The vanishing longitudinal resistance is a sign that for those magnetic fields the current flows from one end to the other of the 2DES without dissipating any energy in the interior of the sample. The astonishing aspect of the IQHE is the value at which the plateau in the Hall resistance appears. For each plateau the Hall resistance is given by the Plank's constant h divided by the square of the elementary electron charge e multiplied by an integer i which represents the number of completely filled Landau levels ($R_{\mathrm{xy}} = h/ie^2 = 25812.807\Omega/i = R_{\mathrm{K-90}}/i$ where $R_{\mathrm{K-90}} = h/e^2$ is the von Klitzing's constant).

The precision of the quantized Hall resistance (a relative uncertainty of about 1 part in 10^9), the reproducibility from one sample to another at high level of accuracy and the independence from the sample geometry recommended the QHE and finally in 1990 to be accepted as an international standard of resistance [11]. For the discovery of the QHE, K. von Klitzing was awarded the Nobel prize in Physics in 1985 [12].

After the discovery of QHE, extensive theoretical works were done in order to explain this effect [13, 14]. Laughlin explained the quantization of the Hall conductivity of two-dimensional metals as a consequence of gauge invariance and the existence of a mobility gap. In 1982 D. C. Tsui, H. L. Störmer and A. C. Gossard discovered another quantized Hall effect, where the Hall resistance is $R_{\mathrm{xy}} = h/ie^2$ where $i = 1/3$ and $i = 2/3$. Since the QH plateaus occur for filling factors equal to rational fractions, this effect is known as the *fractional quantum Hall effect* (FQHE). The FQHE was discovered in a *GaAs/AlGaAs* heterostructure ($n_{\mathrm{s}} \approx 1.4 \times 10^{11}\mathrm{cm}^{-1}$, $\mu_{\mathrm{el}} \approx 0.1 \times 10^6\mathrm{cm}^2V^{-1}s^{-1}$) at low temperatures ($T \leq 0.5\mathrm{K}$) and high magnetic fields ($B = 15\mathrm{T}$) [15]. In 1983, R. B. Laughlin presented a variational ground-state and excited-state wave functions which describe the condensation of a two-dimensional electron gas into a new state of matter [16]. For the discovery of FQHE and for the theoretical contribution to understand the FQHE, D. C. Tsui, H. L. Störmer and R. B. Laughlin were awarded the Nobel prize for Physics in 1998 [17–19].

Since the discovery of the IQHE many mechanisms have been proposed to explain the effect on the basis of transmission and reflection of electrons [20, 21], electrons flowing in the edge states at the boundary of the 2DES [22–24], or recently due to the presence of the incompressible strips [25]. Another important aspect studied intensively was represented by the determination of the limitation of this effect by the sample properties (electron density n_{s}, electron mobility μ_{el}), the sample temperature and the current through the sample. The increase of the temperature induces the reduction of the QH plateau. By exceeding a critical temperature (usually above $T_{\mathrm{crit}} > 4\mathrm{K}$) the QH plateau vanishes. The electrical breakdown of the QHE means that above a critical current the longitudinal resistivity increases abruptly to finite values (by orders of magnitude), leading for the

---

[5] The longitudinal resistance becomes very small and depends strongly on the temperature and on the filling factor.

corresponding magnetic fields to the disappearance of the plateaus of the Hall resistivity (see [26] for a review of the breakdown of the QHE). The electrical breakdown of the QHE has been extensively investigated due to its importance for metrology on one hand and due to the physics behind this effect. From the metrology point of view the limit, at which the breakdown occurs, is important since the breakdown means the limit of high precision measurements to determine the resistance standard. In order to perform high precision measurements, the current through the sample must not exceed the critical value but should be as high as possible, so that the QHE still holds. From the point of view of basic research the breakdown of the QHE is interesting since so far there is no complete and conclusive theory which could explain the large variety of breakdown measurements and the microscopic processes that are behind the breakdown of the QHE. The breakdown of the QHE could be characterized by the excitation of electrons from the filled Landau levels (LL's) below the Fermi level (FL) to the empty LL's above the FL. If the excited electrons relax, after a characteristic time τ_{rel}, to the energy levels below the FL, the QHE is restored. Many previous studies on QH devices have shown that both the excitation [27–36] and the relaxation [30–37] of electrons develop only after a certain drifting distance of electrons, depending on the intrinsic properties of the samples. Some of these results have been explained by different mechanisms: an avalanche-like electron heating [30–40], intra-Landau-level transitions [41], inter-Landau-level transitions [33, 40, 42], the influence of potential fluctuations [27–29, 40] and the formation of compressible and incompressible islands [25, 40, 43].

The space-resolved measurements performed previously provide only an indirect approach to the excitation and relaxation times, which are deduced from the stationary profile of the longitudinal resistivity $\rho_{\mathrm{xx}}(x)$ for a drift velocity assuming a linear profile of the Hall voltage, $\partial V_{\mathrm{y}}/\partial y = \mathrm{const.}$ From the previous works [31, 33, 37] the energy relaxation times were deduced ($0.24\mathrm{ns} \leq \tau_{\mathrm{rel}} \leq 2.6\mathrm{ns}$ for sample mobilities $0.04 \times 10^{6}\mathrm{cm}^{2}V^{-1}s^{-1} \leq \mu_{\mathrm{el}} \leq 0.53 \times 10^{6}\mathrm{cm}^{2}V^{-1}s^{-1}$), assuming a drift velocity v_{D} being constant along the sample. If $\ell_{\mathrm{D}} \approx \ell_{\mathrm{mfp}}$ (as found in Refs. [31, 33, 37]), it means that the scattering at impurity potentials/potential fluctuations plays a comparable role for both relaxation and excitation (also given arguments/discussions for that in particular in Ref. [33]). The order of magnitude of the relaxation times is in good agreement with earlier assumptions [39], explained by phonon-assisted dissipation. The essential parameter deduced from these space-resolved measurements is the relaxation length. The corresponding time scale of τ_{exc} has not been measured. However, the time-resolved measurements of the generation and relaxation processes provide a direct access to the corresponding excitation and relaxation times. To accomplish this the response of QH samples to rectangular and short electric pulses of pulse widths of the order of nanoseconds is monitored, and these time-resolved (integrating) measurements yield the trend of the generation and relaxation times being approximately equal [35, 36, 44]. From those experimental findings the authors concluded $\tau_{\mathrm{rel}} \geq \tau_{\mathrm{exc}}$, but by decreasing the pulse width to around $\tau_{\mathrm{exc}} = 1\mathrm{ns}$ the system relaxes in a time which approaches the limit $\tau_{\mathrm{rel}} = \tau_{\mathrm{exc}}$. The trend of $\tau_{\mathrm{rel}} \leq \tau_{\mathrm{exc}}$ was predicted by a recent theory of the avalanche heating of electrons [40], based on a two-Landau level model with the argument that in the opposite situation the $(l+1)$-th level would become overpopulated (inversion population) with respect to the l-th level. In this study we have performed real-time measurements of the electrical excitation and optical excitation and relaxation at the breakdown of the QHE since from previous time-integrating measurements of electrical excitation and relaxation [35, 36, 44] it had not been possible to monitor the individual pulse shape of the sample response.

A special sample geometry of QH devices we used in this study is the *Corbino geometry*[6], which allows a direct measurements of the longitudinal conductivity σ_{xx}. Further, Corbino samples were used in the first magnetotransport measurements [2]. By applying a voltage between the inner (*source-S*) and outer (*drain-D*) contacts of the Corbino disc, a radial current flows in between the contacts. If an uniform and constant magnetic field is applied perpendicularly to the Corbino disc, a circular current will flow inside the disc[7]. If the applied source-drain voltage V_{SD} exceeds a critical value the electrons leave the circular trajectory around the *S* contact, and a radial current between *S* and *D* contacts establishes. This corresponds to the breakdown of QHE in QH devices with Corbino geometry.

In this study we have performed real-time measurements of the electrical excitation and optical excitation and relaxation at the breakdown of the QHE on devices with Corbino geometry. The reason of these real-time measurements was the deficiency of monitoring individual pulse shape of the sample response of the previous time-integrating measurements of electrical excitation and relaxation [35, 36, 44].

This thesis is structured as follows:

- **Chapter 2**: contains the description of the 2DES in *GaAs/AlGaAs* heterostructure and the behavior of the 2DES without and with applied magnetic field. A description of the IQHE, the FQHE and the electrical breakdown of the IQHE is given here;
- **Chapter 3**: describes the design and fabrication of the QH devices with Corbino geometry (photolithography, chemical etching and contact lithography), the preparation of the measurements (electrical bonding, sample holders and cryostats) and the measurements devices used during our measurements;
- **Chapter 4**: contains the description of the two-Landau levels model for the excitation and relaxation of hot electrons, used for the understanding of our real-time measurements of the electrical excitation;
- **Chapter 5**: contains the description of the real-time measurements of the electrical excitation. The dependence of the excitation time τ_{exc} on the applied pulse amplitude, electron mobility, magnetic field and temperature are investigated. These

---

[6] The name of this device comes from the Italian physicist O. M. Corbino that in 1911 studied theoretically and experimentally the case of a conducting disc with a hole at its center (a German translation of the article appeared in [45]).

[7] K. von Klitzing pointed out that "the QHE may be considered as an ideal (and quantized) version of the Corbino effect corresponding to the case in which the current in the disc, with an applied radial voltage, is only circular" [46].

dependences are discussed under the assumption of the quasi-classical drift model [35,36,44], a two-Landau levels model [40] and a quasi-local transport model [25]. These models could explain qualitatively (and partially quantitativelly) the presented results;

- **Chapter 6**: describes the real-time measurements of the optical excitation and relaxation. The dependence of the excitation τ_{exc} and relaxation τ_{rel} times on the applied pulse amplitude, electron mobility, magnetic field and temperature are investigated. The dependences of the relaxation time are discussed applying a two-Landau levels model [31]. The model could explain qualitatively the presented results. Further we introduce the photoresponse (PR) measurements and the two contributions observed in this type of optically induced breakdown measurements: the bolometric (BO) and cyclotron resonance (CR) contributions. An explanation of the often observed BO double-peak structure of the PR based on a electron temperature picture is given;

- **Chapter 7**: contains a proposed theoretical approach for the explanation of the BO double-peak structure of the PR due to the interaction of THz radiation with 2DES under the Self-Consistent Born Approximation (SCBA) model;

- **Chapter 8**: finally summarizes the present work.

Chapter 2

Low-Dimensional Electron System and the Quantum Hall Effect

In 1957 J. R. Schrieffer[1] stated that electrons confined a narrow potential well of an inversion layer would not behave classically. The pioneering work of Fowler *et al.* [2] has opened the field of two-dimensional electron system (2DES). One easy way to obtain a 2DES is to use two semiconductor materials with different energy gaps. Thus, by enclosing a layer of one semiconductor with a smaller gap between two layers of another semiconductor with a larger gap, a quantum well is established. The band discontinuity leads to a potential well inside the layer with the smaller energy gap. This potential well is characterized by a quantization of the electron motion perpendicular to the semiconductor interface.

2.1 Properties of 2DES without magnetic field ($B = 0$)

A 2DES is an electron system in which the electrons are quasi-free to move in two spatial directions (*x*-*y* plane)[2]. In the third spatial direction (*z*-direction)[3] the electron motion is quantized. This happens because the motion of electrons in the *z*-direction is suppressed by a band offset at the conduction bands of the two semiconductors. This band offset cannot be overcome by low-energy excitations from the equilibrium state in which electrons are confined without any external excitation (for a review of electronic properties of 2DES see [47]).

A 2DES can be obtained in different materials: thin films [48], on the surface of liquid

---

[1] J. R. Schrieffer together with J. Bardeen and L. Cooper won the 1972 Nobel Prize in Physics for developing the BCS theory, the first successful microscopic theory of superconductivity.

[2] In the *x*-*y* plane, the electron energy can be described by the kinetic energy of free electrons with k_x and k_y the wave vectors in the plane of 2DES, $\hbar^2(k_\mathrm{x}^2 + k_\mathrm{y}^2)/2m^*$.

[3] In the *z*-direction, electrons have quantized energy levels E_z^i.

Helium (*He*) [49], at semiconductor-oxide interfaces or in semiconductor heterostructures [50].
The best known material systems in which the electronic properties of 2DES have been investigated are the *Si*-MOSFET[4] and the *GaAs/AlGaAs* heterostructure[5]. The 2DES appears at the interface between the *Si* (semiconductor) and the SiO_2 (insulator) in the case of a MOSFET and at the interface between the *GaAs* (semiconductor) and the *Si-AlGaAs* (insulator) in the case of a *GaAs/AlGaAs* heterostructure. The electrons[6] are confined at the interface by the electrostatic potential, if the potential $\Phi(z)$ is approximated by a triangular potential ($\Phi(z) = -z \cdot F$, with F the electric field) normal to the interface, due to the positive charges[7], which cause a drop in the electron potential toward the interface [12, 51]. If the width of the triangular well is smaller than the *de Broglie* wavelength of electrons ($d < \lambda_{\mathrm{dB}} = h/p_{\mathrm{F}} = 2\pi/k_{\mathrm{F}}$, with d the width of the potential well, λ_{dB} the *de Broglie* wavelength, p_{F} and k_{F} the Fermi momentum and the Fermi wave vector of the electrons, respectively), then the energy of the electrons is quantized in electric subbands E_i^{z} corresponding to the quantized levels i for the motion in the *z*-direction. By assuming an electron in an (asymmetric) triangular potential with an infinite barrier $V(z) = \infty$ at the interface $z = 0$ and a linear potential $V(z) = eFz$) at $z > 0$, the electric subbands could be determined by solving the time-independent Schrödinger equation

$$\left[-\frac{\hbar^2}{2m^*}\frac{\partial^2}{\partial z^2} + V(z)\right]\Psi(z) = E\Psi(z)\,. \tag{2.1}$$

The energy subbands are the eigenvalues determined from eq. 2.1

$$E_i^{\mathrm{z}} = a_i \cdot \left[\frac{(e\hbar F)^2}{2m^*}\right]^{\frac{1}{3}}\,, \tag{2.2}$$

---

[4] The IQHE has been discovered on this material system.

[5] The FQHE has been discovered on this material system.

[6] For the MOSFET system the electrons are provided by the *Si* semiconductor while for the *GaAs/AlGaAs* heterostructure, electrons are coming from the positively charged donors *Si*.

[7] For a MOSFET, by applying a positive gate voltage, an electrostatic potential is induced. This electrostatic potential tends the electrons to be attracted toward the gate contact. If the gate voltage exceeds a critical value $V_{\mathrm{g}} > V_{\mathrm{crit}}$, the bending of the *Si* energy bands is so strong that the conduction band falls below the chemical potential μ_{Si} and forms a triangular potential well with the electrostatic potential discontinuity at the interface. Thus, the electrons are trapped in this inversion layer at the *Si*-SiO_2 interface. For a *GaAs/AlGaAs* heterostructure, at the interface of these two materials, electrons leave the positively charged donors, cross the interface and accumulate in the *GaAs* layer. The positively charged donors set up an electrostatic potential $\Phi(z) = -z \cdot F$ which in turn tends to drive the electrons back into the *AlGaAs*. Due to the band discontinuity between *GaAs* and *AlGaAs*, which prevents the electrons to come back to the donors by the electric field F, the electrons are confined by the field near the interface. The electrochemical equilibrium is achieved only if an inversion layer at the interface forms, which leads to the strong bending of the conduction band edge of *GaAs* below the equilibrium electrochemical potential. Thus, an approximately triangular well is formed by the conduction band edge of *GaAs* and the electrostatic potential discontinuity at the *GaAs/AlGaAs* interface (see Fig. 3.2).

where $i = 0, 1, \ldots$ and a_i are the zeros of the Airy function $\mathrm{Ai}(z)$ [52]. The corresponding eigenfunctions are given by

$$\Psi_i(z) = \frac{1}{N_i} \cdot \mathrm{Ai}\left(\frac{eFz - E_i^\mathrm{z}}{E_0^\mathrm{z}}\right) , \tag{2.3}$$

where N_i are the normalization constants, $z_0 = [\hbar^2/(2m^* eF)]^{1/3}$ and $E_0^\mathrm{z} = eFz_0$ are the units of length and energy, respectively. From eq. 2.2 follows that by increasing i the energy spacing of two adjacent levels decreases. This is because the triangular well broadens by increasing the energy [51, 53, 54]. The occupation of more than one electric subband means that electrons have different position in the *z*-direction (perpendicular to the plane where the 2DES exists) and therefore the electron system is called *quasi*-2DES. In order to describe the properties of the 2DES, we shall recall the time-independent Schrödinger equation (three-dimensional)

$$\left[-\frac{\hbar^2 \nabla^2}{2m^*} + V(\vec{r})\right] \Psi(\vec{r}) = E\Psi(\vec{r})\,, \tag{2.4}$$

where $V(\vec{r})$ is the electric potential energy and the position $\vec{r} = (x, y, z)$. Since in the our case, the potential energy depends only on z and the electrons are free to move in the *x*-*y* plane (perpendicular to *z*-direction), eq. 2.4 becomes

$$\left[-\frac{\hbar^2}{2m^*}\left(\frac{\partial^2}{\partial x^2} + \frac{\partial^2}{\partial y^2} + \frac{\partial^2}{\partial z^2}\right) + V(z)\right] \Psi(x, y, z) = E\Psi(x, y, z)\,. \tag{2.5}$$

As mentioned before, in the 2DES the electrons are quasi-free to move in *x*-*y* plane but quantized in the *z*-direction and the potential energy depends only on z which means in turn that the wave functions in the *x*-*y* plane could assumed to be plane waves

$$\Psi(x, y, z) = \exp(ik_\mathrm{x}x) \cdot \exp(ik_\mathrm{y}y) \cdot \Psi_i(z)\,, \tag{2.6}$$

where k_x and k_y are the wave vectors in the plane of 2DES, $\Psi_i(z)$ are the eigenfunctions defined by eq. 2.3. By inserting eq. 2.6 into eq. 2.5 and after some algebra steps we obtain a one-dimensional (*z*-dependent) time-independent Schrödinger equation (see eq. 2.1). This type of equation has been already solved and therefore the initial three-dimensional time-independent Schrödinger equation 2.4, for the motion of electrons in *x*-*y* plane, gives the eigenvalues from the solving of eq. 2.5 (Schrödinger equation for 3 dimensions in real space):

$$E_i(k_\mathrm{x}, k_\mathrm{y}) = E_i^\mathrm{z} + \frac{\hbar^2}{2m^*}\left(k_\mathrm{x}^2 + k_\mathrm{y}^2\right) , \tag{2.7}$$

where $i = 0, 1, 2, \ldots$, E_i are the total energy of the 2D subbands, m^* is the electron effective mass (due to asymmetry of the potential well, the wave function of the electrons in the *z*-direction is mainly localized in *GaAs* and $m^* = 0.067 \times m_\mathrm{e}$, m_e is the free electron mass), k_x and k_y are the wave vectors in the plane of 2DES and E_i^z are the electrical subband levels of the 2D subbands.

From solving eq. 2.5 we also obtain the eigenfunctions as waves described by eq. 2.6. We should mention here that according to eq. 2.7, for $\vec{k} = 0$ (with $\vec{k} = (k_\mathrm{x}, k_\mathrm{y}, 0)$) the total energy E_i is given by the electrical subband levels E_i^z. Thus, $E_\mathrm{i}(\vec{k} = 0) = E_\mathrm{i}^\mathrm{z}$. Since the magnetotransport measurements are performed at low temperatures ($T < 4\mathrm{K}$) and the 2DES has usually small electron density, the electrons occupy only the lowest electric subband[8] E_0^z. This situation corresponds to the *electric quantum limit*, leading to a 2DES for $E_1^\mathrm{z} - E_0^\mathrm{z} - E_\mathrm{F} >> k_\mathrm{B}T$.
The motion of electrons in the $\vec{k}$-space (in the *x*-*y* plane) is described by the kinetic energy

$$E_\mathrm{k} = \frac{\hbar^2}{2m^*}k^2 = \frac{\hbar^2}{2m^*}\left(k_\mathrm{x}^2 + k_\mathrm{y}^2\right) . \tag{2.8}$$

The electrons in the lowest electric subband may be considered as points inside a circle, the so called the *Fermi circle*[9], in the $\vec{k}$-space. We consider the 2DES having area $A = L_\mathrm{x}L_\mathrm{y}$ with L_x and L_y are the lengths of the 2DES in the *x*- and *y*-directions and each electron occupies an $\Delta k_\mathrm{x} \cdot \Delta k_\mathrm{y} = 4\pi^2/(L_\mathrm{x}L_\mathrm{y})$ area element in the $\vec{k}$-space [55]. The magnitude of the wave vectors at the Fermi circle is the *Fermi wave vector* $\vec{k}_\mathrm{F}$ and the energy at the edge of the Fermi circle is the *Fermi energy* (see Fig. 2.1)

$$E_\mathrm{F} = \frac{\hbar^2}{2m^*}k_\mathrm{F}^2 . \tag{2.9}$$

Since an electron occupies an area element $\Delta k_\mathrm{x} \cdot \Delta k_\mathrm{y}$ in the $\vec{k}$-space and the area of the Fermi circle A_F is defined by $\pi \cdot k_\mathrm{F}^2$, we can determine the number of electrons N_el existing in the Fermi circle

$$N_\mathrm{el} = \frac{A_\mathrm{F}}{\Delta k_\mathrm{x} \cdot \Delta k_\mathrm{y}} = \frac{\pi \cdot k_\mathrm{F}^2}{\frac{4\pi^2}{L_\mathrm{x}L_\mathrm{y}}} = \frac{Ak_\mathrm{F}^2}{4\pi} , \tag{2.10}$$

where $A = L_\mathrm{x}L_\mathrm{y}$ is the area of 2DES. At this stage we can calculate the electron density in 2DES by dividing the number of electrons N_el by the area A of the 2DES. By counting both allowed spin states: spin-up and spin-down states a factor 2 must be included in eq. 2.10. Thus, the electron density of 2DES is derived

$$n_\mathrm{s} = \frac{N_\mathrm{el}}{A} = \frac{k_\mathrm{F}^2}{2\pi} , \tag{2.11}$$

and consequently the Fermi wave vector is deduced from eq. 2.10

$$k_\mathrm{F} = \sqrt{2\pi n_\mathrm{s}} . \tag{2.12}$$

---

[8] The electrons are in the ground state.

[9] The Fermi circle is determined by the cross section of the 2-dimensional paraboloid described by the kinetic energy at the Fermi energy E_F. All electron states inside the Fermi circle are occupied while the states outside the Fermi circle are empty.

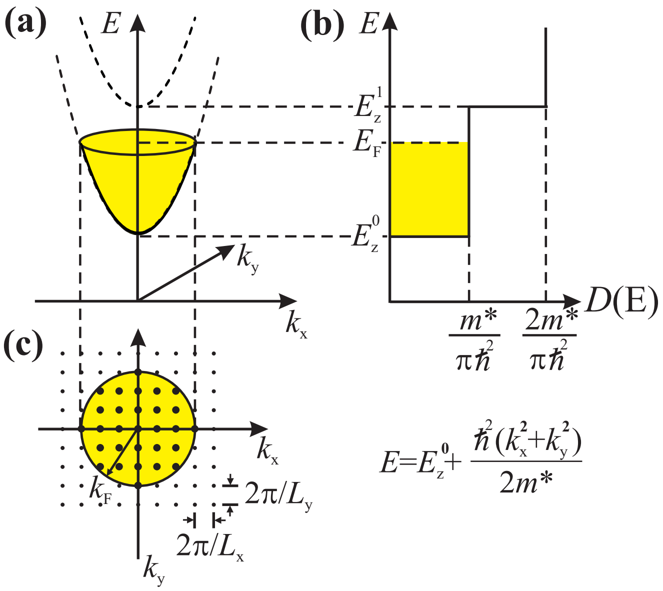

Figure 2.1: A schematic view of the energy spectrum and of the DOS of the 2DES without magnetic field. (a) Total energy of the 2DES without magnetic field. (b) DOS of the 2DES without magnetic field. (c) 2DES in the k-space [36].

By inserting eq. 2.12 in eq. 2.9, a direct relation between the Fermi energy E_F and the electron density n_s is established

$$E_\mathrm{F} = \frac{\pi\hbar^2}{m^*} \cdot n_\mathrm{s}\,. \tag{2.13}$$

Due to eq. 2.13, the Fermi energy is a measure of the electron density. This is very important: Since the electron density does not vary with temperature, the Fermi energy then has to decrease in order to maintain a constant electron density in the 2DES. In other words, the Fermi energy decreases to keep the number of electrons in the system constant. Another very important characteristic of the 2DES is the density of states $D(E)$ which describes the distribution of energies in the system

$$D(E) = \frac{\partial n_\mathrm{s}}{\partial E} = \frac{m^*}{\pi\hbar^2}\,. \tag{2.14}$$

Equation 2.14 shows that the density of states (DOS) $D(E)$ is independent of the energy E for the 2DES. This is because, according to eq. 2.8, the energy $E(k)$ is proportional to the square of the wave vector k ($E(k) \propto k^2$ - the parabolic dispersion). The DOS is a step function of $m^*/\pi\hbar^2$ step height and $E_{i+1}^\mathrm{z} - E_i^\mathrm{z}$ step width. Thus, each electrical subband contributes with the same amount of electrons to the total DOS (see Fig. 2.1).

In the following we study the effect of the electric field on the electron transport. By applying the electrical field, the electrons drift according to the Newton's law. We assume that due to the presence of impurities and dislocations the electron are scattered. The effect of scattering on the 2DES can be modeled by introducing a frictional term in the Newton's equation of motion for the average velocity

$$\vec{F} = -e\vec{E} = m^* \left(\frac{d}{dt} + \frac{1}{\tau} \right) \vec{v} \, . \tag{2.15}$$

The velocity approaches a steady state at large times and therefore $d\vec{v}/dt = 0$. The velocity components become

$$v_{\mathrm{x}} = -\frac{e\tau}{m^*} \cdot E_{\mathrm{x}} \tag{2.16}$$

and

$$v_{\mathrm{y}} = -\frac{e\tau}{m^*} \cdot E_{\mathrm{y}} \, . \tag{2.17}$$

The electric current density[10] in a constant electric field is

$$\vec{j} = -e \cdot n_{\mathrm{s}} \cdot \vec{v} \, . \tag{2.18}$$

By decomposing the current density vector in its *x*-*y* components, with the help of Ohm's law $\vec{j} = \sigma \cdot \vec{E}$ we can define the Drude electrical conductivity as

$$\sigma = \frac{e^2 \cdot n_{\mathrm{s}} \cdot \tau}{m^*} = e \cdot \mu_{\mathrm{el}} \cdot n_{\mathrm{s}} \, , \tag{2.19}$$

with n_{s} the electron density and $\mu_{\mathrm{el}} = e\tau/m^*$ the electron mobility.

2.2 Properties of 2DES with magnetic field ($B \neq 0$)

In this subsection we describe the effect of the perpendicular magnetic field on the 2DES (Faraday configuration). In order to describe the 2DES properties in a magnetic field B,[11] we shall solve again the time-independent Schrödinger equation

$$\left[\frac{\hbar^2}{2m^*} \left(-i\nabla + \frac{e}{\hbar}\vec{A} \right)^2 + g^* \mu_{\mathrm{B}} \vec{B}\vec{S} + V(z) \right] \Psi(\vec{r}) = E\Psi(\vec{r}) \, , \tag{2.20}$$

where we assumed the vector potential in the Landau gauge, $\vec{A} = (0, Bx, 0)$, $g^* = -0.44$ is the effective gyromagnetic factor in *GaAs*, $\mu_{\mathrm{B}} = 9.274 \times 10^{-24} \mathrm{J} \cdot T^{-1}$ is the Bohr magneton[12] and $\vec{S}$ is the spin vector.

---

[10] The current density describes the charge carrier current per area.

[11] The magnetic field B is introduced by the vector potential $\vec{A}$, $\vec{B} = \mathrm{curl}\vec{A} = \nabla \times \vec{A} \Rightarrow B_{\mathrm{z}} = \partial A_{\mathrm{y}}/\partial x - \partial A_{\mathrm{x}}/\partial y$ (for $\vec{A} = (0, Bx, 0)$ we obtain $\vec{B} = (0, 0, B_{\mathrm{z}})$-the Landau gauge).

[12] The Bohr magneton was first calculated in 1913 by the Romanian physicist Stefan Procopiu and published in 1913 under the title "Calculation of the molecular magnetic momentum by the M. Planck's quantum theory" in "Bulletin Scientifique de l'Academie Roumaine de Sciences"). The Bohr magneton is also known as the Bohr-Procopiu magneton.

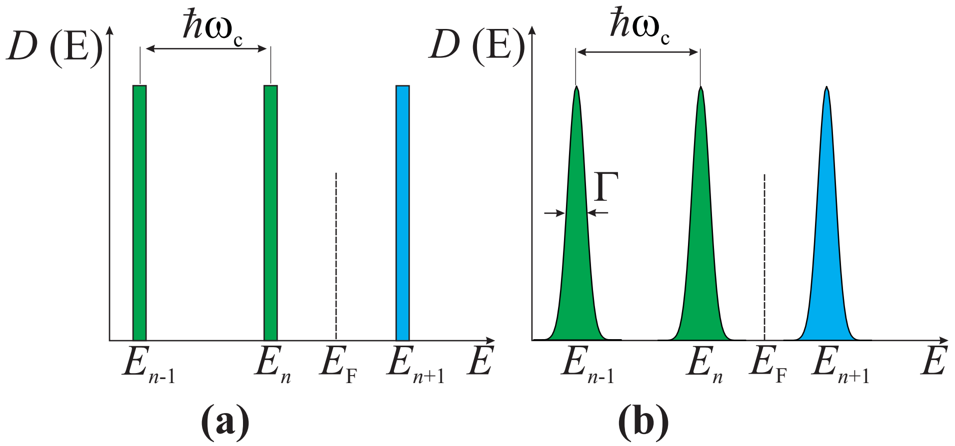

Figure 2.2: A schematic view of the DOS of the 2DES with magnetic field. (a) DOS with δ-functions Landau levels for the ideal sample (no scattering). (b) DOS with the broad Landau levels for the real sample (with scattering). green - denotes the filled Landau level and blue - denotes the empty Landau level.

By solving the time-independent Schrödinger eq. 2.20 for the electron motion in the *x*-*y* plane gives the eigenvalues:

$$E_n = \left(n + \frac{1}{2}\right) \cdot \hbar\omega_{\mathrm{c}} + s \cdot g^* \cdot \mu_{\mathrm{B}} \cdot B \,, \tag{2.21}$$

where $n = 0, 1, 2, \ldots$ is the principal quantum number, $\omega_{\mathrm{c}} = eB/m^*$ is the cyclotron angular frequency, $s = \pm 1/2$ the electron spin (for spin-down state and spin-up state respectively). The application of the magnetic field B alters dramatically the DOS. While, without magnetic field, the DOS is a step function, with magnetic field the DOS turns into a series of δ-functions, known as *Landau levels* (LL's), see Fig. 2.2, localized at the energies given by eq. 2.21. We observe that the spin splitting energy $\Delta E_{\mathrm{s}} = g^* \mu_{\mathrm{B}} B$ depends linearly on the magnetic field B (if we neglect many-body effects). At small values of B the spin splitting energy is small and the DOS contains both spin states. By increasing B the spin splitting also increases and therefore the spin states start to separate. At high values of B, the spin states are completely separated.
From solving eq.2.20, we also obtain the eigenfunctions:

$$\Psi_{\mathrm{k_y},n}(x, y) \propto H_n \cdot \left(\frac{x + k_{\mathrm{y}}\ell_{\mathrm{B}}^2}{\ell_{\mathrm{B}}}\right) \cdot \exp\left[-\frac{(x + k_{\mathrm{y}}\ell_{\mathrm{B}}^2)^2}{2\ell_{\mathrm{B}}^2}\right] \cdot \exp(ik_{\mathrm{y}}y) \,, \tag{2.22}$$

where H_n are the *Hermite* polynomials, $\ell_{\mathrm{B}} = \sqrt{\hbar/eB}$ is the *magnetic length*. As mentioned the DOS in magnetic fields undergoes the transition from the step-like spectrum into a discrete spectrum (series of δ-functions) for each n. By using the semiclassical

Bohr-Sommerfeld model, the electrons can be considered as points inside a circle for each value of n and therefore corresponding to each LL.

In order to calculate the occupation of each circle, we consider two adjacent LL's and therefore two adjacent circles (corresponding to $n = i$ and $n = i + 1$ respectively). The area between two adjacent circles in the $\vec{k}$-space is given by

$$A_{i,i+1} = \pi\Delta(k^2) = \frac{2\pi m^* \omega_{\mathrm{c}}}{\hbar} = \frac{2\pi eB}{\hbar} \tag{2.23}$$

where $\Delta(k^2) = (2m^*\Delta E)/\hbar^2$, $\Delta E = \hbar\omega_{\mathrm{c}}$ is the energy difference between two circles and $\omega_{\mathrm{c}} = eB/m^*$ is the cyclotron angular frequency. Following the same formalism as we used to find the occupation of the states in the case of no magnetic field, we keep in mind that an electron occupies an area element $\Delta k_{\mathrm{x}} \cdot \Delta k_{\mathrm{y}}$ in the $\vec{k}$-space, the number of electrons N_{L} existing in one circle (LL) is

$$N_{\mathrm{L}} = \frac{A_{i,i+1}}{\Delta k_{\mathrm{x}} \cdot \Delta k_{\mathrm{y}}} = \frac{L_{\mathrm{x}} L_{\mathrm{y}} eB}{2\pi\hbar} = \frac{L_{\mathrm{x}} L_{\mathrm{y}} eB}{h} \,, \tag{2.24}$$

where $h = 2\pi\hbar = 6.626 \times 10^{-34}\mathrm{J} \cdot \mathrm{s}$ is the Planck's constant and $\hbar = 1.054 \times 10^{-34}\mathrm{J} \cdot \mathrm{s}$ is the reduced Planck's constant. At this stage we can calculate the electron density in each Landau level (LL), by dividing the number of electrons N_{L} per Landau level by the area $A = L_{\mathrm{x}} L_{\mathrm{y}}$ of the 2DES

$$n_{\mathrm{L}} = \frac{N_{\mathrm{L}}}{A} = \frac{eB}{h} = \frac{m^*\omega_{\mathrm{c}}}{2\pi\hbar} = \frac{1}{2} \cdot \frac{m^*}{\pi\hbar^2} \cdot \hbar\omega_{\mathrm{c}} \,. \tag{2.25}$$

Thus, each spin-splitted Landau level contains half of the number of states as the 2DES (without magnetic field) has, multiplied by $\hbar\omega_{\mathrm{c}}$, the energy difference between two-adjacent LL's. Further we calculate the number ν of filled spin-splitted LL's by dividing the electron density in the 2DES to the electron density in each LL

$$\nu = \frac{n_{\mathrm{s}}}{n_{\mathrm{L}}} = \frac{n_{\mathrm{s}} h}{eB} = 2\pi \cdot \ell_{\mathrm{B}}^2 \cdot n_{\mathrm{s}} \,. \tag{2.26}$$

The formula of the filling factor of the LL's is very important because it shows a dependence on the electron density n_{s} and on the magnetic field B. Therefore by keeping constant the electron density ($n_{\mathrm{s}} = \mathrm{const.}$, as in the most experiments) and by changing the magnetic field the filling factor is variable (the number of filled LL's). Equation 2.26 shows an inverse proportionality between filling factor and magnetic field ($\nu \propto 1/B$). Thus, by increasing the magnetic field B, the filling factor ν decreases.

Before we discuss the effect of the magnetic field on the filling factor in order to prevent any misleading, I denote the *Fermi energy* at zero temperature ($T = 0$) and no magnetic field ($B = 0$) by E_{F}^0, where $E_{\mathrm{F}}^0 = E_{\mathrm{F}} = \mathrm{const.}$ according to eq. 2.13 for $n_{\mathrm{s}} = \mathrm{const.}$ and the *Fermi energy* at finite temperature ($T \neq 0$) and finite magnetic field ($B \neq 0$) by $E_{\mathrm{F}} = \mu_{\mathrm{ch}}$, where μ_{ch} is the chemical potential.

So far we have considered the DOS of 2DES in magnetic field as a series of δ-functions.

But this is true only for an ideal sample, where electrons are not scattered by impurities, defects or/and phonons. But, in a real sample, due to the impurities or defects, the electrons are scattered and drift for a characteristic time τ_{q} between the scattering events. The energy of scattered electrons fluctuates and leads to a broadening of the $D(E)$ (see fig. 2.2). The average of these fluctuations in the energy is equal to the broadening of the LL's, defined as the full width at half height $\Gamma = \hbar/\tau_{\mathrm{q}}$, with τ_{q} the *quantum lifetime*[13]. The magnitude of the broadening of the Landau levels is important because it influences the behavior of DOS. If $\Gamma > \hbar\omega_{\mathrm{c}} \Leftrightarrow \omega_{\mathrm{c}}\tau_{\mathrm{q}} < 1$, the LL's are widely broadened and are not separated distinctively even at large B, because the electrons are scattered before they complete an orbit in the magnetic field. If $\Gamma < \hbar\omega_{\mathrm{c}} \Leftrightarrow \omega_{\mathrm{c}}\tau_{\mathrm{q}} > 1$, the LL's are separated because the electrons are scattered after they complete more orbits.

2.3 Magnetotransport in the classical regime

Magnetotransport measurements are used to determine some properties of different materials (the electron density n_{s}, the electron mobility μ_{el}) subjected to crossed electric and magnetic fields ($\vec{E} \times \vec{B}$). Classically, an electric field exerts a force on a charged particle and induces a drift of the particle in the direction of the electric field lines. Unlike the electric field, the magnetic field exerts a force, the *Lorentz force*, only on moving charged particles. The magnitude of the Lorentz force is proportional to the particle velocity and to the magnitude of the magnetic field. Its direction is perpendicular to both the particle's direction of motion and the direction of the magnetic field. Thus, the charged particle is moving in a circle since the magnetic field exerts always a perpendicular force that curves the particle trajectory. The radius of this circle is inversely proportional to the strength of the magnetic field[14] ($r = m^{*}v/eB$). This means that higher B values lead to smaller orbits for the charge carriers.

The occurrence of crossed electric and magnetic fields $\vec{E} \times \vec{B}$ induces a cycloidal path of the charged particle. Due to the magnetic field it moves on orbits around the circle center, known also as the *guiding center*. But due to the applied electric field the guiding center moves in a straight line, perpendicular to both the electric field and the magnetic field[15]. This perpendicular motion induces an accumulation of the electrons on one edge of the sample while on the other side an accumulation of positive charges is established. The

---

[13] The quantum lifetime τ_{q} is usually different from the relaxation time τ in the Drude mobility. This τ, in others studies appears as τ_{tr}, is called the *transport lifetime*. The main difference is that, while for quantum lifetime the contributions on τ_{q} of all collisions is the same, for the transport lifetime the contributions on τ depend on the change of direction that occurs.

[14] The angular frequency of the particle moving in the circle is direct proportional to the strength of the magnetic field $\omega = \omega_{\mathrm{c}} = eB/m^{*}$

[15] The guiding center moves with a speed, called the *drift velocity* $v_{\mathrm{D}} = E/B$. The guiding center moves faster in regions where the tangent to the cycloidal path has the same direction with the electric field (the drift velocity is direct proportional to the electric field). If the magnetic field is weaker or the electric field is stronger, the electron motion is more linear and the guiding center moves faster.

potential difference induces an electrical field perpendicular to the direction of the current flow.

Within this classical approach, we consider the electrons as noninteracting particles moving according to Newtons's equation. We assume that due to the presence of impurities, dislocations and phonons, the electron are scattered. The effect of scattering on the 2DES can be modeled by introducing a frictional term in the Newton's equation of motion in crossed electric and magnetic fields for the average velocity:

$$\vec{F} = m^* \cdot \vec{a} \Longleftrightarrow -e(\vec{E} + \vec{v} \times \vec{B}) = m^* \left(\frac{d}{dt} + \frac{1}{\tau} \right) \vec{v} \,, \tag{2.27}$$

where $\tau = (m^* \sigma)/(e^2 n_\mathrm{s})$ is the momentum relaxation time. In a steady state the time derivatives are zero and the drift velocity becomes

$$\vec{v}_\mathrm{D} = -\frac{e\tau}{m^*} \cdot (\vec{E} + \vec{v}_\mathrm{D} \times \vec{B}) \,. \tag{2.28}$$

The components of $\vec{v}_\mathrm{D}$ are

$$v_\mathrm{x} = -\frac{e\tau}{m^*(1+\omega_\mathrm{c}^2\tau^2)}(E_\mathrm{x} - \omega_\mathrm{c}\tau E_\mathrm{y}) \tag{2.29}$$

and

$$v_\mathrm{y} = -\frac{e\tau}{m^*(1+\omega_\mathrm{c}^2\tau^2)}(E_\mathrm{y} + \omega_\mathrm{c}\tau E_\mathrm{x}) \,. \tag{2.30}$$

The electric current density in a constant electric field is given by eq. 2.18 (with the help of eq. 2.29 and eq. 2.30), by decomposing the current density vector in its *x*-*y* components. Comparing with Ohm's law $\vec{j} = \hat{\sigma} \cdot \vec{E}$ we determine the two-dimensional dc conductivity tensor as

$$\hat{\sigma} = \begin{pmatrix} \sigma_\mathrm{xx} & \sigma_\mathrm{xy} \\ \sigma_\mathrm{yx} & \sigma_\mathrm{yy} \end{pmatrix} = \frac{\sigma_0}{1+\omega_\mathrm{c}^2\tau^2} \cdot \begin{pmatrix} 1 & -\omega_\mathrm{c}\tau \\ \omega_\mathrm{c}\tau & 1 \end{pmatrix} \tag{2.31}$$

with the longitudinal component

$$\sigma_\mathrm{l} = \sigma_\mathrm{xx} = \sigma_\mathrm{yy} = \frac{\sigma_0}{1+\omega_\mathrm{c}^2\tau^2} \tag{2.32}$$

and the transversal (Hall) component

$$\sigma_\mathrm{H} = -\sigma_\mathrm{xy} = \sigma_\mathrm{yx} = \sigma_0 \cdot \frac{\omega_\mathrm{c}\tau}{1+\omega_\mathrm{c}^2\tau^2} \,, \tag{2.33}$$

where $\sigma_0 = n_\mathrm{s} e^2 \tau / m^*$ is the *DC* Drude conductivity (see eq. 2.19). If $B = 0$, $\sigma_\mathrm{l} = \sigma_\mathrm{xx} = \sigma_\mathrm{yy} = \sigma_0$ and $\sigma_\mathrm{H} = -\sigma_\mathrm{xy} = \sigma_\mathrm{yx} = 0$. The resistivity tensor $\hat{\rho}$ is defined as the inverse of the conductivity tensor $\hat{\sigma}$. Thus, the resistivity tensor can be written as

$$\hat{\rho} = \begin{pmatrix} \rho_\mathrm{xx} & \rho_\mathrm{xy} \\ \rho_\mathrm{yx} & \rho_\mathrm{yy} \end{pmatrix} = \frac{1}{\hat{\sigma}} = \frac{1}{\sigma_\mathrm{xx}^2 + \sigma_\mathrm{xy}^2} \cdot \begin{pmatrix} \sigma_\mathrm{xx} & -\sigma_\mathrm{xy} \\ \sigma_\mathrm{xy} & \sigma_\mathrm{yy} \end{pmatrix} = \rho_0 \cdot \begin{pmatrix} 1 & \omega_\mathrm{c}\tau \\ -\omega_\mathrm{c}\tau & 1 \end{pmatrix} \,, \tag{2.34}$$

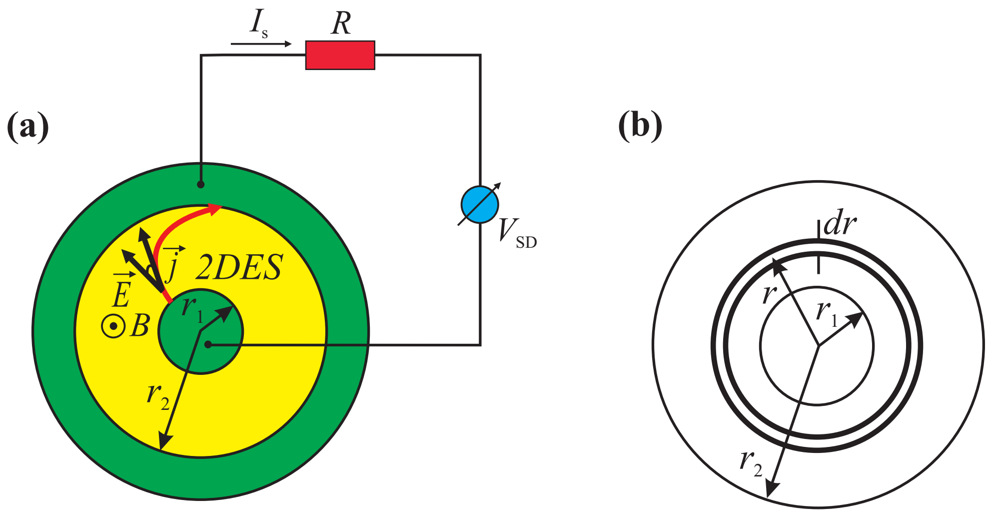

Figure 2.3: (a) A schematic view of the magnetotransport measurement setup on a QH device with Corbino geometry (green - the contacts where the source-drain voltage is applied, red - resistor where the current I_{s} is measured, yellow - 2DES. (b) A scheme used to calculate the resistance of the length element L placed at distance r from the center.

where $\rho_0 = 1/\sigma_0 = m^*/n_{\text{s}}e^2\tau$ is the *DC* Drude resistivity. Thus, the longitudinal component is

$$\rho_{\text{l}} = \rho_{\text{xx}} = \rho_{\text{yy}} = \rho_0 = \frac{m^*}{n_{\text{s}}e^2\tau} = \frac{1}{e \cdot \mu_{\text{el}} \cdot n_{\text{s}}} \tag{2.35}$$

and the transversal (Hall) component

$$\rho_{\text{H}} = -\rho_{\text{xy}} = \rho_{\text{yx}} = \rho_0\omega_{\text{c}}\tau = \frac{B}{e \cdot n_{\text{s}}}\,, \tag{2.36}$$

where we have included also $\mu_{\text{el}} = e\tau/m^*$ and $\omega_{\text{c}} = eB/m^*$. Thus, we observe that the longitudinal resistivity is independent of B while the Hall component is directly proportional to the strength of the magnetic field B. This linear dependence of the $\rho_{\text{xy}}(B)$ is known as the *classical Hall effect* (CHE).

By using eq. 2.36 we can determine the electron density n_{s} of the investigated sample. By inserting the obtained value of the electron density in eq. 2.35 the electron mobility μ_{el} is determined.

Let us consider a QH device with Corbino geometry (r_1 and r_2 are the inner and outer radii) placed in a perpendicular magnetic field (see Fig. 2.3 (a)). By applying a voltage between the *source* (*S*) and the *drain* (*D*) contacts, an electric field $\vec{E}$ is established. The electrons drift in crossed electric and magnetic fields $\vec{E} \times \vec{B}$. During the magnetotransport measurements, the applied source-drain voltage is constant and therefore also the established electric field is constant. As a result, the electrons move in cycloidal paths, and they reach after a certain time the outer (*drain*) contact. This time depends on the strength of the magnetic field. At a constant electric field, this time is shorter if the magnetic field is weaker. In other words, at high magnetic fields, electrons complete many cycloidal orbits before they reach the outer contact. By reaching the drain contact, between the source and drain contacts a current I_s is established. I_s can be measured through a serial resistor with the sample, as a function of the magnetic field B.

In order to calculate the resistance of the QH device with Corbino geometry, let us consider a length element $L = 2\pi r$ of width dr, situated at a distance r from the center of the QH device with Corbino geometry (see Fig. 2.3 (b)). In general, for a three-dimensional (3D) system, a conductor, the resistance is proportional to its electrical resistivity ρ and the length l of the conductor but inversely proportional to the area A of the cross-section of the conductor ($R = \rho \cdot l/A$). However, in the case of a 2D system, like our 2DES of our QH device with Corbino geometry, the area A is replaced by the appropriate length element $L = 2\pi r$. The length l is replaced by the width dr. Thus, the resistance can be calculated as

$$dR_\mathrm{xx} = \rho_\mathrm{xx} \cdot \frac{dr}{L} = \rho_\mathrm{xx} \cdot \frac{dr}{2\pi r} \Longrightarrow R_\mathrm{xx} = \frac{\rho_\mathrm{xx}}{2\pi} \cdot \int_{r_1}^{r_2} \frac{dr}{r} = \frac{\rho_\mathrm{xx}}{2\pi} \cdot \ln\left(\frac{r_2}{r_1}\right) . \tag{2.37}$$

The resistance is defined by the applied source-drain voltage V_SD and the current I_s through the device ($R_\mathrm{xx} = V_\mathrm{SD}/I_\mathrm{s}$). Applying this relation to the eq. 2.37 we determine the longitudinal electrical resistivity

$$\rho_\mathrm{xx} = \frac{V_\mathrm{SD}}{I_\mathrm{s}} \cdot \frac{2\pi}{\ln(r_2/r_1)} . \tag{2.38}$$

Since in the magnetotransport measurements, for a Corbino disc the longitudinal conductivity is measured, we calculate the conductivity σ_xx from the Ohm's law

$$\vec{j} = \hat{\sigma} \cdot \vec{E} \Longleftrightarrow \begin{pmatrix} j_\mathrm{a} \\ j_\mathrm{r} \end{pmatrix} = \begin{pmatrix} \sigma_\mathrm{xx} & \sigma_\mathrm{xy} \\ \sigma_\mathrm{yx} & \sigma_\mathrm{yy} \end{pmatrix} \cdot \begin{pmatrix} E_\mathrm{a} \\ E_\mathrm{r} \end{pmatrix} , \tag{2.39}$$

and by considering that the azimuthal component is zero ($E_\mathrm{a} = 0$) and the symmetry relations $\sigma_\mathrm{xx} = \sigma_\mathrm{yy}$ and $\sigma_\mathrm{xy} = -\sigma_\mathrm{yx}$. Thus, eq. 2.39 becomes

$$\begin{pmatrix} j_\mathrm{a} \\ j_\mathrm{r} \end{pmatrix} = \begin{pmatrix} \sigma_\mathrm{xx} & \sigma_\mathrm{xy} \\ -\sigma_\mathrm{xy} & \sigma_\mathrm{xx} \end{pmatrix} \cdot \begin{pmatrix} 0 \\ E_\mathrm{r} \end{pmatrix} = \begin{pmatrix} \sigma_\mathrm{xy} \cdot E_\mathrm{r} \\ \sigma_\mathrm{xx} \cdot E_\mathrm{r} \end{pmatrix} . \tag{2.40}$$

Since the radial current density j_r is

$$j_\mathrm{r} = \sigma_\mathrm{xx} \cdot E_\mathrm{r} = \frac{I_\mathrm{s}}{2\pi r} , \tag{2.41}$$

the longitudinal conductivity σ_xx can be calculated as

$$\sigma_\mathrm{xx} = \frac{I_\mathrm{s}}{2\pi} \cdot \frac{1}{V_\mathrm{SD}} \cdot \int_{r_1}^{r_2} \frac{dr}{r} = \frac{I_\mathrm{s}}{V_\mathrm{SD}} \cdot \frac{\ln(r_2/r_1)}{2\pi} , \tag{2.42}$$

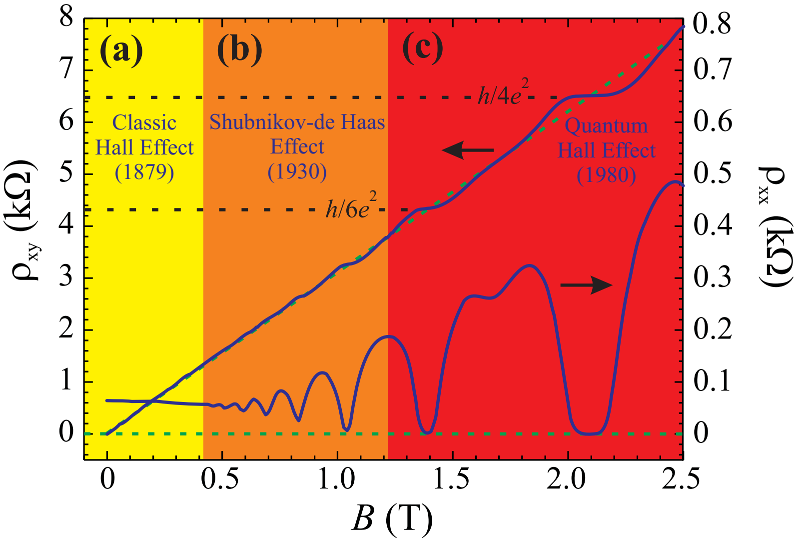

Figure 2.4: A typical magnetotransport curve taken at a QH device with Hall bar geometry ($n_\mathrm{s} \approx 2 \times 10^{11}\mathrm{cm}^{-2}$). This magnetotransport curve shows three regimes of the magnetotransport at the 2DES with increasing B: (a) Classical Hall Effect (CHE), (b) Shubnikov-de Haas Effect (SdHE) and (c) Quantum Hall Effect (QHE) [36].

where I_s is the measured sample current through the resistor, $V_\mathrm{SD} = \int_{r_1}^{r_2} E_\mathrm{r} dr$ is the applied source-drain voltage and r_1, r_2 are the inner and the outer radii of contacts of the QH device with Corbino geometry. Whereas the longitudinal conductivity σ_xx is determined directly from the measured current I_s and applied source-drain voltage V_SD, the Hall conductivity σ_xy is not directly determined. However, the Hall conductivity σ_xy can be determined from the longitudinal ρ_xx and Hall ρ_xy resistivities measured on samples with Hall bar geometry

$$\sigma_\mathrm{xy} = -\frac{\rho_\mathrm{xy}}{\rho_\mathrm{xx}^2 + \rho_\mathrm{xy}^2}\,. \tag{2.43}$$

2.4 Magnetotransport in the quantum regime

The linear dependence of the Hall resistance R_xy or Hall resistivity ρ_xy on the strength of the magnetic field B applies only at low magnetic fields where the number of filled LL's is larger. But by increasing the magnetic field and reducing the number of filled LL's, the resistance (resistivity) shows a different behavior.

Figure 2.4 shows a typical magnetotransport curve taken for a QH device with Hall bar geometry. At low magnetic fields, up to $0.4\mathrm{T}$ for this sample, the 2DES behaves classically. The Hall resistivity shows a linear increase with the magnetic field ($\rho_\mathrm{xy} \propto B$, according to eq. 2.36) and the longitudinal resistivity remains more or less constant with an slight decrease with the magnetic field (see eq. 2.35). This region corresponds to the *classical Hall (CH) regime*. By increasing the strength of the magnetic field B further, up to $1.2\mathrm{T}$ for this sample, the 2DES leaves the CHE regime and enters a new regime, called the *Shubnikov-de Haas regime*. In the Shubnikov-de Haas regime, the Hall resistivity starts to deviate from the previous linear behavior and the longitudinal resistivity oscillates strongly with the B. The amplitude of these oscillations (of the longitudinal resistivity), known as the *Shubnikov-de Haas (SdH) oscillations*, increases with B. This dependence is very important since at high magnetic fields, above $1.2\mathrm{T}$ for this sample, the 2DES shows very interesting and remarkable behavior. The minima of the longitudinal resistivity oscillations tend toward zero[16]. Around the B values where the longitudinal resistivity ρ_{xx} tends to zero, the Hall resistivity ρ_{xy} becomes independent of the B and exhibits a plateau. This regime is called the *quantum Hall (QH) regime*.

As we see, the 2DES, by increasing the strength of B, undergoes different regimes characterized by different behaviors of the longitudinal and Hall resistivities. We focus now on the other two regimes: the SdH regime and QH regime, corresponding to the SdH effect, the integer quantum Hall effect (IQHE) and the fractional quantum Hall effect (FQHE).

2.4.1 Shubnikov-de Haas (SdH) effect

To explain the SdH effect we use fig. 2.5 that shows the oscillating chemical potential at zero and finite temperatures as a function of the magnetic field B. By increasing the strength of the magnetic field B, the LL's increase their energies and the chemical potential μ_{ch} starts to oscillate since it has to follow the occupation of the LL's, until at integer filling factor $\nu = i$ (at $B_{\nu=i} = hn_{\mathrm{s}}/e\nu$) the LL gets depopulated and the chemical potential jumps to the next lower LL. With the spin-splitting included, at even filling factors $\nu = 2i$ (i-integer) the magnitude of the jump of the chemical potential is $\hbar\omega_{\mathrm{c}} - g^{*}\mu_{\mathrm{B}}B$ and at odd filling factors $\nu = 2i+1$ (i-integer) the magnitude of the jump of the chemical potential is $g^{*}\mu_{\mathrm{B}}B$.

At finite T the oscillations of the chemical potential die out at low magnetic fields, even if collision broadening of the LL's is not considered. This domain of low magnetic fields corresponds to the CH regime where the longitudinal resistivity is constant. Due to the scattering and the finite temperature, the jump of the chemical potential from one LL to the next lower LL is not abrupt anymore. The oscillatory behavior of μ_{ch} is reflected in the oscillatory behavior of the longitudinal resistivity. The oscillations of the longitudinal resistivity[17] are known as the *Shubnikov-de Haas oscillations*[18]. Minima of the SdH oscillations occur at magnetic fields $B_{\nu=i} = hn_{\mathrm{s}}/e\nu$, when the filling factor is an integer

---

[16] In real quantum Hall systems, the longitudinal resistivity is not exactly zero, but rather very small. Consequently, the longitudinal resistivity is set to zero.

[17] The behavior of the longitudinal conductivity is similar.

[18] The SdH oscillations have been discovered on a *Bi* crystal by L. Shubnikov and W. J. de Haas in 1930 in Leiden-Netherlands [56].

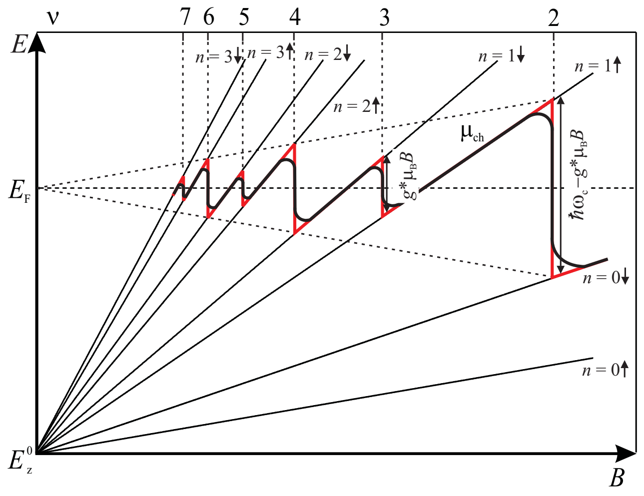

Figure 2.5: The Landau fan with the Landau energies E_n for $n = 0, 1, 2, 3$ for both the spin-up and the spin-down states and the oscillating chemical potential μ_{ch} as a function of the magnetic field B (black line of μ_{ch} - chemical potential at $T = 0$, red line of μ_{ch} - chemical potential at $T \neq 0$ [36]).

($\nu = i$). This is because for integer filling factor, the highest LL is completely filled and therefore the chemical potential is in between the highest occupied and lowest unoccupied LL's. This means that, since the chemical potential is the highest energy of the filled LL, there are no available states around the chemical potential in the gap. This corresponds to the free electron case without scattering. The longitudinal conductivity vanishes, and the Hall conductivity is quantized at the free electron value corresponding to the integer filling factor. At high magnetic fields, according to eq. 2.32, eq. 2.33 and eq. 2.34, the longitudinal conductivity and resistivity are proportional ($\rho_{\text{xx}} \propto \sigma_{\text{xx}}$). Thus, the longitudinal resistivity also shows minima in oscillations at integer filling factors.
From the periodicity of the SdH oscillations, taken during the magnetotransport measurement, the electron density n_{s} can be determined by plotting the longitudinal conductivity or resistivity as a function of inverse magnetic field (with help of eq. 2.26):

$$B_\nu = \frac{h \cdot n_{\text{s}}}{e \cdot \nu} \Longleftrightarrow \frac{1}{B} = \frac{e \cdot \nu}{h \cdot n_{\text{s}}} \Longrightarrow \Delta \left(\frac{1}{B}\right) = \frac{2e}{h \cdot n_{\text{s}}}\,, \tag{2.44}$$

with the spin degeneracy taken into account (characteristic to low magnetic fields).

2.4.2 Integer Quantum Hall Effect (IQHE)

Figure 2.4 shows that, if the magnetic field increases above 1.2T (for this sample), the minima of the SdH oscillations tend to zero and persist over *B*-intervals of finite widths.

The vanishing longitudinal resistivity[19] indicates that for those magnetic fields the current flows from one end to the other of the 2DES without dissipating any energy in the interior of the sample. At the same time, for these *B*-intervals, the Hall resistivity is quantized[20]:

$$\rho_{\mathrm{xy}} = \frac{1}{i} \cdot \frac{h}{e^2} = \frac{R_{\mathrm{K-90}}}{i}\,, \tag{2.45}$$

where h is the Planck's constant, e is the elementary charge, i is an integer and $R_{\mathrm{K-90}} = 25812.807\Omega$ is the *von Klitzing's constant*. The quantization of the Hall resistivity has been found by von Klitzing *et al.* [10] and is know as the *integer quantum Hall effect (IQHE)*. One astonishing feature of the IQHE is that the values of the Hall resistivity are defined by the fundamental constants h and e and can be measured with high accuracy (relative uncertainty of about 10^{-9}).

The precision of the quantized Hall resistance (a relative uncertainty of about 1 part in 10^9), the reproducibility from one sample to another one at a high level of accuracy and the independence from the sample geometry resulted in a definition of the international standard of resistance [11] by the QHE. For the discovery of the QHE, K. von Klitzing was awarded the Nobel prize in Physics in 1985 [12]. Due to the high accuracy of measuring the Hall resistivity, the QHE is also a very good method to give a highly accurate value of the *fine-structure constant* $\alpha = e^2/\hbar c = 1/137.035999$. In fact, the QHE was announced in the original paper as a new method to determine the value of the fine-structure constant α.

Although, eq. 2.45 shows that the quantized Hall resistivity occurs only at integer filling factors, which in turn means only at certain values of the magnetic field, in experiments the QH plateaus exist over *B*-intervals. These *B*-intervals, for which the Hall resistivity is quantized and longitudinal resistivity vanishes, do not imply necessarily an accurate fixing of the magnetic field in order to perform high-precision measurements of the quantized Hall resistivity.

The explanation of the QHE is based on *disorder*, induced by the random potential from impurities or defects in real samples. This approach assumes that the disorder causes *localization*, where the *localized states* are situated energetically in the tails of the broadened LL's (see Fig. 2.6). In these localized states, the electrons are localized in the vicinity of an impurity or defect and cannot carry any net current (do not contribute to the electron transport in the 2DES). On the other hand, the center of the LL's contains so called *extended (delocalized) states* which carry the current and thus contribute to the electron transport[21]. In the delocalized state, the electrons can flow over a large area of the crystal. Therefore, the increase of the magnetic field would correspond to a sweep of the chemical potential through regions of alternatively localized and delocalized states. A confirmation of this picture was given by Ando [57]. He showed that the states are exponentially localized (thus in the tails of the LL's) unless they are in the center or the vicinity of the center

---

[19] The longitudinal conductivity also vanishes at integer filling factors because the electrons move only perpendicularly to the electric field, and any diffusion in the direction of the electric field is not possible.

[20] The Hall resistivity ρ_{xy} develops plateaus, with constant values around integer filling factor $\nu = i$.

[21] The crystal electric properties are determined only by the electrons in the delocalized states.

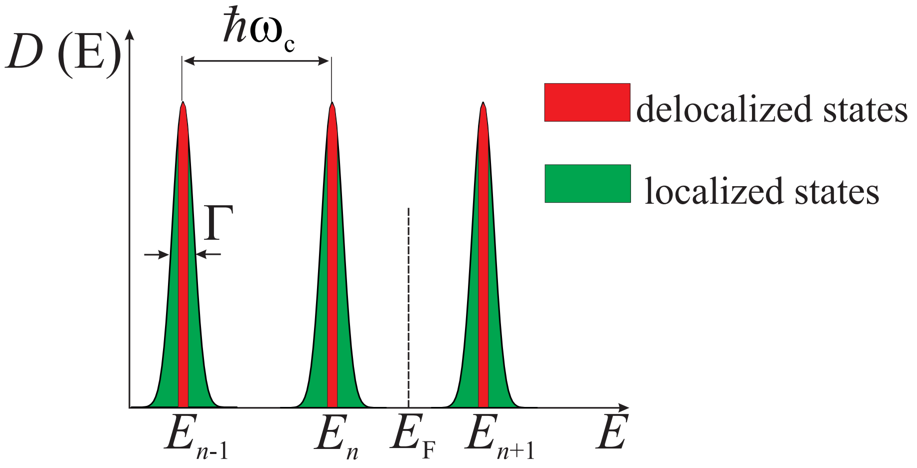

Figure 2.6: Localized and delocalized (extended) states due to the disorder in 2DES.

of the LL's.

At magnetic fields where the filling factor is an integer $\nu = i$ (or an even integer without the spin splitting taken into account), the chemical potential lies in the Landau gap and equals the Fermi energy at zero magnetic fields ($\mu_{\mathrm{ch}} = E_{\mathrm{F}}^{0}$). Since the chemical potential is situated in the localized states, the highest filled LL is completely filled. There are no empty states available at energies around the chemical potential μ_{ch}. This means that no current can flow. Therefore, the longitudinal resistivity ρ_{xx} (and conductivity σ_{xx}) become zero and the Hall resistivity ρ_{xy} is quantized. By increasing the magnetic fields, the chemical potential moves closer and closer to the extended states. As long as the chemical potential is still in the localized states, the Hall resistivity remains quantized and the longitudinal conductivity and resistivity remain zero. As soon as the chemical potential enters the extended states, there are available empty states at energies around the μ_{ch}. Thus, in the delocalized states electrons can move and carry a current. This leads to a finite and increasing longitudinal resistivity ρ_{xx} (and conductivity σ_{xx}) and to an increasing Hall resistivity ρ_{xy}. If the magnetic field is increased further, the chemical potential moves down through the localized states at the bottom of the LL to the localized states and afterward to the delocalized states at the center of the next lower LL. The Hall resistivity remains constant at its new plateau value during the sweep of the chemical potential through the localized states until the chemical potential reaches the region of the delocalized states of the next lower LL.

The localization explains the occurrence of the quantized Hall plateaus but cannot explain the high accuracy of the quantized Hall values. The quantized Hall plateaus are due to the electrons in the localized states around the tails of the LL where the longitudinal conductivity vanishes. Therefore, the number of localized and delocalized states can be described by $N_{\mathrm{loc}} = eB/h$ and $N_{\mathrm{deloc}} = keB/h$ with $0 < k < 1$. Consequently, the electron density in the localized and delocalized states can be described by $n_{\mathrm{s}}^{\mathrm{loc}} = i \cdot N_{\mathrm{loc}} = ieB/h$ and $n_{\mathrm{s}}^{\mathrm{deloc}} = i \cdot N_{\mathrm{deloc}} = ikeB/h$ with i integer filling factor. Since the conductivity (resistivity) is related to the delocalized states we can write the Hall conductivity by $\rho_{\mathrm{xy}} = B/(en_{\mathrm{s}}^{\mathrm{deloc}}) = 1/(ik) \cdot (h/e^2)$ which is in contradiction with the measured value of the Hall conductivity at integer filling factor i (see eq. 2.45). In larger samples and mostly in the high-mobility samples (mobility above $10^6\mathrm{cm}^2\mathrm{Vs}^{-1}$) the localization could be explained on the basis of the long-range fluctuations contributions, where the fluctuation length is of the order of the size sample. However, samples with a mobility below $10^6\mathrm{cm}^2\mathrm{Vs}^{-1}$ show better Hall plateaus due to a larger amount of localized states.

In the previous discussions, we have neglected the Coulomb interaction of the electrons. This is not completely justifiable because the Coulomb interaction induces screening effects which leads to two different types of regions: the *quasi-metallic compressible*[22] and the *quasi-insulating incompressible* regions[23] [25, 58–61]. The Coulomb potential has a short-range and long-range contributions. In a narrow sample the long-range contributions are neglected, and the screening is treated under the assumption of the Self-Consistent Born Approximation (SCBA). The SCBA assumes that the coherent scattering of an electron by more than one impurity can be neglected. The result of these studies was that the Hall voltage drops only along the incompressible regions. The current flows only along these incompressible regions and that the vanishing longitudinal and quantized Hall conductivities are due to the incompressible regions. These QH plateaus develop as long as the incompressible regions (strips) persist. However, in wider samples the long-range fluctuation cannot be neglected. At certain B-values additional incompressible strips may occur inside the sample and therefore broaden and stabilize the QH plateaus.

So far, we have discussed the situation in which the filling factor is still an integer and does not exceed the magnetic quantum limit ($\nu = 1$) where all the electrons are aligned in one direction[24]. But for $\nu < 1$, QH plateaus occur when the LL is partially filled (at filling factors equal to rational fractions) $\rho_{\mathrm{xy}} = h/ie^2$, where $i = 1/3,\ 1/5,\ 1/7,\ 2/3,\ 4/5,\ 6/7$. This effect is called the *fractional quantum Hall effect (FQHE)* and was discovered by D. C. Tsui, H. L. Störmer and A. C. Gossard in 1982 [15]. For the discovery of FQHE and for the theoretical contribution to understand the FQHE, D. C. Tsui, H. L. Störmer and R. B. Laughlin were awarded the Nobel prize for Physics in 1998 [17–19]. In 1983, R. B. Laughlin presented a theory with a variational ground-state and excited-state wave functions which describes the condensation of a 2DES into a new state of matter. This state of matter is described by an incompressible quantum liquid where the excitation over its ground state carry a fractional electric charge ($e^* = e/3$ for example) [16]. An alternative explanation of the FQHE is based on the idea of composite fermions (CF's) [62]. One version of the CF's are electrons with an even number of flux quanta bound to them.

---

[22] The compressible regions are those regions where the Fermi level lies within a LL in the delocalized states. The screening is perfect and the potential profile is constant (flat).

[23] The incompressible regions are those regions where the Fermi level is in the gap, the electron density is constant and the potential varies by an amount of a cyclotron energy across the incompressible region due to the absence of screening.

[24] At $\nu = 1$ electrons occupy the spin-up state since this is the lowest energy state according to eq. 2.21

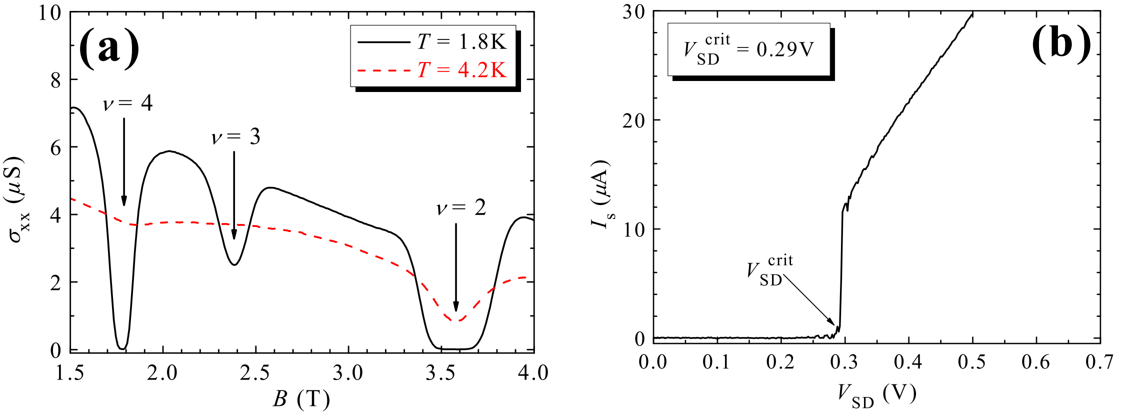

Figure 2.7: (a) Magnetotransport curves taken for a high-mobility sample ($\mu_{\mathrm{el}} = 1.6 \times 10^6 \mathrm{cm}^2\mathrm{V}^{-1}\mathrm{s}^{-1}$, $r_1 = 250\mu\mathrm{m}$, $r_2 = 750\mu\mathrm{m}$) for two lattice temperatures at fixed applied source-drain voltage $V_{\mathrm{SD}} = 0.02\mathrm{V}$. (b) $I - V$ characteristic of a QH device with Corbino geometry ($n_{\mathrm{s}} = 2.4 \times 10^{11}\mathrm{cm}^{-2}$, $\mu_{\mathrm{el}} = 0.2 \times 10^6 \mathrm{cm}^2\mathrm{V}^{-1}\mathrm{s}^{-1}$, $r_1 = 100\mu\mathrm{m}$, $r_2 = 150\mu\mathrm{m}$) at $B(\nu = 2) = 4.88\mathrm{T}$.

These composite fermions move in an effective field B^* that vanishes when $\nu = 1/2$ (for two flux quanta bound to one electron).

2.4.3 Breakdown of the Integer Quantum Hall effect

One important aspect concerning the IQHE is the determination of the limitation of this effect by the sample properties (electron density n_{s}, electron mobility μ_{el}), the sample temperature and the current through the sample. The increase of the temperature induces the reduction of the QH plateau. By exceeding a critical temperature (usually above $T_{\mathrm{crit}} > 4\mathrm{K}$) the QH plateau vanishes (see Fig. 2.7 (a)). Figure 2.7 (a) shows that for the lattice temperature $T = 4.2\mathrm{K}$, the QH plateau vanishes and the QHE breaks down.
However, a similar effect is obtained by increasing the current (the applied source-drain voltage) through the sample. Due to increasing current, the Joule heating results in a shrinking of the QH plateaus. The electrical breakdown of the QHE means that above a critical current (a critical source-drain voltage) the longitudinal resistivity increases abruptly to finite values (by orders of magnitude), leading for the corresponding magnetic fields to a deviation of ρ_{xy} from the QH plateau values (see [26] for a review of the breakdown of the QHE). This effect can be nicely observed in the current-voltage ($I - V$) characteristics (see Fig. 2.7 (b)). The figure shows the $I - V$ curves of a QH device with Corbino geometry for filling factor $\nu = 2$. When the applied source-drain voltage exceeds the critical source-drain voltage ($V_{\mathrm{SD}} > V_{\mathrm{SD}}^{\mathrm{crit}} = 0.3\mathrm{V}$ for this investigated sample), the sample current I_{s} (or the longitudinal conductivity σ_{xx}) increases suddenly to finite values.

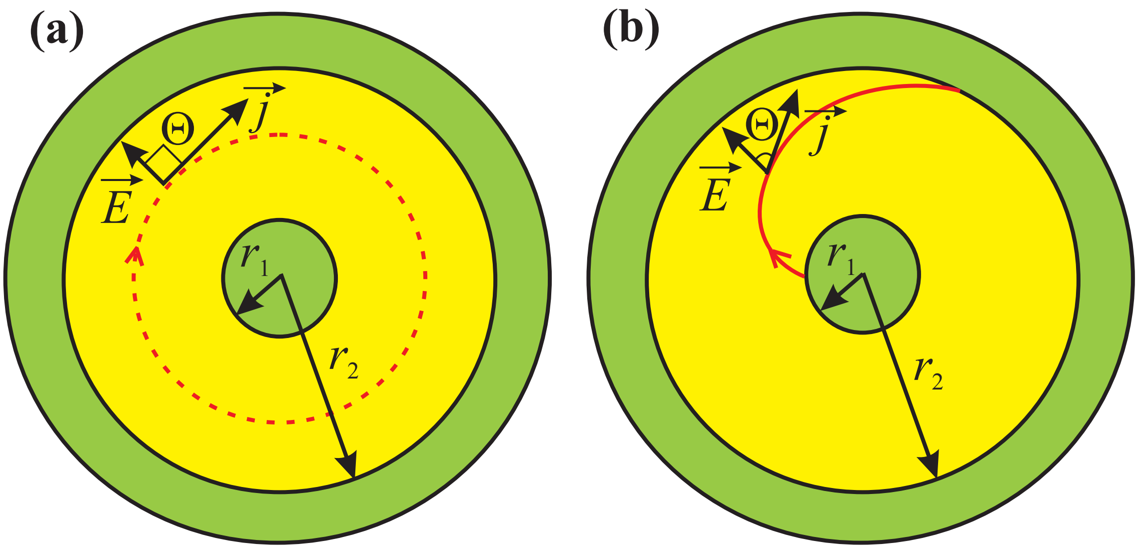

Figure 2.8: A phenomenological description of the QHE and the breakdown of the QHE. (a) In the QHE regime, the electrons orbit around the contact and no current between contacts is established. (b) In the breakdown of the QHE regime, the electrons reach the outer contact (*D*) and the current is measured.

In the following I will present a phenomenological description of the breakdown of the QHE in a QH device with Corbino geometry (see Fig. 2.8). A similar discussion is possible for QH devices with Hall bar geometry [36].

In the QH regime ($\sigma_{\mathrm{xx}} = 0$), and with Ohm's law we determine the components of the current density $\vec{j}$ (see Fig. 2.8 (a)), described by eq. 2.39. By considering that in the QH regime the longitudinal conductivity vanishes ($\sigma_{\mathrm{xx}} = \sigma_{\mathrm{yy}} = 0$), $\sigma_{\mathrm{xy}} = -\sigma_{\mathrm{yx}} \neq 0$ and by considering that the azimuthal component is zero ($E_{\mathrm{a}} = 0$), we obtain from the Ohm's law

$$\begin{pmatrix} j_{\mathrm{a}} \\ j_{\mathrm{r}} \end{pmatrix} = \begin{pmatrix} 0 & \sigma_{\mathrm{xy}} \\ -\sigma_{\mathrm{xy}} & 0 \end{pmatrix} \cdot \begin{pmatrix} 0 \\ E_{\mathrm{r}} \end{pmatrix} = \begin{pmatrix} \sigma_{\mathrm{xy}} \cdot E_{\mathrm{r}} \\ 0 \end{pmatrix} . \tag{2.46}$$

This confirms that electrons orbit around the contacts since the azimuthal component of the current density is finite ($j_{\mathrm{a}} \neq 0$) and the radial component of the current density is zero ($j_{\mathrm{r}} = 0$), see Fig. 2.8 (a). In order to describe the power dissipation in the QH device with Corbino geometry we introduce the *Hall angle* Θ.[25] For the QH regime the radial field and the current density direction are perpendicular to each other ($\vec{E}_{\mathrm{r}} \perp \vec{j}_{\mathrm{a}}$). Therefore, for $\Theta = 90^\circ$, in the QH regime, the interior power dissipation per unit area is zero:

$$\frac{\delta P_{\mathrm{int}}}{\delta A} = \vec{j} \cdot \vec{E} = \begin{pmatrix} \sigma_{\mathrm{xy}} \cdot E_{\mathrm{r}} \\ 0 \end{pmatrix} \cdot \begin{pmatrix} 0 \\ E_{\mathrm{r}} \end{pmatrix} = 0 . \tag{2.47}$$

---

[25] The Hall angle is the angle between the radial field $\vec{E}_{\mathrm{r}}$ and the current density direction $\vec{j}_{\mathrm{a}}$.

Thus, the total power dissipation is zero $P_{\text{total}} = 0$.
In the breakdown of the QHE regime ($\sigma_{\text{xx}} \neq 0$), and with Ohm's law we determine the components of the current density $\vec{j}$ (see Fig. 2.8 (b))

$$\vec{j} = \hat{\sigma} \cdot \vec{E} \Longleftrightarrow \begin{pmatrix} j_{\text{a}} \\ j_{\text{r}} \end{pmatrix} = \begin{pmatrix} \sigma_{\text{xx}} & \sigma_{\text{xy}} \\ \sigma_{\text{yx}} & \sigma_{\text{yy}} \end{pmatrix} \cdot \begin{pmatrix} E_{\text{a}} \\ E_{\text{r}} \end{pmatrix} . \tag{2.48}$$

By considering that for the breakdown of the QHE ($\sigma_{\text{xx}} = \sigma_{\text{yy}} \neq 0$), $\sigma_{\text{xy}} = -\sigma_{\text{yx}} \neq 0$ and the azimuthal component is zero ($E_{\text{a}} = 0$), Ohm's law yields

$$\begin{pmatrix} j_{\text{a}} \\ j_{\text{r}} \end{pmatrix} = \begin{pmatrix} \sigma_{\text{xx}} & \sigma_{\text{xy}} \\ -\sigma_{\text{xy}} & \sigma_{\text{xx}} \end{pmatrix} \cdot \begin{pmatrix} 0 \\ E_{\text{r}} \end{pmatrix} = \begin{pmatrix} \sigma_{\text{xy}} \cdot E_{\text{r}} \\ \sigma_{\text{xx}} \cdot E_{\text{r}} \end{pmatrix} . \tag{2.49}$$

This confirms that electrons deviate from the circular trajectories around the contacts and start to move toward the outer contact. This is because the azimuthal component of the current density is finite ($j_{\text{a}} \neq 0$) and the radial component of the current density is finite ($j_{\text{r}} \neq 0$), see Fig. 2.8 (b). In the QHE breakdown regime, the Hall angle becomes less than 90° (the radial field and the current density direction are not perpendicular anymore to each other) and the interior power dissipation per unit area is finite:

$$\frac{\delta P_{\text{int}}}{\delta A} = \vec{j} \cdot \vec{E} = \begin{pmatrix} \sigma_{\text{xy}} \cdot E_{\text{r}} \\ \sigma_{\text{xx}} \cdot E_{\text{r}} \end{pmatrix} \cdot \begin{pmatrix} 0 \\ E_{\text{r}} \end{pmatrix} = \sigma_{\text{xx}} \cdot E_{\text{r}}^2 . \tag{2.50}$$

Thus, the total power dissipation is finite $P_{\text{total}} = \sigma_{\text{xx}} \cdot E_{\text{r}}^2$.

2.5 Conclusions

In order to observe the QHE, a 2DES at low temperatures (below $T < 4\text{K}$) and high-magnetic fields are necessary. Here, the 2DES is formed at the interface of the *GaAs/ AlGaAs* heterostructure due to the trapped electrons in the approximately triangular potential well at the discontinuity of the conduction bands between *AlGaAs* and *GaAs* layers. In the 2DES the electrons move quasi-free in two spatial dimensions. Their energy is quantized in the third spatial dimension.
Applying a perpendicular magnetic field to the 2DES leads to the Landau quantization of the energies. As a result quantum effects are observed: the SdH effect, the IQHE and the FQHE (the LL's are partially filled at filling factors equal to rational fractions, $\rho_{\text{xy}} = h/ie^2$, where $i = 1/3,\ 1/5,\ 1/7,\ 2/3,\ 4/5,\ 6/7$).
When the current (applied source-drain voltage) exceeds a critical value, the longitudinal resistivity increases rapidly by orders of magnitudes while the Hall resistivity deviates from the QH values.

Chapter 3

Design of the QH devices with Corbino geometry and preparation

In this chapter the description of the fabrication of the quantum Hall (QH) samples with Corbino geometry and the experimental setup (cryostats of the magnet system, electrical pulse-generator, optical excitation source) are presented in detail. All the devices used in this work were made from *GaAs/AlGaAs* wafers of the Molecular Beam Epitaxy (MBE) facilities of the Max Planck Institut für Festkörperforschung (MPI-FKF) in Stuttgart. The preparation of the samples (cleaning, photolithography, etching, electrical bonding) was performed in the Clean Room Center (CRC) of the Physikalisch Technische Bundesanstalt (PTB) in Braunschweig.

3.1 Molecular Beam Epitaxy (MBE)

The starting point of making QH devices is the two-dimensional electron system (2DES) formed at the interface of a *GaAs/AlGaAs* heterostructure (for a review see [63]). The reason why these two materials are used is that both have nearly the same lattice constant (*GaAs* - 5.653Å and *AlGaAs* - 5.660Å), while the energy gaps between the conduction and valence bands differ considerably (*GaAs* - 1.51eV and $Al_xGa_{1-x}As$ - $(1.5+0.7x)\text{eV}$ at $T = 300\text{K}$, where *x* is the *Al* concentration) leading to a band discontinuity at their interface (see Fig. 3.2). Our samples have the *Al* concentration of $x \approx 0.3$ typically. By using the MBE technique (see Fig. 3.1) the semiconductor materials are grown on top of each other. The scheme of the MBE growth is the following: a first layer of *GaAs* is grown as *substrate*, followed by a layer of undoped *AlGaAs* grown on top of it as a *spacer layer*. Since all the samples during the experiments are at liquid *helium* (*He*) temperature (4K and below), the undoped semiconductors are insulating and therefore the doping of the *AlGaAs* layer with *Si* atoms is mandatory. In the following gedanken experiment [53, 64], we describe the formation of a 2DES at the interface between *GaAs*

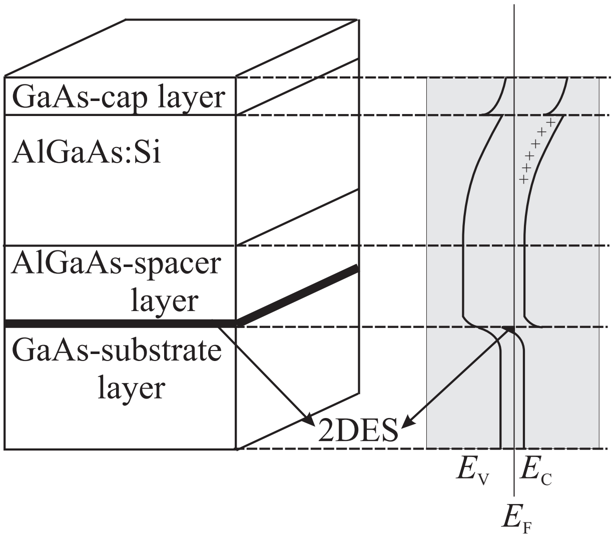

Figure 3.1: MBE growth sketch and the corresponding band structure of the GaAs/AlGaAs heterostructure.

(undoped, but *p*-type due to the growth conditions) and *AlGaAs* (*n*-type due to the *Si* atoms implanted). When the *GaAs* layer comes in contact with the *AlGaAs* the electrons flow across the *GaAs/AlGaAs* interface. The flow occurs until the charge distribution is in equilibrium, characterized by a continuous chemical potential across the interface (see Fig. 3.2). At the *GaAs/AlGaAs* interface, at the conduction band discontinuity, a nearly triangular potential well is formed. The conduction electrons are confined by this potential to a layer of a few nanometers thickness, leading to a quantization of the electron motion perpendicular to the interface and a quasi-free motion in the *x*-*y* plane parallel to the *GaAs/AlGaAs* interface [47]. The energy spectrum is given by

$$E = E_i + \frac{\hbar^2}{2m^*}\left(k_{\mathrm{x}}^2 + k_{\mathrm{y}}^2\right) , \tag{3.1}$$

where $i = 0, 1, 2, \ldots$, E is the total energy of the 2DES, m^* is the electron effective mass, k_{x} and k_{y} are the wave vectors in the plane of 2DES and E_i are the electrical subband levels of the 2D subbands.

To avoid diffusion of the *Si* atoms into the *AlGaAs* and an oxidation of *Al* atoms, one thin layer of *GaAs* is grown on top of the *Si:AlGaAs*, a so called *cap layer*. The use of the spacer layer is to minimize scattering of the electrons in the 2DES by the ionized donors (the *Si* atoms act as donors and the spacer layer acts as a barrier between electrons and donors by decreasing the Coulomb interaction between them, improving the electron mobility of the 2DES). At sufficiently large distances ($\approx 300\mathrm{nm}$) underneath the 2DES, a *Si*-layer is integrated which serves as a *backgate* and allows the modulation of the electron density n_{s} by adjusting the gate voltage V_{g}. The distance to the backgate is chosen in such

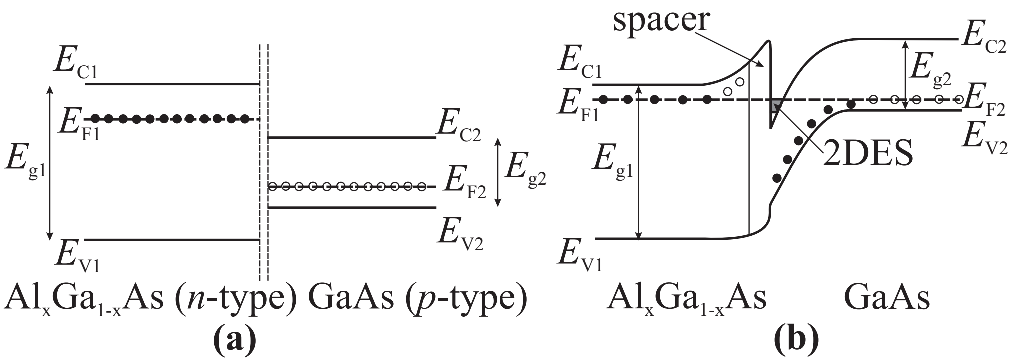

Figure 3.2: A schematic view of the band structure at the heterostructure interface for separated layers (see Fig. a)) and of the conduction band edge of the heterostructure (see Fig. b)).

a way that the 2DES can be treated being independent from the *Si*-layer.

3.2 Design of the QH devices with Corbino geometry

Starting from the MBE-grown heterostructure described in Chapter 1.1, the samples are further processed for a design of the QH devices with Corbino geometry (see Fig. 3.3). The whole processes were carried out in the CRC of PTB-Braunschweig.

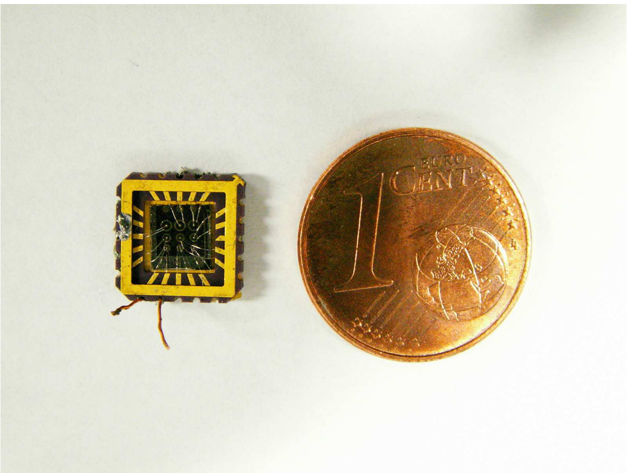

Figure 3.3: A view of the QH-device with Corbino geometry; comparison in size with the coin of 1 Eurocent.

3.2.1 Photolithography

The sample wafer is cut initially into smaller pieces of $4.5 \times 4.5\mathrm{mm}^2$ to fit into the chip carrier (see Fig. 3.3). The cleaning operations (see Fig. 3.4 a)) are performed in order to remove any possible undesired contamination from the wafer surface by spinning the wafer at about $3000\mathrm{min}^{-1}$ and rinsing it at the same time by pouring *acetone* and *isopropanol* (*isopropyl alcohol*). After about $30\mathrm{s}$ the wafer sample is removed from the rotatory plate (the wafer being fixed on the plate by vacuum), and the cleanness of the surface is checked under the optical microscope. If the surface is clean the wafer is kept into an oven at $120\,^\circ\mathrm{C}$ for about $5\mathrm{min}$. This procedure helps to improve the adhesion of the photoresist on the wafer surface by removing the remaining water contamination. In order to grow or to etch structures on the sample, it is necessary to deposit on it a kind of resist, a polymer solution. The photoresist, *AZ5214E* produced by *Clariant Inc.*, is deposited when spinning the wafer at about $3500\mathrm{min}^{-1}$ for $25\mathrm{s}$ which assures a thin photoresist film of $2\mu\mathrm{m}$ on the wafer (see Fig. 3.4 b)). After this procedure the wafer is prebaked at $90\,^\circ\mathrm{C}$ for $3\mathrm{min}$ in order to evaporate the disolvant components of the photoresist. After the previously accomplished steps the samples were ready for the exposure of the desired patterns. The patterns are obtained by using photomasks and a photolithography machine. The photomasks used in the CRC of PTB are glasses on which the desired patterns are defined in thin film of *chromium* (*Cr*). The photolithography machine uses a *Hg* lamp which produces ultra-violet (UV) light. The photoresist is sensitive to the *h* ($\lambda = 405\mathrm{nm}$)- and *i* ($\lambda = 365\mathrm{nm}$)- lines of the spectrum of the *Hg* lamp. The resist is selectively radiated according to the desired pattern, [65], by illuminating the photomask for about $20\mathrm{s}$ (see Fig. 3.4 c)). The UV radiation breaks the chemical bonds where the photoresist is exposed to radiation. The resolution of the pattern in the photoresist depends on the wavelength of the radiation used. After the exposure, the wafer is placed into a solution $(1 : 1)$ of $100\mathrm{ml}$ *deionized water* and $100\mathrm{ml}$ of *AZ developer* for $25\mathrm{s}$ (see Fig. 3.4 d)). The wafer is rinsed and dry and finally checked under the microscope whether there is any photoresist remaining.

3.2.2 Chemical etching and contact lithography

Chemical etching and contact lithography allow on one hand individual operation of designed device patterns and restricts on the other hand the flow of the electric current only in the desired (designed) area. With the etching technique, it is required to transfer the mask pattern exactly onto the material surface which means that the etching process should be anisotropic and performed only downwards into the material. The etching solution is a mixture of $30\mathrm{ml}$ *ethanol* (C_2H_5OH), $10\mathrm{ml}$ H_2O_2 and $10\mathrm{ml}$ *phosphoric acid* (H_3PO_4) in the ratio $3 : 1 : 1$. After immersing it for $20\mathrm{s}$ into the solution the wafer is etched down for about $600\mathrm{nm}$ ($30\mathrm{nm/s}$) (see Fig. 3.4 e)). The remaining photoresist was removed by the standard cleaning procedure, by using *acetone* and *isopropanol*, described previously (see Fig. 3.4 f)). The contact lithography repeats at the beginning the previ-

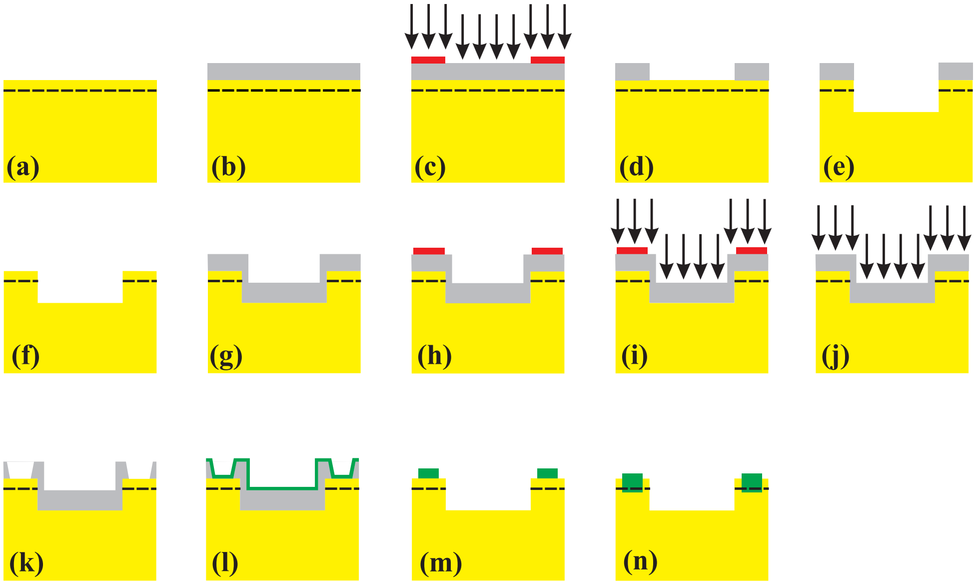

Figure 3.4: A schematic figure of the photolithography, chemical etching and contact lithography. The dashed line represents the 2DES (yellow - substrate, gray - photoresist, red - photomask and green - metal).

ously described steps accomplished during the photolithography on the mesa (wafer), by exposing and developing the photoresist areas where the contacts should be placed (see Fig. 3.4 g), h), i), j) and k)). The exposure requests a perfect match between the alignment marks of the substrate and the photomask (the tolerance is $\approx 1\mathrm{mm}$). The samples are loaded into the metalization chamber used for deposition of thin films of $200\mathrm{nm}$ *AuGe* and $25\mathrm{nm}$ *Ni* by evaporation at very low chamber pressure of $10^{-6}\mathrm{mbar}$ (see Fig. 3.4 l)). After the deposition, the samples are immersed in an *acetone* bath for $10\mathrm{min}$ which causes the photoresist to dissolve and the metallic layer on top of the resist to peel off from the surface, revealing the pattern of the designed contacts (see Fig. 3.4 m)). The annealing is performed at about $460\,^{\circ}\mathrm{C}$ and $25\mathrm{s}$ in a gas atmosphere (5% H_2 and 95% N_2) to avoid oxidation. During this process the *Ge* atoms diffuse into the *GaAs* substrate and the *Ga* atoms diffuse to the surface and form a metallic *AuGa* alloy (see Fig. 3.4 n)).

3.3 Preparation of the measurements

To perform magnetotransport measurements and further optical and electrical excitation measurements, with our samples other processes are performed like gluing the sample on the chip carrier, the electrical bonding of the sample contacts and the pins of the chip carrier, attaching the chip carrier to a sample holder and placing the sample holder into a cryostat. During the measurements, some measurement devices are controlled by a measurement automation which also performed the data acquisition. The measurement automation is accomplished by the LabVIEW written codes [66].

3.3.1 Electrical bonding

Before starting the electrical bonding, the sample should be attached to the chip carrier. To do so a cleaning process is performed by pouring *acetone* on the chip carrier surface. After drying the chip carrier by a hairdryer a small droplet of glue *GE7031 CRYOPHYSICS* or *UHU Hart* is deposited. Then, the sample is pressed on the chip carrier and left for $15\mathrm{min}$ to dry. As soon as this process is accomplished the electrical bonding can start. The electrical bonding provides the connections between the contacts and the pins of the chip carrier. *Aluminum* (*Al*) and *gold* (*Au*) are usually used as the bonding wire. A bonding machine *West Bond Model 7401* has been used as an ultrasonic 45° wedge bonder (see Fig. 3.5). The ultrasonic energy attaches a thin *Al* wire at room temperature. The wire is clamped and threaded under the bonding wedge, requiring front-to-back bonding direction.

Figure 3.5: A view of the bonding machine West Bond (1 - control panel, 2 - control display, 3 - chip carrier holder, 4 - microscope, 5 - manual control of the bonding pin, 6 - bonding pin).

3.3.2 Sample holders and cryostats

After bonding, the chip carriers with the sample (see Fig. 3.6), were connected to the sample holder. In principle, a sample holder also protects the electrical cables through which the informations flow between the measurement devices at room temperature and the chip carrier with the sample at liquid *He* temperature ($4\mathrm{K}$ or below). Both sample holders used during the real-time electrical excitation measurements and the real-time optical excitation and relaxation measurements were designed in the MPI-FKF (Stuttgart). In order to implement a rather good time resolution of our experimental setup a semirigid coaxial cable, with 50Ω impedance-matching, has been inserted into the sample holder. The cut-off frequency of the *HF* cables is $f = 26\mathrm{GHz}$ and the series capacitance is about $C_\mathrm{s} \approx 100\mathrm{pF}$.

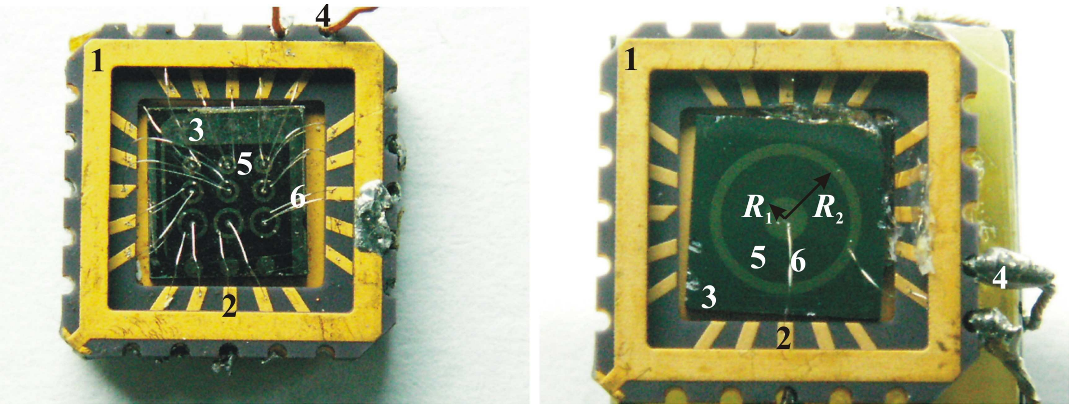

Figure 3.6: Corbino samples used for the real-time electrical excitation (left) and real-time optical excitation and relaxation measurements (right). The numbers represent: 1 - chip carrier, 2 - pin of the chip carrier, 3 - wafer, 4 - electrical wires to connect the coaxial cable, 5 - Corbino devices, 6 - electrical bondings, R_1 - inner radius, R_2 - outer radius).

The sample holder with the QH devices (see Fig. 3.7) is inserted into the cryostat such that the sample is placed exactly at the center of the magnet. The cryostat, produced by *Oxford Instruments*, is a vacuum insulated, all-metal construction with intermediate temperature shielding [67]. It consists mainly of the liquid He reservoir, a superconductive magnet and contains a variable temperature insert (VTI) (see Fig. 3.8). The *He* reservoir is a large chamber thermally isolated from outside by the outer vacuum case (OVC). In order to maintain this high thermal isolation, the OVC is pumped using a turbo molecular pump to about $2 \times 10^{-5}\mathrm{mbar}$. The liquid *He* reservoir supplies *He* to the inner chamber, the VTI, through a pick-up tube with an adjustable needle valve. At the same time it keeps the magnet at liquid *He* temperature in order to maintain the superconductive properties of the magnet coils. The VTI contains the place where the QH device is situated. The temperature can be varied by pumping the VTI with a rotary pump to

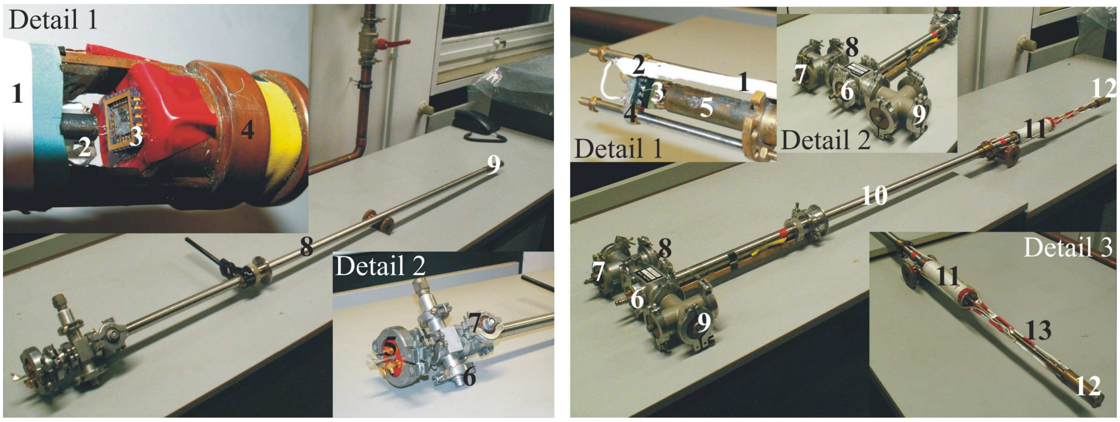

Figure 3.7: Sample holders used for the real-time electrical excitation (left) and real-time optical excitation and relaxation measurements (right). The numbers represent: 1 - Teflon tape, 2 - 50Ω resistors, 3 - chip carrier with sample, 4 - support of the chip carrier, 5 - electrical plug (left) or THz waveguide (right), 6 and 7 - electrical plugs, 8 - sample holder (left) or electrical plug (right), 9 - shield of the sample (left) or electrical plug (right), 10 - sample holder (right), 11 - superconductive laser coil (right), 12 - shield of the sample (right), 13 - electrical cables (right)).

about $10\mathrm{mbar}$, a pressure corresponding to a temperature of $1.7\mathrm{K}$. For better thermal isolation, the inner vacuum case (IVC) between the liquid *He* reservoir and the VTI was pumped to $2 \times 10^{-6}\mathrm{mbar}$. The superconducting magnet consists of a number of concentric solenoid sections together with compensating coils. Each section is wound from multifilamentary superconducting wire formed from *Niobium Titanium* ($NbTi$) filaments[1] surrounded by a stabilizing matrix of *copper* (*Cu*). The inner coils were made of *Niobium Tin* (Nb_3Sn)[2]. The main advantage of the superconducting magnets is the production of extremely high magnetic fields in laboratory scale cryostats using typically $3\mathrm{kW}$ instead of some megawatts (MW) power supplies needed for non-superconducting magnets [68]. Another advantage is its ability to operate in the *persistent mode*. In this type of operation, the superconducting circuit is closed to form a continuous loop, and the power supply can then be switched off, leaving the magnet *at field*. The field decays only very slowly, at a rate depending on the inductance, the design and the number of superconducting joints and the choice of the conductor. Protection resistors and diodes are provided for all the magnet sections, restricting the development of potentially high voltages in the event of a magnet quench. The magnet quench is accompanied by a rapid conversion from the superconducting to the normal resistive state. If any part of the windings goes *normal* or *resistive*, the current passing through it will cause the Joule heating ($\approx I^2R$); in turn

---

[1] Superconducting alloy used as a wire for superconducting magnets. Its critical temperature is $10\mathrm{K}$ and can withstand magnetic field intensity values up to $15\mathrm{T}$.

[2] Superconducting alloy which has its critical temperature of about $18\mathrm{K}$ and withstand magnetic field intensity values up to $30\mathrm{T}$. More expensive material than *Niobium Titanium* ($NbTi$).

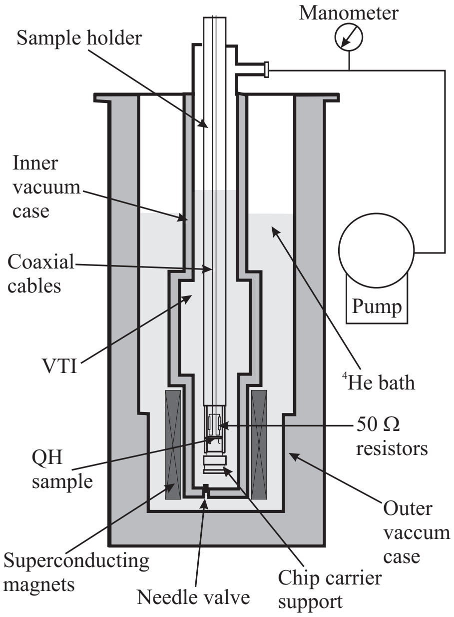

Figure 3.8: Sketch of the cryostat with the sample holder. With the control of the needle valve the temperature of the liquid *He* in VTI can be varied by pumping the VTI.

this heating increases the size of the resistive zone. Once the process has started it is impossible to stop and the stored energy in the magnet is dissipated rapidly, causing the liquid *He* to boil off very quickly and warming the magnet to a temperature which can be significantly above $4.2\mathrm{K}$.

3.3.3 Measurement devices

During the measurements many electrical devices have been used (see Fig. 3.9). The *intelligent superconducting magnet power supply Oxford IPS*$^{120-10}$, which can provide $I_{max} = 120\mathrm{A}$ and $V_{max} = 10\mathrm{V}$, controls and runs the superconducting magnet. The voltage, which is proportional to the magnetic field (and taken from a shunt resistor inside the current supply), is measured by a digital (*Keitley196*) voltmeter and recorded by a LabVIEW written code. The *intelligent level meter Oxford ILM*^{210} measures the *He* level inside the *He* reservoir. The *intelligent temperature controller Oxford ITC*^{502} measures the temperature inside the *He* reservoir and the VTI. It also controls the motion of the needle valve. The needle valve controls the flow of the liquid *He* between the *He* reservoir and the VTI. Digital multimeters *Keithley2000* measure *DC/AC* voltages ($0.1\mu\mathrm{V} - 100\mathrm{V}/750\mathrm{V}$), *DC/AC* currents ($10\mathrm{nA}/1\mu\mathrm{A} - 3\mathrm{A}$), temperatures ($-200\,^{\circ}\mathrm{C}$ - $+1372\,^{\circ}\mathrm{C}$) and frequencies ($3\mathrm{Hz} - 500\mathrm{KHz}$). A source measure unit *Keithley236* works in two modes *source-*

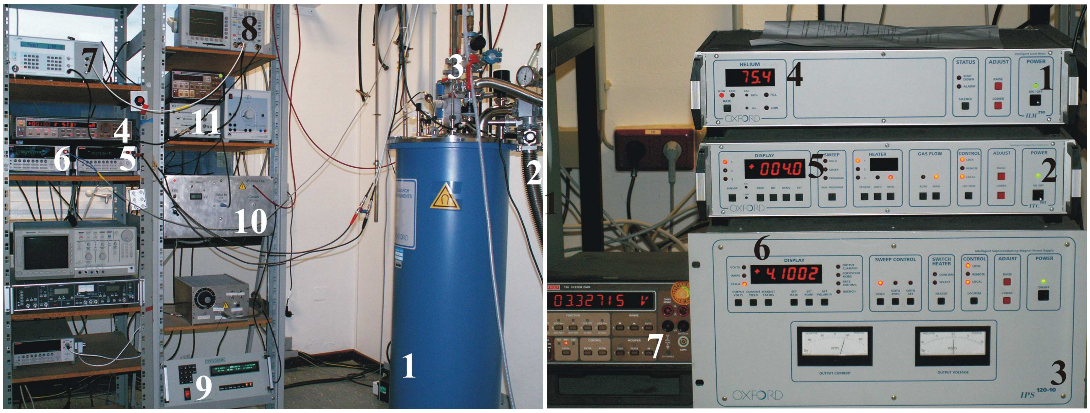

Figure 3.9: Measurement devices used for the SdH characterization and real-time measurements (1 - cryostat (left) or *Oxford ILM*^{210} (right), 2 - recovery line (left) or *Oxford ITC*^{502} (right), 3 - sample holder (left) or *Oxford IPS*$^{120-10}$ (right), 4 - *Keithley236* (left) or *He* level control display (right), 5 - *Keithley2000* gives the sample response to the applied voltage (left) or temperature control display (right), 6 - *Keithley2000* gives the resistance of the Allen-Bradley resistor (left) or magnetic field control display (right), 7 - *Berkley Nucleonics Corp. BNC 6040 Model201E* (left) or *Keitley196* (right), 8 - *Tektronix TDS3052*, 9 - magnet power supply *Cryogenic* (left), 10 - high power FET-based source for the *p*-Ge laser, 11 - *Hewlett Packard 8013B*).

measure: $I - V$ ($-100\text{fA} < I < 100\text{mA}$) and $V - I$ ($100\mu\text{V} < V < 100\text{V}$). During our measurements the source unit was set in the $V - I$ mode and provided the voltage between the source (*S*) and drain (*D*) contacts of the QH device with Corbino geometry. During the real-time measurements of electrical excitation I have used besides the previously described measurement devices also the universal pulse generator *Berkley Nucleonics Corp. BNC 6040 Model201E* which produces rectangular electrical pulses of pulse widths $3\text{ns} - 640\text{s}$. The pulse period (minimum) for pulse widths $< 160\text{ns}$ is 5ns and for pulse widths $\geq 160\text{ns}$ is 150ns at a repetition rate of $0.01\text{Hz} - 100\text{MHz}$. The sample response picked up by the serial 50Ω resistor is displayed and measured by a digital phosphor oscilloscope *Tektronix TDS3052*. This digital oscilloscope has two channels, and is able to see in parallel the excitation electrical pulse and the electrical sample pulse (sample response). The *TDS3052* has a bandwidth of 500MHz. For performing the real-time optical measurements of excitation and relaxation, all the previous measurement devices have been used. Additionally, the magnet power supply *Cryogenic* was used to control the superconducting coils of the *p*-Ge laser. The energy of the laser is controlled by the high power FET (field effect transistor)-based electrical pumping source. Further, the pulse generator *Hewlett Packard 8013B* (transition time 3.5ns, pulse width: $10\text{ns} - 1\text{s}$, pulse delay $< 35\text{ns} - 1\text{s}$, repetition rate $1\text{Hz} - 50\text{MHz}$) controls the operation of the laser in the pulse mode. The measurement devices have been controlled and the data acquisition have been performed by using LabVIEW software from *National Instruments*. For

Shubnikov-de Haas (SdH) oscillations and for $I - V$ characterization, for the real-time of electrical and optical excitation measurements, a number of LabVIEW written codes were developed, which automated the device control and data acquisition [66].

Chapter 4

Two-Landau levels model for the excitation and relaxation of hot electrons

In this chapter the two-Landau levels model for the excitation and relaxation of hot electrons is discussed [40]. The model discusses the time evolution and the spatial evolution of the excited electrons near the breakdown of the QHE. It also simulates the space-resolved excitation measurements described in Ref. [32, 33, 36]. To describe the breakdown of the QHE, two ideas are combined: the avalanche-like electron heating [30–40] and the inter-Landau-level scattering [33, 40, 42].

4.1 Description of the two-Landau levels model

It is well known that for $T = 0\mathrm{K}$ at an integer filling factor ν the Fermi energy is within the band gap, the gap between two adjacent Landau levels (LL's). The presence of the Fermi level (FL) in the band gap leads to a vanishing resistivity $\rho_{\mathrm{xx}} = 0$. The quantum Hall effect (QHE) breakdown can be characterized by the excitation of electrons from the filled LL's below the FL to the empty LL's above the FL. In other words the electron system shows a transition from vanishing resistivity into a non-vanishing resistivity $\rho_{\mathrm{xx}} \neq 0$, characterizing a dissipative regime. In this model the resistivity ρ_{xx} is assumed proportional to the number of excited electrons N across the band gap ($\rho_{\mathrm{xx}} \propto N$) as considered in previous works [31, 32, 36]. Electrons are excited to the upper LL with a characteristic gain rate due to the Joule heating, and the electrons relax after a certain relaxation time τ_{rel} to the lower LL due to energy loss processes (electron-phonon scattering and so on), see Fig. 4.1. In reality, due to the presence of impurities, defects, roughnesses, the Landau energy levels broaden (see Fig. 4.2 a)) and are considered theoretically to have a Gaussian

shape. By using a microscopic picture the LL's may be displayed as in Fig. 4.2 b).
How can the electrons be excited? The electrons can be excited to upper LL's by different means of excitation. One excitation mechanism is *the optical excitation* - by illuminating the electron system with a laser of energy $\hbar\omega_{\text{laser}}$. Another mechanism is *the thermal excitation* - by simply increasing the temperature of the electron system the electrons elevate in their energies by $k_{\text{B}}T$ (where k_{B} is the Boltzmann's constant, T is the temperature of the electron system) provided that the thermal energy $k_{\text{B}}T$ is comparable with the energy gap between two LL's. *The tunneling* is another possibility to excite electrons and can be achieved by applying an electric field and thus a current through the electron system subjected to a perpendicular magnetic field. As a result *the Hall field* $\vec{E}_{\text{H}}$, perpendicular to the current flow, tilts the LL's and thus increases the probability of the electrons to tunnel from the lower occupied state (LL) to the upper empty state (LL), see Fig. 4.2 b).
The change in time of the population of the upper level dN/dt, depends on the balance between the generation rate dN_{gain}/dt and the relaxation rate dN_{loss}/dt.

$$\frac{dN}{dt} = \frac{dN_{\text{gain}}}{dt} - \frac{dN_{\text{loss}}}{dt}\,. \tag{4.1}$$

Due to different energy-loss processes [33, 40], the density of electrons in the upper LL decays in a characteristic time scale τ_{rel}:

$$\frac{dN_{\text{loss}}}{dt} = \frac{N}{\tau_{\text{rel}}}\,. \tag{4.2}$$

As already mentioned, the effect of the Hall field is the tilting of the LL's. This increases the probability of the electron to tunnel from the lower LL to the upper LL. A possible mechanism for the occurrence of this transition is the *quasi-elastic-inter-Landau-level scattering* (QUILLS). The QUILLS-model is based on the assumption of an overlap of the tails of the wave functions belonging to adjacent LL's[1] and it assumes tunneling of electrons between the occupied initial and the empty final states due to the Hall field, leading to a gain rate of:

$$\frac{dN_{\text{gain}}}{dt} = \frac{n_{\text{low}}}{\tau_{\text{exc}}} \cdot \exp\left[-\frac{\Delta y^2}{4\ell_{\text{B}}^2}\right], \tag{4.3}$$

where: n_{low} is the electron density of available initial states in the lower LL, Δy is the spatial separation between the initial and final states, and $\ell_{\text{B}}^2 = \hbar/eB$ is the square of the magnetic length (corresponding to the length scale of the overlap of the corresponding electron wave functions).
By assuming a homogeneous current flow along the Hall bar (in x direction, at filling factor $\nu = 2$) the resulting Hall field in y direction determines the tilting of the LL's across the Hall bar. The electrons are excited to the upper level at a rate depending exponentially on the Hall field by

$$\Delta y = \frac{\hbar\omega_{\text{c}}}{eE_{\text{H}}}\,. \tag{4.4}$$

---

[1] QUILLS-model requires a spatial overlap of the wave function of the highest occupied LL and the wave function of the lowest empty LL.

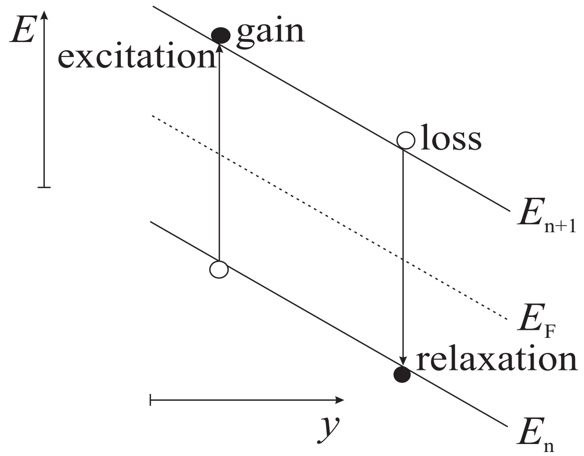

Figure 4.1: Simple sketch of the excitation and relaxation processes between two tilted Landau levels (LL's).

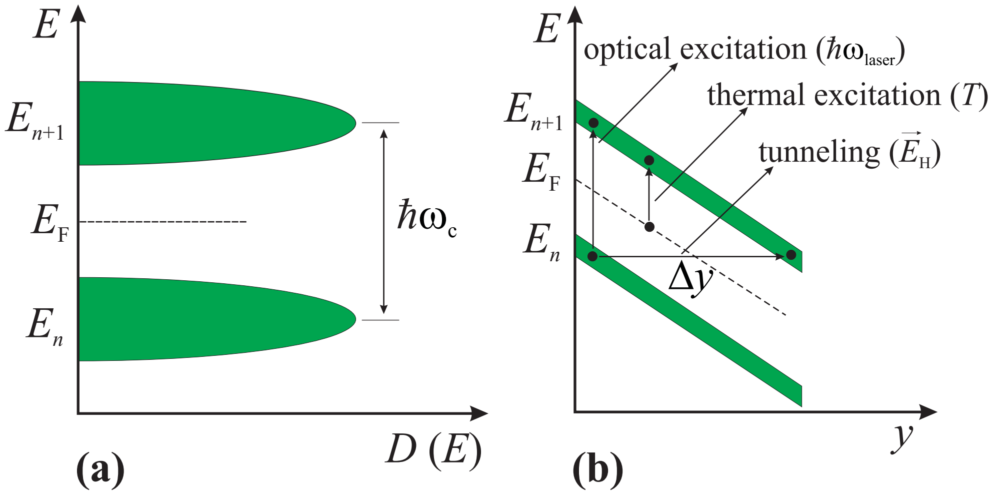

Figure 4.2: (a) Density of states with broad LL's due to the impurities. (b) Different mechanisms to excite electrons between 2 LL's.

This leads to a gain rate of

$$\frac{dN_{\mathrm{gain}}}{dt} = \frac{n_{\mathrm{low}}}{\tau_{\mathrm{exc}}} \cdot \exp\left[-\left(\frac{\hbar\omega_{\mathrm{c}}}{2e\ell_{\mathrm{B}}E_{\mathrm{H}}}\right)^2\right] = \frac{n_{\mathrm{low}}}{\tau_{\mathrm{exc}}} \cdot \exp\left[-\left(\frac{\hbar\omega_{\mathrm{c}}}{eV_{\mathrm{H}}} \cdot \frac{w}{2\ell_{\mathrm{B}}}\right)^2\right], \tag{4.5}$$

where $V_{\mathrm{H}} = w \cdot E_{\mathrm{H}}$ is the Hall voltage and w is the width of the sample.
An estimation of the spatial separation between initial and final states Δy gives a value of the order of $\approx 1\mu\mathrm{m}$, which is two orders of magnitude bigger than the magnetic length $\ell_{\mathrm{B}} \approx 12\mathrm{nm}$, leading to a negligibly small tunneling rate of eq. 4.3. To overcome this small tunneling rate, inside the electron system must be other mechanisms which enhance the tunneling rate considerably. The presence of impurities, defects and roughnesses induces

potential fluctuations (locally enhanced electrical potentials) [27–29]. These potential fluctuations lead clearly to a decrease of the average separation between the LL's and lead to an additional tunneling rate. The screening effects create quasi-metallic (so-called *compressible*) regions and insulator-like *incompressible* strips (with constant electron density $n_\mathrm{s} = \nu eB/h$, where the potential drop occurs) which separate adjacent compressible islands[2] (the electrons localized in these islands do not contribute to the general current)[3] [43,58,69–71]. As a consequence, the presence of the compressible islands reduces the effective width of the incompressible regions (strips) to a value $w_0 \leq w$ (where w is the geometrical width of the Hall bar). The excited electrons to the upper LL come from the incompressible strips since the electrons in the compressible islands are localized and do not contribute to the dissipationless current. Since in time, the electrons are excited more and more to the upper LL, the area and the effective width of the incompressible strips decreases while the area of compressible islands increases practically linearly with the number of the excited electrons N. The shrink of the incompressible strips stops when the effective width becomes too small to carry dissipationless current. At this critical moment the density of excited electrons in the upper LL reaches the critical value N_bd, at which the breakdown of the QHE is complete.

The effective width of remaining incompressible channels decreases with the square root of the number of the excited electrons across the gap (for a circular shape of the compressible islands [40]), and can be modeled as (see Fig. 4.3):

$$w_\mathrm{eff} = w(N) = \sum_\mathrm{i} \Delta y_\mathrm{i} = w_0 \left(1 - \sqrt{\frac{N}{N_\mathrm{bd}}}\right) . \tag{4.6}$$

Only those remaining and available states in incompressible strips contribute to the excitation process ($n_\mathrm{low} = n_\mathrm{s} - N$ and $E_\mathrm{H}(N) = V_\mathrm{H}/w_\mathrm{eff}$). Thus, eq. 4.6 shows that by decreasing the effective width of the remaining incompressible strips $w(N)$ with increasing the number (density) of the excited electrons N the gain rate of the excited electrons increases exponentially (an avalanche-like excitation to the upper LL and the breakdown of the QHE).

The previous gain rate eq. 4.5 transforms into:

$$\frac{dN_\mathrm{gain}}{dt} = \frac{n_\mathrm{s} - N}{\tau_\mathrm{exc}} \cdot \exp\left\{ - \left[\frac{\hbar\omega_\mathrm{c}}{eV_\mathrm{H}} \cdot \frac{w_0}{2\ell_\mathrm{B}} \left(1 - \sqrt{\frac{N}{N_\mathrm{bd}}}\right)\right]^2 \right\} . \tag{4.7}$$

The change in time of the population N of the upper LL (see eq. 4.1) can now be written as

$$\frac{dN}{dt} = \frac{n_\mathrm{s} - N}{\tau_\mathrm{exc}} \cdot \exp\left\{ - \left[\frac{\hbar\omega_\mathrm{c}}{eV_\mathrm{H}} \cdot \frac{w_0}{2\ell_\mathrm{B}} \left(1 - \sqrt{\frac{N}{N_\mathrm{bd}}}\right)\right]^2 \right\} - \frac{N}{\tau_\mathrm{rel}} . \tag{4.8}$$

---

[2] Compressible region means that, due to perfect screening, one (flat) Landau level is there pinned to the Fermi level (more precisely: the electrochemical potential, which is spatially constant in thermodynamic equilibrium).

[3] For the IQHE, incompressible and compressible strips correspond to integer and noninteger, respectively, filling factors ν.

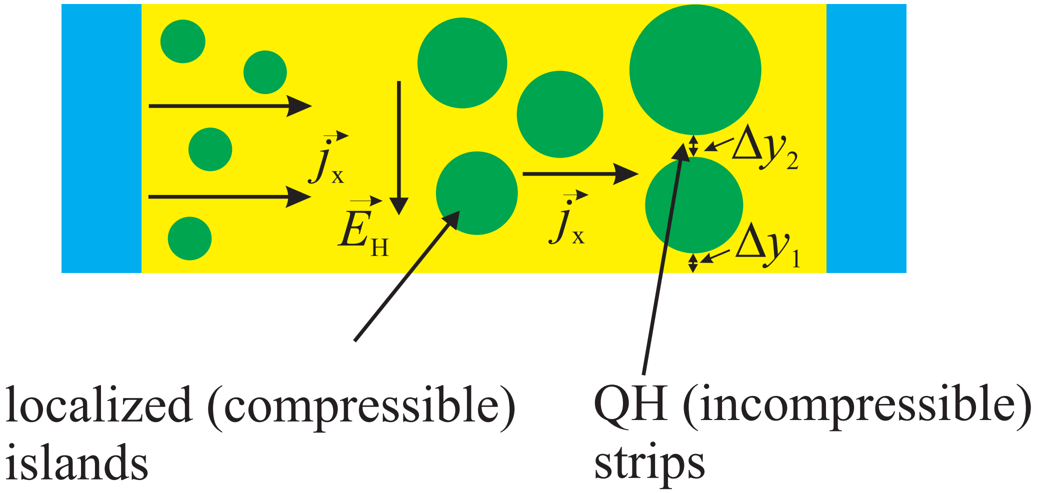

Figure 4.3: A phenomenological picture of the evolution of the incompressible strips and compressible islands during the avalanche-like excitation, the transition from QH state to QHE breakdown state. In reality this picture would be more complicated since enlarging a compressible region by excitation of electrons from incompressible regions involves always two compressible regions (e.g. a hole-like and an electron-like) with a potential difference equal to the cyclotron energy. Moreover, the compressible islands are induced by local potential landscape and can therefore be of noncircular form.

Because the QUILLS process is a heating process, then the density of electrons N in the upper LL cannot exceed the density of electrons n_{low} in the lower LL,

$$N \leq n_{\mathrm{low}} = n_{\mathrm{s}} - N \Longrightarrow N \leq \frac{n_{\mathrm{s}}}{2} \Longleftrightarrow N_{\mathrm{bd}} \leq \frac{n_{\mathrm{s}}}{2} \,. \tag{4.9}$$

If the density of electrons N in the upper LL exceeds the density of electrons n_{low} in the lower LL then the system would develop an inversion population ($N_{\mathrm{bd}} \geq n_{\mathrm{s}}/2$). Since the breakdown of the QHE implies $N = N_{\mathrm{bd}}$ (at the saturation), then $N(t) = N_{\mathrm{bd}}$ must be a stationary solution of eq. 4.8 after the saturation:

$$\frac{dN}{dt} = 0 = \frac{n_{\mathrm{s}} - N_{\mathrm{bd}}}{\tau_{\mathrm{exc}}} - \frac{N_{\mathrm{bd}}}{\tau_{\mathrm{rel}}} \Longrightarrow \frac{\tau_{\mathrm{exc}}}{\tau_{\mathrm{rel}}} = \frac{n_{\mathrm{s}}}{N_{\mathrm{bd}}} - 1 \geq 1 \Longleftrightarrow \tau_{\mathrm{exc}} \geq \tau_{\mathrm{rel}} \,. \tag{4.10}$$

The eq. (4.10) represents a kind of *boundary condition* of the electron system not to develop an inversion population ($\tau_{\mathrm{exc}} \leq \tau_{\mathrm{rel}} \longrightarrow$ accumulation of electrons on the upper LL $\Longleftrightarrow$ inversion population). This condition also restricts the electron system from exciting all electrons between two LL's by the balance between excitation and relaxation processes.
In order to solve the nonlinear differential eq. 4.8 numerically, some dimensionless vari-

ables are introduced,

$$\widetilde{N}=\frac{N}{N_{\rm bd}}\,,\;\widetilde{t}=\frac{t}{\tau_{\rm rel}}\,,\;\alpha=\frac{\hbar\omega_{\rm c}}{eV_{\rm H}}\cdot\frac{w_0}{2\ell_{\rm B}}\,,\;\widetilde{\tau}=\frac{\tau_{\rm exc}}{\tau_{\rm rel}}\,,\tag{4.11}$$

and thus our differential eq. 4.8 turns into:

$$\frac{d\widetilde{N}}{d\widetilde{t}}=\frac{1+\widetilde{\tau}-\widetilde{N}}{\widetilde{\tau}}\cdot\exp\left[-\alpha^2\left(1-\sqrt{\widetilde{N}}\right)^2\right]-\widetilde{N}\equiv\Phi(\widetilde{N})\,.\tag{4.12}$$

By considering the case of equal excitation and relaxation times $\tau_{\rm exc}=\tau_{\rm rel}\iff\widetilde{\tau}=1$ the differential eq. 4.12 is inverted into an integral,

$$\widetilde{t}=\int_0^{\widetilde{N}}\frac{dy}{f(y)}\,,\tag{4.13}$$

where for simplicity we have introduced the following notation: $\widetilde{N}=y$ and $\Phi(\widetilde{N})=f(y)$.

Since $y=\widetilde{N}$ is proportional to the number of excited electrons in the upper LL, the initial solution is $y(\widetilde{t}=0)=0$, which determines the lower limit of the integral 4.13. If, with increasing y, $f(y)$ approaches the value zero at $y=y_0$ ($f(y)=0$ and y_0 - smallest of the possible zeros), the integrand of eq. 4.13 has a nonintegrable singularity at y_0. Thus, y_0 is the uppermost possible upper limit of the integral 4.13 and corresponds to the number of electrons in the upper LL which will be approximated in the limit $\widetilde{t}\to\infty$. For any $y(\widetilde{t})$ satisfying the condition $0<y(\widetilde{t})<y_0$ we evaluate the integral 4.13 taking $y(\widetilde{t})$ as the upper limit in order to determine $\widetilde{t}(y)$, the inverse of $y(\widetilde{t})$, the desired time evolution of the number of excited electrons in the upper LL.

The behavior of the integrand y as a function of

$$\alpha=\frac{\hbar\omega_{\rm c}}{eV_{\rm H}}\cdot\frac{w_0}{2\ell_{\rm B}}\tag{4.14}$$

can be discussed for two situation:

- no breakdown: equation $f(y,\widetilde{\tau},\alpha)$ has two zeros

  $$f(y_0)=f(y_1)=0\,,\tag{4.15}$$

  in the interval $0<y<1$ ($0<y_0<y_1<1$ and y_0,y_1 depend on $\widetilde{\tau}$ and α);

- breakdown: equation $f(y,\widetilde{\tau},\alpha)$, for given $\widetilde{\tau}$ there is exactly one critical value $\alpha_{\rm crit}$ for which the two zeros coincide ($y_0=y_1$). In this situation the function $f(y)$ must have a minimum at this y_0 and its first derivative $f^{'}(y)=df(y)/dy$ must be zero in this point ($f^{'}(y_0)=0$). By denoting the position of the two-fold zeros by $y_{\rm crit}$, with $y_{\rm crit}=y_0=y_1$, for $\forall\widetilde{\tau}$ there are two equations from which the two critical variables ($\alpha_{\rm crit}$ and $y_{\rm crit}$) are determined:

  $$f(y_{\rm crit},\widetilde{\tau},\alpha_{\rm crit})=0\,,\tag{4.16}$$

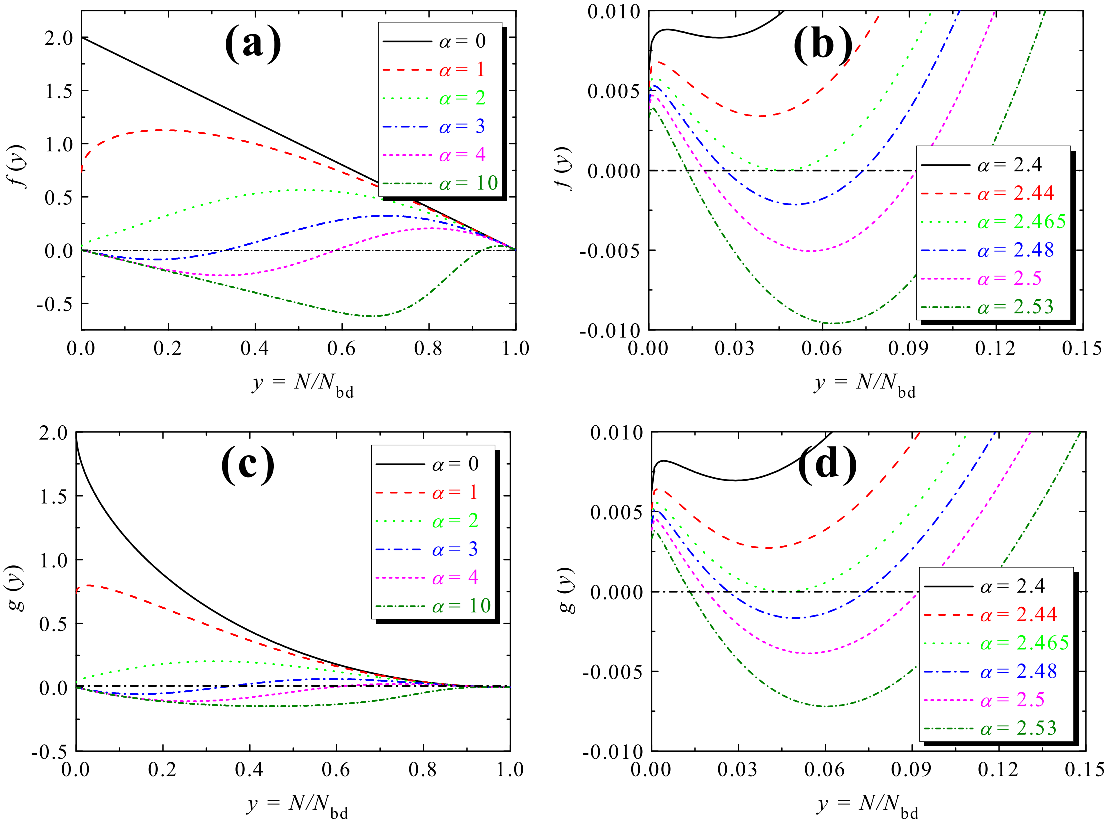

Figure 4.4: Behavior of the functions $f(y) = \Phi(N/N_{\mathrm{bd}})$ (a)-(b) and $g(y) = (1 - \sqrt{N/N_{\mathrm{bd}}}) \cdot f(N/N_{\mathrm{bd}})$ (c)-(d) calculated for $\widetilde{\tau} = 1$ and plotted for different α values. (b)-(d) show magnifications of (a)-(c), respectively, near $N/N_{\mathrm{bd}} \to 0$ and for different α values. For $\alpha = \alpha_{\mathrm{crit}} = 2.465$ our functions have only one zero $(0 < y_0 = y_1 < 1)$. The behavior of the function $g(y) = (1 - \sqrt{N/N_{\mathrm{bd}}}) \cdot f(N/N_{\mathrm{bd}})$ (right) would be important later, for the description of the space evolution of the excited electrons N/N_{bd} (see the integrand of eq. 4.24) when the drift velocity of the electrons, imposed by the current, changes with the number of the excited electrons (see eq. 4.22).

and

$$f'(y_{\mathrm{crit}}, \widetilde{\tau}, \alpha_{\mathrm{crit}}) = 0\,. \tag{4.17}$$

Equation 4.16 is used to express α_{crit} in terms of y_{crit}

$$f(y_{\mathrm{crit}}, \widetilde{\tau}, \alpha_{\mathrm{crit}}) = 0 \Longrightarrow \alpha_{\mathrm{crit}} = \alpha_{\mathrm{crit}}(y_{\mathrm{crit}}, \widetilde{\tau})\,, \tag{4.18}$$

and therefore eq. 4.17 could be rewritten as

$$f'(y_{\mathrm{crit}}, \widetilde{\tau}, \alpha_{\mathrm{crit}}(y_{\mathrm{crit}}, \widetilde{\tau})) = 0\,. \tag{4.19}$$

Solving eq. 4.16 for the case of equal excitation and relaxation times, $\widetilde{\tau} = 1$, we determine α_{crit}

$$\alpha_{\mathrm{crit}} = \frac{\sqrt{ln\frac{2-y_{\mathrm{crit}}}{y_{\mathrm{crit}}}}}{1-\sqrt{y_{\mathrm{crit}}}} \,. \tag{4.20}$$

By inserting eq. 4.20 into eq. 4.17 for a given parameter $\widetilde{\tau} = 1$ we solve eq. 4.17 numerically by using NAG subroutines and determine $y_{\mathrm{crit}} = 0.045991$, the value of y corresponding to α_{crit}. The determined y_{crit} is introduced into eq. 4.20 and determine α_{crit} being $\alpha_{\mathrm{crit}} = 2.46489 \approx 2.465$ (see Fig. 4.4).

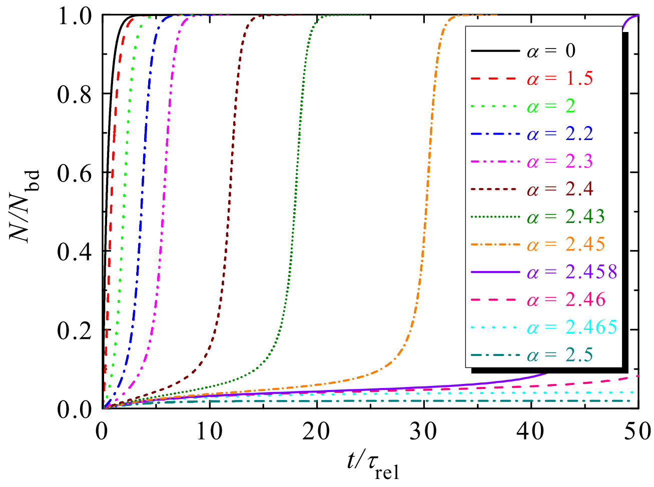

Figure 4.5: Time evolution of N/N_{bd} electrons for different α values, calculated from eq. 4.13, where $f(y) = \Phi(N/N_{\mathrm{bd}})$ defined by eq. 4.12 with $\widetilde{\tau} = 1$.

Finally we divide the interval $0 < y < y_0$ into about 1000 subintervals and calculate the integral 4.13 in each subinterval. Starting with the lowest subinterval and adding successive results, we obtain $\widetilde{t}(y)$ (see Fig. 4.5). Thus, typical traces result from solving eq. 4.13 for given values of α, that addresses the inverse Hall potential V_{H} or imposed current I.
Looking at the Fig. 4.5 we distinguish the discussed 2 situations:

- no breakdown for $\boldsymbol{\alpha > \alpha_{\mathrm{crit}}}$: N approaches a small value bounded $N_{\mathrm{crit}} << N_{\mathrm{bd}}$;
- breakdown for $\boldsymbol{\alpha < \alpha_{\mathrm{crit}}}$: N increases toward the much larger breakdown value N_{bd}, which is however $N_{\mathrm{bd}} << eB/h$.

The physically interesting result of this model is that, for small α-values (high imposed currents), the number of excited electrons $N(t)$ approaches the limit $N/N_{\mathrm{bd}} = 1$, corresponding to the QHE breakdown, after some characteristic time. For large α-values (low

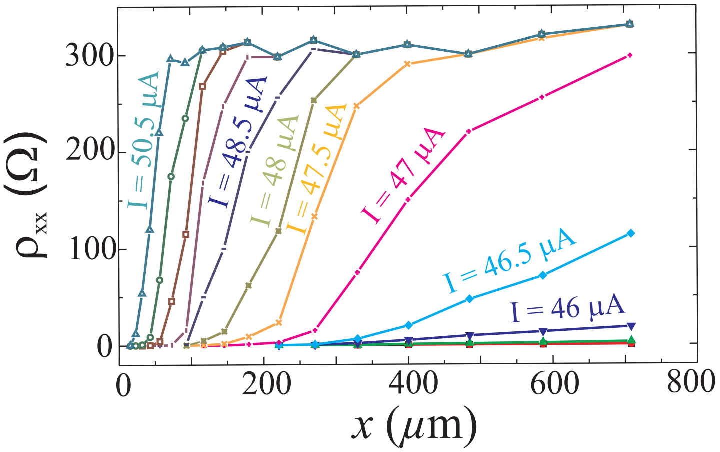

Figure 4.6: Space-resolved measurements shows the measured ρ_{xx} as a function of the contact position x from the constriction $x = 0$. The resistivity increases faster for higher imposed currents and reaches the saturation value $\rho_0 = 300\Omega$ after characteristic lengths [33].

imposed currents) this limit is smaller than N_{bd} by orders of magnitude, corresponding to the QHE regime, and therefore there is no breakdown. The rapid change from no-breakdown to breakdown behavior in a narrow interval of applied current strengths is an interesting feature of this model. The time evolution of excited electrons in the upper LL behaves qualitatively similar to the spatial evolution of the resistance in the experiments monitoring the spatial evolution of the QHE breakdown [32, 33].

4.2 Adaption of the two-Landau levels model to the experiments

In order to adapt the model to the experiment [33], see Fig. 4.6, the time evolution of the excited electrons in the upper LL is changed into spatial evolution by implementing the imposed current, which causes a drift of the electrons with the drift velocity v_{D}.

$$v_{\mathrm{D}} = \frac{E_{\mathrm{H}}}{B} = \frac{V_{\mathrm{H}}}{B \cdot w_0} \,. \tag{4.21}$$

In the following treatment, we consider two different situations:

Situation 1: $\boldsymbol{v_{\mathrm{D}} = v_{\mathrm{D}}(\widetilde{N})}$ $\longrightarrow$ the drift velocity v_{D} depends on the number of excited electrons $\widetilde{N} = N/N_{\mathrm{bd}}$. This means that the drift velocity increases with decreasing width of the remaining incompressible strips (see eq. 4.6) carrying the dissipationless current and diverges at the breakdown (see eq. 4.22):

$$v_{\mathrm{D}}(\widetilde{N}) = \frac{E_{\mathrm{H}}}{B} = \frac{V_{\mathrm{H}}}{B \cdot w_{\mathrm{eff}}(\widetilde{N})} = \frac{V_{\mathrm{H}}}{B \cdot w_0 (1 - \sqrt{\widetilde{N}})} \,, \tag{4.22}$$

and thus the spatial evolution $x(\widetilde{N})$ of the excited electrons is determined from

$$dx(\widetilde{N}) = v_{\mathrm{D}}(\widetilde{N}) \cdot dt = v_{\mathrm{D}}(\widetilde{N}) \cdot \tau_{\mathrm{rel}} \cdot \frac{d\widetilde{N}}{\Phi(\widetilde{N})} \Longrightarrow x(\widetilde{N}) = \tau_{\mathrm{rel}} \cdot \int_0^{\widetilde{N}} \frac{v_{\mathrm{D}}(y) \cdot dy}{\Phi(y)} \,, \tag{4.23}$$

where we have also included eq. (4.11) and eq. (4.12). By including eq. 4.22 the spatial evolution eq. 4.23 changes into:

$$x(\widetilde{N}) = \tau_{\mathrm{rel}} \cdot \frac{V_{\mathrm{H}}}{B \cdot w_0} \cdot \int_0^{\widetilde{N}} \frac{dy}{(1 - \sqrt{y}) \cdot f(y)} \,, \tag{4.24}$$

with $f(y) = \Phi(y)$.
At the beginning we have assumed a homogeneous current distribution across the Hall bar, that the Hall field is constant ($E_{\mathrm{H}} = V_{\mathrm{H}}/w_{\mathrm{bar}}$ with $w_{\mathrm{bar}} = 50\mu\mathrm{m}$). With this assumption and with the experimental data from the experiments [33] we notice that the evaluation of eq. (4.11), with $w_0 = w$, leads to a very large $\alpha \approx 40$. This value corresponds to a QHE regime very far from the breakdown regime for V_{SD}-values far smaller than measured for the breakdown (see Fig. 4.5). Thus the use of w as a replacement of w_0 in eq. (4.11) is not sufficient to reach a quantitatively satisfying description of the measurements.
But as we already mentioned in advance, in the real space, the samples are not perfect, they contain either defects or impurities which induce potential fluctuations. The screening of the potential fluctuations induces the appearance of compressible islands surrounded by the incompressible strips where the dissipationless current flows. Taking into account that the Hall voltage drops only across the incompressible strips [25,43,58,71,72], we determine w_0, the effective width of the incompressible strips, being $w_0 = 3.1\mu\mathrm{m}$ by using $I_{\mathrm{crit}} = 46\mu\mathrm{A}$ and $\alpha_{\mathrm{crit}} = 2.465$. By using $\widetilde{\tau} = 1$ and eq. 4.11 we determine the relation between α and the imposed currents I (with $V_{\mathrm{H}} = R_{\mathrm{H}} \cdot I$ and $R_{\mathrm{H}}(\nu = 2) = 12.9\mathrm{k}\Omega$) being $\alpha(I) = \alpha_{\mathrm{crit}} I_{\mathrm{crit}}/I$ ($2.25 \leq \alpha \leq 2.52$). With the choice of the experimental data $V_{\mathrm{H}} = 0.59\mathrm{V}$, $B = 5.8\mathrm{T}$, $\tau_{\mathrm{rel}} = 1\mathrm{ns}$ and the determined $w_0 = 3.1\mu\mathrm{m}$ the spatial evolution eq. 4.24 becomes:

$$x(\widetilde{N}) = 32.8[\mu\mathrm{m}] \cdot \frac{I}{I_{\mathrm{crit}}} \cdot \int_0^{\widetilde{N}} \frac{dy}{(1 - \sqrt{y}) \cdot f(y)} \,. \tag{4.25}$$

With the assumption of a resistivity proportional to the number of electrons excited across the gap we finally calculate the resistivity profile as a function of the position x,

$$\rho_{\mathrm{xx}}(x) = \rho_0 \cdot \widetilde{N}(x) = \rho_0 \cdot \frac{N(x)}{N_{\mathrm{bd}}} \,, \tag{4.26}$$

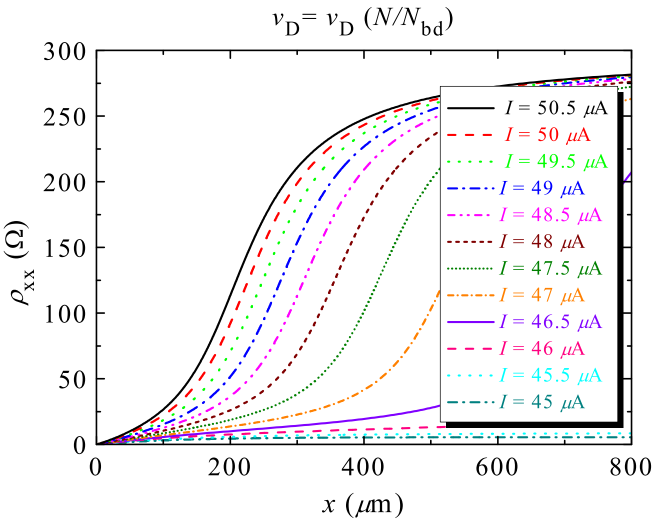

Figure 4.7: Calculated resistivities ρ_{xx} (see eq. 4.26) for different imposed currents $I = 45\mu\text{A} \ldots 50.5\mu\text{A}$ measured during the experiments [33].

where $\rho_0 = 300\Omega$ is the saturation value of the measured longitudinal resistivity ρ_{xx} (see Fig. 4.6).
The resistivity profile $\rho_{\text{xx}}(x)$ versus the position x (see Fig. 4.7) shows an avalanche-like excitation like in the experiments [33] but some important disagreements still remain. The QHE breakdown develops after some characteristic drift length as a function of the imposed current in the interesting avalanche regime. We notice in Fig. 4.7 at the highest currents the QHE breakdown is reached only at very large x values compared to the measured values (Fig. 4.6). This considerable difference could be explained on the basis of a misleading assumption: the drift velocity increases with the number of excited electrons which in turn decreases the effective width of the incompressible strips and diverges at the breakdown when N approaches the saturation value N_{bd} of eq. 4.6. However, this assumption does not explain the remaining quantitative difference between the model and the experimental data.

Situation 2: $v_{\mathbf{D}} = \mathbf{const.}$ $\longrightarrow$ the drift velocity v_{D} does not depend on the number of excited electrons N in the upper LL, so that the electrons move at constant drift velocity through the Hall bar (see eq. 4.21). The spatial evolution of the number of excited electrons is determined from:

$$dx = v_{\text{D}} \cdot dt = v_{\text{D}} \cdot \tau_{\text{rel}} \cdot \frac{d\widetilde{N}}{\Phi(\widetilde{N})} \Longrightarrow x = v_{\text{D}} \cdot \tau_{\text{rel}} \cdot \int_0^{\widetilde{N}} \frac{dy}{\Phi(y)} \tag{4.27}$$

and with help of eq. 4.21, it turns into

$$x = \frac{V_{\text{H}}}{B \cdot w_0} \cdot \tau_{\text{rel}} \cdot \int_0^{\widetilde{N}} \frac{dy}{f(y)} = 32.8[\mu\text{m}] \cdot \frac{I}{I_{\text{crit}}} \cdot \int_0^{\widetilde{N}} \frac{dy}{f(y)}\,, \tag{4.28}$$

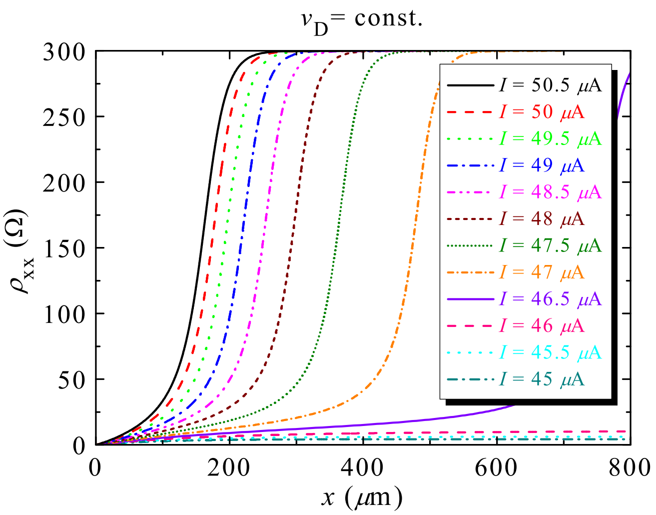

Figure 4.8: Calculated resistivities $\rho_{\rm xx}$ (see eq. 4.26) for different imposed currents $I = 45\mu$A…50.5μA measured during the experiments [33].

where: $V_{\rm H} = 0.59$V, $B = 5.8$T, $\tau_{\rm rel} = 1$ns, $w_0 = 3.1\mu$m, $f(y) = \Phi(y)$ and we have included also eq. 4.11 and eq. 4.12. Going further and assuming the proportionality relation between the longitudinal resistivity and the number of the excited electrons in the upper LL (see eq. 4.26) we see that, for constant drift velocity $v_{\rm D}$, the longitudinal resistivity $\rho_{\rm xx}$ is given by Fig. 4.8.

The numerical results of the resistivity show a remarkable qualitative agreement of the calculated longitudinal resistivity with the measured longitudinal resistivity. The calculated resistivity displays a very nice avalanche-like excitation of the electrons which develops over a characteristic distance and reaches the saturation value at reasonable distances depending on the imposed current. Moreover, the calculation shows also a reasonable quantitative agreement with the experiment. The biggest difference between experiment and numerical evaluation of the model consists of the fact that in the experiment (see Fig. 4.6) the high current curves increase at lower x values (for example near $x = 50\mu$m for $I = 50.5\mu$A) than in the calculations ($x = 150\mu$m for $I = 50.5\mu$A). The reason for these quantitative differences may be that the values of $\alpha = (\alpha_{\rm crit} \cdot I_{\rm crit})/I$, corresponding to high currents, are too large and therefore the curves increase at larger x. This could be if the assumed width w_0 of the incompressible strips at high currents is too large which corresponds, according to eq. 4.11, to larger α. To improve the agreement between numerical analysis (see Fig. 4.8) and the experiments (see Fig. 4.6), one would need that, for $I > I_{\rm crit}$, $\alpha(I)$ decreases faster than $\alpha(I) \propto 1/I$, as given by eq. 4.11.

However, the discrepancy between the two-Landau levels model and the experiments is not very severe. With the scaling $x = v_{\rm D}\tau_{\rm rel}(t/\tau_{\rm rel})$ and by comparison of Figs. 4.5 and 4.6, from the shape of the curves of each value of I to determine the corresponding value $\alpha(I)$. By plotting $\alpha(I)$ as a function of I, we can compare it with the QUILLS

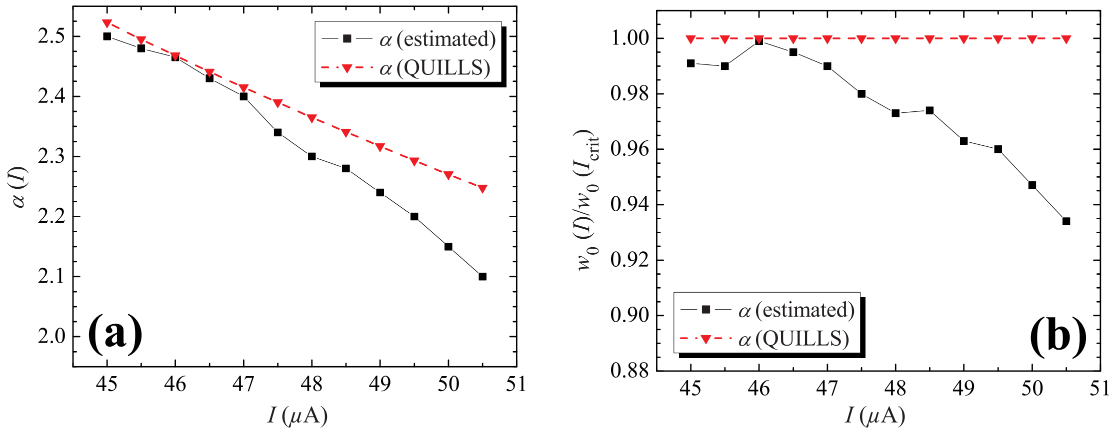

Figure 4.9: (a) $\alpha(I)$ as a function of the current I determined by comparing Figs. 4.5 and 4.6 and determined according to QUILLS relation $\alpha(I) = \alpha_{\text{crit}} I_{\text{crit}}/I$. (b) Width ration 4.29 as a function of the current I determined by comparing Figs. 4.5 and 4.6 and determined according to QUILLS relation $\alpha(I) = \alpha_{\text{crit}} I_{\text{crit}}/I$.

relation $\alpha(I) = \alpha_{\text{crit}} I_{\text{crit}}/I$ (see Fig. 4.9 (a)). This deviation could be explained by an I-dependent width $w_0(I)$ of the incompressible strips [58]

$$\frac{w_0(I)}{w_0(I_{\text{crit}})} = \frac{\alpha(I) \cdot I}{\alpha_{\text{crit}} \cdot I_{\text{crit}}} . \tag{4.29}$$

Figure 4.9 (b) shows that for our range of currents $45\mu\text{m} \leq I \leq 50.5\mu\text{m}$ the width ration decreases with increasing the current by only a few percent.

4.3 Conclusions

The two-Landau levels model simulates the excitation of the electrons to the upper LL which corresponds to the QHE breakdown. It combines several ideas to describe the QHE breakdown: the avalanche-like electron heating, the quasi-elastic-inter-Landau-level scattering (QUILLS) and the presence of the incompressible strips surrounding the compressible islands due to the presence of potential fluctuations induced by impurities or defects. In order to adapt the model to the experiments we assumed that the Hall potential drops only across the incompressible strips, and that the effective width of the incompressible strips is much smaller than the actual width of the sample due to the random inhomogeneities in the sample. In another paper, [58], the authors investigate the variation of the current density and of the Hall potential across a Hall sample. Further, they found in agreement with the experiment [72] that the Hall potential effectively drops only across the incompressible strips, which have usually a width much smaller than the width of the sample. These findings provide an alternative justification of the investigated model. The model shows a very nice qualitative agreement, an avalanche-like excitation and a reasonable quantitative agreement with the experiment. The best fit with the experiments have been obtained also considering equal excitation and relaxation times ($\widetilde{\tau} = \tau_{\rm exc}/\tau_{\rm rel} = 1$) and circular shape of the compressible islands. These facts indicate that the basic ideas of this Landau levels model are correct. However, it should be stated that the physical reality corresponding to the QH breakdown is more complex than described by this two-level model. Also higher LL's can be involved in the excitation and relaxation processes.

Chapter 5

Real-time measurements of the electrical excitation of quantum Hall devices with Corbino geometry

In this chapter the real-time measurements of the electrical excitation of QH devices with Corbino geometry are presented. The motivation of the real-time measurements of the electrical excitation was coming from the time-integrating measurements of the electrical excitation [35, 36, 44]. From these time-integrating excitation measurements it was concluded that the electrical breakdown of the QHE develops only after a certain critical pulse width $t_{\mathrm{p}}^{\mathrm{crit}}$, if the pulse amplitude A is higher than the critical *DC* source-drain voltage value $V_{\mathrm{SD}}^{\mathrm{crit}}$. These critical excitation times $\tau_{\mathrm{exc}}^{\mathrm{crit}}$ are of the order of nanoseconds and depend on the pulse amplitude, magnetic field, carrier mobility and on the temperature. Since from the previous time-integrating excitation measurements [35, 36, 44] it had not been possible to monitor the individual pulse shape of the sample response, the real-time measurements of the electrical excitation have been performed in this study. In order to achieve this goal an experimental setup has been made as described below.

5.1 Experimental setup

The QH devices used for our real-time measurements of the electrical excitation were fabricated from three different *GaAs/AlGaAs* wafers $\#1$, $\#2$ and $\#3$ with electron densities in the range of $1.9 \times 10^{11}\,\mathrm{cm}^{-2} \leq n_{\mathrm{s}} \leq 2.7 \times 10^{11}\,\mathrm{cm}^{-2}$ and electron mobilities in the range of $0.1 \times 10^{6}\,\mathrm{cm}^{2}\mathrm{V}^{-1}\mathrm{s}^{-1} \leq \mu_{\mathrm{el}} \leq 1.6 \times 10^{6}\,\mathrm{cm}^{2}\mathrm{V}^{-1}\mathrm{s}^{-1}$ (see Table 5.1). All devices were patterned as devices with Corbino geometry of $r_1 = 100\mu\mathrm{m}$, $r_2 = 150\mu\mathrm{m}$ the inner and outer radii of the QH device with Corbino geometry [73, 74].

The experimental setup of the real-time measurements of the electrical excitation is shown

Table 5.1: Electron density n_s and electron mobility μ_el of the wafers from which the QH devices with Corbino geometry were obtained (parameters were determined from transport measurements at $1.7\mathrm{K}$).

Wafers	$n_\mathrm{s}\,(\mathrm{cm}^{-2})$	$\mu_\mathrm{el}\,(\mathrm{cm}^2\mathrm{V}^{-1}\mathrm{s}^{-1})$	$r_1\,(\mu\mathrm{m})$	$r_2\,(\mu\mathrm{m})$
$\#1$	2.7×10^{11}	0.1×10^{6}	100	150
$\#2$	2.1×10^{11}	0.8×10^{6}	100	150
$\#3$	1.9×10^{11}	1.6×10^{6}	100	150

schematically in Figure 5.1. A pulse generator produces rectangular electrical pulses $V_\mathrm{A}(t)$ of the amplitude voltage A, with pulse widths of $3\mathrm{ns} \leq t_\mathrm{p} \leq 640\mathrm{s}$ and pulse periods of $10\mathrm{ns} \leq T_\mathrm{p} \leq 100\mathrm{s}$ (with a rise time - $0.5\mathrm{ns}$ and a fall time - $1.5\mathrm{ns}$). This pulse generator sends the electrical pulses through a high frequency (*HF*) coaxial cable, with 50Ω-resistor for impedance-matching [75], connected in the immediate vicinity of the sample. Impedance matching is to make the output impedance of a source equal or at least comparable to the input impedance of the load to which it is finally connected, usually in order to maximize the power transfer and minimize reflections from the load. The QH device with Corbino geometry itself is not appropriate for impedance matching due to its high resistance in the Hall regime ($50\mathrm{k}\Omega \leq R_\mathrm{C} \leq \infty$). Another 50Ω resistor was attached in series with the sample (between the drain contact *D* and the ground) in order to measure the current I_s passing through the sample and to display $I_\mathrm{s}(t)$ on a digital oscilloscope (also by a 50Ω-resistor impedance-matched) that monitors the individual response shape $I_\mathrm{s}(t)$ of the sample. In order to determine the time resolution of our experimental setup the *RC*-time is calculated and determined by test measurements. By taking into account the series capacitance of our *HF* cables ($C_\mathrm{s} \approx 100\mathrm{pF}$) and the circuit parallel resistor ($R_\mathrm{p} = 25\Omega$) we deduce a *RC*-time $t_\mathrm{RC}^\mathrm{calc} = 2.5\mathrm{ns}$. In order to verify the calculated *RC*-time we performed test measurements by replacing the QH device with Corbino geometry by a test resistor. We determined the time resolution of about $t_\mathrm{RC}^\mathrm{exp} = 2.7\mathrm{ns} - 3\mathrm{ns}$ which is in good agreement with the calculated value $t_\mathrm{RC}^\mathrm{calc} = 2.5\mathrm{ns}$.

The real-time measurements of electrical excitation have been performed at different temperatures ($T = 1.7\mathrm{K}$, $2.5\mathrm{K}$, $3.3\mathrm{K}$ and $4.1\mathrm{K}$) and magnetic fields B up to $6\mathrm{T}$ (applied perpendicular to the 2DES). Due to geometrical reasons of the QH devices with Corbino geometry, it is not possible to apply a direct current and measure the voltage as it is done in the case of the QH devices with Hall bar geometry. In the case of QH devices with Hall bar geometry, the longitudinal ρ_xx and transversal (Hall) ρ_xy resistivities are measured. Since in the measurements of the QH devices with Corbino geometry a source-drain voltage V_SD is applied and the current is measured (opposite to the QH devices with Hall bar geometry), the longitudinal conductivity σ_xx was calculated according to:

$$\sigma_\mathrm{xx} = \frac{I_\mathrm{s}}{V_\mathrm{SD}} \cdot \frac{ln(r_2/r_1)}{2\pi}\,, \tag{5.1}$$

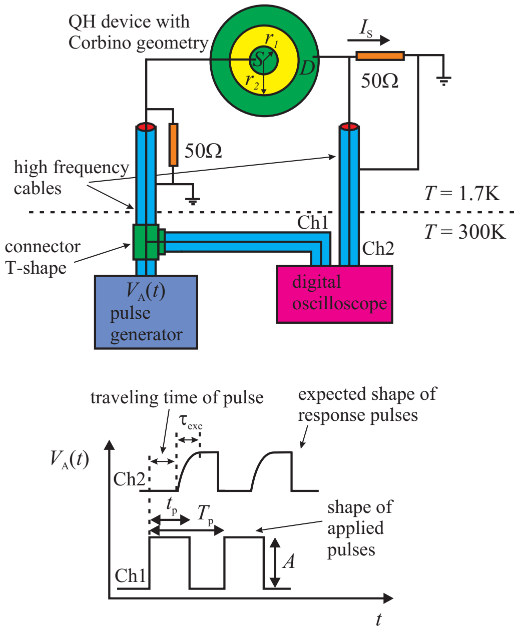

Figure 5.1: Sketch of the experimental setup to measure $I_s(t)$ for the breakdown of the QHE in the real-time domain.

where I_s is the measured sample current through the 50Ω resistor, V_{SD} is the applied source-drain voltage and r_2, r_1 are the outer and inner radii of contacts of the QH device with Corbino geometry (see Fig. 5.1).

5.2 Characterization of the samples (*DC* measurements)

We characterized our QH devices with Corbino geometry by Shubnikov-de Haas (SdH) measurements $\sigma_{\mathrm{xx}}(B)$ to determine the electron density n_{s} (from the period of the SdH-oscillations, see eq. 5.2) and the electron mobility μ_{el} (see eq. 5.3) and by measuring the source-drain current I_{s} as a function of the magnetic field B, for fixed *DC* values of the source-drain voltage V_{SD}:

$$n_{\mathrm{s}} = \frac{2e}{h \cdot \Delta(1/B)}\,, \tag{5.2}$$

and

$$\mu_{\mathrm{el}} = \frac{\sigma_{\mathrm{xx}}(B=0)}{n_{\mathrm{s}} \cdot e}\,, \tag{5.3}$$

where e is the elementary charge of the electron, h is the Planck's constant, $\Delta 1/B$ is the period of the SdH-oscillations. A typical SdH trace of the QH device with Corbino geom-

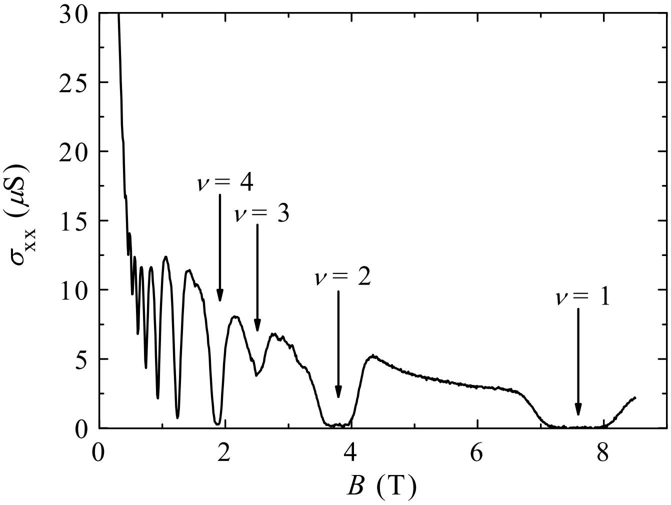

Figure 5.2: Shubnikov-de Haas oscillations of a QH device with Corbino geometry (sample $\#2$) taken at the applied source-drain voltage $V_{\rm SD} = 0.01$V and temperature $T = 1.7$K.

etry is shown in Fig. 5.2. By increasing the strength of the magnetic field, the longitudinal conductivity $\sigma_{\rm xx}$ starts to decrease and begins to oscillate (so called *SdH-oscillations*) from a certain magnetic field value on. The conductivity $\sigma_{\rm xx}$ develops vanishing longitudinal conductivity plateaus for a certain range of magnetic field values. The Fig. 5.2 shows a magnetotransport (SdH-measured) curve for one studied sample with well developed QH plateaus corresponding to filling factors $\nu = 2$ and $\nu = 1$. In order to determine the breakdown conditions, for filling factor $\nu = 2$, several current-voltage $I - V$ traces at different magnetic fields (around the middle of the second plateau $\nu = 2$) were taken for the determination of the corresponding critical *DC* voltages for the breakdown of the QHE and to determine the magnetic field ranges corresponding to integer filling factors. Figure 5.3 shows such $I - V$ curves of a QH device with Corbino geometry at filling factor $\nu = 2$ from which the critical *DC* voltages were determined ($V_{\rm SD}^{\rm crit} = 0.19$V for the up-sweep and $V_{\rm SD}^{\rm crit} = 0.18$V for the down-sweep).

The further real-time measurements of the electrical excitation of QH devices with Corbino geometry were performed only for filling factor $\nu = 2$ since for higher filling factors $\nu = 4$ and $\nu = 6$ the QHE was not well observable (see Fig. 5.2). Although for filling factor $\nu = 1$ we had a well pronounced QHE nevertheless we were not able to determine the corresponding excitation times due to a limited quality of the sample response. From this response, we could not determine satisfactorily the excitation times $\tau_{\rm exc}$ of the electron system.

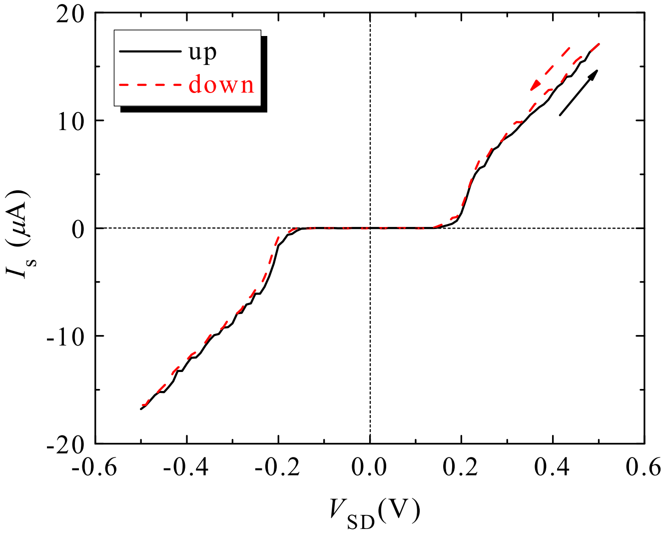

Figure 5.3: $I - V$ curves of a QH device with Corbino geometry (sample $\#2$) taken for up- and down- sweep of the applied source-drain voltage $V_{\rm SD}$ at magnetic field $B(\nu = 2) = 3.78$T and temperature $T = 1.7$K.

5.3 Pulse-induced breakdown of the quantum Hall effect (QHE)

In the real-time pulse-induced breakdown measurements on QH devices with Corbino geometry, we have investigated the excitation times $\tau_{\rm exc}$ of the electron system as a function of the amplitude, the magnetic field, the electron mobility and the temperature.

In order to get a certain accuracy for our measured weak signals we performed some tests (Fig. 5.4). The work with *HF* signals can be difficult due to the *HF* internal noise generated by the electronics. The internal noise (noise generated within or coupled to the circuit or system) corrupts the signal and can adversely affect the final performance and prevent the high-resolution potential of the system from being realized. Since possible cross-talking between wires or electronics (any metallic part behaves like an antenna) of the *HF* signals can occur, the 50Ω resistors of the impedance-matched circuitry (see Fig. 5.1) are shielded and the *HF* coaxial cables are connected as close as possible to the sample and to the resistors in order to obtain a signal as less noisy as possible. Between the applied electrical pulses and the sample response pulses there is a time delay due to the traveling time of the current through the wires. The traveling time changes both the onset time and the fall time of the response pulses. Their sequences (pulse duration and pause duration) are not altered by the traveling time.

By applying electrical pulses on the sample we monitor the real-time sample response

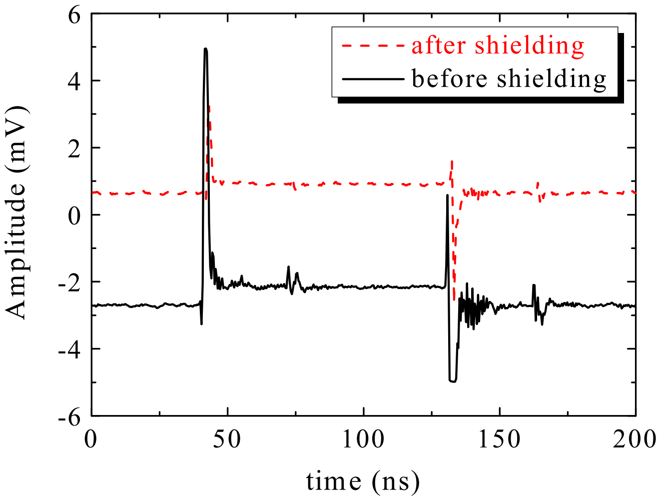

Figure 5.4: Test measurements performed in order to reduce the noise of the measured signal. Before the shielding (black-solid curve) the measured amplitude shows a noisy signal but after shielding (red-dash dot curve) of the test resistor and the electrical connections the noise is reduced significantly.

(excitation time) by measuring the source-drain current I_s, according to eq. 5.4, through the serial 50Ω resistor, as a function of time (see Fig. 5.5).

$$I_s = \frac{V_{SD} - V_{offset}}{R_{50\Omega}}\,. \tag{5.4}$$

In order to extract the excitation times τ_{exc} from the measured $I_s(t)$ traces we fit an exponential function (see eq. 5.5) to the measured trace $I_s(t)$:

$$I(t) = I_0 + I_A \cdot \exp\left(-\frac{t}{\tau_{exc}}\right)\,. \tag{5.5}$$

where I_0 is the offset, I_A is the amplitude and τ_{exc} is the decay constant of the exponential function. From the slope we determine the excitation time τ_{exc} (of the order of a few nanoseconds up to a few tens of nanoseconds, see figure caption 5.5). The reason why we fit an exponential function to the experimental traces is that the observed increase current profile seems to follow an exponential function. The accuracy of this fit function is at its best 10^{-9}s. Thus, the error bars of the determined excitation times τ_{exc} are in the range of $\pm5\% - \pm15\%$ of the estimated excitation times.
The excitation time τ_{exc} could be understood as the time required for the system to evolve from a QH state to a dissipative state (QH breakdown). The present spikes (see Fig. 5.5) are assumed to be due to the cross-talking between cables and electronics.

The time resolution of the setup is limited by various properties:

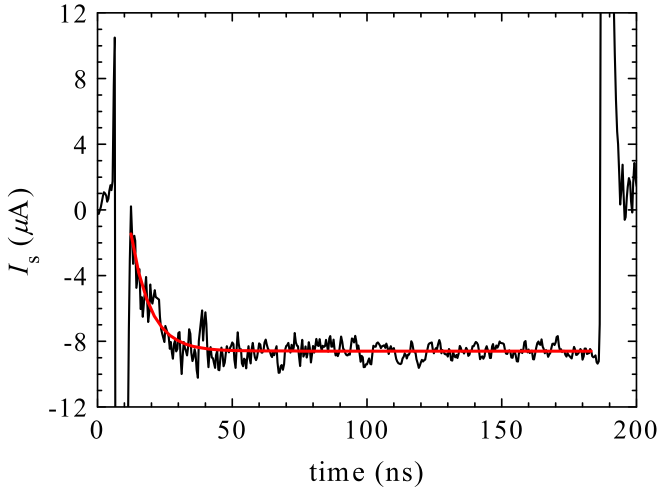

Figure 5.5: Time evolution of the measured source-drain current I_s (solid-black curve) and the exponential function (see eq. 5.5, red-solid curve) fitted to the experimental trace $I_\mathrm{s}(t)$. The QH device with Corbino geometry (sample #2) was subjected to electrical pulses of pulse-widths $t_\mathrm{p} = 180\mathrm{ns}$, applied pulse amplitudes $|A| = 0.8\mathrm{V}$ and pulse periods $T_\mathrm{p} = 300\mathrm{ns}$, at temperature $T = 2.5\mathrm{K}$ and magnetic field $B(\nu = 2) = 4.53\mathrm{T}$. The determined excitation time for this peculiar example was $\tau_\mathrm{exc} = 7.2\mathrm{ns} \pm 0.5\mathrm{ns}$.

- the rise and fall times of the pulse generator ($0.5\mathrm{ns}$ and $1.5\mathrm{ns}$ in the present case as mentioned in the text);
- the *RC*-time of the setup is about $3\mathrm{ns}$;
- the *time-width* of the spikes of cross-talking (as shown in Fig. 5.5) is about $4\mathrm{ns}-5\mathrm{ns}$ which in the worst case (the longest time) is limiting the time resolution.

5.3.1 Amplitude dependence of the excitation time

Before starting the excitation measurements, we have determined the *DC* breakdown conditions for the investigated QH devices with Corbino geometry (see Table 5.1) for filling factor $\nu = 2$. The *DC* breakdown voltages determined for our QH devices with Corbino geometry (see Table 5.1) are in the range of $0.1\mathrm{V} \leq V_\mathrm{SD}^\mathrm{crit} \leq 0.3\mathrm{V}$. The critical source-drain voltage $V_\mathrm{SD}^\mathrm{crit}$ varies with the electron mobility, magnetic field and temperature. Thus, as long as the applied pulses have their amplitudes $|A|$ lower than the *DC* critical source-drain voltage $V_\mathrm{SD}^\mathrm{crit}$ ($|A| < V_\mathrm{SD}^\mathrm{crit}$) there is no response of the QH devices with Corbino geometry since the system remains in the QH state. By increasing pulse

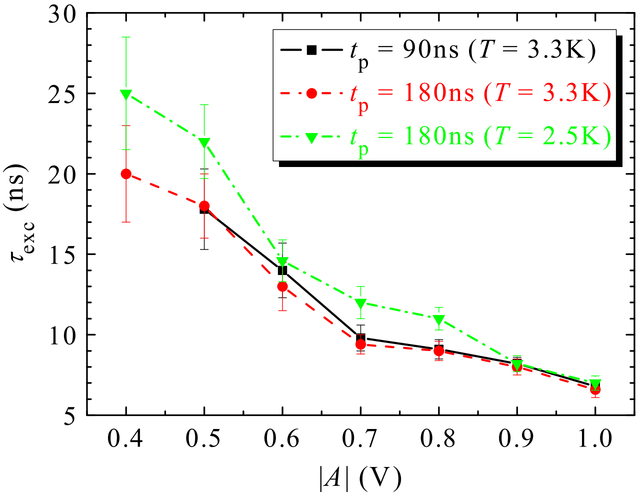

Figure 5.6: Excitation time τ_{exc} as a function of the applied pulse amplitude $|A|$, determined for the high-mobility sample $\#3$: $\mu_{\text{el}} = 1.6 \times 10^6 \text{cm}^2\text{V}^{-1}\text{s}^{-1}$. The estimated excitation times $\tau_{\text{exc}}(A)$ correspond to measurements done for two pulse widths $t_{\text{p}} = 90\text{ns} - 180\text{ns}$, two temperatures $T = 2.5\text{K} - 3.3\text{K}$ at fixed magnetic field $B(\nu = 2) = 3.94\text{T}$.

amplitude A above the *DC* breakdown value $V_{\text{SD}}^{\text{crit}}$ ($|A| > V_{\text{SD}}^{\text{crit}}$), in the QH device with Corbino geometry the breakdown of the QHE occurs. The sample response $I_{\text{s}}(t)$ is measured through the 50Ω resistor and displayed on the screen of the electronic oscilloscope (see Fig. 5.5).

By increasing the pulse amplitude above the *DC* breakdown value ($|A| > V_{\text{SD}}^{\text{crit}} \approx 0.25\text{V}$), the response of the QH sample is measured, as seen in Fig. 5.5. The estimated excitation time τ_{exc} decreases with increasing pulse amplitude $|A|$. Thus, the system evolves quicker from a nondissipative QH state to a dissipative state. Figure 5.6 shows the pulse amplitude dependence of the excitation time for the QH sample with Corbino geometry $\#3$ (see Table 5.1), for two different pulse-widths ($t_{\text{p}} = 90\text{ns}$ and $t_{\text{p}} = 180\text{ns}$) and two different temperatures at the same magnetic field. Figure 5.6 shows the decrease of the excitation times $\tau_{\text{exc}}(|A|)$ with increasing pulse amplitude. Moreover, it shows also that the estimated excitation times, corresponding to the two different pulse widths ($t_{\text{p}} = 90\text{ns} - 180\text{ns}$), almost coincide at the same pulse amplitude. Thus, the chosen two pulse widths have no influence on the excitation times τ_{exc} despite to the conclusion of earlier time-integrating measurements [35, 36, 44]. From these time-integrating measurements it was concluded that the breakdown of the QHE starts only after the pulse width of the excitation pulses reaches a critical value $t_{\text{p}}^{\text{crit}}$, which was the order of a few nanoseconds. However, our excitation pulse widths ($t_{\text{p}} = 90\text{ns} - 180\text{ns} >> t_{\text{p}}^{\text{crit}}$) are far from the determined critical pulse width $t_{\text{p}}^{\text{crit}} \approx 3\text{ns}$ [35, 36, 44].

Why does the increase of the pulse amplitude lead to a reduction of the response time?

To answer this question, I will discuss in the following two possible models which are intended to understand the decrease of the excitation times τ_{exc} with increasing pulse amplitude A.

The first model intended to explain phenomenologically this dependence is a *quasi-classical drift model*. In a solid, the electrons move around randomly with the Fermi velocity $\vec{v}_{\text{F}}$[1] in the absence of an applied electric field $\vec{E}$. Therefore, if one averages the movement over time there will be no overall motion of charge carriers in any particular direction. Within this classical approach, we consider the electrons as non-interacting particles[2] moving according to Newtons's equation. We assume that due to the presence of impurities, dislocations the electron are scattered and prevents the electrons on the average from being accelerated. The effect of scattering on the 2DES can be modeled by introducing a frictional term, described by a constant term τ, so-called *momentum relaxation time*, in the Newton's equation of motion for the average velocity. By solving this equation and with Ohm's law the Drude conductivity formula is obtained (see eq. 2.19). Now we can define the average distance the electrons travel between collisions with impurities, dislocations. This average distance ℓ_{mfp} is called the *mean free path* and can be defined by:

$$\ell_{\text{mfp}} = v_{\text{F}} \cdot \tau \,. \tag{5.6}$$

However, upon applying an electric field $\vec{E}$, due to the presence of a voltage pulse, electrons will be accelerated in an opposite direction to the electric field. The summation of the time between acceleration of electrons due to electric field and deceleration of electrons due to collisions and lattice scattering events (caused by phonons, crystal defects, impurities, etc.) over the mean free path between scattering events results in the electrons having an average drift velocity $\vec{v}_{\text{D}}$. By subjecting the electrons to a perpendicular magnetic field $\vec{B}(0, 0, B)$, the resulting $\vec{E} \times \vec{B}$-drift shifts the electrons on an average by a distance

$$\ell_{\text{D}} = v_{\text{D}} \cdot \tau_{\text{exc}} \,, \tag{5.7}$$

where ℓ_{D} is the drift length, v_{D} is the drift velocity and τ_{exc} is the excitation time. The damping effect, the friction due to the electron-impurity interaction, becomes effective and the excited current approaches a stationary value. By assuming a homogeneous distribution of the impurities throughout the QH device with Corbino geometry, the average distance ℓ_{imp} between two adjacent impurities is constant. Figure 5.7 shows a sketch of the drift of the electron through the QH device with Corbino geometry. At low lattice temperature, the mean time between inelastic electron-phonon scattering events is much larger than the mean time between elastic electron-impurity scattering events. Thus, the elastic scattering dominates the momentum relaxation. These impurities scatter the electrons elastically, without dissipation, from one scattering center (impurity) to another scattering center (see Fig. 5.7 a)). If the drift length is not the average distance between the impurities ($\ell_{\text{D}} < \ell_{\text{imp}}$), the electrons do not encounter enough scattering centers (impurities),

---

[1] The velocity that corresponds to a kinetic energy equal to the Fermi energy.

[2] However, the Coulomb interaction between electrons conserves their total momentum and therefore the *e-e* scattering cannot lead alone to a relaxation of the total momentum of the electron system.

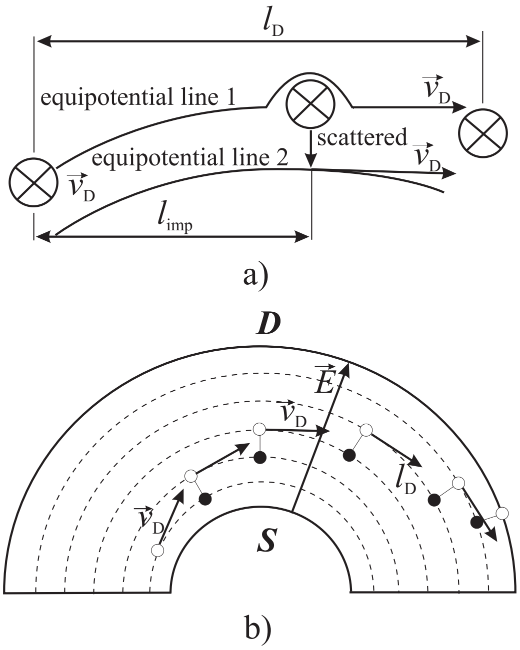

Figure 5.7: Phenomenological sketch for the movement of the electrons between impurities and the drift of electrons through the QH device with Corbino geometry due to the application of the electric field $\vec{E}$. Electrons undergo elastic collisions and may pass by the next impurity and drift further, or they are scattered by the next impurity, deviated on a length of the order of ℓ_B, and drift further until they reach another impurity.

necessary for the breakdown of the QHE, and revolve around the inner contact. In this situation the electron system stays in a QH state. If the drift length is the average distance between the impurities ($\ell_D = \ell_{imp}$), the electrons can encounter enough impurities and move from one impurity to another until reach the outer contact (see Fig. 5.7 b)). This situation corresponds to the breakdown of the QHE, the electron system is in a dissipative (resistive) state.

Equation 5.7 can be written in terms of the applied pulse amplitude A,

$$\ell_D = \frac{E_r}{B} \cdot \tau_{exc} = \frac{A}{G(r_1, r_2) \cdot B} \cdot \tau_{exc} \,, \tag{5.8}$$

where $E_r = A/G(r_1, r_2)$ is the maximum of the radial component of the electric field at $r = r_1$ in the QH device with Corbino geometry and $G(r_1, r_2) = r_1 \cdot ln(r_2/r_1)$ is the geometry factor of the QH device with Corbino geometry (with r_1 and r_2 the inner and outer radii of the contacts). From the arguments of eq. 5.8 one would expect that the excitation time τ_{exc} is inversely proportional to the applied pulse amplitude A. Thus, we expect a linear relation between the excitation time and the inverse of the pulse amplitude:

$$\tau_{\text{exc}} \propto \frac{1}{A}\,. \tag{5.9}$$

By increasing the applied pulse amplitude A, at constant magnetic field B, the drift velocity increases, the electrons drift faster since $v_{\text{D}} \propto E_{\text{r}} \propto A$ and therefore they need a shorter traveling time τ_{exc} to accomplish the breakdown of the QHE.
As we see, the quasi-classical drift model could in principle explain the inverse proportionality of the excitation time τ_{exc} with increasing the pulse amplitude A but this approximation cannot say the entire story. This is because this approximation relies on a few inconsistent assumptions. The approximation does not take into account any possible electron-electron (Coulomb) interactions, which could alter the effect of the scattering mechanisms by screening the impurity interaction potentials. This quasi-classical drift model describes the scattering of electrons by a constant relaxation time τ, independent of the magnetic field B. A constant relaxation time, independent of the B, looses the relevant quantum effects (SdH-effect, QHE) which are observable in the experiments but at high magnetic fields. We assumed a homogeneous distribution of impurities which is not the case in a real sample.

The second model, which could explain the inverse proportionality of the excitation time with the amplitude is the tunneling two-Landau levels model presented in the previous chapter and in Ref. [40]. The voltage pulse of amplitude A applied to the QH device with Corbino geometry, subjected to a perpendicular magnetic field, induces an azimuthal current flow through the QH device between the contacts. As a result the radial electric field $\vec{E}_{\text{r}}$, perpendicular to the current flow, tilts the LL's and thus increases the probability of the electron to tunnel from the highest occupied LL to the lowest empty LL (see Fig. 4.2). The tilting of the LL's decreases the average spatial separation Δy (see eq. 4.4) between two adjacent LL's, which can be rewritten as

$$\Delta y = \frac{\hbar\omega_{\text{c}}}{eE_{\text{r}}} = \frac{\hbar\omega_{\text{c}}}{eA} \cdot G(r_1, r_2)\,. \tag{5.10}$$

The reduction of the average spatial separation Δy causes a higher tunneling rate $1/\tau_{\text{exc}}$ of electrons [36, 40, 76] between the initial and the final tunneling states,

$$\frac{1}{\tau_{\text{exc}}} \propto \exp\left[-\frac{\Delta y^2}{4\ell_{\text{B}}^2}\right] = \exp\left[-\left(\frac{\hbar\omega_{\text{c}}}{2e\ell_{\text{B}}} \cdot \frac{G(r_1, r_2)}{A}\right)^2\right] = \exp\left[-\frac{C}{A^2}\right], \tag{5.11}$$

where $\ell_{\text{B}}^2 = \hbar/eB$ is the square of the magnetic length and $C = (e\hbar B^3/4m^{*2}) \cdot G^2(r_1, r_2)$ is assumed to be constant for fixed magnetic field. The higher the tunneling rate $1/\tau_{\text{exc}}$ is, the shorter is the traveling (tunneling) time τ_{exc}. As we discussed earlier in the quasi-classical drift model, we found that by applying the pulse voltage A, in a perpendicular magnetic field B, the electrons drift in a characteristic time $\tau_{\text{exc}} \propto 1/A$. Our real-time measurements confirm linear dependence of $\tau_{\text{exc}}(1/A)$ (see Fig. 5.8).
The presence of impurities bends the LL's (see Fig. 5.9) and induces potential fluctuations

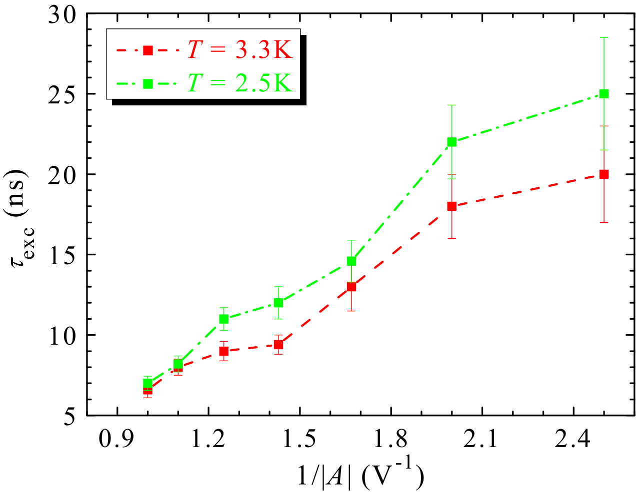

Figure 5.8: Excitation time τ_{exc} as a function of the inverse of the applied pulse amplitude $1/|A|$, determined for the high-mobility sample $\#3$: $\mu_{\text{el}} = 1.6 \times 10^6 \text{cm}^2\text{V}^{-1}\text{s}^{-1}$. The estimated excitation times correspond to measurements done for pulse widths $t_{\text{p}} = 180\text{ns}$), for temperatures $T = 2.5\text{K} - 3.3\text{K}$ at fixed magnetic field $B(\nu = 2) = 3.94\text{T}$.

(locally enhanced electrical potential) [27–29]. These electric fields reduce the average spatial separation between the LL's and lead to an additional tunneling rate. At higher electron mobilities, the function $\tau_{\text{exc}} = f(1/A)$ becomes nonlinear due to an inhomogeneous current flow induced by the impurity-related potential fluctuations [26, 77–79].
The Coulomb interaction leads to the screening of the potential fluctuations in strong magnetic fields. The screening creates quasi-metallic (so-called *compressible*) regions and insulator-like *incompressible* regions (strips). The incompressible strips carry the dissipationless current and separate adjacent compressible islands. As a consequence, the presence of the compressible islands reduces the effective width of the incompressible strips to a value $w_{\text{eff}} < G(r_1, r_2)$. This is because only the incompressible strips are responsible for the electron transport.
Following the ansatz, the tunneling rate equation 5.11 becomes:

$$\frac{1}{\tau_{\text{exc}}} \propto \exp\left[-\frac{C}{A^2}\right] \Longrightarrow \tau_{\text{exc}} \propto \exp\left[\frac{C}{A^2}\right]. \tag{5.12}$$

The value of C is determined from the slope of the function $ln\tau_{\text{exc}} = f(1/A^2)$. Thus, the effective widths of the incompressible strips w_{eff} (see eq. 5.13), corresponding to those two different amplitude regimes, might be estimated (see Fig. 5.10),

$$w_{\text{eff}} = \frac{2m^*}{B} \cdot \sqrt{\frac{C}{e\hbar B}}. \tag{5.13}$$

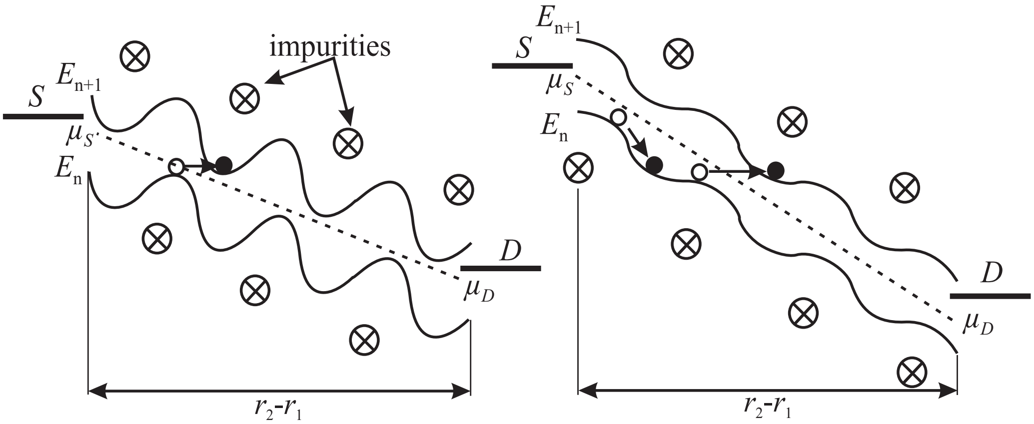

Figure 5.9: A phenomenological sketch of the LL's bending by the applied pulse amplitude A and the presence of the impurities, which induce potential fluctuations (locally distorted LL's). The effect of low-voltage appliance (left)-$\vec{E}_\mathrm{r} << \vec{E}_\mathrm{fluct}$: less bending of the LL's and strong influence of the impurity presence (strong oscillations of the LL energy in space); the effect of high-voltage appliance (right)-$\vec{E}_\mathrm{r} \approx \vec{E}_\mathrm{fluct}$: more bending of the LL's and less influence of the impurity presence (small oscillations of the LL energy in space). $r_2 - r_1$ is the distance between the inner and outer contacts of the QH device with Corbino geometry, μ_S is the chemical potential at the source *S* contact and μ_D is the chemical potential at the source *D* contact.

Figure 5.10 shows the linear fit of $ln\tau_\mathrm{exc}$ with respect to the square of the inverse of the applied pulse-amplitude $1/A^2$, data taken from Fig. 5.6, but only for pulse width $t_\mathrm{p} = 180\mathrm{ns}$. From data corresponding to temperature $T = 2.5\mathrm{K}$ we could estimate the effective widths of the incompressible strips corresponding to the high-amplitude regime-$w_\mathrm{eff}^\mathrm{high} = 3.1\mu\mathrm{m}$ and to the low-amplitude regime-$w_\mathrm{eff}^\mathrm{low} = 1.8\mu\mathrm{m}$. A single linear fit for either high-voltage or low-voltage data does lead an average effective width $w_\mathrm{eff}^\mathrm{average} = 1.9\mu\mathrm{m}$. Going further and check the data corresponding to temperature $T = 3.3\mathrm{K}$ we could estimate the effective widths of the incompressible strips corresponding to the high-amplitude regime-$w_\mathrm{eff}^\mathrm{high} = 2.2\mu\mathrm{m}$ and to the low-amplitude regime-$w_\mathrm{eff}^\mathrm{low} = 1.9\mu\mathrm{m}$. As we see now, the slopes corresponding to both voltage regimes almost coincide which leads in turn to almost equal effective width of the incompressible strips. Thus, the linear fit for all data points, either high-voltage or low-voltage regimes, leads to an average effective width $w_\mathrm{eff}^\mathrm{average} = 1.85\mu\mathrm{m}$. The determined effective widths $w_\mathrm{eff}(A)$ corresponding to the two amplitude regimes show an unexpected behavior $w_\mathrm{eff}^\mathrm{high}(A^\mathrm{high}) > w_\mathrm{eff}^\mathrm{low}(A^\mathrm{low})$. By increasing the applied voltage, due to the Joule heating, the width of incompressible strips would start to decrease [25, 71]. Thus, we would have expected a shorter effective width corresponding to the high-amplitude regime and larger effective width for the low-amplitude regime $w_\mathrm{eff}^\mathrm{high}(A^\mathrm{high}) < w_\mathrm{eff}^\mathrm{low}(A^\mathrm{low})$. But so far we have no clear answer why we got such results and still remains an open question. What is important to emphasize here is the fact that the effective width of the incompressible strips w_eff is much smaller

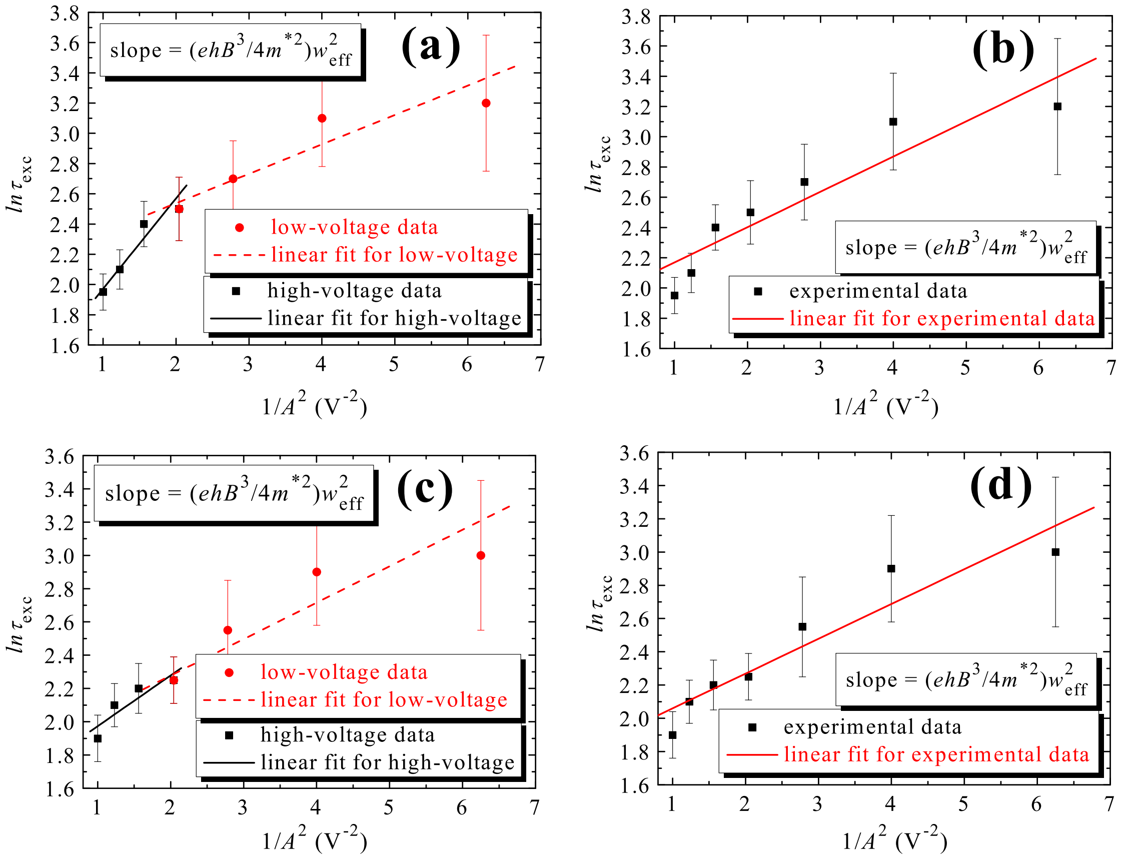

Figure 5.10: Logarithm of the response time $ln\tau_{\mathrm{exc}}$ as a function of the square of the inverse of the applied pulse-amplitude $1/A^2$ (see eq. 5.12) from which we could estimate the effective widths of the incompressible regions in the high-mobility sample $\#3$: $\mu_{\mathrm{el}} = 1.6 \times 10^6 \mathrm{cm}^2\mathrm{V}^{-1}\mathrm{s}^{-1}$ for two temperatures $T = 2.5\mathrm{K} - 3.3\mathrm{K}$. (a)-(b) show two possible linear fits for data extracted from measurements done at $T = 2.5\mathrm{K}$; (c)-(d) show two possible linear fits for data extracted from measurements done at $T = 3.3\mathrm{K}$. Thus, for the data shown in (a) and (c), a fit according to eq. 5.12 appears not appropriate.

than the geometrical factor $G(r_1, r_2)$ of the QH device with Corbino geometry ($1.8\mu\mathrm{m} \leq w_{\mathrm{eff}} \leq 3.1\mu\mathrm{m}$ and $G(r_1, r_2) \approx 40\mu\mathrm{m}$. This result agrees with a previous estimation of the effective width of the incompressible strips [40] determined from the experimental data presented in [33].

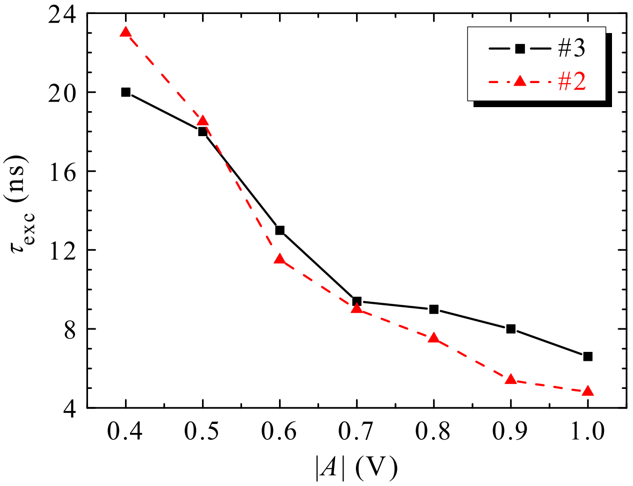

Figure 5.11: Mobility dependence of the excitation time $\tau_{\mathrm{exc}}(A)$ determined for medium-mobility $\#2 : \mu_{\mathrm{el}} = 0.8 \times 10^6 \mathrm{cm}^2\mathrm{V}^{-1}\mathrm{s}^{-1}$ and high-mobility samples $\#3 : \mu_{\mathrm{el}} = 1.6 \times 10^6 \mathrm{cm}^2\mathrm{V}^{-1}\mathrm{s}^{-1}$ at filling factor $\nu = 2$ and temperature $T = 3.3\mathrm{K}$.

5.3.2 Mobility dependence of the excitation time

The real-time measurements of electrical excitation of QH devices with Corbino geometry were performed on samples with different electron densities n_{s} and electron mobilities μ_{el} (see Table 5.1). The reason was to check the mobility dependence of the excitation time. Figure 5.11 shows the mobility dependence of the excitation time with respect to the applied voltage: the lower the electron mobility is, the shorter is the excitation times at constant applied pulse amplitude. The excitation time, corresponding to the medium-mobility sample $\#2$ increases linearly with decreasing applied voltage as the high-mobility $\#3$. However, it is believed that in high-mobility samples other mechanisms, dominated by high-nonlinear potential distribution are present. This nonlinear potential distribution may cause an inhomogeneous distribution of the current flow [77–81]. In the medium- and low-mobility samples ($\mu_{\mathrm{el}} < 1.0 \times 10^6 \mathrm{cm}^2\mathrm{V}^{-1}\mathrm{s}^{-1}$) with short-range potential fluctuations (far smaller than the sample width but larger than the magnetic length) may cause a homogeneous distribution of the current flow [27, 32, 82].

To understand the mobility dependence of the excitation times, we have to keep in mind one important intrinsic property of the sample: the electron mobility is determined by the density of scatterers (impurities, dislocations). Samples with low mobility have more scattering centers responsible for the onset of the breakdown of the QHE. This means that, on the basis of the quasi-classical drift model that higher density of scattering centers (corresponding to lower mobility samples) leads to shorter average drift lengths of the electrons between the scattering events and starts the breakdown of the QHE at lower pulse amplitudes. According to eq. 5.8 shorter average drift lengths at constant pulse amplitudes and constant magnetic fields leads to shorter excitation times (see Fig. 5.11). The lower the mobility is the closer is the excitation time to the linearity $\tau_{\mathrm{exc}} \propto 1/A$ (see Fig. 5.13). From eq. 5.9, one would expect that the drift length ℓ_{D} would increase linearly with decreasing the drift velocity or the pulse amplitude. Figure 5.12 shows the mobility dependence of the estimated drift lengths ℓ_{D} of the electrons for two samples with medium- and high-electron mobilities at filling factor $\nu = 2$ and temperature $T = 2.5\mathrm{K}$. The drift lengths are estimated by inserting in eq. 5.8 the experimental values of the pulse amplitude A, the corresponding excitation times τ_{exc}, the magnetic field B corresponding to $\nu = 2$ and the geometry factor $G(r_1, r_2)$. Our estimation shows that for the high-mobility sample #3 ($\mu_{\mathrm{el}} = 1.6 \times 10^6 \mathrm{cm}^2\mathrm{V}^{-1}\mathrm{s}^{-1}$) the expected linearity of the drift length with the amplitude is not achieved. This nonlinear behavior is not observed for the medium-mobility sample #2 ($\mu_{\mathrm{el}} = 0.8 \times 10^6 \mathrm{cm}^2\mathrm{V}^{-1}\mathrm{s}^{-1}$), see Fig. 5.12; the drift length increases, more or less monotonously, with decreasing pulse amplitude.

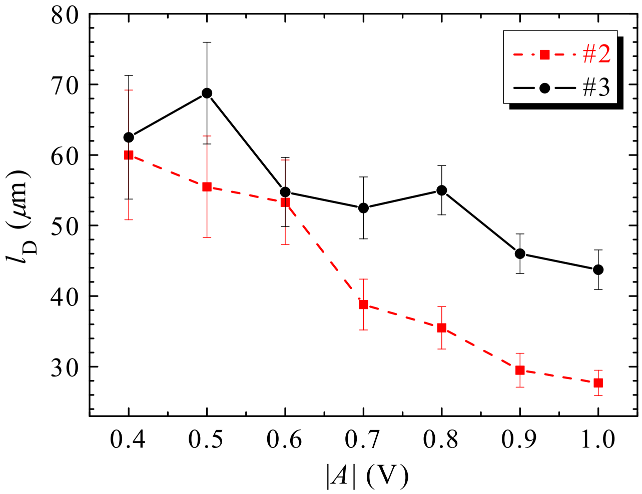

Figure 5.12: Estimated drift lengths ℓ_{D} as a function of the applied pulse amplitude $|A|$ determined for medium-mobility $\#2$: $\mu_{\mathrm{el}} = 0.8 \times 10^6 \mathrm{cm}^2\mathrm{V}^{-1}\mathrm{s}^{-1}$ and high-mobility $\#3$: $\mu_{\mathrm{el}} = 1.6 \times 10^6 \mathrm{cm}^2\mathrm{V}^{-1}\mathrm{s}^{-1}$ samples at fixed filling factor $\nu = 2$ and temperature $T = 2.5\mathrm{K}$.

Higher density of scattering centers, on the basis of the two-level model, determines smaller effective Landau gap between two adjacent LL's. Smaller effective Landau gap induces a higher tunneling rate (see eq. 5.11) of the electrons between the highest filled LL, under the FL, and the lowest empty LL, above the Fermi level. A higher tunneling rate would lead to a shorter excitation time. Figure 5.14 presents data for all three samples for different filling factors, around $\nu = 2$, at the temperature $T = 2.5\mathrm{K}$ and fixed applied pulse amplitude $|A| = 0.4\mathrm{V}$. It shows the general trend: the lower the electron mobility is, the shorter is the excitation time at constant applied pulse amplitude,

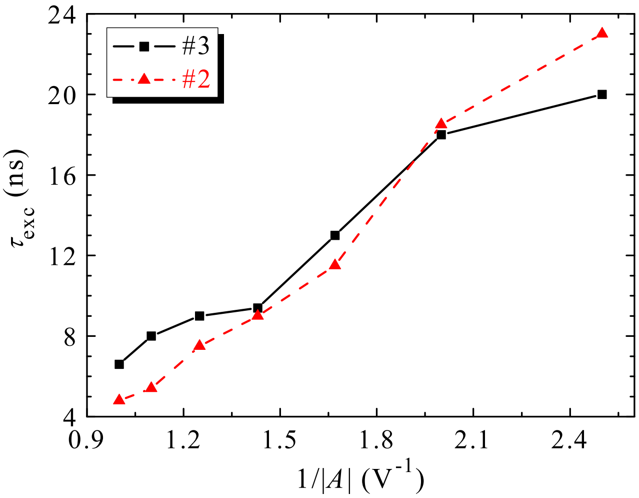

Figure 5.13: Excitation time $\tau_{\text{exc}}(1/A)$ determined for the medium-mobility $\#2 : \mu_{\text{el}} = 0.8 \times 10^6\text{cm}^2\text{V}^{-1}\text{s}^{-1}$ and high-mobility samples $\#3 : \mu_{\text{el}} = 1.6 \times 10^6\text{cm}^2\text{V}^{-1}\text{s}^{-1}$ at filling factor $\nu = 2$ and temperature $T = 3.3\text{K}$, shows a linearity of the excitation time ($\tau_{\text{exc}} \propto 1/A$) for both the medium- and high-mobility samples ($\#2$ and $\#3$.

typical for all our investigated samples (see Table 5.1). The right scale of the excitation time of Fig. 5.14 corresponds to the medium-mobility $\#2$ and the high-mobility $\#3$ samples. The large difference between the scales corresponding to the low-mobility sample $\#1$, on one hand, and the medium- $\#2$ and high-mobility $\#3$ samples, on the other hand, might be explained by the large scale of magnitudes between the low-mobility $\#1 : \mu_{\text{el}} = 0.1 \times 10^6\text{cm}^2\text{V}^{-1}\text{s}^{-1}$, the medium- $\#2 : \mu_{\text{el}} = 0.8 \times 10^6\text{cm}^2\text{V}^{-1}\text{s}^{-1}$ and the high-mobility $\#3 : \mu_{\text{el}} = 1.6 \times 10^6\text{cm}^2\text{V}^{-1}\text{s}^{-1}$ samples.

5.3.3 Magnetic field dependence of the excitation time

If the magnetic field is varied from its position at the middle of the second QH plateau ($\nu = 2$) to higher or to lower values, the breakdown of the QHE occurs in shorter times for a constant applied pulse amplitude (see Figs. 5.14, 5.15 and 5.16). The higher the deviation $\Delta\nu$ from the integer filling factor $\nu = 2$ the earlier the breakdown of the QHE occurs (corresponding to smaller breakdown voltages, see Fig. 5.15). Figure 5.16 shows also the magnetic field dependence of the excitation time at fixed temperature $T = 3.3\text{K}$ for two applied pulse amplitudes $|A| = 0.5\text{V} - 0.8\text{V}$. The smaller scale $6\text{ns} \leq \tau_{\text{exc}} \leq 12\text{ns}$ corresponds to $|A| = 0.8\text{V}$ (red-dash curve) while the larger scale $14\text{ns} \leq \tau_{\text{exc}} \leq 19\text{ns}$ corresponds to $|A| = 0.5\text{V}$ (green-dash dot curve). Since higher applied pulse amplitudes leads to stronger tilting of the LL's, according to the two-level model, the tilting reduces

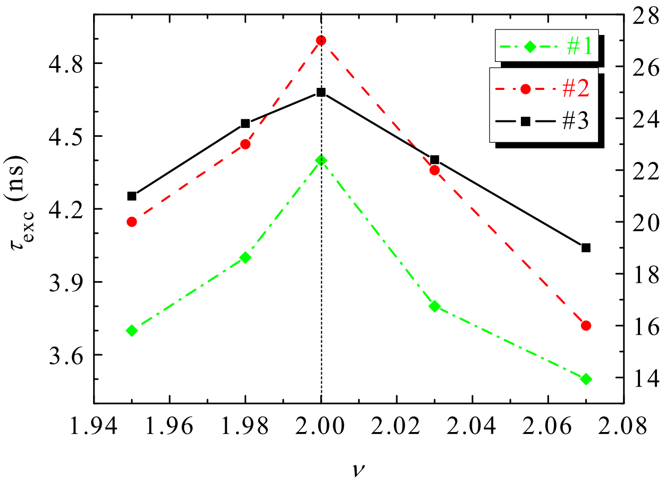

Figure 5.14: Mobility and magnetic field dependence of the excitation time $\tau_{\text{exc}}(\nu)$ determined for low-mobility $\#1$: $\mu_{\text{el}} = 0.1 \times 10^6 \text{cm}^2\text{V}^{-1}\text{s}^{-1}$, medium-mobility $\#2$: $\mu_{\text{el}} = 0.8 \times 10^6 \text{cm}^2\text{V}^{-1}\text{s}^{-1}$ and high-mobility samples $\#3$: $\mu_{\text{el}} = 1.6 \times 10^6 \text{cm}^2\text{V}^{-1}\text{s}^{-1}$ at fixed pulse amplitude $|A| = 0.4\text{V}$, temperature $T = 2.5\text{K}$ for various values of the magnetic field around filling factor $\nu = 2$. The scale of τ_{exc} for sample $\#1$ is on the left side of the $\tau_{\text{exc}}(\nu)$ axis while the scale of τ_{exc} corresponding to the samples $\#2$ and $\#3$ is on the right side of the $\tau_{\text{exc}}(\nu)$ axis.

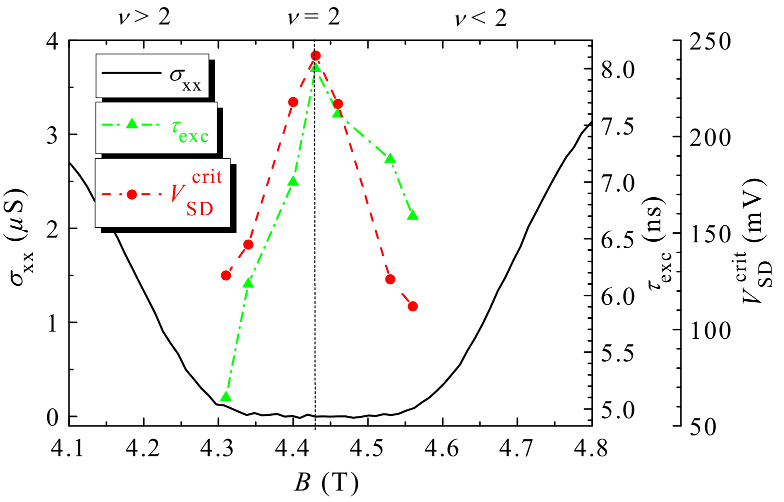

Figure 5.15: Magnetic field dependence of the excitation time $\tau_{\text{exc}}(B)$ determined for medium-mobility sample $\#2$: $\mu_{\text{el}} = 0.8 \times 10^6 \text{cm}^2\text{V}^{-1}\text{s}^{-1}$ at fixed pulse amplitude $|A| = 0.8\text{V}$ and temperature $T = 2.5\text{K}$.

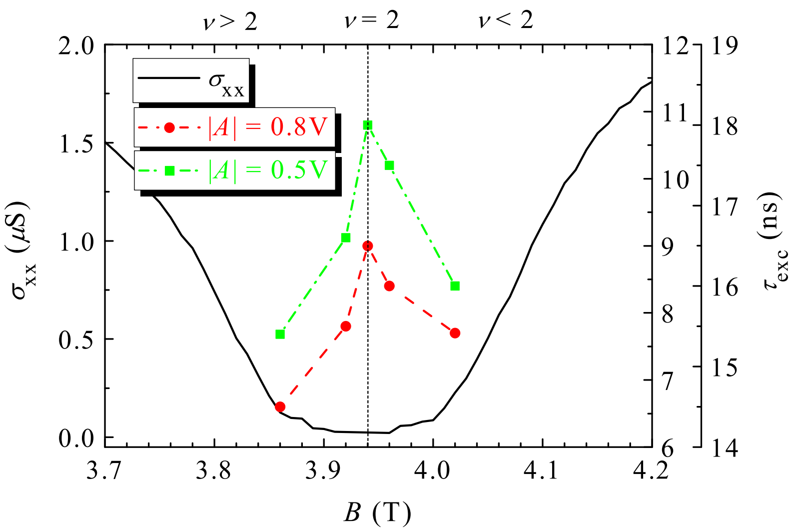

Figure 5.16: Magnetic field dependence of the excitation time $\tau_{\rm exc}(B)$ determined for high-mobility sample #3 : $\mu_{\rm el} = 1.6 \times 10^6 {\rm cm}^2{\rm V}^{-1}{\rm s}^{-1}$ for two pulse amplitudes $|A| = 0.5{\rm V}$ (green-dash dot curve) and $|A| = 0.8{\rm V}$ (red-dash curve) at fixed temperature $T = 3.3{\rm K}$.

the average spatial separation Δy (see eq. 5.10), increases the tunneling rate (see eq. 5.11) and consequently reduce the tunneling (excitation) times $\tau_{\rm exc}$ (see eq. 5.12). Moreover, the higher the applied pulse amplitude A is the shorter is the excitation time $\tau_{\rm exc}$ (see more arguments given in the subsection - Amplitude dependence of the excitation time). Thus, the excitation times $\tau_{\rm exc}$ around filling factor $\nu = 2$ corresponding to $|A| = 0.8{\rm V}$ are shorter than the corresponding excitation times (same magnetic field B) corresponding to $|A| = 0.5{\rm V}$.

The quasi-classical drift model cannot help very much the understanding of the magnetic field dependence since according to eq. 5.8, at constant drift length and constant applied pulse amplitude, the excitation time is proportional to the magnetic field ($\tau_{\rm exc} \propto B$). In other words, the lower the magnetic field is the shorter is the excitation time. But this is not completely true since this theory says nothing about the dependence of the excitation time on B around the integer filling factor ν. The measurements show the dependence: the higher the deviation $\Delta\nu \propto \Delta B$ from the integer filling factor $\nu = 2$ is the earlier the breakdown of the QHE occurs.

The two-Landau levels model predicts that the average spatial separation Δy (see eq. 5.10 increases with increasing the magnetic field, at constant applied pulse amplitude. Thus, the tunneling rate decreases with increasing magnetic field which means longer tunneling (excitation) times. However, the two-level model says nothing about the dependence of the excitation time on B around the integer filling factor ν.

Ref. [25] describes a quasi-local transport model which could explain nicely the observed

magnetic field dependence of the excitation time. The data are interpreted on the basis of *incompressible strips* which are expected to develop in an inhomogeneous 2DES as a consequence of its strongly nonlinear low-temperature screening properties [59] in a strong perpendicular magnetic field. The screening effects create quasi-metallic *compressible* regions[3] and insulator-like *incompressible* strips[4] which separate adjacent compressible islands. The proposed quasi-local transport model allows to calculate, on one hand, the potential and current distribution in 2DES under the conditions of the QHE and, on the other hand, the longitudinal and the Hall resistances in the plateau regimes of the QHE and in between. The model proves that the exactly quantized plateaus result from the existence of the incompressible strips. For the incompressible strips, locally $\sigma_{\mathrm{xx}} = 0$ holds. The Hall potential drops only across the incompressible strips while the filling factor in the center of the sample was slightly larger than an integer [79, 83].
At sufficiently large magnetic fields (local filling factor $\nu(x) < 2$) the 2DES is completely compressible. At lower magnetic fields ($\nu \approx 2$) the center of the sample becomes incompressible with local filling factor $\nu(x) = 2$, while the local filling factor $\nu(x)$ gradually increases (the magnetic field B decreases) outside the incompressible center and falls off to zero at the edges. By applying this model we could explain the magnetic field dependence of the excitation time $\tau_{\mathrm{exc}}(B)$. The reduction of the excitation time is a result of the reduction of the width of the incompressible strips with decreasing magnetic field near the integer filling factor $\nu = 2$. When the magnetic field reaches the value corresponding to the integer filling factor the width of the incompressible strips reaches its maximum value [25]. The magnetic field dependence around filling factor $\nu = 2$ of the voltage characteristics of the QHE breakdown follow the same trend as the excitation time (see Fig. 5.15): the critical breakdown voltage $V_{\mathrm{SD}}^{\mathrm{crit}}$ reaches its maximum value at the integer filling factor $\nu = 2$ [38]. The asymmetry of the excitation time $\tau_{\mathrm{exc}}(B)$ (shorter at lower magnetic fields $B(\nu > 2)$ and higher at higher magnetic fields $B(\nu < 2)$ with respect to the largest $\tau_{\mathrm{exc}}(B)$ determined at $B(\nu = 2)$) can be attributed to the variation of the width of the incompressible strips. By coming from higher magnetic fields $B(\nu < 2)$ the width of the incompressible strips increases to a maximum value corresponding to $B(\nu = 2)$. By decreasing further the magnetic field $B(\nu > 2)$ the width of the incompressible strips decreases faster in comparison to the width corresponding to higher magnetic fields $B(\nu < 2)$ (see Figs. 5.14, 5.15 and 5.16).

5.3.4 Temperature dependence of the excitation time

At low temperatures ($T \leq 4$K, $k_{\mathrm{B}}T << E_{\mathrm{F}}$), phonons are frozen out and therefore the electron-phonon scattering is assumed not important. The elastic electron-impurity scattering mechanism is assumed to be more effective. This means that the occupied initial

---

[3] In a compressible strip a partially filled LL is pinned to the Fermi energy, so that at zero temperature the total potential within the strip is flat, while the density varies smoothly.

[4] In a incompressible strip the FL is between adjacent LL's, the potential varies by the amount of a cyclotron energy, while the density is constant.

and the empty final states of the electron-impurity scattering processes must have the same or very close energy, which is possible only if both are in the immediate vicinity of the Fermi level E_F.

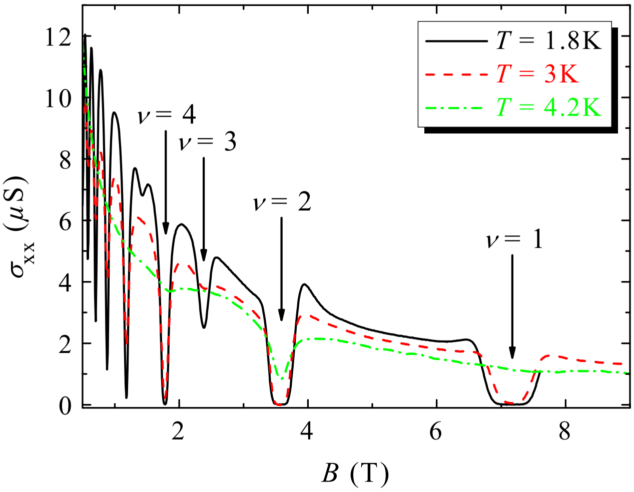

Figure 5.17: Temperature dependence of the SdH-oscillations for high-mobility sample $\mu_\mathrm{el} = 1.6 \times 10^6 \mathrm{cm}^2\mathrm{V}^{-1}\mathrm{s}^{-1}$, $r_1 = 250\mu\mathrm{m}$, $r_2 = 750\mu\mathrm{m}$) for three lattice temperatures at fixed applied source-drain voltage $V_\mathrm{SD} = 0.02\mathrm{V}$.

The pulse-induced breakdown experiments were performed at different lattice temperatures of $T = 4.1\mathrm{K}$, $T = 3.3\mathrm{K}$, $T = 2.5\mathrm{K}$ and $T = 1.7\mathrm{K}$. The ambient temperature was varied in the variable temperature insert (VTI) by varying the pumping rate of the VTI. The effect of the elevated temperatures is the shrinking of the QH plateau. If the lattice temperature exceeds a critical value, $T > T_\mathrm{c}$, the breakdown of the QHE is achieved and the QHE vanishes (see Fig. 5.17). Thus, the longitudinal conductivity σ_xx increases rapidly, by orders of magnitude, from a vanishing $\sigma_\mathrm{xx} = 0$ to a nonvanishing $\sigma_\mathrm{xx} > 0$. A similar effect can be obtained by varying the applied source-drain voltage V_SD which cause a variance of the corresponding Joule heating. The higher the source-drain voltage applied the higher is the Joule heating. By increasing the Joule heating the local electron temperature increases and leads to a shrinking of the QH plateau (see Fig. 5.18). If the applied source-drain voltage exceeds the critical source-drain voltage value (V_SD>$V_\mathrm{SD}^\mathrm{crit}$) [38] then a sudden increase of the longitudinal conductivity $\sigma_\mathrm{xx} = 0$ by orders of magnitude to $\sigma_\mathrm{xx} > 0$ occurs. Above the critical source-drain voltage value, an onset of dissipation at the inner contact occurs which is propagated fast to the outer contact and a current between contacts is established. As a conclusion, by increasing either the temperature or voltage, which in turn increases the temperature, over a critical value of the temperature T_crit or the applied source-drain voltage $V_\mathrm{SD}^\mathrm{crit}$ the QH plateau shrinks to zero.

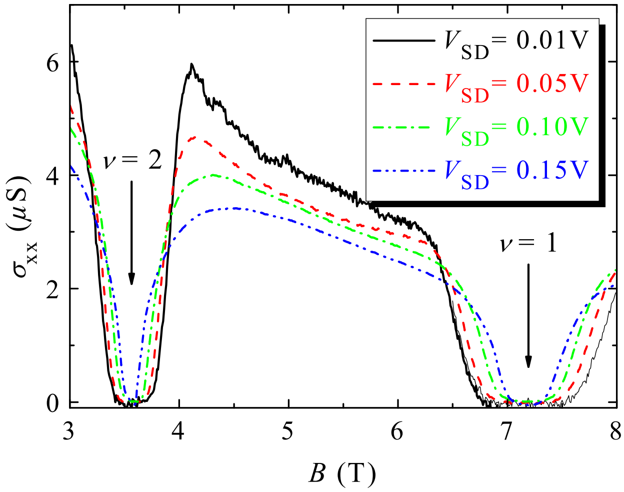

Figure 5.18: Voltage dependence of the SdH-oscillations for medium-mobility sample $\#2 : n_{\rm s} = 1.7 \times 10^{11}{\rm cm}^{-2}$, $\mu_{\rm el} = 0.8 \times 10^{6}{\rm cm}^{2}{\rm V}^{-1}{\rm s}^{-1}$ for four applied source-drain voltages $V_{\rm SD}$ at fixed lattice temperature $T = 1.7{\rm K}$.

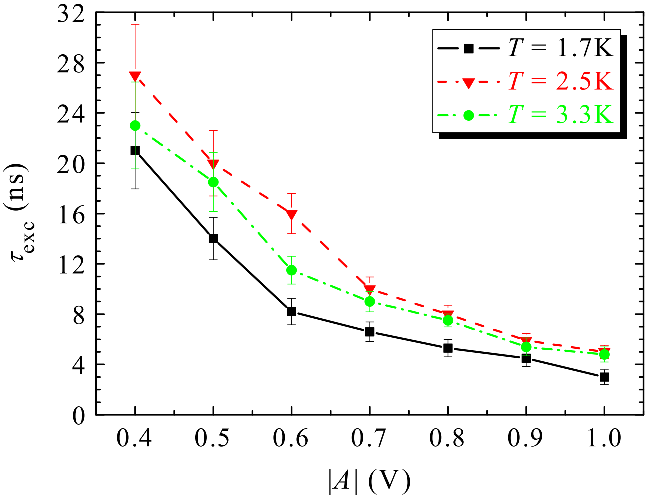

Figure 5.19: Temperature dependence of the excitation time $\tau_{\rm exc}$ as a function of the applied pulse amplitude A at a fixed magnetic field $B(\nu = 2) = 4.43{\rm T}$ for medium-mobility sample $\#2 : \mu_{\rm el} = 0.8 \times 10^{6}{\rm cm}^{2}{\rm V}^{-1}{\rm s}^{-1}$.

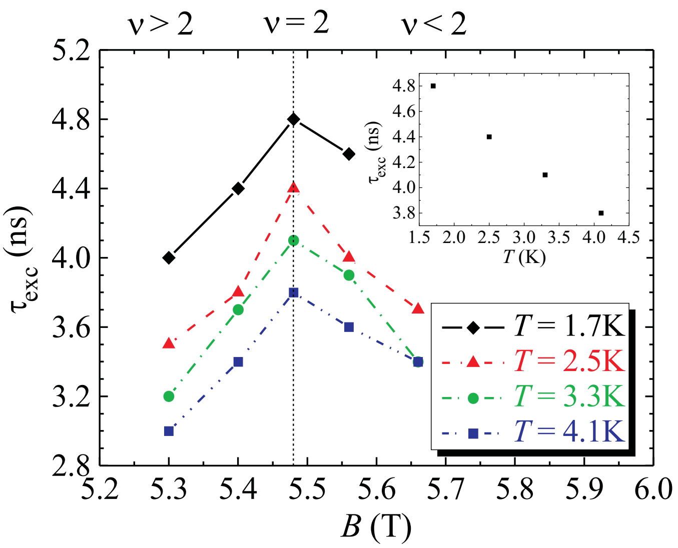

Figure 5.20: Excitation time $\tau_{\rm exc}$ determined for four temperatures, as a function of the magnetic field around the filling factor $\nu = 2$ and fixed applied pulse amplitude $|A| = 0.4{\rm V}$ for low-mobility sample $\#1$: $\mu_{\rm el} = 0.1 \times 10^6 {\rm cm}^2{\rm V}^{-1}{\rm s}^{-1}$. The inset shows that the maxima of $\tau_{\rm exc}$ at $\nu = 2$ decreases with increasing temperature T.

Figure 5.19 shows the temperature dependence of the excitation times $\tau_{\rm exc}(|A|)$ for different applied pulse amplitudes A. The higher the pulse amplitudes applied the shorter are the excitation times, at constant temperature. For different temperatures but at constant applied pulse amplitudes, the corresponding excitation times slightly differ. Since the data corresponding to lattice temperatures $T = 2.5{\rm K} - 3.3{\rm K}$ slightly differ, we could conclude that there is no significant temperature dependence of the scattering process in this temperature range, as we expected (electron-phonon scattering is obviously not dominant, see also Fig. 5.6). Slight differences between the curves corresponding to temperatures $T = 2.5{\rm K} - 3.3{\rm K}$ (see Fig. 5.19) on one hand and the curve corresponding to $T = 1.7{\rm K}$ on the other hand may come from different cooling cycles. In different cooling cycles different values of the excitation time $\tau_{\rm exc}$ are found (but of the same order of magnitude), even under the same experimental conditions. A possible reason would be that different "landscapes" of the potential fluctuations are "built up" (frozen), leading to different times. However, we should also add that the presence of phonons is inevitable to mediate inelastic electron transitions between LL's across the Corbino disc. An electron, changing its position Δy, has to change its momentum $p = \hbar k$ due to the change Δy of the cyclotron-orbit position $\Delta k = \Delta y/\ell_{\rm B}^2$ [84].

Figure 5.20 shows the temperature dependence of the excitation time $\tau_{\rm exc}$ with varying the magnetic fields at fixed applied pulse amplitude. We notice that the excitation time $\tau_{\rm exc}$ decreases with increasing temperature (but not very much, within $\approx 1{\rm ns}$), reaching a maximum value at the integer filling factor $\nu = 2$ in the middle of the plateau (see insert of Fig. 5.20). The quasi-classical drift model could not give a direct relation between the drift length or drift (excitation) time with the temperature. The two-Landau levels model could in principle explain shorter excitation times with higher lattice temperatures. By increasing the lattice temperature the electrons elevate in their energies by $k_{\mathrm{B}}T$. Due to the tilting of the LL's under the electric field and provided that the thermal energy $k_{\mathrm{B}}T$ is large enough, the electrons could tunnel between two adjacent LL's. The tunneling rate would increase with increasing the temperature and therefore the tunneling (excitation) time would be inversely proportional to the temperature. But this model would fail to explain the magnetic dependence of the excitation times, for constant applied pulse amplitude, also observed for different temperature. And again we call the quasi-local transport model described in Ref. [25] and also discussed in the previous subsection-Magnetic field dependence of the excitation time. In the absence of collision broadening, the incompressible strips have a finite width at zero temperature [71]. But at finite, increasing temperatures, the width shrinks (while the filling factor remains exactly constant within the remaining strip) until to a sufficiently high temperature ($k_{\mathrm{B}}T/\hbar\omega_{\mathrm{c}} = 0.06$, according to [71]) where the width of the incompressible strip collapses to zero. Moreover, the existence of the incompressible strips is also related to the existence of the gap between two adjacent broadened LL's, provided that the temperature is low enough. From the study [25], it is concluded that the width of the QH plateau, consequently the width of the incompressible strips, increases monotonically with decreasing temperature and has apparently a finite width for $T \to 0$. This means that the lower the temperatures are the wider the incompressible strips are. Thus, the traveling (excitation) times increases with increasing the width of the incompressible strips which corresponds to a reduction of the temperature.

5.4 Conclusions

To conclude, we have investigated the time scale of the excitation of the electrons in the 2DES of GaAs/AlGaAs heterostructures with Corbino geometry in the breakdown of the QHE regime. The real-time measurements of the electrical excitation were performed by applying to the QH devices with Corbino geometry rectangular electrical pulses of two different pulse widths ($t_{\mathrm{p}} = 90\mathrm{ns}$ and $t_{\mathrm{p}} = 180\mathrm{ns}$), constant pulse period $T_{\mathrm{p}} = 300\mathrm{ns}$, while the pulse amplitude is changed $0.4\mathrm{V} \leq A \leq 1\mathrm{V}$ at fixed magnetic field B (filling factors around $\nu = 2$). The investigated QH devices with Corbino geometry have electron densities differing in a narrow range ($1.9 \times 10^{11}\mathrm{cm}^{-2} \leq n_{\mathrm{s}} \leq 2.7 \times 10^{11}\mathrm{cm}^{-2}$) and different carrier mobilities ($0.1 \times 10^{6}\mathrm{cm}^{2}/\mathrm{Vs} \leq \mu_{\mathrm{el}} \leq 1.6 \times 10^{6}\mathrm{cm}^{2}/\mathrm{Vs}$, see Table 5.1). Further, the investigations were performed at different lattice temperatures ($1.7\mathrm{K} \leq T \leq 4.1\mathrm{K}$).

The time scale of excitation ($3\mathrm{ns} \leq \tau_{\mathrm{exc}} \leq 30\mathrm{ns}$) determined with our real-time measurements of the electrical excitation agrees with an estimation given in a previous work [28] and agrees well with the results of the previous time-integrating measurements of the electrical excitation [35, 36, 44].

The breakdown of the QHE starts only after a certain excitation time $3\mathrm{ns} \leq \tau_{\mathrm{exc}} \leq 30\mathrm{ns}$, $\tau_{\mathrm{exc}} << t_{\mathrm{p}}$, depending on the applied pulse amplitude A, on the carrier mobility μ_{el} of the sample and on the strength of the perpendicular applied magnetic field B (filling factors around $\nu = 2$). Due to the possibility to investigate the single pulses of the sample response our method gives a better insight into the electronic properties. Moreover, we try to explain our results, the dependence of the excitation time on the applied pulse amplitude, the electron mobility, the magnetic field and the temperature, on the basis of a quasi-classical drift model, a two-Landau levels model and a quasi-local transport model.
The quasi-classical drift model could explain the inverse proportionality of the excitation time with respect to the applied amplitude. Even if the measurements showed that the excitation time increases with decreasing pulse amplitude, however, this proportionality was not linear, at least not for the studied high-mobility sample ($\mu_{\mathrm{el}} = 1.6 \times 10^6\mathrm{cm}^2\mathrm{V}^{-1}\mathrm{s}^{-1}$). An estimation of the mean free path lengths and of the scattering times (according to the quasi-classical drift model) leads to mean free paths of $0.9\mu\mathrm{m} \leq \ell_{\mathrm{mfp}} \leq 12\mu\mathrm{m}$ instead of $7\mu\mathrm{m} \leq \ell_{\mathrm{D}} \leq 70\mu\mathrm{m}$ (determined with our measurements) and scattering times of $3.8\mathrm{ps} \leq \tau_{\mathrm{Drude}} \leq 60\mathrm{ps}$ instead of the measured $3\mathrm{ns} \leq \tau_{\mathrm{exc}} \leq 30\mathrm{ns}$. But the quasi-classical drift model does not take into account the quantum effects at high magnetic fields due to the Landau quantization. Therefore we employed a two-Landau levels model that shows that the excitation time is inversely proportional to the square of the applied pulse amplitude. The higher the pulse amplitude is applied the shorter is the tunneling (excitation) time. This happens due to the increasing tilting of LL's with the pulse amplitude and therefore increases the probability of electrons to tunnel between adjacent LL's.
The mobility dependence is studied with the help of the quasi-classical drift model and the two-Landau levels model. The quasi-classical drift model shows that the lower the mobility of the electrons the shorter is the drifting time between scattering events, due to the higher density of scatterers which imply the reduction of the drifting time. The two-Landau levels model describes the mobility dependence by the higher density of scatterers that increases electric field of the potential fluctuations. These electric fields reduce the average spatial separation between adjacent LL's and therefore increase the probability of tunneling electrons between adjacent LL's. A lower electron mobility induces a higher collision broadening that decreases the effective gap between LL's and therefore decreases the energy necessary for the electrons to tunnel between LL's.
However, the magnetic field dependence could not be satisfactory described by both the quasi-classical drift model and the two-Landau levels model. The quasi-classical drift model predicts that at constant drift length and applied pulse amplitude, the excitation time is proportional to the magnetic field ($\tau_{\mathrm{exc}} \propto B$). In other words, the lower the magnetic field is the shorter is the excitation time. In principle we also observe an average reduction of the excitation times when reducing the magnetic fields, but this theory could not explain the dependence of the excitation time on B around the integer filling factor ν. On the other hand, the two-Landau levels model shows that the average spatial separation Δy (see eq. 5.10) increases with increasing magnetic field, at constant applied pulse amplitude. Thus, the tunneling rate decreases with increasing magnetic field which means longer tunneling (excitation) times. The measurements show that the higher the

deviation $\Delta\nu \propto \Delta B$ from the integer filling factor $\nu = 2$ the earlier the breakdown of the QHE occurs. A good understanding of the measurements is given instead by the quasi-local transport model described by Ref. [25]. The model proves that the exactly quantized plateaus result from the existence of the incompressible strips (locally $\sigma_{\mathrm{xx}} = 0$ holds). The reduction of the excitation time is a result of the reduction of the width of the incompressible strips with decreasing magnetic field near the integer filling factor $\nu = 2$. When the magnetic field reaches the value corresponding to the integer filling factor the width of the incompressible strips reaches its maximum value [25]. The asymmetry of the excitation time $\tau_{\mathrm{exc}}(B)$ (shorter at lower magnetic fields $B(\nu > 2)$ and higher at higher magnetic fields $B(\nu < 2)$ with respect to the largest $\tau_{\mathrm{exc}}(B)$ determined at $B(\nu = 2)$) can be attributed to the variation of the width of the incompressible strips. By coming from higher magnetic fields $B(\nu < 2)$ the width of the incompressible strips increases to a maximum value corresponding to $B(\nu = 2)$. By decreasing further the magnetic field $B(\nu > 2)$ the width of the incompressible strips decreases faster in comparison to the width corresponding to higher magnetic fields $B(\nu < 2)$.

Due to the low temperatures ($T \leq 4.1\mathrm{K}$), used during our real-time measurements, the electron-phonon (inelastic) scattering mechanism is assumed not very important and the electron-impurity (elastic) scattering mechanism is more effective. Therefore we could not see a strong temperature dependence of the excitation times. However, a slight increase of the excitation times with decreasing temperature is observed. This can be understood by the reduction of the width of the incompressible strips with increasing temperature which leads to shorter traveling (excitation) times.

Chapter 6

Real-time measurements of the optical excitation and relaxation of quantum Hall samples with Corbino geometry

In this chapter, on one hand the real-time measurements of the optical excitation and relaxation of QH devices with Corbino geometry are presented. On the other hand, photoresponse measurements are presented and an electron heating picture has been experimentally investigated to explain the occurrence of the double-peak bolometric contribution of the photoresponse. The motivation of the real-time measurements of the optical excitation and relaxation was coming from previous space-resolved measurements of the electrical excitation and relaxation [31, 33, 37], the time-integrating measurements of the electrical excitation and relaxation [35, 36, 44] and the real-time measurements of the electrical excitation [73, 74]. The conclusions of the space-resolved measurements of excitation and relaxation [31,33,37] were that the electrons, excited by an array of parallel narrow wires, relax back to the lattice temperature and return to the QH state only after a characteristic drift length ℓ_{D}. This characteristic relaxation length ℓ_{D} increases with the mobility of the sample and it is comparable to the mean free path ℓ_{mfp}. From the determined values of the relaxation length ℓ_{D} and the drift velocity $v_{\mathrm{D}} = E_{\mathrm{H}}/B$, the relaxation time $\tau_{\mathrm{rel}} = \ell_{\mathrm{D}}/v_{\mathrm{D}}$ is determined in the range of a few nanoseconds ($0.26\mathrm{ns} \leq \tau_{\mathrm{rel}} \leq 2.6\mathrm{ns}$ for carrier mobilities of $4 \times 10^{4}\mathrm{cm}^{-2}\mathrm{V}^{-1}\mathrm{s}^{-1} \leq \mu \leq 5.3 \times 10^{5}\mathrm{cm}^{-2}\mathrm{V}^{-1}\mathrm{s}^{-1}$). However, this was an indirect method to estimate the relaxation times and therefore a direct determination of the relaxation times was desirable. A direct method to determine the time scales was provided by the time-integrating measurements of excitation and relaxation [35, 36, 44]. These measurements were supplementing the previous space-resolved relaxation measurements in the time-domain by considering the use of the supercritical electrical pulses (pulse amplitude above the critical source-drain voltage, $A > V_{\mathrm{SD}}$) to excite the electrons. It was concluded that $\tau_{\mathrm{exc}} \leq \tau_{\mathrm{rel}}$, but by decreasing the pulse width to around $\tau_{\mathrm{exc}} = 1\mathrm{ns}$ the system relaxes in a time which approaches the limit $\tau_{\mathrm{exc}} = \tau_{\mathrm{rel}}$. A step forward was the performance of real-time measurements of the electrical excitation [73, 74] which could investigate the individual pulse shape of the sample response. The conclusions were that the excitation times τ_{exc} of the electron system are of the order of nanoseconds and depend on the pulse amplitude, carrier mobility of the sample and on the magnetic field. Since from the previous time-integrating measurements of excitation and relaxation [35, 36, 44] it had not been possible to monitor the individual pulse shape of the sample response in the real-time domain, we performed real-time measurements of the optical excitation and relaxation of the QH devices with Corbino geometry.

6.1 Optical excitation source (*p*-Ge laser system)

The real-time measurements of the optical excitation and relaxation of QH devices with Corbino geometry are, to some extent, comparable to the real-time measurements of the electrical excitation of QH devices with Corbino geometry [73, 74]. The main and the important difference to these measurements is the excitation source. While for the real-time measurements of the electrical excitation the supercritical electrical pulses, provided by a electrical pulse generator, represent the excitation source, for the real-time measurements of the optical excitation and relaxation the excitation is generated by an optical excitation source, the *p*-Ge laser system (see Fig. 6.1). The *p*-Ge laser system, described by various theoretical [85, 86] and experimental studies [87–92], operates applying crossed electric and magnetic fields.
The advantages of using the *p*-Ge laser system as the excitation source are:

- *compactness*: enables the use of the laser mounted into a sample holder and inserted in a cryostat together with the QH device with Corbino geometry;

- *tunability*: the possibility to tune the emission frequency continuously in a certain frequency range. Our *p*-Ge laser crystal is tunable in the frequency range of $1.7\mathrm{THz} \leq f_{\mathrm{laser}} \leq 2.5\mathrm{THz}$ which corresponds to a wavelength range of $180\mu\mathrm{m} \geq \lambda_{\mathrm{laser}} \geq 120\mu\mathrm{m}$. The wavelength range is determined by the impurity concentration ($p \approx 10^{13}\mathrm{cm}^{-3}$) [90, 92];

However, the *p*-Ge laser system has also some disadvantages, which are not critical as long as it is used for scientific purposes:

- *high voltages and currents*: the laser is operated by means of electrical pumping with pulses of peak voltages of $0.6\mathrm{kV} - 2\mathrm{kV}$ at high currents of $20\mathrm{A} - 35\mathrm{A}$ through the *p*-Ge crystal. Because of the use of high currents and to avoid overheating, the laser emits about one pulse per second $f = 1\mathrm{Hz}$ with a duration adjustable by the electrical pumping source of $0.3\mu\mathrm{s} \leq t_{\mathrm{p}}^{\mathrm{laser}} \leq 50\mu\mathrm{s}$. The decay time of the laser pulse $t_{\mathrm{laser}}^{\mathrm{fall}} \leq 20\mathrm{ns}$ (measured with a *p*-Ge detector) is mainly determined by

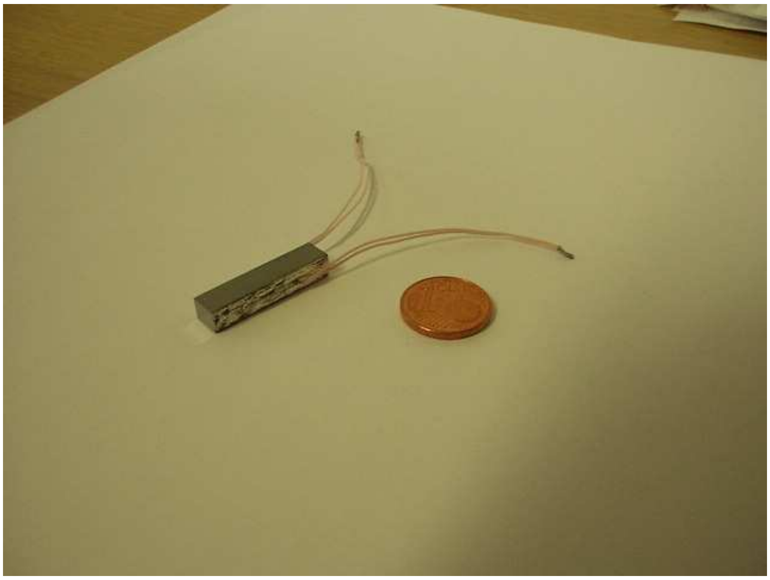

Figure 6.1: A view of the *p*-Ge laser crystal besides a coin of 1 Eurocent. The *Al*-electrodes are located at the two parallel sides to apply the electric field.

the switch-off flank of the high power FET (field effect transistor)-based electrical pumping source;

- *cryogenic conditions*: the use of liquid *He* is necessary for two reasons: the magnetic field required for the laser is produced by superconducting magnet coils and the high input power, necessary to establish an inversion population, heats the active medium and destroys the inversion population.

As a consequence, there is a *limited commercial usability* of such *p*-Ge laser systems.

The pumping mechanisms which determine the inversion population in lasers based on *p*-Ge crystals are described by three different transitions between the LL's: *light hole-heavy hole transitions* [93,94] (emits light in THz range of the electromagnetic spectrum), *light hole cyclotron resonance transitions* (emits light in THz range of the electromagnetic spectrum) [87,88,92,94] and *heavy hole cyclotron resonance transitions* (emits light in microwave (MW) range of the electromagnetic spectrum) [95, 96].
Since our *p*-Ge laser crystal produces light due to the light hole cyclotron resonance transitions between the corresponding LL's, in the next passage I describe a possible mechanism underlying the operation of the light hole cyclotron resonance laser. Stimulated emission is only possible in a certain window of the $\vec{E} \times \vec{B}$ in which the light holes are in accumulation and the heavy holes are in streaming motion. The application of the electric field $\vec{E}$ to the *p*-Ge crystal generates a movement of the free carriers (light and heavy

holes). The application of the magnetic field determines the quantization of the state of holes into LL's. In the streaming motion, due to the electric field, the heavy holes are accelerated collisionless to the optical phonon edge where they emit an optical phonon and are scattered back to the origin of the momentum space $|\vec{k}| = 0$. There is a finite probability that the heavy holes are scattered into the LL's of the light holes. The light holes, due to the crossed electric and magnetic fields $\vec{E} \times \vec{B}$, make cyclotron orbits of radius $|-E/B|$ in the momentum $\vec{k}$-space. A further increase of the electric field would alter the populations of the LL's, by moving on one orbit with larger radius. Carriers inside the circle $|\vec{k}| = |\vec{k}_{\mathrm{op}}|$ are influenced only by acoustic phonons and impurity scattering but not disturbed by optical phonons. This area of this circle is called the *accumulation area* (*passive region*). The carriers outside the accumulation area are scattered to $|\vec{k}| = 0$. Thus, the population of one LL with the orbit passing through or nearby the origin $|\vec{k}| = 0$ of the velocity space is increased (see the LL labeled $n = 3$ in Fig. 6.2). Since the population of lower LL's ($n = 0, 1, 2$) are not increased by optical phonons scattering, an inversion population can occur between the LL ($n = 3$), with the orbit through the origin $|\vec{k}| = 0$, and the lower LL's ($n = 0, 1, 2$) [89, 97].

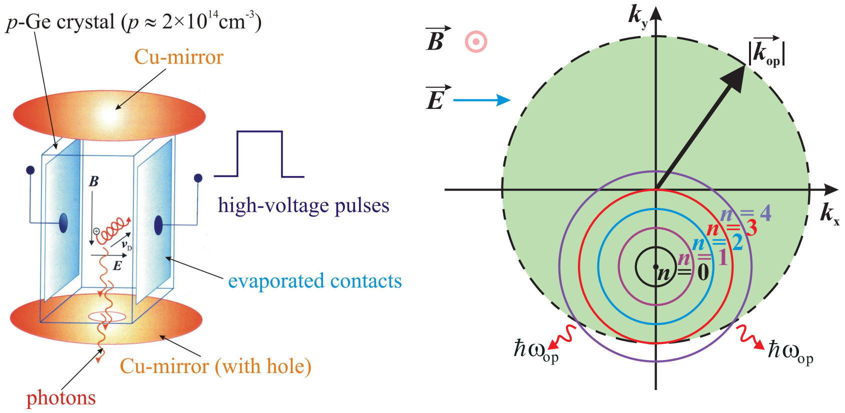

Figure 6.2: Scheme of the *p*-Ge laser (left). A schematic view (the LL's of light holes in *Ge* are approximated by circles in the $\vec{k}$-space) of the function principle of the *p*-Ge laser crystal (right). Cyclotron orbits of the first 4 Landau levels in momentum space $\vec{k}$ in crossed electric and magnetic fields $\vec{E} \times \vec{B}$. The dashed circle corresponds to the critical momentum $\vec{k}_{\mathrm{op}}$ where optical phonon emission occurs.

6.2 Experimental setup

The QH devices used for our real-time measurements of the optical excitation and relaxation were fabricated from three different *GaAs/AlGaAs* wafers $\#4$, $\#5$ and $\#6$ with electron densities in the range of $2 \times 10^{11}\,\mathrm{cm}^{-2} \leq n_\mathrm{s} \leq 2.7 \times 10^{11}\,\mathrm{cm}^{-2}$ and electron mobilities in the range of $0.1 \times 10^{6}\,\mathrm{cm}^2\mathrm{V}^{-1}\mathrm{s}^{-1} \leq \mu_\mathrm{el} \leq 1.6 \times 10^{6}\,\mathrm{cm}^2\mathrm{V}^{-1}\mathrm{s}^{-1}$ (see Table 6.1). All devices investigated in this study were patterned as devices with Corbino geometry of $r_1 = 500\mu\mathrm{m}$, $r_2 = 1500\mu\mathrm{m}$ the inner and outer radii of the QH device with Corbino geometry and large large photoactive area $A_\mathrm{ph} \approx 6.3\mathrm{mm}^2$.

Table 6.1: Electron density n_s and carrier mobility μ_el of the wafers from which the QH devices with Corbino geometry were obtained (parameters were determined from transport measurements at $1.7\mathrm{K}$).

Wafers	$n_\mathrm{s}\,(\mathrm{cm}^{-2})$	$\mu_\mathrm{el}\,(\mathrm{cm}^2\mathrm{V}^{-1}\mathrm{s}^{-1})$	$r_1\,(\mu\mathrm{m})$	$r_2\,(\mu\mathrm{m})$
#4	2.7×10^{11}	0.1×10^{6}	500	1500
#5	2.1×10^{11}	0.5×10^{6}	500	1500
#6	2×10^{11}	1.6×10^{6}	500	1500

The experimental setup of the real-time measurements of the optical excitation and relaxation is shown schematically in Figure 6.3. A pulse generator produces rectangular electrical pulses $V_\mathrm{A}(t)$ of the amplitude voltage $A_\mathrm{p}^\mathrm{elec}$, with pulse widths of $3\mathrm{ns} \leq t_\mathrm{p}^\mathrm{elec} \leq 640\mathrm{s}$ and pulse periods of $10\mathrm{ns} \leq T_\mathrm{p}^\mathrm{elec} \leq 100\mathrm{s}$ (with a rise time - $0.5\mathrm{ns}$ and a fall time - $1.5\mathrm{ns}$). This pulse generator sends the electrical pulses through a high frequency (*HF*) coaxial cable, connected to a 50Ω-resistor for impedance-matching and connected to the sample in its immediate vicinity. The applied electrical pulse amplitude $A_\mathrm{p}^\mathrm{elec}$ does not exceed the critical value of the *DC* applied source-drain voltage $V_\mathrm{SD}^\mathrm{crit}$ ($A_\mathrm{p}^\mathrm{elec} < V_\mathrm{SD}^\mathrm{crit}$). At the same time the QH device with Corbino geometry is subjected to the THz radiation emitted by the *p*-Ge laser crystal. The THz laser is operated by the high power FET-based electrical pumping source with pulses of peak voltages of $0.6\mathrm{kV} \leq A_\mathrm{p}^\mathrm{laser} \leq 2\mathrm{kV}$ at high currents of $20\mathrm{A} \leq I_\mathrm{laser} \leq 35\mathrm{A}$ through the *p*-Ge crystal. Due to the use of high currents and to avoid overheating of the QH device, the laser emits about one pulse per second $f = 1\mathrm{Hz}$ ($T_\mathrm{p}^\mathrm{laser} = 1\mathrm{s}$ with the pulse width adjustable by the electrical pumping source of $0.3\mu\mathrm{s} \leq t_\mathrm{p}^\mathrm{laser} \leq 50\mu\mathrm{s}$). The optical decay time of the laser pulse $t_\mathrm{laser}^\mathrm{fall} \leq 20\mathrm{ns}$ (measured with a *p*-Ge detector) is determined by the switch-off flank of the high power FET-based electrical pumping source. The characteristics of the output THz laser are a spectral width of approximately $0.2\mathrm{cm}^{-1}$ and a laser power of approximately $1\mathrm{W}$.

In order to perform real-time measurements of the optical excitation and relaxation we need a synchronism between the electrical pulses and the optical pulses. Thus, the electrical pulse generator is connected by a *T*-shape connector to the laser pulse generator. The third output of the *T*-shape connector is connected to the digital oscilloscope and is therefore able to see the individual pulses generated by these pulse generators (channel 1). By connecting also the optical pulse generator to the high power FET-based electrical pumping source the synchronism is achieved ($T_\mathrm{p}^\mathrm{elec} = T_\mathrm{p}^\mathrm{laser} = 1\mathrm{s}$). In order to apply electrical pulses the electrical pulse generator is connected through another *T*-shape con-

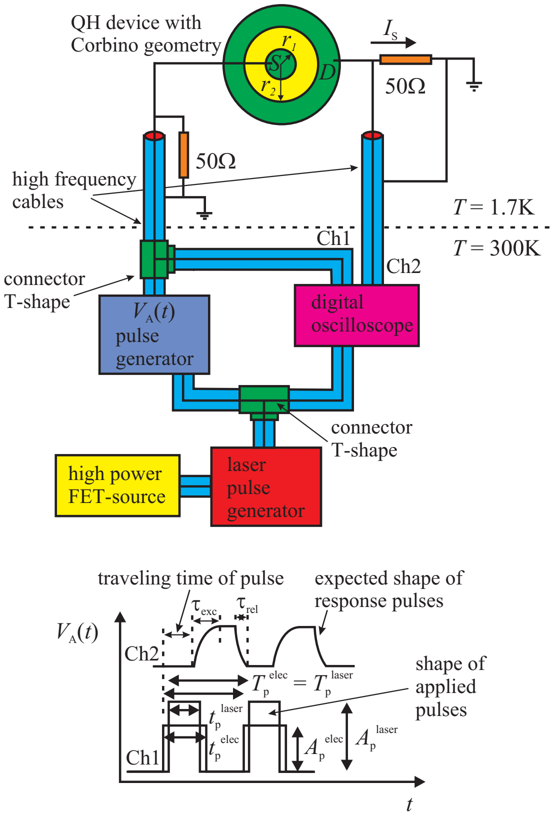

Figure 6.3: Sketch of the experimental setup for the optical excitation and relaxation measurements of the breakdown of the QHE in the real-time domain.

nector to the digital oscilloscope (channel 1) and to the sample (source - *S*). The response of the sample is obtained by connecting the sample (drain - *D*) to the digital oscilloscope (channel 2) (see Fig. 6.3).

Another 50Ω resistor was attached in series with the sample (between the drain contact *D* and the ground) in order to measure the current I_s passing through the sample and display $I_s(t)$ on a digital oscilloscope (also impedance-matched by a 50Ω resistor) that monitors the individual response shape $I_s(t)$ of the sample. The calculated time resolution of our experimental setup is $t_{\mathrm{RC}} = 2.5\mathrm{ns}$ (the series capacitance of our *HF* cables $C_s \approx 100\mathrm{pF}$ and the circuit parallel resistor $R_p = 25\Omega$). When replacing the QH device with Corbino geometry by a test resistor we determine the time resolution of about $t_{\mathrm{RC}}^{\mathrm{exp}} = 2.7\mathrm{ns} - 3\mathrm{ns}$, in good agreement with the calculated value $t_{\mathrm{RC}}^{\mathrm{calc}} = 2.5\mathrm{ns}$.

The real-time measurements of optical excitation and relaxation have been performed at different temperatures ($T = 3\mathrm{K}, 3.5\mathrm{K}, 4.1\mathrm{K}$) and magnetic fields B up to $6\mathrm{T}$ (applied perpendicular to the 2DES). With our experimental setup we could not achieve lower temperatures than $3\mathrm{K}$ due to the rather high consumption of the liquid *He* in order to keep

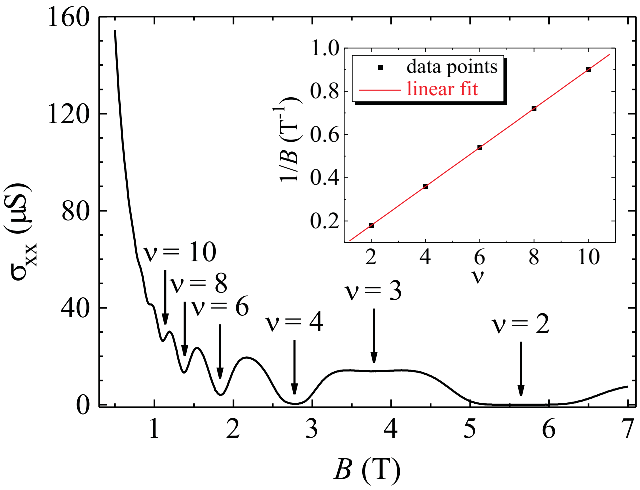

Figure 6.4: Shubnikov-de Haas oscillations of a QH device with Corbino geometry (sample $\#4$) taken at the applied source-drain voltage $V_{\mathrm{SD}} = 0.1\mathrm{V}$ and lattice temperature $T = 4\mathrm{K}$. The inset shows the linear dependence of the minima of SdH oscillations corresponding on the integer filling factors $\nu = 2, 4, 6, 8, 10$ (Landau plot).

the sample, the big superconducting coils and at the same time the superconducting coils of the *p*-Ge laser crystal cold. These measurements were done at constant laser pulse amplitude $A_{\mathrm{p}}^{\mathrm{laser}} = 1.68\mathrm{kV}$ and constant laser current $I_{\mathrm{laser}} = 25\mathrm{A}$ from which the photon (laser) energy is determined:

$$E_{\mathrm{photon}} = \hbar\omega_{\mathrm{laser}} = \hbar \cdot \frac{eB_{\mathrm{L}}}{m_{\mathrm{L}}^{*}}\,, \tag{6.1}$$

where $B_{\mathrm{L}} = I_{\mathrm{laser}} \cdot 0.135\mathrm{T/A}$ is the magnetic field induced by the current I_{laser} (applied to the superconducting coil of the laser), $0.135\mathrm{T/A}$ is the coil constant (characteristic for our laser system) and $m_{\mathrm{L}} = 0.046 \cdot m_{\mathrm{e}}$ is the effective mass of the light holes in the *p*-Ge laser crystal. By chosing the value of the laser current $I_{\mathrm{laser}} = 25\mathrm{A}$ we determine the corresponding emitted photon energy $E_{\mathrm{photon}} = 8.5\mathrm{meV}$.

6.3 Characterization of the system (*DC* measurements)

We characterized our QH devices with Corbino geometry by SdH measurements $\sigma_{\mathrm{xx}}(B)$ to determine the electron density n_{s} (see eq. 5.2 and the inset of Fig. 6.4), the carrier mobility μ_{el} (see eq. 5.3) and to check whether our sample develops QH states. The SdH measurements are done by measuring the source-drain current I_{s} as a function of the magnetic field B, for fixed *DC* values of the source-drain voltage V_{SD}. Finally, we calculate the longitudinal conductivity σ_{xx} according to eq. 5.1. A typical experimental SdH trace is shown in Fig. 6.4. By increasing the strength of the magnetic field, the longitudinal conductivity σ_{xx} starts to decrease and begins to oscillate (so called *SdH-oscillations*). For certain ranges of magnetic fields these oscillations have deep minima where the longitudinal conductivity σ_{xx} approaches zero. This is due to that the electron system is in QH state around integer filling factors $\nu = i$. Figure 6.4 shows a magneto-transport curve for the sample $\#4$ (see Table 6.1) with a well developed QH plateau at the filling factor $\nu = 2$. The minima of the SdH oscillations, corresponding to the integer filling factors $\nu = i$, are periodic with respect of the inverse of magnetic field $1/B$ (see inset of the Fig. 6.4, Landau plot). From this periodicity the electron density n_{s} (see eq. 5.2) is determined.

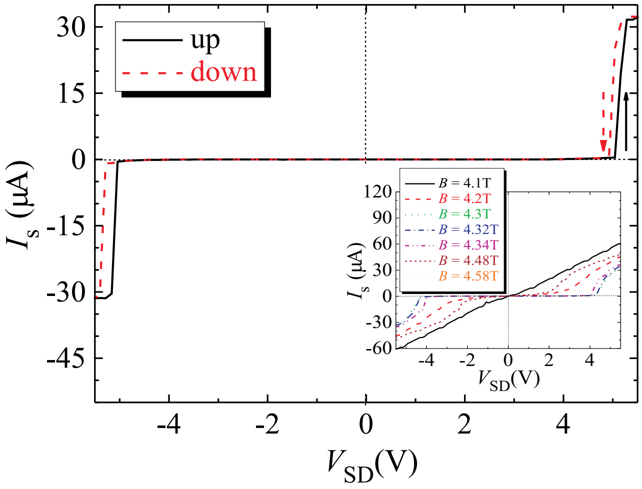

Figure 6.5: $I - V$ curves of a QH device with Corbino geometry (sample $\#5$) taken for up- and down- sweep of the applied source-drain voltage V_{SD} at magnetic field $B(\nu = 2) = 4.37\mathrm{T}$ and temperature $T = 1.7\mathrm{K}$. The inset shows several $I - V$ curves corresponding to different magnetic fields B taken for sample $\#5$ at a temperature $T = 4\mathrm{K}$.

In order to determine the electrical breakdown conditions for filling factor $\nu = 2$, the condition for which the breakdown of the QHE occurs, several current-voltage $I - V$ traces at different magnetic fields (around the middle of the second plateau $\nu = 2$) are taken. These $I - V$ traces were taken in order to determine the corresponding critical *DC* source-drain voltages $V_{\mathrm{SD}}^{\mathrm{crit}}$ for each magnetic field (or filling factor) within the range of the QH plateau (see inset of Fig. 6.5). At values of the magnetic field outside or in the vicinity of the flanks of the QH plateau, the $I - V$ curves show transitions from negative to positive voltages without a well defined plateau around the voltage $V_{\mathrm{SD}} = 0$. By getting closer to the integer filling factor, at the middle of the QH plateau, the $I - V$ curves develop an *S*-like shape. The closer the filling factor is to the integer values, the larger the plateau in the $I-V$ curves becomes. The largest plateau in the $I-V$ curves corresponds to the integer filling factor (see inset of Fig. 6.5).

Figure 6.5 shows the $I-V$ curves at filling factor $\nu = 2$ with different critical *DC* source-drain voltages corresponding to the up- and down- sweeps ($V_{\mathrm{SD}}^{\mathrm{crit}} = 5.04\mathrm{V}$ for the up-sweep and $V_{\mathrm{SD}}^{\mathrm{crit}} = 4.92\mathrm{V}$ for the down-sweep). The existence of the hysteresis of the current-voltage characteristics (different critical *DC* source-drain voltages corresponding to the up- and down- sweeps) near the breakdown of the QHE [26,98], could be explained on the basis of thermal instabilities of the electron system by the electron heating model [38, 39, 79, 99]. These thermal instabilities of the electron system come from the power balance between the energy gain $P_{\mathrm{gain}} = \sigma_{\mathrm{xx}} E_{\mathrm{r}}^2$ and the energy loss $[\epsilon(T_{\mathrm{el}}) - \epsilon(T_{\mathrm{lat}})]/\tau_{\mathrm{rel}}$ rates. The gain energy represents the electrical energy fed to the system per time and area. The loss energy describes the relaxation of the enhanced energy $\epsilon(T_{\mathrm{el}})$ at the elevated electron temperature T_{el} back to the energy $\epsilon(T_{\mathrm{lat}})$ at the lattice temperature T_{lat} (for detailed discussions see Refs. [38, 39, 99]).

The further real-time measurements of optical excitation and relaxation of the QH devices with Corbino geometry were performed near the filling factor $\nu = 2$, since for higher filling factors $\nu = 4$ and $\nu = 6$ the QHE was not well observable at a temperature $T = 4\mathrm{K}$ (see Fig. 6.4).

6.4 Laser pulse-induced breakdown of the QHE

In the real-time breakdown measurements (breakdown of the QHE induced by laser pulses) on QH devices with Corbino geometry, we have investigated the excitation times τ_{exc} and the relaxation times τ_{rel} of the electron system as a function of the amplitude, the magnetic field, the electron mobility and the temperature.

Strong disturbances appear after switching the laser on and off, due to the electric coupling between the high-power laser supply cable and the detector cable (so called "cross talking"). In order to keep the high-time resolution and consequently a low level of the possible cross-talking between wires or electronics, the 50Ω resistors of the impedance-matched circuitry (see Fig. 6.3) are shielded and the ends of the *HF* coaxial cables are shielded and connected as close as possible to the sample and to the resistors. However, the *HF* cross-talking cannot be avoided completely but to diminish it we use reference measurements at $|A_{\mathrm{p}}^{\mathrm{elec}}| = 0\mathrm{V}$ and calculate the difference between the signals at $|A_{\mathrm{p}}^{\mathrm{elec}}| > 0\mathrm{V}$ and $|A_{\mathrm{p}}^{\mathrm{elec}}| = 0\mathrm{V}$ (see Fig. 6.6).

By applying electrical pulses of pulse width $t_{\mathrm{p}}^{\mathrm{elec}}$ and laser pulses of pulse width $t_{\mathrm{p}}^{\mathrm{laser}}$ on the QH devices with Corbino geometry, we monitor the real-time sample response (excitation and relaxation times) by measuring the source-drain current I_{s}, according to eq. 5.4, through the serial 50Ω resistor, as a function of time (see Fig. 6.6). We fit an exponential function (see eq. 5.5) to the measured trace $I_{\mathrm{s}}(t)$,

$$I(t) \propto \exp\left(-\frac{t}{\tau}\right) . \tag{6.2}$$

From the slopes we determine the excitation τ_{exc} and the relaxation times τ_{rel} of the order of a few tens up to hundreds of nanoseconds, see figure caption 6.6). The accuracy of this fit function is at its best 10^{-9}s. Thus, the error bars of the determined excitation times τ_{exc} and relaxation times τ_{rel} are in the range of $\pm 10\% - \pm 17\%$ of the estimated excitation and relaxation times.

While the excitation time τ_{exc} can be understood as the time required for the system to evolve from a QH state to a dissipative state (QH breakdown), the relaxation time τ_{rel} can be understood as the time required for the system to relax from a dissipative state back to the QH state. The spikes (see Fig. 6.6) are assumed to be due to the cross-talking between cables and electronics.

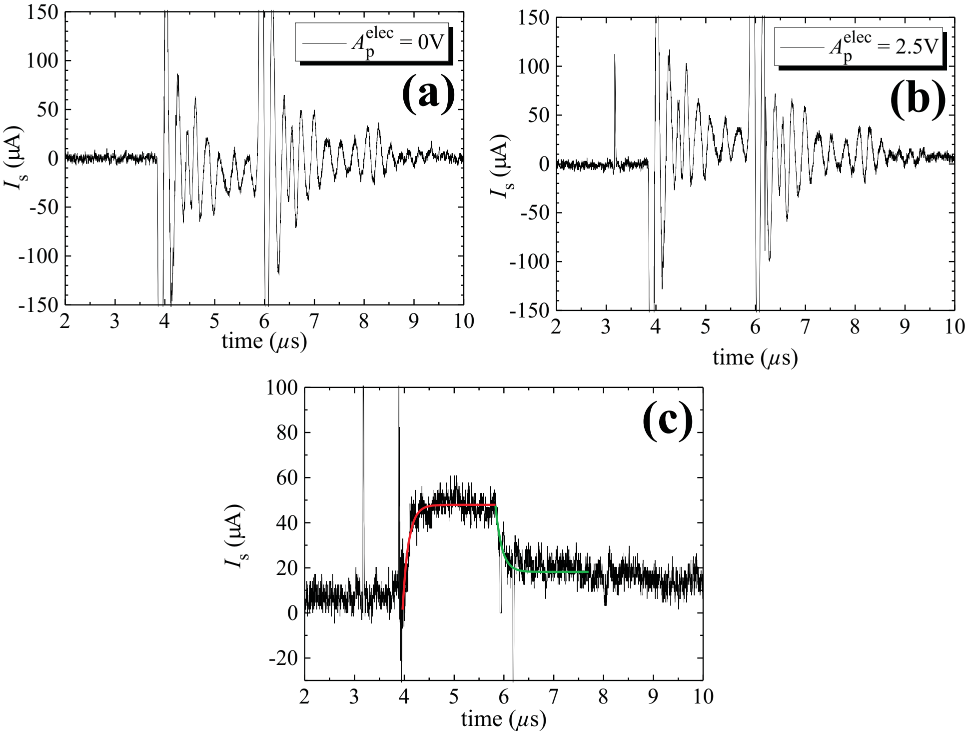

Figure 6.6: Time evolution of the measured source-drain current I_s (solid-black curve), the exponential function (see eq. 6.2, red- and green- solid curves) fitted to the experimental trace $I_s(t)$. The QH device with Corbino geometry (sample #5) was subjected to electrical pulses (pulse-widths $t_p^{\text{elec}} = 3\mu$s, applied pulse amplitudes $A_p^{\text{elec}} = 2.5$V) and synchronized laser pulses (pulse-widths $t_p^{\text{laser}} = 1.5\mu$s, applied pulse amplitudes $A_p^{\text{laser}} = 1.67$kV) at temperature $T = 4$K and magnetic field $B = 4.3$T. The determined excitation and relaxation times for this particular example were $\tau_{\text{exc}} = 122\text{ns}\pm 10\text{ns}$ and $\tau_{\text{rel}} = 128\text{ns}\pm 13\text{ns}$. Figure (a) shows the sample response without applied electrical pulse amplitude $A_p^{\text{elec}} = 0$V, figure (b) shows the sample response with applied electrical pulse amplitude $|A_p^{\text{elec}}| > 0$V and figure (c) shows the sample response resulting from the difference between the signals corresponding to $A_p^{\text{elec}} = 0$V and $|A_p^{\text{elec}}| > 0$V.

6.4.1 Amplitude and mobility dependences of the excitation and relaxation times

Before starting the excitation and relaxation measurements, we have determined the *DC* breakdown conditions for the investigated QH devices with Corbino geometry (see Table 6.1) for filling factor $\nu = 2$. The critical source-drain voltage $V_{\mathrm{SD}}^{\mathrm{crit}}$ varies with the electron mobility, magnetic field and temperature. The determined *DC* breakdown value (at filling factor $\nu = 2$) for the high-mobility sample $\#6$ was $V_{\mathrm{SD}}^{\mathrm{crit}} = 2.3\mathrm{V}$ while for the low- and medium-mobility samples $\#4$ and $\#5$ (see Table 6.1) the breakdown values were $V_{\mathrm{SD}}^{\mathrm{crit}} = 4.2\mathrm{V} - 4.3\mathrm{V}$. By applying the electrical pulses, the laser pulses cause an optically induced breakdown of the QHE and result in a sharp increase of the photoresponse (PR)[1] during this process. While the laser is on, the PR stays constant. However, as soon as the laser is switched off, the QHE is recovered and consequently the PR relaxes fast to zero, characterized by a specific relaxation time τ_{rel}. Thus, the sample response $I_{\mathrm{s}}(t)$ is measured through the 50Ω resistor and displayed on the screen of the electronic oscilloscope (see Fig. 6.6).

The real-time measurements of the optical excitation and relaxation were performed by applying electrical pulse amplitudes below the *DC* breakdown value of the source-drain voltage ($A_{\mathrm{p}}^{\mathrm{elec}} < V_{\mathrm{SD}}^{\mathrm{crit}} \approx 4.3\mathrm{V}$), at constant laser pulse amplitude and constant photon (laser) energy. Only for the high-mobility sample $\#6$ we exceeded the *DC* breakdown value ($A_{\mathrm{p}}^{\mathrm{elec}} > V_{\mathrm{SD}}^{\mathrm{crit}} \approx 2.3\mathrm{V}$). $A_{\mathrm{p}}^{\mathrm{elec}} < V_{\mathrm{SD}}^{\mathrm{crit}}$ means that by having the laser off there is no electrical breakdown and the sample remains into the QH state. By operating the laser, during the laser pulses, the electron system leaves the QH state and run into a dissipative state. Thus, an optically induced breakdown of the QHE is achieved. When the laser is switched off, the electron system relaxes back into the dissipationless QH state. The laser pulse widths do not exceed the electrical pulse widths ($t_{\mathrm{p}}^{\mathrm{laser}} \leq t_{\mathrm{p}}^{\mathrm{elec}}$). By increasing gradually the electrical pulse amplitude up to the *DC* breakdown value ($A_{\mathrm{p}}^{\mathrm{elec}} < V_{\mathrm{SD}}^{\mathrm{crit}} \approx 4.3\mathrm{V}$), at constant laser pulse amplitude and constant photon energy, the response of the QH device with Corbino geometry is measured, as seen in Fig. 6.6. By applying the exponential fitting function 6.2 we could determine the excitation and relaxation times for various electrical pulse amplitudes, electron mobilities and various magnetic field values. The determined excitation times τ_{exc} decrease with increasing the electrical pulse amplitude $A_{\mathrm{p}}^{\mathrm{elec}}$ at constant photon energy. Thus, the system evolves quicker from a dissipationless QH state into a dissipative state with increasing the electrical pulse amplitude. The determined relaxation times τ_{rel} increase with increasing the electrical pulse amplitude $A_{\mathrm{p}}^{\mathrm{elec}}$ at constant photon energy. Thus, the system relaxes slower from a dissipative state into the dissipationless state with increasing the electrical pulse amplitude. Figure 6.7 shows the electrical pulse amplitude dependence of the excitation times and the relaxation times for the QH sample with Corbino geometry $\#4$ (see Table 6.1), for electrical pulse widths $t_{\mathrm{p}}^{\mathrm{elec}} = 2\mu\mathrm{s}$ and laser pulse widths $t_{\mathrm{p}}^{\mathrm{laser}} = 1.5\mu\mathrm{s}$ ($T = 4\mathrm{K}$ and $\nu = 2$). Figure 6.7 shows

---

[1] The photoresponse (PR) is the difference between the measured sample responses $I_{\mathrm{s}}(t)$ with and without laser illumination ($\mathrm{PR} \propto \Delta I_{\mathrm{s}}$).

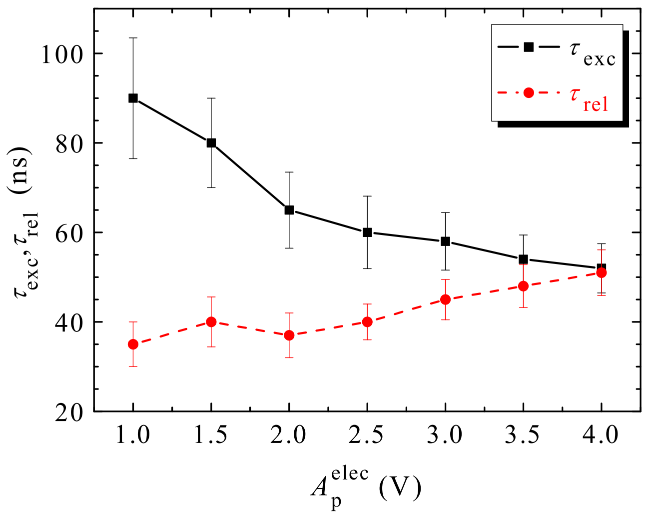

Figure 6.7: Excitation times τ_{exc} and relaxation times τ_{rel} as a function of the applied electrical pulse amplitude $A_{\mathrm{p}}^{\mathrm{elec}}$, determined for the low-mobility sample $\#4$: $\mu_{\mathrm{el}} = 0.1 \times 10^{6}\mathrm{cm}^{2}\mathrm{V}^{-1}\mathrm{s}^{-1}$. The determined excitation times $\tau_{\mathrm{exc}}(A)$ and relaxation times τ_{rel} correspond to measurements performed for electrical pulse widths $t_{\mathrm{p}}^{\mathrm{elec}} = 2\mu\mathrm{s}$ and laser pulse widths $t_{\mathrm{p}}^{\mathrm{laser}} = 1.5\mu\mathrm{s}$, at $T = 4\mathrm{K}$ and $B(\nu = 2) = 5.66\mathrm{T}$.

shorter relaxation times than the excitation times for the corresponding values of the electrical pulse amplitudes. These results are consistent with the thermodynamical arguments given in the previous chapter concerning the two-Landau levels model and in Ref. [40]. However, we found that $\tau_{\mathrm{rel}} \leq \tau_{\mathrm{exc}}$ holds for the low- and medium- mobility samples $\#4$ and $\#5$ and $\tau_{\mathrm{rel}} \geq \tau_{\mathrm{exc}}$ holds for the high-mobility sample $\#6$. We find excitation and relaxation times of the order of $30\mathrm{ns} - 170\mathrm{ns}$. The highest values of τ_{rel} correspond to the high-mobility sample $\#6$. For the low- and medium- mobility samples $\#4$ and $\#5$ the relaxation times increase with increasing the electrical pulse amplitudes $A_{\mathrm{p}}^{\mathrm{elec}}$ below the *DC* breakdown value $V_{\mathrm{SD}}^{\mathrm{crit}}$. Thus, we observe a definite mobility dependence of the relaxation times: the lower mobility of the sample is the shorter relaxation times are (see Fig. 6.8). Since for the high-mobility sample $\#6$ the applied electrical pulse amplitudes exceeded the *DC* breakdown value we could observe a dependence of τ_{rel} on the applied electrical pulse amplitudes $A_{\mathrm{p}}^{\mathrm{elec}} > V_{\mathrm{SD}}^{\mathrm{crit}}$. This pulse amplitude dependence could be a proof that the determined excitation and relaxation times are due to intrinsic properties of the electron systems and not due to the chosen experimental setup. For the high-mobility sample $\#6$ the relaxation time reaches a maximum (corresponding to an electrical pulse amplitude slightly below the *DC* breakdown value of the pulse amplitude $V_{\mathrm{SD}}^{\mathrm{crit}}$). By exceeding the *DC* breakdown value of the pulse amplitude, the relaxation times decrease when increasing further the electrical pulse amplitude (see Fig. 6.8). A similar behavior could not be observed for the low- and medium- mobility samples $\#4$ and $\#5$ since the electrical pulse amplitudes did not exceeded the *DC* breakdown value of the pulse amplitude $A_{\mathrm{p}}^{\mathrm{elec}} < V_{\mathrm{SD}}^{\mathrm{crit}} \approx 4.3\mathrm{V}$. However, a previous work [100] reported a similar behavior (maxima of relaxation times slightly below the *DC* breakdown value also for the low- and medium- mobility samples).

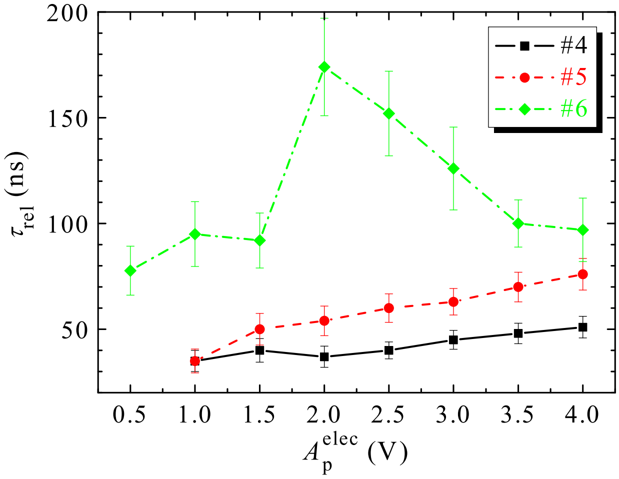

Figure 6.8: Relaxation times τ_{rel} determined for different carrier mobilities ($\#4 : \mu_{\mathrm{el}} = 0.1 \times 10^{6}\mathrm{cm}^{2}\mathrm{V}^{-1}\mathrm{s}^{-1}$, $\#5 : \mu_{\mathrm{el}} = 0.5 \times 10^{6}\mathrm{cm}^{2}\mathrm{V}^{-1}\mathrm{s}^{-1}$ and $\#6 : \mu_{\mathrm{el}} = 1.6 \times 10^{6}\mathrm{cm}^{2}\mathrm{V}^{-1}\mathrm{s}^{-1}$), as a function of the applied electrical pulse amplitudes $A_{\mathrm{p}}^{\mathrm{elec}}$ at lattice temperature $T = 4\mathrm{K}$ and at filling factor $\nu = 2$.

We can rise the question: “Why does the increase of the electrical pulse amplitude lead to an increase of the relaxation time?”. A possible explanation based on a heating picture follows here. As mentioned already, after switching off the laser and still for $A_{\mathrm{p}}^{\mathrm{elec}} < V_{\mathrm{SD}}^{\mathrm{crit}}$, the PR decreases fastly and the electron system undergoes a transition from a dissipative state into a dissipationless QH state. This relaxation process is comparable to the situation reported in Ref. [31, 33, 37] where space-resolved measurements of the electrical excitation and relaxation are discussed. Like in these studies, a two-Landau levels model is used. This version of the two-Landau levels model assumes that the longitudinal conductivity σ_{xx} is proportional to the number of excited electrons N to the upper LL ($\Delta\sigma_{\mathrm{xx}} \propto N$) [2]. The occupation of the upper LL decays by a characteristic time τ_0 but depends on the applied electrical pulse amplitudes due to the induced Joule heating ($\approx A_{\mathrm{p}}^{\mathrm{elec}} \cdot I_{\mathrm{s}}$). Thus, a higher applied electrical pulse amplitude prevents the electrons to relax faster. This might explain the results shown in Fig. 6.8 for $A_{\mathrm{p}}^{\mathrm{elec}} < V_{\mathrm{SD}}^{\mathrm{crit}}$ for all three investigated samples (see Table 6.1). For the high-mobility sample $\#6$, for $A_{\mathrm{p}}^{\mathrm{elec}} > V_{\mathrm{SD}}^{\mathrm{crit}}$, the electron system is already in a dissipative state either with the laser on or off. Thus, the electron system is not so sensitive as before for a further increase of the applied electrical

---

[2] Since $\mathrm{PR} \propto \Delta I_{\mathrm{s}} \propto \Delta\sigma_{\mathrm{xx}}$ it means that $\mathrm{PR} \propto N$.

pulse amplitudes. The situation would correspond to a transition between two dissipative states, which is faster with increasing the applied electrical pulse amplitudes (see Fig. 6.8 for the high-mobility sample $\#6$).
The change of population of the upper LL dN depends on the balance between the number of excited electrons dN_{gain} and the number of relaxed electrons dN_{loss} of the upper LL,

$$dN = dN_{\text{gain}} - dN_{\text{loss}}\,, \tag{6.3}$$

with:

$$dN_{\text{gain}} = \frac{\Delta E}{\hbar\omega_{\text{c}}} = \frac{P\cdot dt}{\hbar\omega_{\text{c}}} = \frac{A_{\text{p}}^{\text{elec}}\cdot I_{\text{s}}\cdot dt}{\hbar\omega_{\text{c}}}\,, \tag{6.4}$$

where the gain energy $\Delta E = P\cdot dt$ is used to elevate dN_{gain} electrons over the Landau gap $\hbar\omega_{\text{c}}$ in time dt. Due to different energy-loss processes [33, 40], the density of electrons in the upper LL decays in a characteristic time scale τ_0 (see 6.5):

$$dN_{\text{loss}} = \frac{N}{\tau_0}\cdot dt\,. \tag{6.5}$$

As mentioned before I assume that the longitudinal conductivity σ_{xx} (see eq. 5.1) is proportional to the number of excited electrons N to the upper LL ($\Delta\sigma_{\text{xx}} \propto N$, $\Delta\sigma_{\text{xx}} = \gamma N$). Thus the change of population of the upper LL is given by:

$$dN = dN_{\text{gain}} - dN_{\text{loss}} = \frac{\gamma\cdot N\cdot (A_{\text{p}}^{\text{elec}})^2\cdot dt}{K\cdot\hbar\omega_{\text{c}}} - \frac{N\cdot dt}{\tau_0}\,, \tag{6.6}$$

where $K = (ln(r_2/r_1))/2\pi$ is a constant and the measured current I_{s} has been expressed as $I_{\text{s}} = (\sigma_{\text{xx}}\cdot A_{\text{p}}^{\text{elec}})/K$ according to eq. 5.1 and inserted in eq. 6.4. After some algebra steps the number of excited electrons across the Landau gap is found,

$$N = N_0\cdot\exp\left[-\frac{t}{\tau_0}\cdot\left(1-\frac{\gamma\cdot(A_{\text{p}}^{\text{elec}})^2\cdot\tau_0}{K\cdot\hbar\omega_{\text{c}}}\right)\right]\,. \tag{6.7}$$

Because the applied electrical pulse amplitude is increased and can reach the critical value of the source-drain voltage ($A_{\text{p}}^{\text{elec}} = V_{\text{SD}}^{\text{crit}}$), the excited electrons reach a critical (saturation) value ($N = N_{\text{crit}}$) and at the breakdown $N(t) = N_{\text{crit}}$ must be a stationary solution of eq. 6.7 after the saturation (the breakdown is complete):

$$\frac{dN}{dt} = 0 = -\frac{1}{\tau_0}\left(1-\frac{\gamma\cdot(V_{\text{SD}}^{\text{crit}})^2\cdot\tau_0}{K\cdot\hbar\omega_{\text{c}}}\right)\cdot N\,, \tag{6.8}$$

from which we find

$$\left(\frac{1}{V_{\text{SD}}^{\text{crit}}}\right)^2 = \frac{\gamma\cdot\tau_0}{K\cdot\hbar\omega_{\text{c}}}\,. \tag{6.9}$$

By inserting eq. 6.9 into eq. 6.7 we determine the number of excited electrons N to upper level and consequently the photoresponse $\text{PR} \propto N$ as a function of the source-drain voltage V_{SD} and the critical value of the *DC* breakdown voltage $V_{\mathrm{SD}}^{\mathrm{crit}}$,

$$\mathrm{PR} \propto N = N_0 \cdot \exp\left\{-\frac{t}{\tau_0} \cdot \left[1 - \left(\frac{A_{\mathrm{p}}^{\mathrm{elec}}}{V_{\mathrm{SD}}^{\mathrm{crit}}}\right)^2\right]\right\} . \tag{6.10}$$

With the observation $\Delta I_{\mathrm{s}} \propto \mathrm{PR} \propto N$ and by comparing eq. 6.10 with eq. 6.2 we can determine the decay (relaxation) time function,

$$\tau = \frac{\tau_0}{1 - \left(\frac{A_{\mathrm{p}}^{\mathrm{elec}}}{V_{\mathrm{SD}}^{\mathrm{crit}}}\right)^2} . \tag{6.11}$$

The decay (relaxation) function $\tau(A_{\mathrm{p}}^{\mathrm{elec}})$ approaches τ_0 at $A_{\mathrm{p}}^{\mathrm{elec}} = 0$ and increases for $A_{\mathrm{p}}^{\mathrm{elec}} < V_{\mathrm{SD}}^{\mathrm{crit}}$, as shown in Fig. 6.8. However, the decay function $\tau(A_{\mathrm{p}}^{\mathrm{elec}})$ could reproduce partially the experimental findings because for the situations characterized by $A_{\mathrm{p}}^{\mathrm{elec}} \geq V_{\mathrm{SD}}^{\mathrm{crit}}$, the relaxation times describe transitions between dissipative states instead of transitions between a dissipative and dissipationless state as for $A_{\mathrm{p}}^{\mathrm{elec}} < V_{\mathrm{SD}}^{\mathrm{crit}}$. The present situation refers to a different kind of relaxation time. Further, the relaxation process to the dissipationless QH state takes infinitely long time, corresponding to the divergence of the relaxation time function given by eq. 6.11 for $A_{\mathrm{p}}^{\mathrm{elec}} = V_{\mathrm{SD}}^{\mathrm{crit}}$.

6.4.2 Magnetic field and temperature dependences of the excitation and relaxation times

If the magnetic field is varied from its position at the middle of the QH plateau (filling factor $\nu = 2$) to higher or to lower values, the electron system relaxes back into a dissipationless QH state in shorter times for a constant applied electrical pulse amplitude (see Fig. 6.9 (a)). Figure 6.9 (b) shows the magnetic field dependence of the relaxation for filling factors around $\nu = 2$ at different applied electrical pulse amplitudes. The further the filling factor is departing from the integer values the shorter is the relaxation time. This would correspond to the situation in which by getting further from the integer filling factor (the middle of the QH plateau), the electron system needs a smaller *DC* critical voltage for the breakdown. Thus, for the same applied electrical pulse amplitudes the electrons could relax from a dissipative state into the QH state for one magnetic field value while for higher magnetic field (but not corresponding to an integer filling factor $\nu = i$) the electrons might undergo transitions between two dissipative states, which are fast. The measurements for the optically induced breakdown have been performed at low temperatures ($T \leq 4\mathrm{K}$). Due to the experimental setup, lattice temperatures lower than $3\mathrm{K}$ could not be achieved due to the rather high consumption of liquid *He* in order to keep cold the superconducting coils of the laser and at the same time the big superconducting coils. By applying the electrical pulse amplitudes and simultaneously by illuminating the QH device with the laser, the temperature raises locally probably to temperatures higher

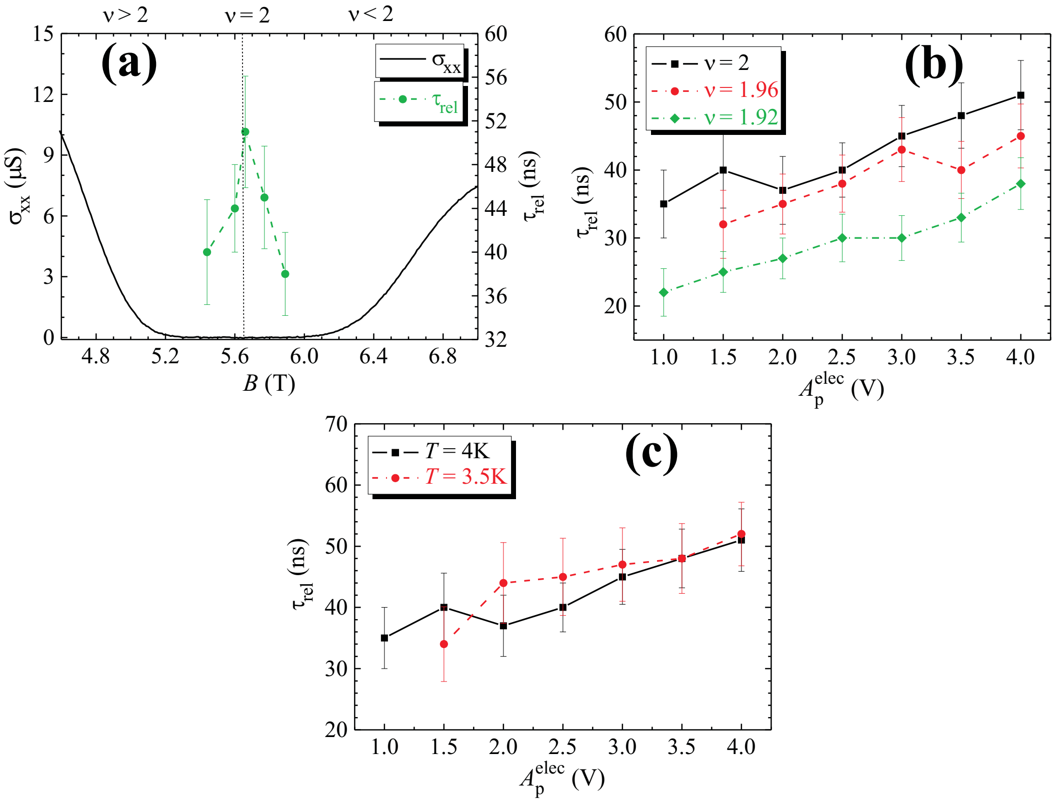

Figure 6.9: (a) Relaxation times τ_{rel} determined for filling factors around $\nu = 2$ for the low-mobility sample ($\#4 : \mu_{\text{el}} = 0.1 \times 10^6 \text{cm}^2\text{V}^{-1}\text{s}^{-1}$), at lattice temperature $T = 4\text{K}$ and constant applied electrical pulse amplitude $A_{\text{p}}^{\text{elec}} = 4\text{V}$; (b) Relaxation times determined for different filling factors for the low-mobility sample ($\#4 : \mu_{\text{el}} = 0.1 \times 10^6 \text{cm}^2\text{V}^{-1}\text{s}^{-1}$), at lattice temperature $T = 4\text{K}$ and various applied electrical pulse amplitudes $1\text{V} \leq A_{\text{p}}^{\text{elec}} \leq 4\text{V}$; (c) Relaxation times determined for two lattice temperatures $T = 3.5\text{K} - 4\text{K}$ at filling factor $\nu = 2$ and various applied electrical pulse amplitudes $1\text{V} \leq A_{\text{p}}^{\text{elec}} \leq 4\text{V}$.

than $T > 4\text{K}$. Figure 6.9 (c) shows a slight temperature dependence of the relaxation for two lattice temperatures $T = 3.5\text{K} - 4\text{K}$ at filling factor $\nu = 2$ at different applied electrical pulse amplitudes $1\text{V} \leq A_{\text{p}}^{\text{elec}} \leq 4\text{V}$.

Further we have varied the laser pulse widths for constant applied electrical pulse width in order to observe whether heat accumulation in the QH device with Corbino geometry occurs. Thus, for the sample #5, we applied electrical pulses with pulse widths of $t_{\text{p}}^{\text{elec}} = 4\mu\text{s}$ and various laser pulse widths $t_{\text{p}}^{\text{laser}} = 1\mu\text{s}, 1.5\mu\text{s}$ and $2\mu\text{s}$. While for the excitation seems that there is no influence of the duration of the laser pulse for the relaxation, an increase of the relaxation time with increasing the laser pulse widths is observable (see Fig. 6.10). This could be an indication of accumulation of Joule heating energy. By increasing the laser pulse width, the electron system is subjected to longer time and therefore it could relax back after longer time.

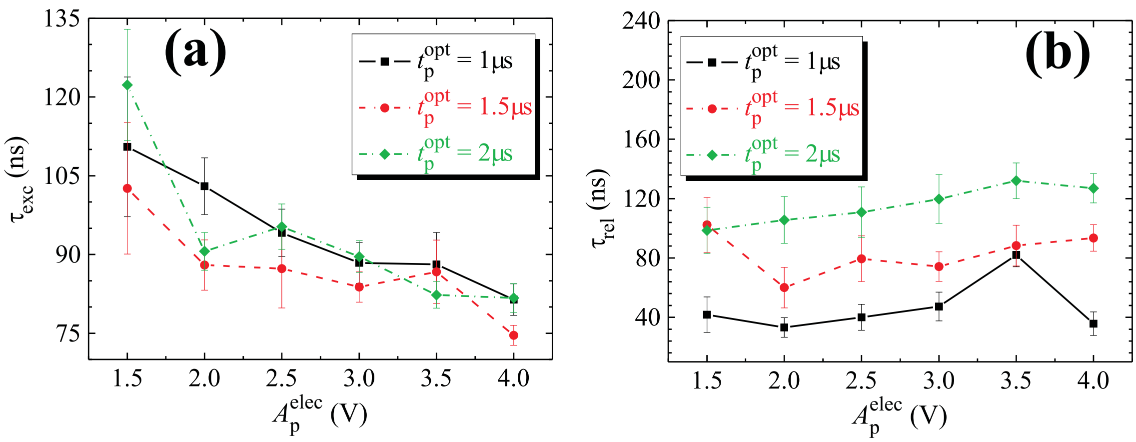

Figure 6.10: (a) Excitation times $\tau_{\rm exc}$ determined for filling factor $\nu = 2$ for the medium-mobility sample ($\#5 : \mu_{\rm el} = 0.5 \times 10^6 {\rm cm}^2{\rm V}^{-1}{\rm s}^{-1}$), at lattice temperature $T = 4{\rm K}$, constant applied electrical pulse width $t_{\rm p}^{\rm elec} = 4\mu{\rm s}$ and various laser pulse widths $t_{\rm p}^{\rm laser} = 1\mu{\rm s}$, $1.5\mu{\rm s}$ and $2\mu{\rm s}$; (b) Relaxation times $\tau_{\rm rel}$ determined for filling factor $\nu = 2$ for the medium-mobility sample ($\#5 : \mu_{\rm el} = 0.5 \times 10^6 {\rm cm}^2{\rm V}^{-1}{\rm s}^{-1}$), at lattice temperature $T = 4{\rm K}$, constant applied electrical pulse width $t_{\rm p}^{\rm elec} = 4\mu{\rm s}$ and various laser pulse widths $t_{\rm p}^{\rm laser} = 1\mu{\rm s}$, $1.5\mu{\rm s}$ and $2\mu{\rm s}$.

So far we did not discuss in detail the behavior of the excitation due to the optically induced breakdown of the QHE. As we have noticed, there is no definite dependence of the excitation on the applied pulse amplitude, on the electron mobility or on the magnetic field. This could be understood on the basis of a saturation of the electron system due to the high output laser power subjecting the electron system.

The output laser power is $P_{\rm laser} \approx 1{\rm W}$. With the known duration of the laser pulse $t_{\rm p}^{\rm laser} = 1\mu{\rm s}$ we determine the output laser energy per pulse $\Delta{\rm W} = P_{\rm laser} \cdot t_{\rm p}^{\rm laser} \approx 10^{-6}{\rm J}$. Thus, the number of photons provided by the laser pulse is $N_{\rm photon} = \Delta{\rm W}/E_{\rm photon}$. For the laser current $I_{\rm laser} = 25{\rm A}$ according to eq. 6.1 we determine the corresponding photon energy $E_{\rm photon} = 8.5{\rm meV}$ which in turn corresponds to a laser radiation with the laser frequency $f_{\rm laser} = 2{\rm THz}$ and laser wavelength $\lambda_{\rm laser} = 150\mu{\rm m}$. Thus, $N_{\rm photon} = \Delta{\rm W}/E_{\rm photon} \approx 7.4 \times 10^{14}{\rm photons}$. Now, we consider an electron system having the electron density $n_{\rm s} = 2 \times 10^{11}{\rm cm}^{-2}$ and the photoactive area of the QH device with Corbino geometry $A_{\rm ph} = \pi(r_2^2 - r_1^2) \approx 6.3{\rm mm}^2$. Thus, the number of electrons could be determined as being $N_{\rm el} = n_{\rm s} \cdot A_{\rm ph} \approx 1.26 \times 10^{10}{\rm electrons}$. By comparing the number of photons $N_{\rm photon} \approx 7.4 \times 10^{14}$ and the number of electrons $N_{\rm el} \approx 1.26 \times 10^{10}$ we see that there is an excess of photons. Thus, for one electron there are available $\approx 5.9 \times 10^4{\rm photons}$. However, near $B = 6{\rm T}$, the cyclotron energy is larger than $10{\rm meV}$. Since the photon energy is $8.5{\rm meV}$, direct one-photon excitation processes are not possible, at least if the width of the LL's is small.

6.4.3 Conclusions

To conclude, we have investigated the time scale of the excitation and the relaxation of the electrons in the 2DES of GaAs/AlGaAs heterostructures with Corbino geometry in the breakdown of the QHE regime and the transitions between the dissipative state and the dissipationless QH state or different dissipative states. The real-time measurements of the optical excitation and relaxation were performed by applying to the QH devices with Corbino geometry rectangular electrical pulses of different pulse widths $1\mu\mathrm{s} \leq t_{\mathrm{p}}^{\mathrm{elec}} \leq 4\mu\mathrm{s}$, constant pulse period $T_{\mathrm{p}}^{\mathrm{elec}} = 1\mathrm{s}$, while the electrical pulse amplitude is changed $1\mathrm{V} \leq A_{\mathrm{p}}^{\mathrm{elec}} \leq 4\mathrm{V}$ at fixed magnetic field B (filling factors around $\nu = 2$).
At the same time the QH devices were illuminated by a pulsed *p*-Ge laser, characterized by laser pulses of laser pulse widths $1\mu\mathrm{s} \leq t_{\mathrm{p}}^{\mathrm{laser}} \leq 4\mu\mathrm{s}$, constant laser pulse period $T_{\mathrm{p}}^{\mathrm{laser}} = 1\mathrm{s}$, high laser current $I_{\mathrm{laser}} = 25\mathrm{A}$ and high voltage pulses $A_{\mathrm{p}}^{\mathrm{laser}} = 1.68\mathrm{kV}$. The output of the laser is characterized by a laser frequency $f_{\mathrm{laser}} = 2\mathrm{THz}$, laser wavelength $\lambda_{\mathrm{laser}} = 150\mu\mathrm{m}$ and laser power $P_{\mathrm{laser}} \approx 1\mathrm{W}$.

The investigated QH devices with Corbino geometry have electron densities varying in a narrow range ($2 \times 10^{11}\mathrm{cm}^{-2} \leq n_{\mathrm{s}} \leq 2.7 \times 10^{11}\mathrm{cm}^{-2}$) and different carrier mobilities ($0.1 \times 10^{6}\mathrm{cm}^{2}/\mathrm{Vs} \leq \mu_{\mathrm{el}} \leq 1.6 \times 10^{6}\mathrm{cm}^{2}/\mathrm{Vs}$, see Table 6.1). Further, the investigations were performed within a small range of lattice temperatures ($3\mathrm{K} \leq T \leq 4\mathrm{K}$) due to the design of our experimental setup.

The time scale of excitation ($40\mathrm{ns} \leq \tau_{\mathrm{exc}} \leq 120\mathrm{ns}$) and relaxation ($30\mathrm{ns} \leq \tau_{\mathrm{rel}} \leq 170\mathrm{ns}$) determined with our real-time measurements of the optical excitation and relaxation agree well with the findings presented in a previous work [100].

By applying the electrical pulses, the laser pulses causes an optically induced breakdown of the QHE and results in a sharp increase of the PR during this process. While the laser is on the PR stays constant but as soon as the laser is switched off, the QHE is recovered and consequently the PR relaxes quickly to zero, characterized by a specific relaxation time τ_{rel}.

The breakdown of the QHE starts only after a certain excitation time ($40\mathrm{ns} \leq \tau_{\mathrm{exc}} \leq 120\mathrm{ns}$, $\tau_{\mathrm{exc}} << t_{\mathrm{p}}^{\mathrm{elec}}$, $t_{\mathrm{p}}^{\mathrm{laser}}$), depending on the applied electrical pulse amplitude $A_{\mathrm{p}}^{\mathrm{elec}}$, on the carrier mobility μ_{el} of the sample and on the strength of the perpendicular applied magnetic field B (filling factors around $\nu = 2$). This could be expected due to high rate of available photons to excite each electron in the 2DES, leading the electron system in a saturation regime. However, this situation does not affect the relaxation of the electrons via inter-LL-scattering processes.

The relaxation of electrons back to a QH state occurs only after a certain relaxation time ($30\mathrm{ns} \leq \tau_{\mathrm{rel}} \leq 170\mathrm{ns}$, $\tau_{\mathrm{rel}} << t_{\mathrm{p}}^{\mathrm{elec}}$, $t_{\mathrm{p}}^{\mathrm{laser}}$), depending on the applied electrical pulse amplitude $A_{\mathrm{p}}^{\mathrm{elec}}$, on the carrier mobility μ_{el} of the sample and on the strength of the perpendicular applied magnetic field B (filling factors around $\nu = 2$). We generally found shorter relaxation times than the excitation times for the corresponding values of the electrical pulse amplitudes. These findings agree well with the thermodynamical arguments given in Ref. [40]. However, we found that $\tau_{\mathrm{rel}} \leq \tau_{\mathrm{exc}}$ holds for the low- and medium-mobility samples $\#4$ and $\#5$ and $\tau_{\mathrm{rel}} \geq \tau_{\mathrm{exc}}$ holds for the high-mobility sample $\#6$. As the transition observed in high-mobility sample $\#6$ is a transition between two dissipative states, we cannot explain this situation by using the model as presented in Ref. [40]. This model was developed to explain the transition between a QH state and a dissipative state. We clearly observe mobility dependence of the relaxation times: the lower mobility of the sample is the shorter relaxation times are. For the low- and medium- mobility samples $\#4$ and $\#5$ the relaxation times increase with increasing the electrical pulse amplitudes $A_{\mathrm{p}}^{\mathrm{elec}}$ below the *DC* breakdown value $V_{\mathrm{SD}}^{\mathrm{crit}}$. For the high-mobility sample $\#6$ the applied electrical pulse amplitudes exceeded the *DC* breakdown value and we could observe an interesting dependence of the relaxation on the applied electrical pulse amplitudes. The relaxation times increases by reaching a maximum corresponding to an electrical pulse amplitude slightly below the *DC* breakdown value of the pulse amplitude. By exceeding the *DC* breakdown value of the pulse amplitude, the relaxation times decrease with increasing further the electrical pulse amplitude. In the Ref. [100], the authors reported a similar behavior, maxima of relaxation times slightly below the *DC* breakdown value and a decrease of relaxation times with increasing the source-drain voltage, also for the low- and medium- mobility samples. This interesting pulse amplitude dependence can be taken as a proof that the determined excitation and relaxation times are due to intrinsic properties of the electron systems and not due to the chosen experimental setup.

We give a possible explanation of this behavior by a heating picture based on a two-Landau levels model. After switching off the laser but still at lower applied electrical pulse amplitudes $A_{\mathrm{p}}^{\mathrm{elec}} < V_{\mathrm{SD}}^{\mathrm{crit}}$, the PR decreases quickly and the electron system relaxes back to the dissipationless QH state. The two-Landau levels model assumes the proportionality of the longitudinal conductivity and consequently of the PR to the N electrons elevated over the Landau gap ($\Delta\sigma_{\mathrm{xx}} \propto N$). The occupation of the upper LL decays by a characteristic time τ_0 but depends on the applied electrical pulse amplitude due to the induced Joule heating. Thus, a higher applied electrical pulse amplitude prevents the electrons to relax faster. This might explain the results determined for $A_{\mathrm{p}}^{\mathrm{elec}} < V_{\mathrm{SD}}^{\mathrm{crit}}$ for all three investigated samples (see Table 6.1). For the high-mobility sample $\#6$, when the applied electrical pulse amplitudes exceed the *DC* breakdown value $A_{\mathrm{p}}^{\mathrm{elec}} > V_{\mathrm{SD}}^{\mathrm{crit}}$, the electron system is already in a dissipative state either with the laser on or off. The situation would correspond to a transition between two dissipative states, which is faster with increasing the applied electrical pulse amplitudes.

The real-time measurements of the optical excitation and relaxation are performed at low temperatures ($T < 4\mathrm{K}$), the electron-phonon scattering mechanism is assumed not very important and the electron-impurity scattering mechanism is more effective. Even if the QH devices were illuminated by the *p*-Ge laser which could provide a huge rate of photons which would lead to a higher electron temperature, we could not see a temperature dependence of the relaxation times. A possible explanation may be that the variance of the lattice temperature during the pumping cycle during the measurements was within $1\mathrm{K}$ ($T = 3\mathrm{K} - 3.5\mathrm{K} - 4\mathrm{K}$) due to the limitation of our experimental setup. Such small variance of temperature cannot lead to a strong temperature dependence even by operating the laser. However, the order of magnitude of the relaxation times ($30\mathrm{ns} - 170\mathrm{ns}$) could indicate also an influence of the electron-phonon coupling. Fal'ko and Challis have calculated the inter-LL-relaxation rates for a 2DES in *GaAs* for one-phonon and two-phonon emission processes [101]. They predict that the two-phonon emission (characterized by a two-phonon relaxation rate τ_2^{-1}) suppresses the one-phonon emission (characterized by a one-phonon relaxation rate τ_1^{-1}) at high magnetic fields and could also estimate the magnetic field B for which $\tau_2^{-1} > \tau_1^{-1}$ holds. By applying the corresponding relations, derived from [101], we obtain inter-LL relaxation times of $60\mathrm{ns}$ for the two-phonon emission process and $20\mu\mathrm{s}$ for the one-phonon emission process for magnetic fields corresponding to magnetic fields at filling factor $\nu = 2$.

6.5 THz photoconductivity in QH devices with Corbino geometry

Photoconductivity is an optical and electrical phenomenon in which a material becomes more conductive due to the absorption of electromagnetic radiation such as visible light, ultraviolet light (UV), infrared light (IF), or gamma γ radiation[3]. To cause excitation the radiation to which the semiconductor is exposed must have enough energy to raise electrons across the forbidden Landau gap or by exciting the impurities within the Landau gap. When a voltage and a resistor are used in series with the semiconductor sample, a voltage drop across the resistor can be measured when the change in electrical conductivity varies the current flowing through the circuit. Why THz radiation is so interesting? One could answer because for many years the THz radiation was hardly accessible due to the so called *THz gap*. But with the new advances in different technologies now the previously unused THz frequency band is better accessible. THz radiation has some properties that open a wide range of applications, particularly for imaging. Applications of THz radiation are security systems in airports or public buildings (detection of weapons concealed underneath clothing), material characterization and quality control (physics and industry), spectroscopy analysis (chemistry, astronomy) and THz tomography for the detection of skin or breast cancer and tooth caries (medicine, dentistry)[4].

Compared to microwaves, THz waves have more energy and therefore could penetrate deeper and make sharper images due to their shorter wavelength. On the other hand, the THz radiation should be scattered less than the visible or near infrared radiations, since the Rayleigh scattering decreases with the fourth power of the wavelength. By illuminating different materials with THz radiation we observe different properties: polar liquids (water) absorb strongly the THz radiation, metals are opaque to THz radiation whereas nonmetals such plastics or paper and non-polar substances are transparent. Dielectrics in contrast have a characteristic absorption, peculiar to each material.

---

[3] To be photoconductive a semiconductor must be in thermal equilibrium (photoresponse measurement conditions) containing free electrons and holes. When light is absorbed by the semiconductor, the configuration of electrons and holes changes and raises the electrical conductivity of the semiconductor.

[4] Although there is a limited penetration depth of the THz radiation due to the strong water absorption, it can be used to examine tissues near the body surface like skin and teeth or dehydrated tissue samples.

THz radiation with wavelength of the order of $\lambda \approx 120\mu\mathrm{m}$ (frequency $f \approx 2.4\mathrm{THz}$ and energy $E \approx 10\mathrm{meV}$) interacts effectively with QH systems due to the perfect match of the THz photon energy with the Landau gap between two adjacent LL's [12]. The typical Landau gap developed by the QH systems is around $10\mathrm{meV}$. But this energy, called also the *cyclotron energy* $\hbar\omega_\mathrm{c}$, is tunable by the magnetic field B. Thus, to achieve a cyclotron energy of $E_\mathrm{c} = \hbar\omega_\mathrm{c} = 10\mathrm{meV}$ the magnetic field should be increased to $B = 2.1\mathrm{T}$ (for the *HgTe/HgCdTe* heterostructures[5]) or to $B = 5.7\mathrm{T}$ (for the *GaAs/AlGaAs* heterostructure[6]). Under cyclotron resonance conditions different studies have been performed: surface cyclotron resonance of the 2DES in inversion and accumulation layers on the (100) *Si* surface [102], transmission and photoconductivity measurements of the 2DES in *GaAs/AlGaAs* heterostructure [103–106]. When the electromagnetic radiation is absorbed by the 2DES, the equilibrium distribution is changed, since the electrons are excited from one LL to the adjacent LL. The effect of this process is also an increase of the electron temperature. The increase of the temperature is indicated by the change in the photoconductivity (known also as the photoresponse-PR). The increase of temperature, known also as the *bolometric effect*, plays an important role around the integer filling factors [105, 107]. In 2002 interesting measurements were reported, the observation of *Zero-resistance states* induced by microwave (MW) radiation in *GaAs/AlGaAs* heterostructure [108–110]. They reported *Zero-resistance states* in ultrahigh-mobility *GaAs/AlGaAs* heterostructures by exhibiting zero longitudinal resistance without Hall resistance quantization at low temperatures and low magnetic fields[7] when the samples are illuminated by an appropriate MW radiation.

As already mentioned, when a QH device is illuminated by THz radiation the conductivity of the 2DES under high perpendicular magnetic fields is affected. Thus, this causes the breakdown of the QH state into a dissipative state by showing a large increase of the PR ($\mathrm{PR} \propto \Delta\sigma_\mathrm{xx}$). Despite extensive studies of the THz induced breakdown of the QHE, the explanation of the PR is still controversial. Whereas earlier studies show both cyclotron resonance (CR) and nonresonant bolometric (BO) contributions [104–106] to the PR, in other papers [111–114] the PR is attributed only to the nonresonant BO contribution. However, a recent investigation of the PR[8] on *GaAs/AlGaAs* heterostructures patterned in Hall bar- [115–117], meander- [117, 118] and Corbino geometries [119] showed both BO and CR contributions to the PR. The PR is measured versus the magnetic field B for different photon (laser) energies E_photon and exhibits a nonresonant BO contribution (single or double-peak structure) pinned at the minimum of the longitudinal conductivity $\sigma_\mathrm{xx}(B)$ and the CR contribution changing its B position with the photon (laser) energy (see Fig. 6.11). The shape of the PR peaks depends strongly on the B position of the photon energy

---

[5] Since the cyclotron energy is $\hbar\omega_\mathrm{c} = \hbar eB/m^* = 10\mathrm{meV}$ and $m^* = 0.025 \times m_\mathrm{e}$ is the effective mass we find the magnetic field B necessary to achieve this cyclotron energy.

[6] Similar way as for the *HgTe/HgCdTe* heterostructure but with higher effective mass $m^* = 0.067 \times m_\mathrm{e}$.

[7] These *Zero-resistance states* occur about magnetic fields $B = (4/5)B_\mathrm{c}$ and $B = (4/9)B_\mathrm{c}$, where $B_\mathrm{c} = \omega_\mathrm{c} m^*/e$ is the magnetic field at which the cyclotron resonance ω_c occurs.

[8] The excitation source used during these investigations is a *p*-Ge laser, tunable in the THz range $(1.7\mathrm{THz} - 2.5\mathrm{THz})$.

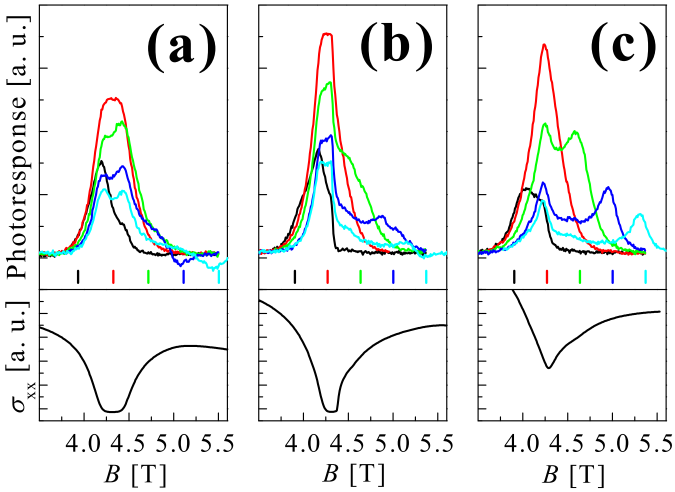

Figure 6.11: PR versus the magnetic fields B for various photon energies taken for medium-mobility sample ($\#5 : \mu_{\mathrm{el}} = 0.5 \times 10^6 \mathrm{cm}^2\mathrm{V}^{-1}\mathrm{s}^{-1}$), at lattice temperature $T = 4\mathrm{K}$. The PR is shown for three applied source-drain voltages V_{SD} and the lower panel shows the corresponding magneto-transport curves $\sigma_{\mathrm{xx}}(B)$. The color vertical lines denote the cyclotron positions of the photon energies. (a) PR measured for $V_{\mathrm{SD}} = 2\mathrm{V}$, (b) PR measured for $V_{\mathrm{SD}} = 3\mathrm{V}$, (c) PR measured for $V_{\mathrm{SD}} = 5\mathrm{V}$ [120].

(whether the B position is inside or outside the second QH plateau (filling factor $\nu = 2$)). If the cyclotron frequency matches the laser frequency at B magnetic fields outside the second plateau, the PR shows distinctively two structures: a peak corresponding to the CR contribution and a single or double-peak bound to the minimum of the QH plateau corresponding to the BO contribution. If the cyclotron frequency matches the laser frequency at B magnetic fields inside the QH plateau, the PR shows a strong signal due to the overlap of the CR and BO contributions.

6.6 Quasi-classical ansatz to explain aspects of the THz photoconductivity

So far we have discussed the occurrence of the PR that shows structures due to the CR contribution, when the photon frequency matches the cyclotron frequency and the BO contribution due to the Joule heating induced by the illumination of the 2DES by the THz radiation. In the following I discuss the CR effect, the BO effect and an electron temperature model used to explain the double-peak structure shown by PR due to the BO contribution.

6.6.1 Cyclotron resonance (CR) contribution

Classically, an electron in a static and uniform magnetic field B will move in a circle due to the Lorentz force $\vec{F}_{\mathrm{L}}$. The angular frequency ($\omega = 2\pi f$) of this circular motion for a given magnetic field strength B is given by $\omega_{\mathrm{c}} = eB/m^*$, where e is the elementary charge and m^* is the effective mass of the electron. If, at the same time, a high-frequency (*AC*) electromagnetic field $\vec{E}$ (imposed by the THz radiation) of frequency $\omega = \omega_{\mathrm{c}}$ is applied on the 2DES, perpendicular to B, the electrons will resonantly absorb energy from the *AC* electric field. The circular motion of the electrons superimposed with an uniform motion perpendicular to the field, in the presence of the *AC* electric field, results in a cycloid.

The electron experiences a force $-e\vec{E}$, due to electric field E, and a force $-e\vec{v} \times \vec{B}$ due to the magnetic field B. These contributions give the Lorentz force equation

$$\vec{F}_{\mathrm{L}} = -e(\vec{E} + \vec{v} \times \vec{B}) = m^* \left(\frac{d}{dt} + \frac{1}{\tau} \right) \vec{v}\,. \tag{6.12}$$

Assuming that the *AC* electric field and the drift velocity have harmonically varying forms

$$\vec{E}(t) = \Re[E(\omega)\exp(-i\omega t)] \tag{6.13}$$

and respectively

$$\vec{v}(t) = \Re[v(\omega)\exp(-i\omega t)]\,. \tag{6.14}$$

with ω the angular frequency of the THz radiation[9].

After some algebra steps, the *x*-*y* components of the drift velocity vector $\vec{v}$ are expressed via the relaxation time τ, photon frequency ω, cyclotron frequency ω_{c}, and the *x*-*y* components of the *AC* electric field vector $\vec{E}$:

$$v_{\mathrm{x}}(\omega) = \frac{e\tau E_{\mathrm{x}}(\omega) + m^*\omega_{\mathrm{c}}\tau v_{\mathrm{y}}(\omega)}{m^*(i\omega\tau - 1)} \tag{6.15}$$

and

$$v_{\mathrm{y}}(\omega) = \frac{e\tau E_{\mathrm{y}}(\omega) - m^*\omega_{\mathrm{c}}\tau v_{\mathrm{x}}(\omega)}{m^*(i\omega\tau - 1)}\,. \tag{6.16}$$

By inserting eq. 6.16 into eq. 6.15 we determine finally v_{x} being

$$v_{\mathrm{x}}(\omega) = \frac{e\tau}{m^*} \cdot \frac{(i\omega\tau - 1)E_{\mathrm{x}}(\omega) + \omega_{\mathrm{c}}\tau E_{\mathrm{y}}(\omega)}{(1 - i\omega\tau)^2 + \omega_{\mathrm{c}}^2\tau^2}\,. \tag{6.17}$$

---

[9] The THz radiation is incident perpendicularly to the 2DES (Faraday configuration), the electrical field component is parallel to the 2DES and induces the drift of the electrons into a direction perpendicular to the $\vec{B} \perp \vec{E}$ plane. The magnetic field component of the THz radiation has no influence on the electrons since it can cause a force only in the *z*-direction. But a motion of the electrons in the *z*-direction is forbidden due to the quantization of the electron motion in this direction. Instead, the static magnetic field $B \parallel z$ affects the motion of the electrons in the *x*-*y* plane.

Now, inserting the eq. 6.17 into eq. 6.16 we determine also v_{y}

$$v_{\mathrm{y}}(\omega) = \frac{e\tau}{m^*} \cdot \frac{(i\omega\tau - 1)E_{\mathrm{y}}(\omega) - \omega_{\mathrm{c}}\tau E_{\mathrm{x}}(\omega)}{(1 - i\omega\tau)^2 + \omega_{\mathrm{c}}^2\tau^2} \, . \tag{6.18}$$

The complex dynamic (*AC*) conductivity tensor $\hat{\sigma}$ is determined through the relation given by the Ohm's law $\vec{j} = -en_{\mathrm{s}}\vec{v} = \hat{\sigma}(\omega) \cdot \vec{E}$ (with help of eq. 6.17 and eq. 6.18),

$$\hat{\sigma} = \begin{pmatrix} \sigma_{\mathrm{xx}} & \sigma_{\mathrm{xy}} \\ \sigma_{\mathrm{yx}} & \sigma_{\mathrm{yy}} \end{pmatrix} = \frac{\sigma_0}{(1 - i\omega\tau)^2 + \omega_{\mathrm{c}}^2\tau^2} \cdot \begin{pmatrix} 1 - i\omega\tau & -\omega_{\mathrm{c}}\tau \\ \omega_{\mathrm{c}}\tau & 1 - i\omega\tau \end{pmatrix} . \tag{6.19}$$

with the longitudinal component

$$\sigma_{\mathrm{l}} = \sigma_{\mathrm{xx}} = \sigma_{\mathrm{yy}} = \sigma_0 \cdot \frac{1 - i\omega\tau}{(1 - i\omega\tau)^2 + \omega_{\mathrm{c}}^2\tau^2} \tag{6.20}$$

and the transversal (Hall) component

$$\sigma_{\mathrm{H}} = -\sigma_{\mathrm{xy}} = \sigma_{\mathrm{yx}} = \sigma_0 \cdot \frac{\omega_{\mathrm{c}}\tau}{(1 - i\omega\tau)^2 + \omega_{\mathrm{c}}^2\tau^2} \, , \tag{6.21}$$

where $\sigma_0 = n_{\mathrm{s}}e^2\tau/m^*$ is the classical (*DC*) Drude conductivity (see eq. 2.19). From these last two equations we deduce the real and imaginary parts of the longitudinal and Hall components of the *AC* conductivity:

$$\Re\sigma_{\mathrm{l}}(\omega) = \sigma_0 \cdot \frac{1 + \omega_{\mathrm{c}}^2\tau^2 + \omega^2\tau^2}{\left[1 - \omega^2\tau^2 + \omega_{\mathrm{c}}^2\tau^2\right]^2 + 4\omega^2\tau^2} \tag{6.22}$$

$$\Im\sigma_{\mathrm{l}}(\omega) = \sigma_0 \cdot \frac{\omega\tau\left[1 - \omega_{\mathrm{c}}^2\tau^2 + \omega^2\tau^2\right]}{\left[1 - \omega^2\tau^2 + \omega_{\mathrm{c}}^2\tau^2\right]^2 + 4\omega^2\tau^2} \tag{6.23}$$

and

$$\Re\sigma_{\mathrm{H}}(\omega) = \sigma_0 \cdot \frac{\omega_{\mathrm{c}}\tau\left[1 - \omega^2\tau^2 + \omega_{\mathrm{c}}^2\tau^2\right]}{\left[1 - \omega^2\tau^2 + \omega_{\mathrm{c}}^2\tau^2\right]^2 + 4\omega^2\tau^2} \tag{6.24}$$

$$\Im\sigma_{\mathrm{H}}(\omega) = \sigma_0 \cdot \frac{2\omega_{\mathrm{c}}\tau\omega\tau}{\left[1 - \omega^2\tau^2 + \omega_{\mathrm{c}}^2\tau^2\right]^2 + 4\omega^2\tau^2} \, . \tag{6.25}$$

Figure 6.12 shows that the *AC* conductivity in the CR conditions develops maxima only along the CR line, the line calculated for the perfect match between the cyclotron and photon frequencies ($\omega_{\mathrm{c}} = \omega$).

A quantum mechanical treatment of the dynamic (*AC*) conductivity at CR has been developed under the self-consistent Born approximation (SCBA) by Ando [121]. The quantum oscillation of the absorption predicted by Ando could be observed experimentally by absorption measurements of Abstreiter *et al*. [102].

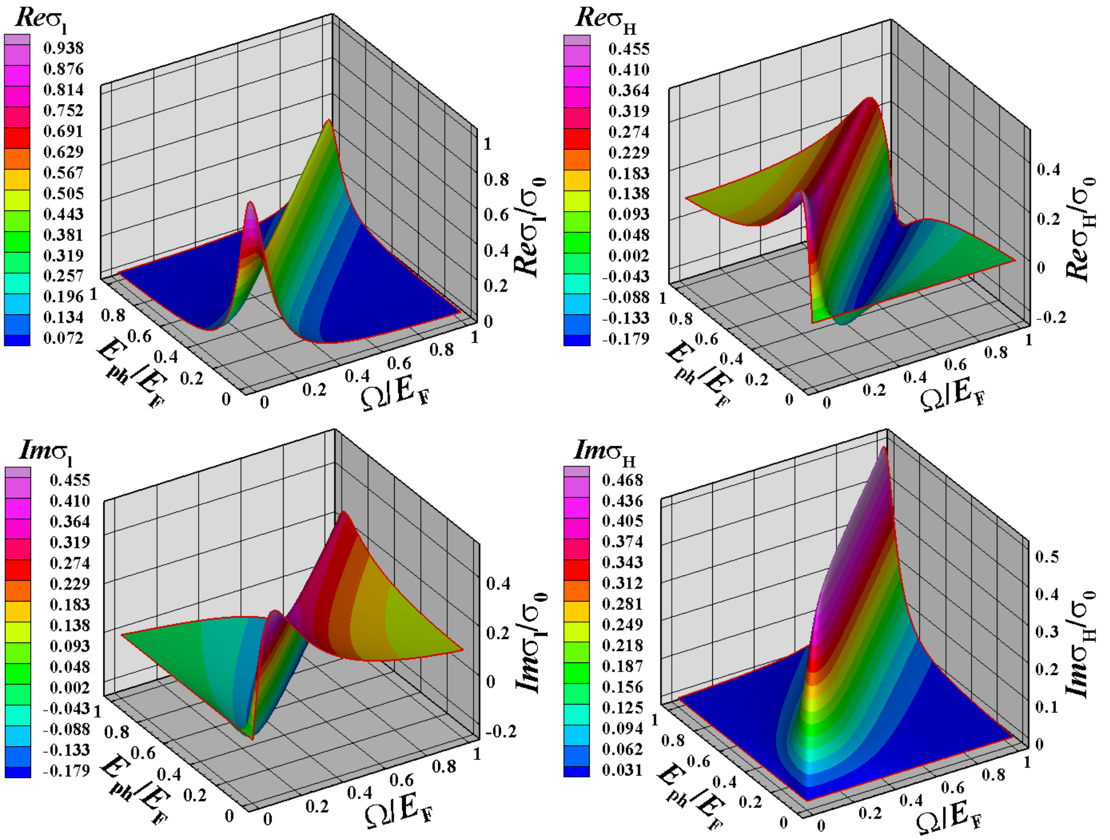

Figure 6.12: *AC* longitudinal $\sigma_{\mathrm{l}}(\omega)$ and Hall $\sigma_{\mathrm{H}}(\omega)$ conductivities, as a function of the cyclotron Ω/E_{F} and the photon $E_{\mathrm{ph}}/E_{\mathrm{F}}$ energies, are calculated for a damping parameter $\omega_{\mathrm{F}}\tau = 10$.

6.6.2 Bolometric (BO) contribution

The bolometric effect is based on the sensitive dependence of the conductivity σ_{xx} on temperature T, being the basis of the function of the bolometers. The absorption of the THz radiation by the 2DES induces an increase of the electron temperature T_{el} relative to the lattice, reflected in the change of the photoresponse (PR). The electron system is very sensitive in the QH regime. Therefore, any external excitation can perturb the system and break the QH state leading to an increase of the PR in the region of the QH plateau. Since outside the QH plateau, the electron system is already in a dissipative state, the application of the THz radiation does not change considerably the PR. On this basis the QH devices could be used as THz detectors.

Figure 6.13 shows a sketch of the heat transport in the thermally coupled system formed by the 2DES, lattice and the *He* bath. Each part of this system has a characteristic specific heat. Since the electrons are coupled with the lattice, an increase of the electron

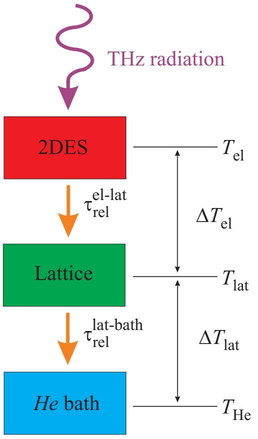

Figure 6.13: A schematic view of the heat transfer in the thermal coupled system: 2DES-lattice-*He* bath.

temperature $\Delta T_{\rm el}$ leads to an increase of the lattice temperature $\Delta T_{\rm lat}$ above the *He* bath temperature. This heat transport between the electrons, the lattice and *He* bath in a steady state could be expressed by:

- heat transfer electrons-lattice,

$$\Delta T_{\rm el} = \frac{P \cdot \tau_{\rm rel}^{\rm el-lat}}{c_{\rm el}} \tag{6.26}$$

  where $\Delta T_{\rm el}$ is the increase of the electron temperature comparing to the lattice, P is the absorbed power, $\tau_{\rm rel}^{\rm el-lat}$ is the relaxation time (the electrons after a characteristic time relax to the lattice temperature[10]) and $c_{\rm el}$ is the specific heat of the electrons;

- heat transfer lattice-*He* bath,

$$\Delta T_{\rm lat} = \frac{P \cdot \tau_{\rm rel}^{\rm lat-bath}}{c_{\rm lat}} \tag{6.27}$$

  where $\Delta T_{\rm lat}$ is the increase of the lattice temperature above the *He* bath temperature ($T_0 = 4{\rm K}$), P is the absorbed power, $\tau_{\rm rel}^{\rm lat-bath}$ is the relaxation time[11] due to the thermal coupling between the sample (lattice) and environment (*He* bath), $c_{\rm lat}$ is the specific heat of the lattice.

An increase of the conductivity due to the incident THz radiation is

$$\Delta\sigma_{\rm xx} = \frac{\partial\sigma_{\rm xx}}{\partial T_{\rm el}}\Delta T_{\rm el} + \frac{\partial\sigma_{\rm xx}}{\partial T_{\rm lat}}\Delta T_{\rm lat} = \frac{\partial\sigma_{\rm xx}}{\partial T_{\rm el}} \cdot \frac{P \cdot \tau_{\rm rel}^{\rm el-lat}}{c_{\rm el}} + \frac{\partial\sigma_{\rm xx}}{\partial T_{\rm lat}} \cdot \frac{P \cdot \tau_{\rm rel}^{\rm lat-bath}}{c_{\rm lat}}\,. \tag{6.28}$$

---

[10] The relaxation time is the time constant of an exponential decay due to the relaxation of the 2DES from the Fermi distribution at $T_{\rm lat} + \Delta T_{\rm el}$ to the one at the equilibrium lattice temperature $T_{\rm lat}$.

[11] This time characterizes the relaxation of the lattice from the Fermi distribution at $T_0 + \Delta T_{\rm lat}$ to the one at the equilibrium *He* bath temperature T_0.

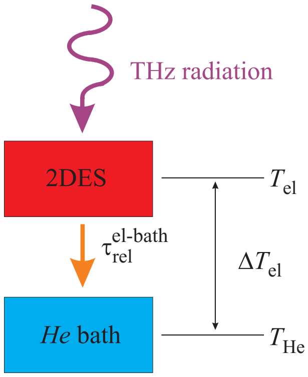

Figure 6.14: A sketch of the heat transfer in the thermal coupled system: 2DES-*He* bath.

With the arguments given by Neppl *et al*. [107], $\Delta T_{\text{el}} >> \Delta T_{\text{lat}}$, eq. 6.28 becomes

$$\Delta\sigma_{\text{xx}} = \frac{\partial\sigma_{\text{xx}}}{\partial T_{\text{el}}}\Delta T_{\text{el}} = \frac{\partial\sigma_{\text{xx}}}{\partial T_{\text{el}}} \cdot \frac{P \cdot \tau_{\text{rel}}^{\text{el-lat}}}{c_{\text{el}}} \,. \tag{6.29}$$

In the following we try to explain the double-peak structure of PR on the basis of an electron temperature picture. We display schematically the case $\Delta T_{\text{el}} > \Delta T_{\text{lat}}$ in fig. 6.14:

The energy density of the laser beams sent to the 2DES is

$$w = \frac{dW}{dV} = \frac{P_{\text{laser}} \cdot dt}{A \cdot dh} \,, \tag{6.30}$$

where dW is the output laser energy per pulse and dV is the volume of the sample. With $c = dh/dt$ the speed of radiation getting into the 2DES at penetration depth dh within the pulse duration dt and $I_{\text{photon}} = P_{\text{laser}}/A$ the intensity of the THz radiation, the energy density becomes

$$w = \frac{dW}{dV} = \frac{I_{\text{photon}}}{c} \,. \tag{6.31}$$

By exposing the QH device to the THz radiation of intensity I_{photon} a heating of the sample occurs. The energy density w could be written in terms of the classical thermodynamics (at $V = \text{const.}$) as

$$w = \frac{dW}{dV} = \frac{dU}{dV} = \frac{d\nu \cdot c_{\text{vm}} \cdot \Delta T}{dV} = \rho_\nu \cdot c_{\text{vm}} \cdot \Delta T \,, \tag{6.32}$$

where $d\nu$ is the number of moles, c_{vm} is the specific heat at $V = \text{const.}$, ΔT is the variation of temperature and $\rho_\nu = d\nu/dV$ is the molar density.

By comparing eq. 6.31 with eq. 6.32, the temperature enhancement is given by

$$\Delta T = \frac{I_{\text{photon}}}{c \cdot \rho_\nu \cdot c_{\text{vm}}} \,. \tag{6.33}$$

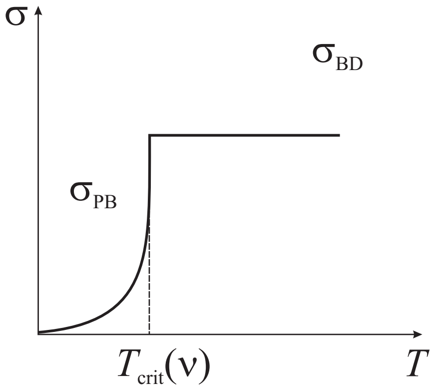

Figure 6.15: Scheme of the temperature dependence of the conductivity $\sigma(T)$; σ_{PB} is the pre-breakdown conductivity and σ_{BD} is the breakdown conductivity.

With the electron contribution to the specific heat in metals

$$c_{\mathrm{el}} = \gamma \cdot T = \frac{\pi^2}{3} \cdot k_{\mathrm{B}}^2 \cdot D(E_{\mathrm{F}}) \cdot T\,, \tag{6.34}$$

we obtain the new formula for the temperature enhancement

$$\Delta T = \frac{3 I_{\mathrm{photon}}}{c \cdot \rho_\nu \cdot \pi^2 \cdot k_{\mathrm{B}}^2 \cdot D(E_{\mathrm{F}}) \cdot T}\,. \tag{6.35}$$

The new formula of ΔT shows that $\Delta T \propto 1/D(E_{\mathrm{F}})$. The higher $D(E_{\mathrm{F}})$ is, the lower is the temperature enhancement ΔT. This dependence is applicable to the situation of the QH regime, if $D(E_{\mathrm{F}})$ is interpreted as $D_T(\mu) = dn_{\mathrm{el}}/d\mu$. The density of states $D(E)$ is higher outside the QH plateau (around the integer filling factor $\nu = 2$) and lower in the QH plateau (the minimum is reached at $\nu = 2$). This in turn corresponds to low ΔT outside the QH plateau and high ΔT in the QH plateau. But, this does not explain the (frequently observed) double-peak structure of the PR with two maxima near the flanks of the QH plateau, as the PR is not a simple monotonous function of ΔT.
We assume the following temperature dependence of the conductivity $\sigma(T)$ in the QH regime [122]: the conductivity increases exponentially in the pre-breakdown regime, at temperatures still lower than the critical temperature T_{crit}, see eq. 6.36

$$\sigma_{\mathrm{PB}}(T) = \sigma_0 \cdot \exp\left[-\frac{\hbar\omega_{\mathrm{c}}}{2k_{\mathrm{B}}T}\right] + \sigma_{\mathrm{bg}}\,, \tag{6.36}$$

with σ_{bg} the background conductivity, while by reaching the critical temperature the conductivity raises fast to a well finite value and than saturates by increasing further the temperature ($\sigma_{\mathrm{BD}} = \mathrm{const.} >> \sigma_{\mathrm{PB}}$), see Fig. 6.15.
We assume the following ansatz for the critical temperature (see Fig. 6.16):

$$T_{\mathrm{crit}}(\nu) = \frac{T_{\mathrm{crit}}(i) \cdot D_0}{D(E_{\mathrm{F}})}\,, \tag{6.37}$$

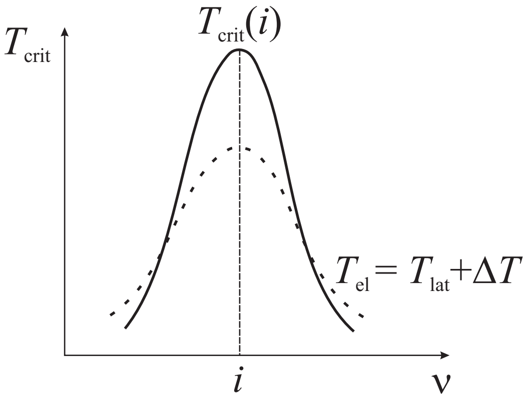

Figure 6.16: Scheme of the filling factor dependence of the critical temperature $T_{\text{crit}}(\nu)$ and the electron temperature $T_{\text{el}}(\nu)$.

with $T_{\text{crit}}(i)$ is the critical temperature for the integer filling factor $\nu = i$ and D_0 is the density of states at $B = 0\text{T}$. Assuming further the validity of the hot-electron model

$$\sigma(T_{\text{el}}) = \sigma(T_{\text{lat}} + \Delta T)\,, \tag{6.38}$$

irrespective of the difference between electron temperature T_{el} and lattice temperature T_{lat}, the magnitude of $\Delta\sigma_{\text{photo}} = \sigma(T_{\text{el}} = T_{\text{lat}} + \Delta T) - \sigma(T_{\text{lat}})$ can be deduced from:

$$T_{\text{el}} = T_{\text{lat}} + \Delta T \geq, \leq T_{\text{crit}}(\nu)\,. \tag{6.39}$$

By combining eq. 6.35, eq. 6.37 with eq. 6.39 we obtain the relation

$$T_{\text{lat}} + \frac{3I_{\text{photon}}}{c \cdot \rho_\nu \cdot \pi^2 \cdot k_{\text{B}}^2 \cdot D(E_{\text{F}}) \cdot T} \geq, \leq \frac{T_{\text{crit}}(i) \cdot D_0}{D(E_{\text{F}})}\,. \tag{6.40}$$

If T can be chosen $T = T_{\text{lat}}$ and considering the following constants $K_1 = T_{\text{crit}}(i) \cdot D_0$ and $K_2 = 3I_{\text{photon}}/(c \cdot \rho_\nu \cdot \pi^2 \cdot k_{\text{B}}^2)$, we obtain a new form of the eq. 6.40

$$T_{\text{lat}} + \frac{K_2}{D(E_{\text{F}}) \cdot T_{\text{lat}}} \geq, \leq \frac{K_1}{D(E_{\text{F}})}\,. \tag{6.41}$$

By multiplying eq. 6.41 by $D(E_{\text{F}}) \cdot T_{\text{lat}}$, it changes into

$$T_{\text{lat}}^2 \cdot D(E_{\text{F}}) + K_2 \geq, \leq K_1 \cdot T_{\text{lat}}\,. \tag{6.42}$$

If the left side of relation 6.42 is larger than the right side then the conductivity is in the breakdown (saturation) regime $\sigma = \sigma_{\text{BD}}$. This case is more likely at higher values for the density of states at the Fermi energy, $D(E_{\text{F}})$, at the flanks of the QH plateau, leading to higher values of $\Delta\sigma_{\text{photo}}$ (see Fig. 6.17). If the opposite case occurs, the left side is smaller than the right one, the conductivity is in pre-breakdown regime $\sigma = \sigma_{\text{PB}} << \sigma_{\text{BD}}$. In the

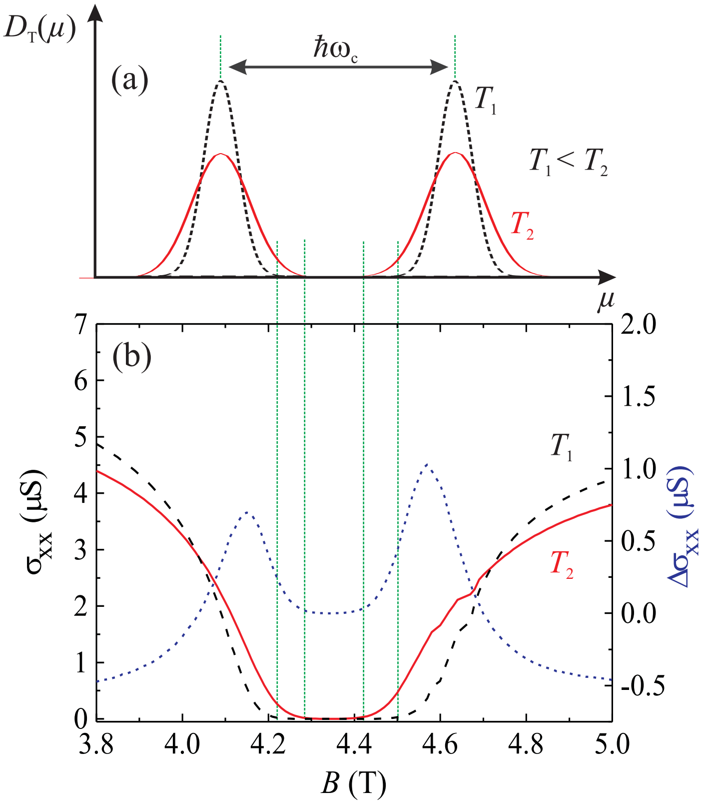

Figure 6.17: (a) Thermodynamic density of states $D_{\mathrm{T}}(\mu)$ at two different temperatures $T_1 < T_2$. (b) Measured $\Delta\sigma_{\mathrm{xx}}(\nu) = \sigma_{\mathrm{xx}}(T_2) - \sigma_{\mathrm{xx}}(T_1)$ (blue short dash curve), where $\sigma_{\mathrm{xx}}(T_1)$ is the longitudinal conductivity $\sigma_{\mathrm{xx}}(B)$ measured for temperature $T_1 = 2\mathrm{K}$ (black dash curve) and $\sigma_{\mathrm{xx}}(T_2)$ is the longitudinal conductivity $\sigma_{\mathrm{xx}}(B)$ measured for temperature $T_2 = 4.1\mathrm{K}$ (red solid curve). The measurements have been performed on the medium-mobility sample $\#5$. For details of these measurements see the text.

QH plateau center, the density of states $D(E_{\mathrm{F}})$ is low, leading to small values of $\Delta\sigma_{\mathrm{photo}}$ (see Fig. 6.17). Thus, the function $T_{\mathrm{crit}}(\nu)$ in relation to $T_{\mathrm{el}}(\nu)$ could explain in principle the double-peak structure of $\Delta\sigma_{\mathrm{photo}}(\nu)$, as $T_{\mathrm{crit}}(\nu)$ is high in the center of the plateau and decreases toward the flanks of the plateau. In order to check whether the assumed dependence of the critical temperature T_{crit} on the filling factor ν, shown in fig. 6.16 could be verified, additional measurements were performed. One type of measurements could be performed in order to determine the dependence of the critical temperature on the filling factor (different magnetic field values). The other type of measurements could yield the change of the electron temperature with the filling factor.

Different lattice temperatures were used to derive the temperature dependence of the QHE at fixed applied source-drain voltage ($V_{\mathrm{SD}} << V_{\mathrm{SD}}^{\mathrm{crit}}$). The QH plateau reduces its width with increasing lattice temperature. Thus, the change of the critical temperature could be obtained by performing temperature dependent magnetotransport measurements $\sigma_{\mathrm{xx}}(T_{\mathrm{el}})$

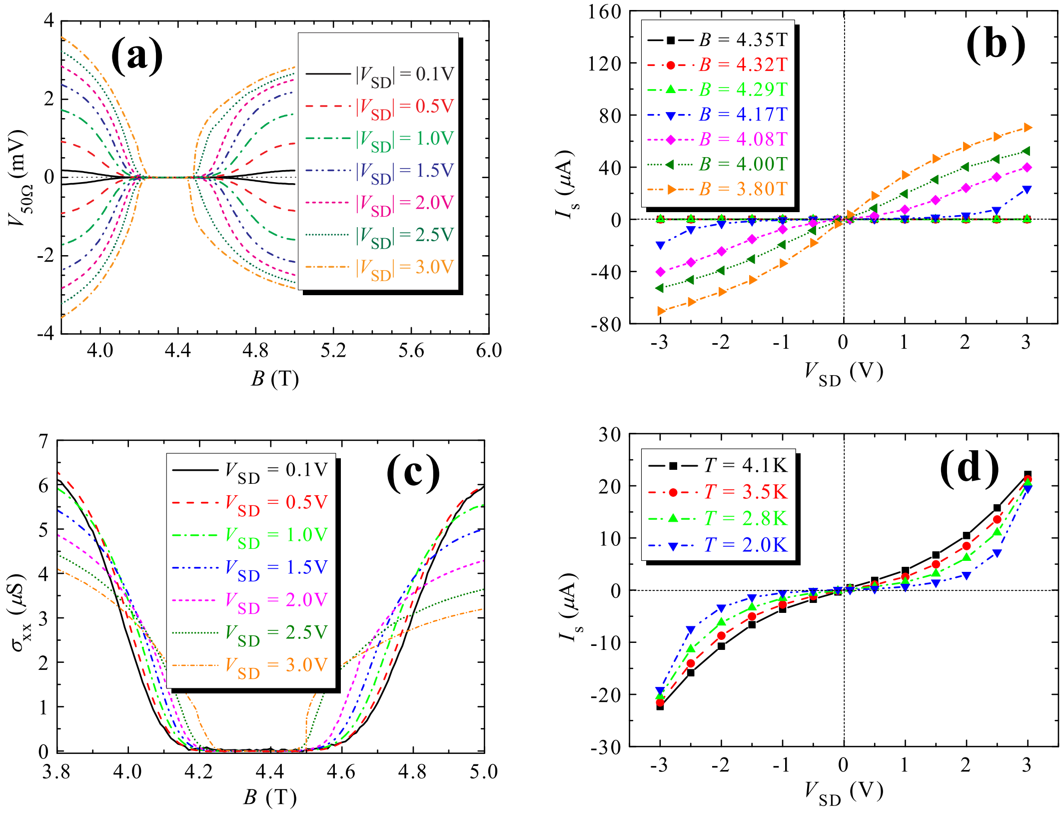

Figure 6.18: (a) Voltage drop $V_{50\Omega}$ measured for different applied source-drain voltages at lattice temperature $T = 2$K (medium-mobility sample $\#5$). The modulus of $V_{\rm SD}$ means that the voltage was also reversed; (b) $I - V$ characteristics determined from voltage dependent magnetotransport measurements at lattice temperature $T = 2$K (medium-mobility sample $\#5$); (c) Voltage dependent magnetotransport measurements around the second QH plateau at lattice temperature $T = 2$K (medium-mobility sample $\#5$); (d) Temperature dependent *I*-*V* characteristics determined for magnetic field $B(\nu = 2.09) = 4.17$T.

at low source-drain voltages and various lattice temperatures[12].

On the other hand, at a fixed lattice temperature a similar effect of reducing the QH plateau width could be obtained by varying the applied source-drain voltage. The application of the source-drain voltage on the 2DES leads to an increase of the electron temperature. Thus, the change of the electron temperature could be obtained by performing voltage dependent magnetotransport measurements $\sigma_{\rm xx}(T_{\rm el})$ at low lattice temperature and various source-drain voltages[13].

To determine the critical temperature we performed magnetotransport measurements at various lattice temperatures and various applied source-drain voltages. From the obtained

---

[12] This magnetotransport measurements corresponds to the situation $T_{\rm el} = T_{\rm lat}$.

[13] This magnetotransport measurements corresponds to the situation $T_{\rm el} > T_{\rm lat}$.

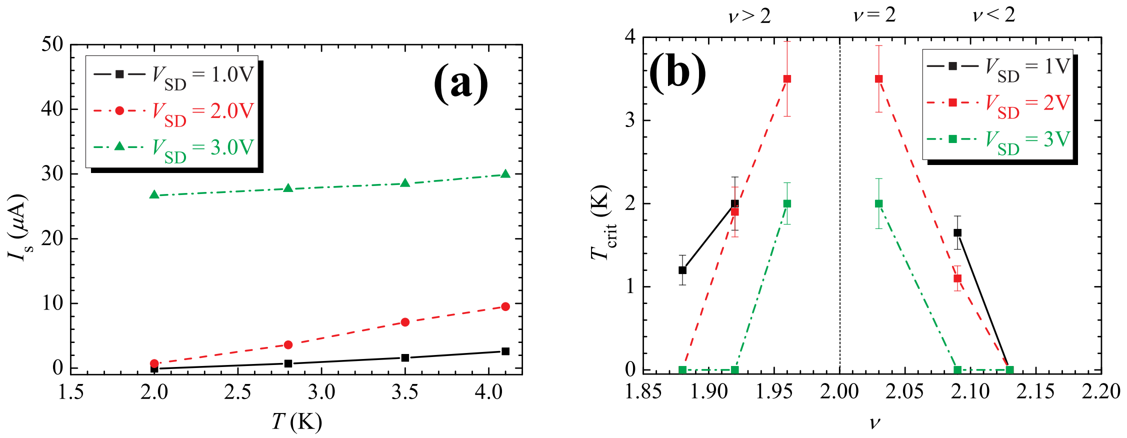

Figure 6.19: (a) Source-drain currents as a function of the temperature at magnetic field $B(\nu = 1.92) = 4.53\text{T}$ and different source-drain voltages; (b) Critical temperature depending on the filling factor, determined for different source-drain voltages.

SdH plots (one lattice temperature and various applied source-drain voltages), for a larger range of B including the flanks and the QH plateau itself, we determine the source-drain current[14] by using either the longitudinal conductivity formula for the QH device with Corbino geometry (see eq. 5.1) or the measured voltage drop $V_{50\Omega} = R_{50\Omega}/I_\text{s}$ across the 50Ω serial resistor (see Fig. 6.18 (a)). At this stage we can construct the $I - V$ characteristics at one temperature and magnetic fields B of our interest (see Fig. 6.18 (b)). By varying the magnetic field B within the QH plateau the source-drain current I_s remains zero since the source-drain voltage does not exceed the breakdown value $V_{\text{SD}^\text{crit}}$. By increasing V_SD the QH plateau width decreases and the breakdown of the QHE occurs earlier, at B values which for lower V_SD the QHE still existed (see Fig. 6.18 (c)). The same behavior was observed in the $I - V$ characteristic: by increasing V_SD and getting further from the QH plateau, the "$I - V$ plateau" shrinks. At B values well away from the integer filling factor $\nu = i$ the $I - V$ characteristic shows a short transition through the zero-current range (see Fig. 6.18 (b)). The same procedure we applied to obtain the $I - V$ characteristics corresponding to other lattice temperatures. We can now create the $I - V$ characteristics for fixed magnetic field B and different lattice temperatures (see Fig. 6.18 (d)). The higher the temperature, the shorter is the transition of the $I - V$ characteristics through the zero-current range. Further we determine, for each magnetic field value of our interest, the temperature dependence of the source-drain current for different applied source-drain voltages (see Fig. 6.19 (a)). By fitting the source-drain current points by a linear function and extrapolating the linear fitting, the intersection of the linear fitting for $I_\text{s} = 0$ with the temperature axis would give the corresponding critical temperature as a function of the filling factor (see Fig. 6.19 (a)). Figure 6.19 (b) shows the filling factor dependence of the critical temperature for different source-drain voltages. At V_SD high

---

[14] The values of source-drain current I_s is determined for each B values within our interest B range.

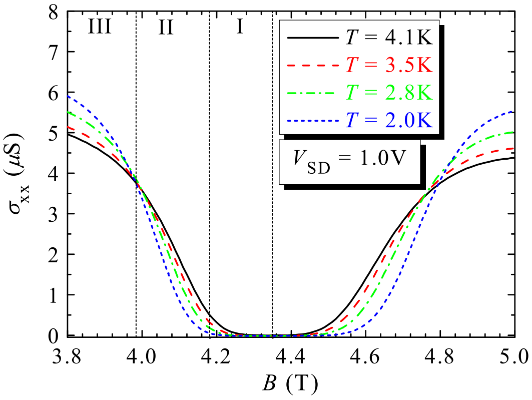

Figure 6.20: Magnetotransport curves taken for a fixed source-drain voltage V_{SD} ($V_{\mathrm{SD}} < V_{\mathrm{SD}}^{\mathrm{crit}}$) and various temperatures for medium-mobility sample $\#5$.

enough and filling factors away from the filling factor $\nu = 2$ the critical temperature is zero since the slope of the linear fitting is small due to a weak temperature dependence of $\sigma_{\mathrm{xx}}(T)$ at these filling factors. As expected, the critical temperature has a maximum at the integer filling factor $\nu = 2$ and decreases by getting further from the integer filling factor $\nu = 2$. However, we could not determine the critical temperature corresponding to filling factor $\nu = 2$ since the applied source-drain voltage never exceeded the breakdown voltage. In our case it could mean that the critical temperature is very high ($T_{\mathrm{crit}} \to \infty$). However, $T_{\mathrm{crit}} \to \infty$ is a physically hardly acceptable assumption.
By varying the magnetic field B, there are different regions for the T-dependence (see Fig. 6.20):

- Region I: σ_{xx} decreases with decreasing T toward the limit $\sigma_{\mathrm{xx}}(T) = 0$;
- Region II: σ_{xx} decreases with decreasing T toward a limit $\sigma_{\mathrm{xx}}(T) > 0$;
- Region III: σ_{xx} increases with decreasing T toward a limit $\sigma_{\mathrm{xx}}(T) > 0$, which is determined by electron impurity scattering.

The next step is to determine the electron temperature of the 2DES. In order to determine the electron temperature we employ the electron heating model. The electron heating model is based on the power balance between the gain energy P_{gain} and the energy loss P_{loss} rates. The gain energy represents the electrical energy fed to the 2DES per time and area. The loss energy describes the relaxation of the enhanced energy $\epsilon(T_{\mathrm{el}})$ at the elevated electron temperature T_{el} back to the energy $\epsilon(T_{\mathrm{lat}})$ at the lattice temperature T_{lat} (for detailed discussions see Refs. [38, 39, 99]):

$$P_{\mathrm{gain}} = P_{\mathrm{loss}} \Longleftrightarrow \sigma_{\mathrm{xx}}(T_{\mathrm{el}}) \cdot E_{\mathrm{r}}^2 = \frac{\epsilon(T_{\mathrm{el}}) - \epsilon(T_{\mathrm{lat}})}{\tau_{\mathrm{rel}}}\,, \tag{6.43}$$

where $\epsilon(T_{\rm el})$ is the energy of 2DES (per unit area) at the electron temperature $T_{\rm el}$, $\epsilon(T_{\rm lat})$ is the energy of 2DES (per unit area) at the lattice temperature $T_{\rm lat}$ and $\tau_{\rm rel}$ is the relaxation time of the hot electrons from the electron energy at the electron temperature $T_{\rm el}$ to the electron energy at the lattice temperature $T_{\rm lat}$. We should mention here that eq. 6.43 is valid only for small differences between the electron and lattice temperatures, since the electron-phonon scattering rate increases with this difference. Assuming that the relaxation rate $1/\tau_{\rm rel}$ is independent of the lattice temperature $T_{\rm lat}$ [39,123], the relaxation time can be expressed by

$$\frac{1}{\tau_{\rm rel}} = C \cdot T_{\rm el}^2 , \tag{6.44}$$

with $C \approx 1.5 \times 10^7 {\rm K}^{-2}{\rm s}^{-1}$ estimated by the authors in Ref. [39, 123]. Since in eq. 6.43 the longitudinal conductivity $\sigma_{\rm xx}$ is dependent only on the electron temperature, the dependence of the electron temperature $T_{\rm el}$ on the filling factor could be obtained by comparing the data of magnetotransport measurements $\sigma_{\rm xx}(B)$ at low source-drain voltages and different lattice temperatures ($T_{\rm el} = T_{\rm lat}$) with those $\sigma_{\rm xx}(B)$ measured at low lattice temperature $T_{\rm lat} = 1.7$K and different source-drain voltages ($T_{\rm el} > T_{\rm lat}$). The magnetotransport measurements were performed on QH device with Corbino geometry $\#5$ (see Table 6.1). By using this method we can deduce the electron temperatures near the breakdown of the QHE at filling factor $\nu = 2$. To find the electron temperature we first plot the longitudinal conductivity versus the applied source-drain voltage and versus the temperature, respectively. By choosing a value of the source-drain voltage, we find its correspondence on the longitudinal conductivity axis. For this value of the conductivity we estimate the corresponding value of the temperature (see Fig. 6.21 (a)). Thus, a correspondence between the electron temperature and the applied source-drain voltage

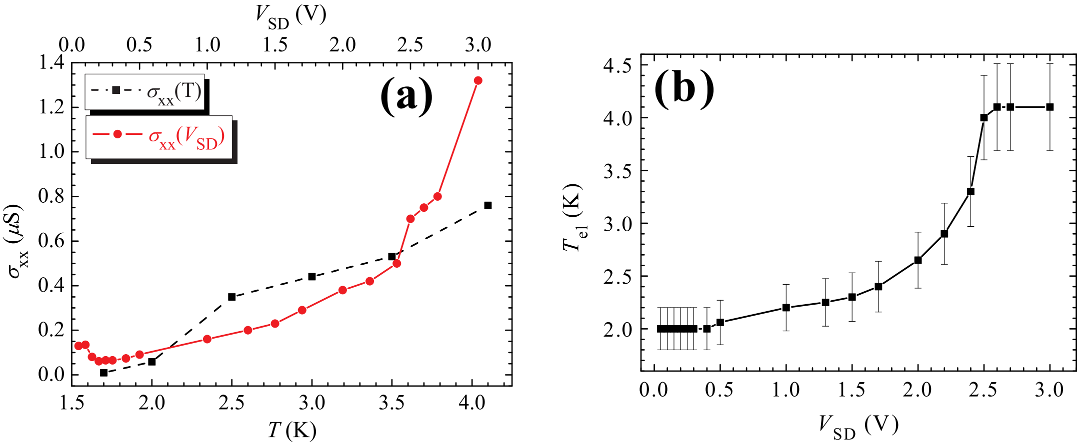

Figure 6.21: (a) Temperature (red dash line) and source-drain voltage (black solid line) dependences of the longitudinal conductivity $\sigma_{\rm xx}$; (b) Electron temperature $T_{\rm el}$ versus the applied source-drain voltage $V_{\rm SD}$ near the breakdown of the QHE at $B(\nu = 2.1) = 4.16$T determined for the medium-mobility sample $\#5$.

is determined (see Fig. 6.21 (b)). We should notice that the values of the electron temperature are estimated and not directly measured. The estimated electron temperature is limited to $T = 4.1\mathrm{K}$ due to the design of our experimental setup and because we have studied the behavior in the pre-breakdown regime. Higher temperatures would destroy the QHE. The temperature $T_{\mathrm{el}} = 4.1\mathrm{K}$ corresponding to the applied source-drain voltage $V_{\mathrm{SD}} = 3\mathrm{V}$ (see Fig. 6.21 (b)) has been chosen arbitrarily since for this voltage its correspondence on the electron temperature axis would be probably at a temperature higher than the attributed one (see Fig. 6.21 (a)). However, Fig. 6.21 (b) shows a weak increase of the electron temperature starting from source-drain voltages higher than $V_{\mathrm{SD}} > 2.3\mathrm{V}$. Again, the last point (for $V_{\mathrm{SD}} = 3\mathrm{V}$) is unreliable since it is affected by the limitation of our experimental setup.

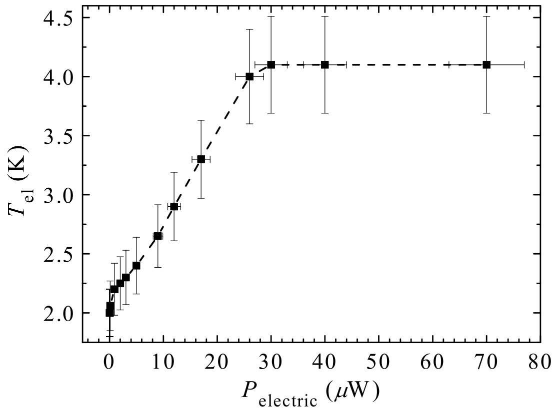

Figure 6.22: The electron temperature as a function of the electrical power determined for the medium-mobility sample #5.

In order to check the electrical power dependence on the electron temperature of the saturation of 2DES, by using eq. 5.1, we calculate the electrical power according to

$$P_{\mathrm{electric}} = V_{\mathrm{SD}} \cdot I_{\mathrm{s}} = \sigma_{\mathrm{xx}} \cdot V_{\mathrm{SD}}^2 \cdot \frac{2\pi}{ln(r_2/r_1)}\,, \tag{6.45}$$

where $r_1 = 500\mu\mathrm{m}$ and $r_2 = 1500\mu\mathrm{m}$ are the inner and outer radii of the QH device with Corbino geometry. Figure 6.22 shows a saturation of the 2DES at low power, of the order of tens of $\mu\mathrm{W}$ despite of the much larger output power provided by the *p*-Ge laser system ($P_{\mathrm{laser}} \approx 1\mathrm{W}$). The giant difference (six orders of magnitude) between the possible power needed to reach the saturation of the 2DES and the output laser power would mean that the 2DES is completely saturated at $P_{\mathrm{laser}} \approx 1\mathrm{W}$, unless the electron-photon coupling is very bad.

In the ideal case, we can consider the saturation limit corresponding to the situation in which one photon excites one electron. Thus, the number of photons is the same as the number of the electrons ($N_{\mathrm{photon}} = N_{\mathrm{el}}$). Let us consider a situation typical for our sample, with an electron system having the electron density $n_{\mathrm{s}} = 2 \times 10^{11}\mathrm{cm}^{-2}$ and the photoactive area of the QH device with Corbino geometry $A_{\mathrm{ph}} = \pi(r_2^2 - r_1^2) \approx 6.3\mathrm{mm}^2$. Thus, the number of electrons could be determined as being $N_{\mathrm{el}} = n_{\mathrm{s}} \cdot A_{\mathrm{ph}} \approx 1.26 \times 10^{10}\mathrm{electrons}$.

The number of photons could be defined by the ratio between the output laser energy per pulse $\Delta\mathrm{W}$ and the photon energy E_{photon} ($N_{\mathrm{photon}} = \Delta\mathrm{W}/E_{\mathrm{photon}}$). For the laser current $I_{\mathrm{laser}} = 25\mathrm{A}$ according to eq. 6.1 we determine the corresponding photon energy $E_{\mathrm{photon}} = 8.5\mathrm{meV}$ which in turn corresponds to a laser radiation with the laser frequency $f_{\mathrm{laser}} = 2\mathrm{THz}$ and laser wavelength $\lambda_{\mathrm{laser}} = 150\mu\mathrm{m}$. Now the output laser energy per pulse $\Delta\mathrm{W}$ could be estimated according to $\Delta\mathrm{W} = N_{\mathrm{photon}} \cdot E_{\mathrm{photon}} \approx 17\mathrm{W} \cdot \mathrm{s}$. Since the output laser power is defined by the output laser energy per pulse and the duration of the laser pulse, then the output laser power would be $P_{\mathrm{laser}} \approx 17\mu\mathrm{W}$. Thus for the saturation limit one photon excites one electron, the calculated output power laser is $P_{\mathrm{laser}} \approx 17\mu\mathrm{W}$, which agrees quite well with the experimentally determined electrical power $P_{\mathrm{electric}} \approx 26\mu\mathrm{W}$ where the saturation starts. If the saturation of the 2DES occurs at such low power then, in principle, any further increase of power would lead to no further change of $\Delta\sigma$ since all the electrons are overexcited to the upper LL's. In the saturation regime the electron temperature can be considered very high. However, this saturation cannot occur at such low power since time- or spectrally-resolved measurements show changes in the PR by varying the magnetic field, the photon energy or the electron density. Thus, the electron-photon coupling is obviously bad (for reasons so far unknown). The saturation would start at much higher power. In earlier studies [115, 116], the authors used some *teflon* blockers in order to diminish the maximum laser power $P_{\mathrm{laser}} \approx 1\mathrm{W}$. At laser powers of $P_{\mathrm{laser}}/5 \approx 0.2\mathrm{W}$ or even at $P_{\mathrm{laser}}/26 \approx 0.04\mathrm{W}$ the PR measurements show the BO and CR contributions and the real-time PR measurements show a "fast" BO-related response time (about $1\mu\mathrm{s}$) and a "slow" CR-related response time (about $4 - 5\mu\mathrm{s}$).

To conclude this part of the study, it seems that our approach based on the electron temperature picture fails to explain the frequently observed double-peak BO contribution of the PR. The failure could be partially due to the limitation imposed by our design of the experimental setup. However, we could determine satisfactorily the filling factor dependence of the critical temperature for different source-drain voltages.

In the next chapter we propose a theoretical approach for the explanation of the PR, the BO and CR contribution, on an electron-heating pictures under Drude and Self-consistent Born approximation methods.

It should be noted that all considerations presented so far concern strongly nonlinear problem. Thus, it can be hardly expected that models based on assumptions like linear response or perturbation theory correctly describe the behavior of 2DES at the breakdown of the QHE.

Chapter 7

Electron heating model proposed for the explanation of the photoresponse (PR)

In this chapter we present a model to explain the single- or double-peak structure of the BO contribution observed in the photoresponse (PR) measurements as a result of the THz radiation incidence.

Since the 1970's people were interested in the investigation of the 2DES properties exposed to electromagnetic radiation. Under CR conditions Abstreiter *et al.* [102] performed surface CR measurements of the 2DES in inversion and accumulation layers on a (100) *Si* surface. Other studies of transmission and photoconductivity measurements of the 2DES were performed in *GaAs/AlGaAs* heterostructures [103–106]. When the electromagnetic radiation is absorbed by the 2DES, the equilibrium distribution of electrons is changed, since the electrons can be excited from one LL to the next LL. Also, the electron-phonon interaction, due to the interaction between the surface acoustic waves (SAW)[1] with the 2DES in *GaAs/AlGaAs* heterostructures have been investigated experimentally by Wixforth *et al.* [124, 125]. Wixforth *et al.* reported the first investigations of the influence of the propagation of SAW (generated at about $70\mathrm{MHz}$) in the 2DES of a *GaAs/AlGaAs* heterostructure. These investigations showed that the quantum oscillations of the SAW intensity, due to the quantization of the 2DES in strong magnetic fields, reflect the SdH oscillations of the 2DES longitudinal conductivity. These quantum oscillations show a characteristic dependence on the amplitude of the SAW at high SAW intensities. Moreover, the acoustoelectric drag effect has been studied experimentally [126] and theoretically [127, 128]. Esslinger *et al.* [126] reported also an interesting feature of the SAW attenuation in the QH regime. The longitudinal acoustoelectric voltage develops a double-peak structure at integer and fractional filling factors ν. Efros *et al.* and Fal'ko *et al.* [127, 128] predicted and explained the oscillation and the quantized behavior of the longitudinal and Hall acoustoelectric voltages due to the SAW in the QH regime by us-

---

[1] The surface acoustic waves are modes of elastic energy propagating along the surface of an elastic medium.

ing a phenomenological local model. The authors explained this double-peak structure as follows: a double-peak occurs because the longitudinal conductivity oscillates with the magnetic field between very small (in the plateau region) and very large values (outside the plateau region). Therefore, the absorption coefficient oscillates strongly with the magnetic field. Each maximum of the longitudinal conductivity causes two maxima of the absorption coefficient, bound to the flank of the QH plateau.

Although the influence of the microwave (MW) radiation on the 2DES properties has been investigated from the 1980's, surprising results have been reported since 2001. Zudov *et al.* reported in high-mobility *GaAs/AlGaAs* heterostructures ($\mu_{\mathrm{el}} = 3 \times 10^6 \mathrm{cm}^2\mathrm{V}^{-1}\mathrm{s}^{-1}$) an oscillatory PR as a response of the 2DES subjected to the MW radiation, as a function of the ratio $\omega/\omega_{\mathrm{c}}$, where ω is the angular frequency of the MW radiation and ω_{c} is the cyclotron frequency [129]. Thus, these oscillation are still visible at small magnetic fields (about $10\mathrm{mT}$) where usually the SdH oscillations are not present. In 2002 Mani *et al.* [108] first reported that in ultrahigh-mobility *GaAs/AlGaAs* heterostructures ($\mu_{\mathrm{el}} = 1.5 - 3 \times 10^7 \mathrm{cm}^2\mathrm{V}^{-1}\mathrm{s}^{-1}$), due to the MW radiation the minima of these oscillations tend to *zero-resistance states* [109]. They observed zero longitudinal resistance without quantized Hall resistance at low temperatures ($T = 0.7\mathrm{K}$) and at low magnetic fields (up to $B = 0.3\mathrm{T}$) whenever the samples are illuminated by an appropriate MW radiation. These MW investigations encouraged a lot of theoretical work to explain the oscillatory PR and the occurrence of the *zero-resistance states*. Thus, Dmitriev *et al.* [130] studied the frequency-dependent conductivity $\sigma_{\mathrm{xx}}(\omega)$ [2] of the 2DES with smooth disorder under the self-consistent Born approximation (SCBA). The authors suggested that the oscillating PR and oscillating *AC* conductivity at low magnetic fields cannot be directly related to the LL quantization and proposed a possible mechanism to explain them, the *quasi-classical memory effect*[3] [131]. From this study they concluded that the oscillations of PR and the zero-resistance states observed in experiments are due to a quantum mechanism dominated by the electron-electron scattering and by the impurity scattering which determines the quantum (single-particle) relaxation time. Further, the authors present a theory of magnetooscillations in the compressibility, of the PR and of the Hall resistivity of the 2DES, based on the main effect of the MW radiation. The effect of the MW radiation is the change of both the electron distribution function-the electrons rearranges within the LL, and of the electron density of states-the electrons are excited to higher LL's [132–134].

On the other hand, experimental investigations of the 2DES under incident THz radiation have been performed. THz radiation with wavelength of the order of $\lambda \approx 120\mu\mathrm{m}$ (frequency $f \approx 2.4\mathrm{THz}$ and energy $E \approx 10\mathrm{meV}$) interacts effectively with QH systems due to the perfect match with the Landau gap between two adjacent LL's [12]. The typical Landau gap developed by the QH systems is around $10\mathrm{meV}$. This energy, called also the *cyclotron energy* $\hbar\omega_{\mathrm{c}}$, is tunable by the magnetic field B. The absorption of the THz

---

[2] The frequency-dependent conductivity $\sigma_{\mathrm{xx}}(\omega)$ is known as the *dynamic* (*AC*) conductivity. To avoid misleading, we denote the dynamic conductivity as the *AC* conductivity.

[3] The memory effect manifests itself in the PR in a more pronounced way through the radiation-induced change of the distribution function.

radiation by the 2DES causes the breakdown of the QHE and leads to an increase of the electron temperature indicated by a marked change of the PR ($\mathrm{PR} \propto \Delta\sigma_{\mathrm{xx}}$).
Despite extensive studies of the THz induced breakdown of the QHE, the explanation of the PR is still controversial. Whereas earlier studies show both cyclotron resonance (CR) and nonresonant bolometric (BO) contributions [104–106] to the PR, in other papers [111–114] the PR is attributed only to the nonresonant BO contribution. However, recent investigations of the PR on *GaAs/AlGaAs* heterostructures patterned with Hall bar- [115–117], meander- [117, 118] and Corbino geometries [119] showed both BO and CR contributions to the PR. The PR is measured versus the magnetic field B for different photon (laser) energies E_{photon}. In our measurements, the PR exhibits a nonresonant BO contribution, single or double-peak structure, located at the minimum of the longitudinal conductivity $\sigma_{\mathrm{xx}}(B)$ and the CR contribution changing its B position with the photon (laser) energy (see Fig. 6.11). The shape of the PR peaks depends strongly on the B-field of the sample in relation to the position of the photon energy (whether the B-field corresponds to a position inside or outside the second QH plateau (filling factor $\nu = 2$)). If the cyclotron frequency matches the laser frequency at B magnetic fields outside the second plateau, the PR shows distinctively two structures: a peak corresponding to the CR contribution and a single or double peak bound to the minimum of the QH plateau corresponding to the BO contribution. If the cyclotron frequency matches the laser frequency at B magnetic fields inside the QH plateau, the PR shows a strong signal due to the overlap of the CR and BO contributions.

7.1 General approach

In order to investigate theoretically the interaction of the THz radiation with the 2DES, we consider THz radiation incident to the 2DES situated at the interface between two non-magnetic materials[4] but different dielectric constants $\epsilon_1 \neq \epsilon_2$. As the THz radiation approaches the 2DES, a part of the incident radiation ($\vec{E}^{\mathrm{e}}$ and $\vec{B}^{\mathrm{e}}$) splits into reflected ($\vec{E}^{\mathrm{r}}$ and $\vec{B}^{\mathrm{r}}$) and transmitted ($\vec{E}^{\mathrm{t}}$ and $\vec{B}^{\mathrm{t}}$) parts (see Fig. 7.1).
Thus, these components can be defined as following

- incident electric and magnetic fields

$$\vec{E}^{\mathrm{e}}(\vec{k}^{\mathrm{e}}) = \vec{E}^{\mathrm{e}}_{\parallel}(\vec{K}) + E^{\mathrm{e}}_{\mathrm{z}} \cdot \vec{e}_{\mathrm{z}}\,, \tag{7.1}$$

  where $\vec{k}^{\mathrm{e}} = \vec{K} + k^{\mathrm{e}}_{\mathrm{z}} \cdot \vec{e}_{\mathrm{z}}$ is the incident wavevector with its *z*- and *in-plane*- components $k^{\mathrm{e}}_{\mathrm{z}} \cdot \vec{e}_{\mathrm{z}}$ and $\vec{K} = K_{\mathrm{x}} \cdot \vec{e}_{\mathrm{x}} + K_{\mathrm{y}} \cdot \vec{e}_{\mathrm{y}}$ respectively.

$$\vec{B}^{\mathrm{e}} = \frac{c}{\omega} \cdot \vec{k}^{\mathrm{e}} \times \vec{E}^{\mathrm{e}}\,, \tag{7.2}$$

---

[4] This means that both materials have the same magnetic permeability $\mu_1 = \mu_2$. We consider further $\mu_1 = \mu_2 \cong 1$.

where c is the speed of light and ω is the angular frequency of the radiation.

- reflected electric and magnetic fields

$$\vec{E}^{\mathrm{r}}(\vec{k}^{\mathrm{r}}) = \vec{E}^{\mathrm{r}}_{\parallel}(\vec{K}) + E^{\mathrm{r}}_{\mathrm{z}} \cdot \vec{e}_{\mathrm{z}}\,, \tag{7.3}$$

where $\vec{k}^{\mathrm{r}} = \vec{K} - k^{\mathrm{e}}_{\mathrm{z}} \cdot \vec{e}_{\mathrm{z}}$ is the reflected wavevector with its *z*-components $k^{\mathrm{e}}_{\mathrm{z}} \cdot \vec{e}_{\mathrm{z}}$.

$$\vec{B}^{\mathrm{r}} = \frac{c}{\omega} \cdot \vec{k}^{\mathrm{r}} \times \vec{E}^{\mathrm{r}}\,; \tag{7.4}$$

- transmitted electric and magnetic fields

$$\vec{E}^{\mathrm{t}}(\vec{k}^{\mathrm{t}}) = \vec{E}^{\mathrm{t}}_{\parallel}(\vec{K}) + E^{\mathrm{t}}_{\mathrm{z}} \cdot \vec{e}_{\mathrm{z}}\,, \tag{7.5}$$

where $\vec{k}^{\mathrm{t}} = \vec{K} + k^{\mathrm{t}}_{\mathrm{z}} \cdot \vec{e}_{\mathrm{z}}$ is the transmitted wavevector with its *z*-component $k^{\mathrm{t}}_{\mathrm{z}} \cdot \vec{e}_{\mathrm{z}}$.

$$\vec{B}^{\mathrm{t}} = \frac{c}{\omega} \cdot \vec{k}^{\mathrm{t}} \times \vec{E}^{\mathrm{t}}\,. \tag{7.6}$$

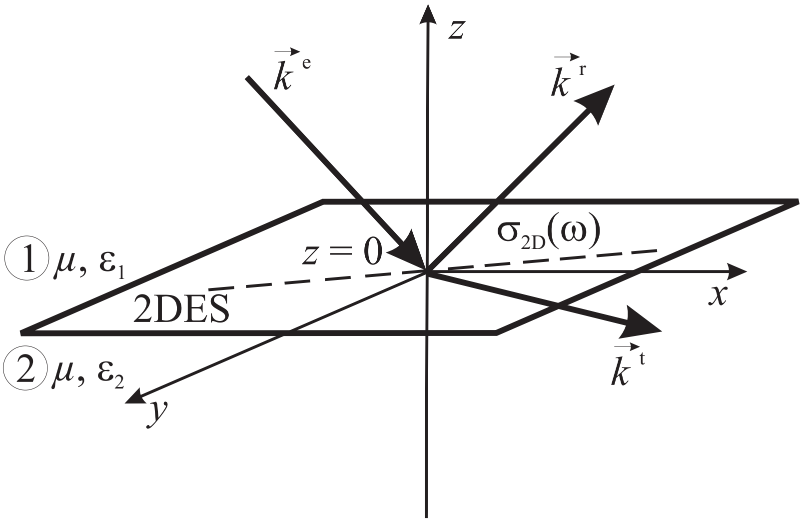

Figure 7.1: Sketch of the splitting of the incident radiation into the reflected and transmitted parts at the plane of a 2DES, which separates two materials of different dielectric constant $\epsilon_1 \neq \epsilon_2$ and the same magnetic permeability $\mu_1 = \mu_2 = \mu$. The THz radiation and the 2DES are coupled.

The dispersion equations for the two materials are

$$K^2 + (k^{\mathrm{e}}_{\mathrm{z}})^2 = \epsilon_1 \cdot \frac{\omega^2}{c^2} \tag{7.7}$$

and

$$K^2 + \left(k^{\mathrm{t}}_{\mathrm{z}}\right)^2 = \epsilon_2 \cdot \frac{\omega^2}{c^2}\,. \tag{7.8}$$

To proceed further, the *in-plane* current density must be determined. The perpendicular magnetic field couples the two-components of the *in-plane* current density $\vec{j}(\vec{K})$ and therefore the electric and magnetic fields components inside and normal to the plane of 2DES (the plane of incidence).
To do so, with the Maxwell's equations (in CGS-units) [135]

$$\left\{\begin{array}{l} \nabla\cdot\vec{D} = 4\pi\rho^{3D} \\ \nabla\cdot\vec{B} = 0 \\ \nabla\times\vec{E} + \frac{1}{c}\cdot\frac{\partial\vec{B}}{dt} = 0 \\ \nabla\times\vec{H} - \frac{1}{c}\cdot\frac{\partial\vec{D}}{dt} = \frac{4\pi}{c}\vec{j} \end{array}\right. \quad \text{with} \left\{\begin{array}{l} \vec{D} = \epsilon\vec{E} \\ \vec{B} = \mu\vec{H} = \vec{H} \end{array}\right. \tag{7.9}$$

and the boundary conditions at the 2DES plane

$$\left\{\begin{array}{l} \vec{e}_{\mathrm{z}}\times\left(\vec{E}^{\mathrm{t}} - \vec{E}^{\mathrm{e}} - \vec{E}^{\mathrm{r}}\right) = 0 \\ \vec{e}_{\mathrm{z}}\times\left(\vec{B}^{\mathrm{t}} - \vec{B}^{\mathrm{e}} - \vec{B}^{\mathrm{r}}\right) = \frac{4\pi}{c}\vec{j} \end{array}\right. , \tag{7.10}$$

we obtain

$$\left\{\begin{array}{l} \vec{e}_{\mathrm{z}}\cdot\left(\vec{E}^{\mathrm{t}} - \vec{E}^{\mathrm{e}} - \vec{E}^{\mathrm{r}}\right) = \frac{4\pi}{\epsilon}\rho \\ \vec{e}_{\mathrm{z}}\cdot\left[\left(\vec{k}^{\mathrm{t}}\times\vec{E}^{\mathrm{t}}\right) - \left(\vec{k}^{\mathrm{e}}\times\vec{E}^{\mathrm{e}}\right) - \left(\vec{k}^{\mathrm{r}}\times\vec{E}^{\mathrm{r}}\right)\right] = 0 \\ \vec{e}_{\mathrm{z}}\times\left(\vec{E}^{\mathrm{t}} - \vec{E}^{\mathrm{e}} - \vec{E}^{\mathrm{r}}\right) = 0 \\ \vec{e}_{\mathrm{z}}\times\left[\left(\vec{k}^{\mathrm{t}}\times\vec{E}^{\mathrm{t}}\right) - \left(\vec{k}^{\mathrm{e}}\times\vec{E}^{\mathrm{e}}\right) - \left(\vec{k}^{\mathrm{r}}\times\vec{E}^{\mathrm{r}}\right)\right] = \frac{4\pi\omega}{c^2}\vec{j} \end{array}\right. , \tag{7.11}$$

where ρ is the charge density of the 2DES and we have already expressed the transversal, incident and reflected B-fields in terms of the crossed $\vec{k}\times\vec{E}$ according to eq. 7.2, eq. 7.4 and eq. 7.6.
To solve these eq. 7.11 we assume plane-wave electro-magnetic fields for the incident, reflected and transmitted field, use the orthogonality of $\vec{k}$- and $\vec{E}$-fields, use the equation of continuity[5] for the current $\vec{j}$ and the charge ρ densities in the 2DES and use the dispersion relations (see eq. 7.7 and eq. 7.8). We finally integrate the local Ohm's law $\vec{j}(\vec{K}) = \hat{\sigma}\cdot\vec{E}^{\mathrm{t}}_{\|}(\vec{K})$ with two equations:

$$\vec{E}^{\mathrm{t}}_{\|}(\vec{K}) = \vec{E}^{\mathrm{e}}_{\|}(\vec{K}) + \vec{E}^{\mathrm{r}}_{\|}(\vec{K}) \tag{7.12}$$

and

$$\left[\left(k^{\mathrm{t}}_{\mathrm{z}} + k^{\mathrm{e}}_{\mathrm{z}}\right)\cdot\hat{1} + \left(\frac{1}{k^{\mathrm{t}}_{\mathrm{z}}} + \frac{1}{k^{\mathrm{e}}_{\mathrm{z}}}\right)\cdot\left(\vec{K}:\vec{K}\right) + \frac{4\pi\omega}{c^2}\cdot\hat{\sigma}\right]\vec{E}^{\mathrm{t}}_{\|} = \frac{2}{k^{\mathrm{e}}_{\mathrm{z}}}\cdot\left((k^{\mathrm{e}}_{\mathrm{z}})^2\cdot\hat{1} + \vec{K}:\vec{K}\right)\vec{E}^{\mathrm{e}}_{\|}, \tag{7.13}$$

---

[5] The equation of continuity is derived from two of Maxwell's equations (Ampère's law and Gauss's law). It states that the divergence of the current density is equal to the negative rate of change of the charge density, $\nabla\vec{j} + \partial\rho/\partial t = 0$.

where $\hat{1}$ is the unity tensor and $(\vec{K}:\vec{K})\vec{E}^{\mathrm{t}}_{\parallel} = \vec{K}\cdot(\vec{E}^{\mathrm{t}}_{\parallel}\cdot\vec{K}) = K^2 E^{\mathrm{t}}_{\mathrm{x}}$, with $E^{\mathrm{t}}_{\mathrm{x}}$ the longitudinal component of $\vec{E}^{\mathrm{t}}_{\parallel}$.
However, eq. 7.13 characterizes the situation of tilted incidence of the electromagnetic radiation. Since in the optically induced breakdown measurements [117–119], the THz is perpendicular to the plane of the 2DES, the *in-plane* $\vec{K}$ component of the wavevector $\vec{k}$ vanishes. By considering an homogeneous 2DES and $\epsilon_1 = \epsilon_2 = \epsilon$, the dispersion relations (see eq. 7.7 and eq. 7.8) unify into

$$\left(k^{\mathrm{t}}_{\mathrm{z}}\right)^2 = \left(k^{\mathrm{e}}_{\mathrm{z}}\right)^2 = \epsilon\cdot\frac{\omega^2}{c^2} \Longleftrightarrow k^{\mathrm{t}}_{\mathrm{z}} = k^{\mathrm{e}}_{\mathrm{z}} = \sqrt{\epsilon}\cdot\frac{\omega}{c}\,. \tag{7.14}$$

Therefore, eq. 7.13 transforms for the perpendicular incidence into:

$$\left(2k^{\mathrm{e}}_{\mathrm{z}}\cdot\hat{1} + \frac{4\pi\omega}{c^2}\cdot\hat{\sigma}\right)\vec{E}^{\mathrm{t}} = 2k^{\mathrm{e}}_{\mathrm{z}}\cdot\hat{1}\cdot\vec{E}^{\mathrm{e}}\,. \tag{7.15}$$

Equation 7.15 can be further solved by rewriting the equation in a matrix form $\hat{A}\cdot\vec{E}^{\mathrm{t}} = \vec{E}^{\mathrm{e}}$

$$\begin{pmatrix} 1+\frac{2\pi}{c\sqrt{\epsilon}}\cdot\sigma_{\mathrm{l}} & -\frac{2\pi}{c\sqrt{\epsilon}}\cdot\sigma_{\mathrm{H}} \\ \frac{2\pi}{c\sqrt{\epsilon}}\cdot\sigma_{\mathrm{H}} & 1+\frac{2\pi}{c\sqrt{\epsilon}}\cdot\sigma_{\mathrm{l}} \end{pmatrix}\cdot\begin{pmatrix} E^{\mathrm{t}}_{\mathrm{x}} \\ E^{\mathrm{t}}_{\mathrm{y}} \end{pmatrix} = \begin{pmatrix} E^{\mathrm{e}}_{\mathrm{x}} \\ E^{\mathrm{e}}_{\mathrm{y}} \end{pmatrix}, \tag{7.16}$$

where $\sigma_{\mathrm{l}} = \sigma_{\mathrm{xx}} = \sigma_{\mathrm{yy}}$ and $\sigma_{\mathrm{H}} = -\sigma_{\mathrm{xy}} = \sigma_{\mathrm{yx}}$ are the longitudinal and the Hall components of the conductivity tensor $\hat{\sigma}$, $E^{\mathrm{e}}_{\mathrm{x}}$ and $E^{\mathrm{e}}_{\mathrm{y}}$ are the *x*- and *y*-components of the incident field $\vec{E}^{\mathrm{e}}$, $E^{\mathrm{t}}_{\mathrm{x}}$ and $E^{\mathrm{t}}_{\mathrm{y}}$ are the *x*- and *y*-components of the transmitted field $\vec{E}^{\mathrm{t}}$.
To determine the transmitted field $\vec{E}^{\mathrm{t}}$, the matrix equation $\hat{A}\cdot\vec{E}^{\mathrm{t}} = \vec{E}^{\mathrm{e}}$ (see eq. 7.16) is multiplied by the inverse $\hat{A}^{-1}$ of the matrix $\hat{A}$ and obtain $\vec{E}^{\mathrm{t}} = \hat{A}^{-1}\cdot\vec{E}^{\mathrm{e}}$. Alternatively we write

$$\begin{pmatrix} E^{\mathrm{t}}_{\mathrm{x}} \\ E^{\mathrm{t}}_{\mathrm{y}} \end{pmatrix} = \frac{1}{(1+\tilde{\alpha}\cdot\tilde{\sigma}_{\mathrm{l}})^2 + (\tilde{\alpha}\cdot\tilde{\sigma}_{\mathrm{H}})^2}\cdot\begin{pmatrix} 1+\tilde{\alpha}\cdot\tilde{\sigma}_{\mathrm{l}} & \tilde{\alpha}\cdot\tilde{\sigma}_{\mathrm{H}} \\ -\tilde{\alpha}\cdot\tilde{\sigma}_{\mathrm{H}} & 1+\tilde{\alpha}\cdot\tilde{\sigma}_{\mathrm{l}} \end{pmatrix}\cdot\begin{pmatrix} E^{\mathrm{e}}_{\mathrm{x}} \\ E^{\mathrm{e}}_{\mathrm{y}} \end{pmatrix} \tag{7.17}$$

where for simplicity we considered $\sigma_{\mathrm{l,H}} = (e^2/h)\cdot\tilde{\sigma}_{\mathrm{l,H}}$, $\tilde{\alpha} = \alpha/\sqrt{\epsilon} = 2.072\times10^{-3}$, $\alpha = e^2/\hbar c = 1/137.0359$ is the fine-structure constant and $\epsilon = 12.4$ is the dielectric constant of the *GaAs*.
If we consider such a situation in which the incident electric field has only a *x*-component $\vec{E}^{\mathrm{e}} = (E^{\mathrm{e}}_{\mathrm{x}}, 0, 0)$ then eq. 7.17 becomes

$$\vec{E}^{\mathrm{t}} = \begin{pmatrix} E^{\mathrm{t}}_{\mathrm{x}} \\ E^{\mathrm{t}}_{\mathrm{y}} \end{pmatrix} = \frac{1}{D}\cdot\begin{pmatrix} (1+\tilde{\alpha}\cdot\tilde{\sigma}_{\mathrm{l}})\cdot E^{\mathrm{e}}_{\mathrm{x}} \\ -\tilde{\alpha}\cdot\tilde{\sigma}_{\mathrm{H}}\cdot E^{\mathrm{e}}_{\mathrm{x}} \end{pmatrix} \tag{7.18}$$

where $D = (1+\tilde{\alpha}\cdot\tilde{\sigma}_{\mathrm{l}})^2 + (\tilde{\alpha}\cdot\tilde{\sigma}_{\mathrm{H}})^2$ is the determinant of matrix $\hat{A}^{-1}$.

In order to describe how effective is the radiation we calculate the transmission coefficients and the power absorption. Generally, the *transmission*[6] *coefficient* is a measure

---

[6] Transmission itself is the property of a substance to permit the passage of an electromagnetic radiation, with some or none of the incident radiation being absorbed in the process.

of how much of an electromagnetic wave passes through a surface or an optical element. These coefficients are used to describe the behavior of the radiation incident on a surface, on a system. The transmission coefficient is defined in terms of the incident and transmitted fields according to:

$$\begin{aligned} T &= \frac{|\vec{E}^{\mathrm{t}}|^2}{|E^{\mathrm{e}}_{\mathrm{x}}|^2} = \frac{|\vec{E}^{\mathrm{t}}_{\mathrm{x}}|^2 + |\vec{E}^{\mathrm{t}}_{\mathrm{y}}|^2}{|E^{\mathrm{e}}_{\mathrm{x}}|^2} = \frac{1}{|D|^2} \cdot \left(|1 + \tilde{\alpha} \cdot \tilde{\sigma}_{\mathrm{l}}|^2 + |\tilde{\alpha} \cdot \tilde{\sigma}_{\mathrm{H}}|^2 \right) \\ &= \frac{1}{|D|^2} \cdot \left\{ (1 + \tilde{\alpha} \cdot \Re\tilde{\sigma}_{\mathrm{l}})^2 + \tilde{\alpha}^2 \cdot \left[(\Im\tilde{\sigma}_{\mathrm{l}})^2 + (\Re\tilde{\sigma}_{\mathrm{H}})^2 + (\Im\tilde{\sigma}_{\mathrm{H}})^2 \right] \right\} , \end{aligned} \tag{7.19}$$

where $\tilde{\sigma}_{\mathrm{l,H}} = \Re\tilde{\sigma}_{\mathrm{l,H}} + i \cdot \Im\tilde{\sigma}_{\mathrm{l,H}}$. If $|\tilde{\alpha} \cdot \tilde{\sigma}_{\mathrm{l,H}}| << 1$ then the transmission coefficient could be approximated $T \approx 1 - 2\tilde{\alpha}\Re\tilde{\sigma}_{\mathrm{l}}$.

The *absorption* is the process by which the energy of an electromagnetic radiation is taken by another entity, for example, by an atom whose valence electrons make transition between two electronic energy levels. The absorbed energy may be re-emitted as radiant energy or transformed into heat energy (Joule heating). For most substances, the amount of absorption varies with the wavelength of the electromagnetic radiation.
The photocurrent absorption (Joule heating) W is calculated as the average power dissipation induced by the current density $\vec{j}$ as a result of the electric field $\vec{E}^{\mathrm{t}}$

$$\begin{aligned} W &= \left\langle \vec{j} \cdot \vec{E}^{\mathrm{t}} \right\rangle_{\mathrm{t}} = \left\langle \frac{1}{2} \left(\vec{j} e^{-i\omega t} + \vec{j}^{*} e^{i\omega t} \right) \cdot \frac{1}{2} \left(\vec{E}^{\mathrm{t}} e^{-i\omega t} + \vec{E}^{\mathrm{t}*} e^{i\omega t} \right) \right\rangle_{\mathrm{t}} \\ &= \frac{1}{2} \Re \left(\vec{E}^{\mathrm{t}*} \cdot \vec{j} \right) = \frac{1}{2} \Re\sigma_{\mathrm{l}} \left(|E^{\mathrm{t}}_{\mathrm{x}}|^2 + |E^{\mathrm{t}}_{\mathrm{y}}|^2 \right) - \Im\sigma_{\mathrm{H}} \cdot \Im \left(E^{\mathrm{t}}_{\mathrm{x}} \cdot E^{\mathrm{t}*}_{\mathrm{y}} \right) , \end{aligned} \tag{7.20}$$

By applying the Ohm's law $\vec{j} = \hat{\sigma} \cdot \vec{E}^{\mathrm{t}}$ and after several algebra steps, the photocurrent absorption becomes

$$\begin{aligned} \frac{h}{e^2} \cdot \frac{W}{|\vec{E}^{\mathrm{e}}_{\mathrm{x}}|^2} &= \frac{1}{|D|^2} \cdot \frac{1}{2} \cdot \Re\tilde{\sigma}_{\mathrm{l}} \left\{ (1 + \tilde{\alpha} \cdot \Re\tilde{\sigma}_{\mathrm{l}})^2 + \tilde{\alpha}^2 \cdot \left[(\Im\tilde{\sigma}_{\mathrm{l}})^2 + (\Re\tilde{\sigma}_{\mathrm{H}})^2 - (\Im\tilde{\sigma}_{\mathrm{H}})^2 \right] \right\} \\ &+ \frac{1}{|D|^2} \cdot \tilde{\alpha} \cdot \Im\tilde{\sigma}_{\mathrm{H}} \cdot (\tilde{\alpha} \cdot \Re\tilde{\sigma}_{\mathrm{H}} \cdot \Im\tilde{\sigma}_{\mathrm{l}} - \Im\tilde{\sigma}_{\mathrm{H}}) \ . \end{aligned} \tag{7.21}$$

Since $\tilde{\alpha}^2 << 1$ and if $|\tilde{\alpha} \cdot \tilde{\sigma}_{\mathrm{l,H}}| << 1$ then the photocurrent absorption could be approximated

$$\frac{h}{e^2} \cdot \frac{W}{|\vec{E}^{\mathrm{e}}_{\mathrm{x}}|^2} \approx \frac{1}{2} \Re\tilde{\sigma}_{\mathrm{l}} - \tilde{\alpha} \cdot \left[(\Re\tilde{\sigma}_{\mathrm{l}})^2 + (\Im\tilde{\sigma}_{\mathrm{H}})^2 \right] . \tag{7.22}$$

From eq. 7.19, eq. 7.21 and eq. 7.22, we observe that both the transmission and absorption, in the case of perpendicular incidence of the radiation, are proportional to the *AC* longitudinal and Hall conductivities, mainly on the real part of the longitudinal conductivity and imaginary part of the Hall conductivity as stated by other theoretical investigations of the *AC* conductivity [121, 136, 137].

7.2 Drude approximation

The simplest model that describes the response of the 2DES to the electromagnetic radiation is the Drude approximation. The Drude approximation describes the scattering of electrons by a constant relaxation time, independent of the laser frequency and the magnetic field. Within this approximation, the *AC* longitudinal and Hall conductivities are determined by solving the Lorentz force equation 6.12 with the assumption that in a steady state the electric field $\vec{E}$ and the velocity $\vec{v}$ are time dependent. Thus, the *AC* longitudinal conductivity is given by

$$\sigma_\mathrm{l}(\omega) = \sigma_0 \cdot \frac{1 - i\omega\tau}{(1 - i\omega\tau)^2 + \omega_\mathrm{c}^2\tau^2} \tag{7.23}$$

and the *AC* Hall conductivity is given by

$$\sigma_\mathrm{H}(\omega) = \sigma_0 \cdot \frac{\omega_\mathrm{c}\tau}{(1 - i\omega\tau)^2 + \omega_\mathrm{c}^2\tau^2}\,, \tag{7.24}$$

where $\sigma_0 = n_\mathrm{s}e^2\tau/m^*$ is the classical (*DC*) Drude conductivity with $B = 0$ (see eq. 2.19). The real and imaginary parts of the *AC* longitudinal and Hall conductivities are given by eq. 6.22, eq. 6.23, eq. 6.24 and eq. 6.25 respectively. According to eq. 7.23 and eq. 7.24 we observe 3 special cases:

- $\boldsymbol{\omega_\mathrm{c} \neq 0,\ \omega = 0}$: the *DC* longitudinal and Hall conductivity with magnetic field

  $$\sigma_\mathrm{l}(\omega = 0) = \sigma_0 \cdot \frac{1}{1 + \omega_\mathrm{c}^2\tau^2} \tag{7.25}$$

  and

  $$\sigma_\mathrm{H}(\omega = 0) = \sigma_0 \cdot \frac{\omega_\mathrm{c}\tau}{1 + \omega_\mathrm{c}^2\tau^2}\,; \tag{7.26}$$

- $\boldsymbol{\omega_\mathrm{c} = 0,\ \omega \neq 0}$: the *AC* longitudinal and Hall conductivity without magnetic field

  $$\sigma_\mathrm{l}(\omega) = \sigma_0 \cdot \frac{1}{1 - i\omega\tau} \tag{7.27}$$

  and

  $$\sigma_\mathrm{H}(\omega) = 0\,; \tag{7.28}$$

- $\boldsymbol{\omega_\mathrm{c} = 0,\ \omega = 0}$: the *DC* longitudinal and Hall conductivity without magnetic field

  $$\sigma_\mathrm{l}(\omega) = \sigma_0 \tag{7.29}$$

  and

  $$\sigma_\mathrm{H}(\omega) = 0\,. \tag{7.30}$$

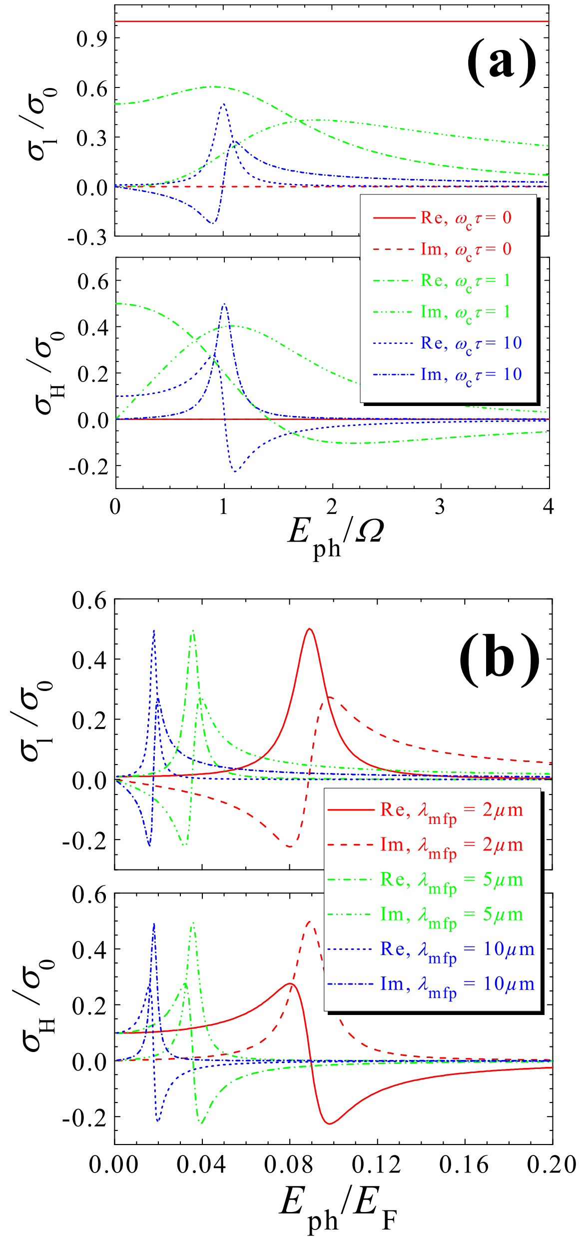

Figure 7.2: (a) *AC* conductivity as a function of the photon energy E_{ph}/Ω (in units of cyclotron energy Ω) for three values of the strength of the magnetic field ($B \propto \omega_{\mathrm{c}}\tau$). $E_{\mathrm{ph}} = \hbar\omega$. (b) *AC* conductivity as a function of the laser energy $E_{\mathrm{ph}}/E_{\mathrm{F}}$ (in units of Fermi energy E_{F}) for different values of the mean free path at fixed $\omega_{\mathrm{c}}\tau = 10$. The real and imaginary parts are calculated for a damping parameter $\omega_{\mathrm{F}}\tau = \pi\lambda_{\mathrm{mfp}}/\lambda_{\mathrm{F}}$ where the value for the mean free path $\lambda_{\mathrm{mfp}} = v_{\mathrm{F}} \cdot \tau = hk_{\mathrm{F}}\tau/m^{*}$ takes different values and the Fermi wavelength $\lambda_{\mathrm{F}} = 2\pi/k_{\mathrm{F}} = 2\pi/\sqrt{2\pi n_{\mathrm{s}}} \approx 56\mathrm{nm}$ is determined by an electron density $n_{\mathrm{s}} = 2 \times 10^{11}\mathrm{cm}^{-2}$.

Within this classical approach, the electrons are noninteracting particles moving according to Newtons's equation. We assume that due to the presence of impurities and dislocations the electron are scattered. The scattering prevents the electrons on the average from being accelerated. The effect of scattering on the 2DES can be modeled by introducing a frictional term, described by the relaxation time τ, in the Newton's law from which with also the Ohm's law, the Drude conductivity formula is obtained (see eq. 2.19).

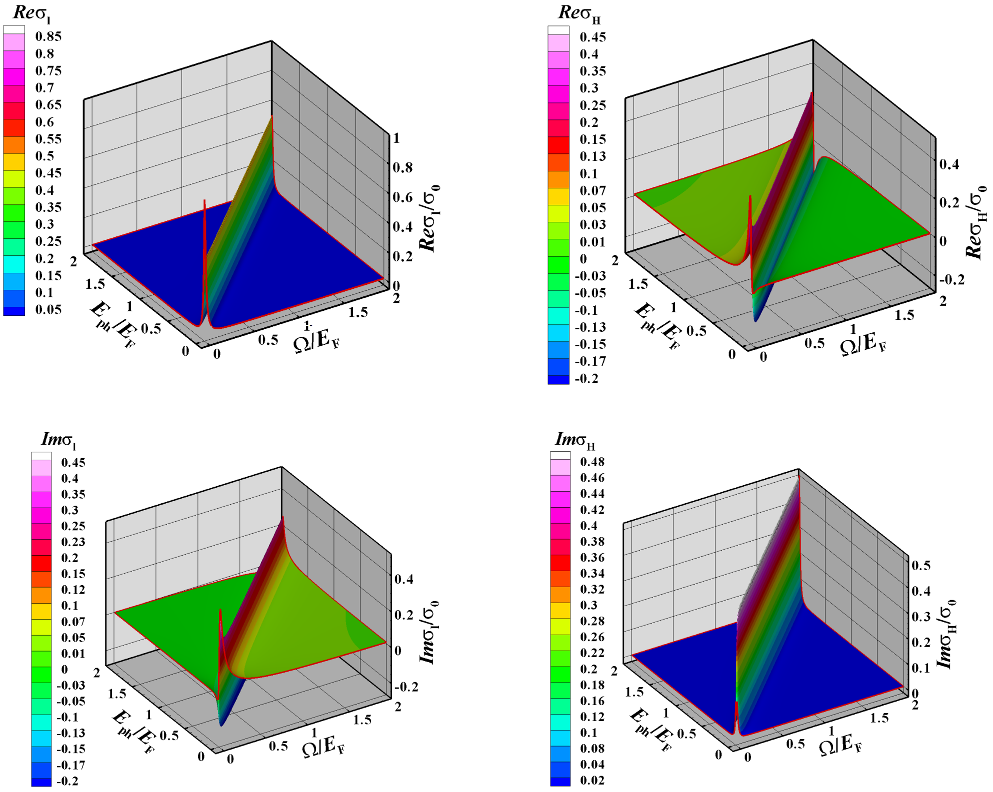

Figure 7.3: *AC* longitudinal $\sigma_\mathrm{l}(\omega)$ and Hall $\sigma_\mathrm{H}(\omega)$ conductivities, as a function of the cyclotron Ω/E_F and photon $E_\mathrm{ph}/E_\mathrm{F}$ energies, are calculated for a damping parameter $\omega_\mathrm{F}\tau = 59$.

The dimensionless parameter $\omega_\mathrm{c}\tau$ gives the strength of the magnetic field and represents the number of orbits made by an electron before it is scattered. Figure 7.2 (a) shows the real and imaginary parts of the *AC* longitudinal σ_l and Hall σ_H conductivities as a function of the photon frequency in cyclotron frequency units for different values of the damping parameter $\omega_\mathrm{c}\tau$. This figure shows that at high magnetic fields the damping is less effective because the electrons make more orbits before they are scattered. The conductivity shows well developed peaks at high magnetic field. By decreasing the strength of the magnetic field ($\omega_\mathrm{c}\tau$) the peak broadens and the damping becomes more effective. Moreover, fig.

7.2 (a) shows that the maximum in amplitude of the conductivity occurs at cyclotron resonance ($\omega/\omega_{\mathrm{c}} = 1$) when the photon frequency matches the cyclotron frequency ($\omega = \omega_{\mathrm{c}}$). However, this figure confirms that the most contribution in the absorption and in the transmission coefficients peaks comes from the real part of the longitudinal conductivity $\Re\sigma_{\mathrm{l}}$ and from the imaginary part of the Hall conductivity $\Im\sigma_{\mathrm{H}}$.

To see the effect of the density of impurities on the *AC* conductivity, we show the dependence of the conductivity as a function of the photon energy in Fermi energy units at fixed magnetic strength $\omega_{\mathrm{c}}\tau$ and different mean free path values. Longer scattering time τ corresponds to longer mean free path λ_{mfp} and higher electron mobility. Longer scattering time describes weaker damping effects. Figure 7.2 (b) shows that for smaller mean free path λ_{mfp} the peak is broader. By increasing the mean free path value, the peaks narrows. Thus, stronger damping (corresponding to shorter mean free path or shorter scattering time) broadens the peak and weaker damping (corresponding to longer mean free path λ_{mfp} or longer scattering time τ) narrows the peak.

Figure 7.3 shows the *AC* longitudinal σ_{l} and Hall σ_{H} conductivities as a function of both the photon and the cyclotron frequencies for a fixed damping parameter. By sweeping both the photon energy and the magnetic field, we observe that the *AC* conductivity shows maxima, without any peculiar structures, only along the cyclotron line, the line calculated for the perfect match between the cyclotron and photon frequencies.

The transmission coefficient T and the photocurrent absorption W are also calculated with the assumptions of the Drude model. They show maxima only along the CR line without any quantum oscillations (see Fig. 7.4).

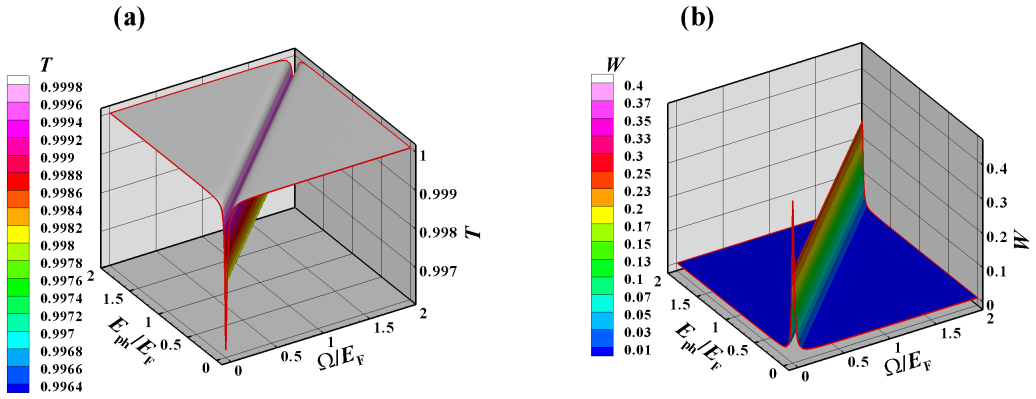

Figure 7.4: The transmission coefficient T (a) and the photocurrent absorption W (b), as a function of the cyclotron Ω/E_{F} and photon $E_{\mathrm{ph}}/E_{\mathrm{F}}$ energies, are calculated for a damping parameter $\omega_{\mathrm{F}}\tau = 59$. The transmission coefficient is defined by eq. 7.19 and the power absorption is plotted with the normalization introduced in eq. 7.21.

The lack of any structure aside the cyclotron line is characteristic to the Drude approximation which works either at high temperatures or at low magnetic fields and therefore does not assume any quantum effects. In conclusion, the Drude approximation does not match our required experimental conditions: high magnetic fields (up to $6\mathrm{T}$) and low temperatures (*liquid He* temperature $T \leq 4\mathrm{K}$).

7.3 Self-Consistent Born Approximation (SCBA)

To explain adequately the experimental situation it is necessary to include the Landau quantization induced by the high magnetic fields under the **S**elf-**C**onsistent **B**orn **A**pproximation (SCBA) [9, 47, 121].
The SCBA is one among the possible methods to describe the broadening effects on the DOS, induced by the impurity presence, and the transport properties. One major advantage of this method is that the SCBA avoids the difficulties of a divergence caused by the singular nature of the DOS [5]. The SCBA assumes that the coherent scattering of an electron by more than one impurity can be neglected. This will affect the shape of the DOS, which results in half ellipses with sharp edges. We assume that the level width Γ is larger than the spin splitting (Zeeman) energy $\Gamma > \Delta E_s = g^* \mu_{\mathrm{B}} B$. The Coulomb potentials of the impurities contain *short-range* and *long-range* contributions. For simplicity, we treat the disorder taking into account only the short-range contribution[7]. This treatment is justified provided that the disorder correlation lengths L satisfies the conditions: $L < \ell_{\mathrm{B}}$ and $L < \ell_{\mathrm{mfp}} = v_{\mathrm{F}} \cdot \tau$. However, for samples with larger length than the correlation length, the long-range contributions should be also taken into account.
The impurities lift the degeneracy of the Landau energies and leads to a broadening of the δ-functions DOS (assumed for the case of no disorder) into spectral functions $A_n(E)$ of finite widths Γ. Since the spectral function applying the SCBA is given by

$$A_n(E) = \frac{1}{\pi\Gamma} \cdot \sqrt{1 - \left(\frac{E - E_n}{2\Gamma}\right)^2}\,, \tag{7.31}$$

where E_n is the Landau energy (see eq. 2.21), the DOS $D(E)$ is a sum over n of the corresponding spectral functions $A_n(E)$

$$D(E) = n_{\mathrm{L}} \cdot \sum_n A_n(E) = \frac{n_{\mathrm{s}}}{\nu} \cdot \sum_n A_n(E) = \frac{1}{2\pi\ell_{\mathrm{B}}^2} \cdot \sum_n A_n(E)\,, \tag{7.32}$$

where n_{L} is the electron density in each LL (see eq. 2.25), ν is the filling factor (see eq. 2.26) and $\ell_{\mathrm{B}} = \sqrt{\hbar/eB}$ is the magnetic length. I should mention that eq. 7.32 refers to one spin direction and, in the case of spin degeneracy, it should my multiplied by the

---

[7] Because the SCBA method does not describe coherent multi-center scattering, the long-range contributions of the Coulomb potentials would lead to large damping effects.

degeneracy factor $g_s = 2$.
In the following we shall use the *Green's function* technique to evaluate the equilibrium quantities (electron density and DOS). The Green's function contains information about the distribution of the impurities in the system. Therefore it includes the effect of all other impurities on the electron motion in the 2DES.
The Green's function is written as

$$G_n(E) = \frac{1}{E - E_n - \Sigma(E)}\,, \tag{7.33}$$

where $\Sigma(E)$ is the *self-energy*[8].
The self-energy in SCBA is given by [54]

$$\begin{aligned} \Sigma(E) &= n_I \cdot \int d^2R \cdot v_{\vec{R}} \cdot G_n(E) \cdot v_{\vec{R}} \\ &= \frac{n_I v_0^2}{2\pi\ell_{\mathrm{B}}^2} \cdot \sum_{n=0}^{\infty} \left(\frac{1}{E - \Sigma(E) - E_n} + \frac{1}{E_c + E_n} \right)\,, \end{aligned} \tag{7.34}$$

where n_I is the impurity density, $v_{\vec{R}}$ is the impurity potential at position $\vec{R}$ and E_c is a cutoff energy introduced to achieve the convergence of the self-energy.
The self-energy can be found iteratively, and afterward the Green's function is determined. To solve eq. 7.34 numerically, we scale our variables in cyclotron energy units:

$$\begin{aligned} \frac{E}{\hbar\omega_{\mathrm{c}}} = \xi,\ \frac{E_n}{\hbar\omega_{\mathrm{c}}} = n + \frac{1}{2},\ \frac{E_c}{\hbar\omega_{\mathrm{c}}} = 1;\ \frac{\Sigma(E)}{\hbar\omega_{\mathrm{c}}} = \kappa(\xi), \\ \gamma_{\mathrm{B}}^2 = \frac{n_I v_0^2}{2\pi\ell_{\mathrm{B}}^2(\hbar\omega_{\mathrm{c}})^2} = \frac{n_I v_0^2 D_0}{(\hbar\omega_{\mathrm{c}})^2} = \frac{\Gamma^2}{(\hbar\omega_{\mathrm{c}})^2}\,, \end{aligned} \tag{7.35}$$

with γ_{B}^2 the damping parameter (measured by the square of the ratio of the half-width of the LL with $\nu = 2$ and the cyclotron energy) being proportional to the impurity density n_I. This feature is important because it relates directly to the electron mobility. Since higher impurity density means lower mobility, therefore a larger damping parameter would correspond to a lower mobility. With these dimensionless quantities eq. 7.34 becomes

$$\kappa(\xi) = \gamma_{\mathrm{B}}^2 \cdot \sum_{n=0}^{\infty} \left(\frac{1}{\xi - \kappa(\xi) - \left(n + \frac{1}{2}\right)} + \frac{1}{n + \frac{3}{2}} \right)\,. \tag{7.36}$$

By solving this equation numerically, we determine the real and imaginary parts of the self-energy. Particular interest is given to the imaginary part of the self-energy since it describes the DOS (see fig. 7.5 (a)):

$$D(E) = \frac{D_0}{\pi\gamma_{\mathrm{B}}^2\hbar\omega_{\mathrm{c}}} \cdot \Im\Sigma^-(E)\,. \tag{7.37}$$

---

[8] The self-energy of a particle represents the contribution to the energy of the particle due to the interaction between the particle and the system it is a part of.

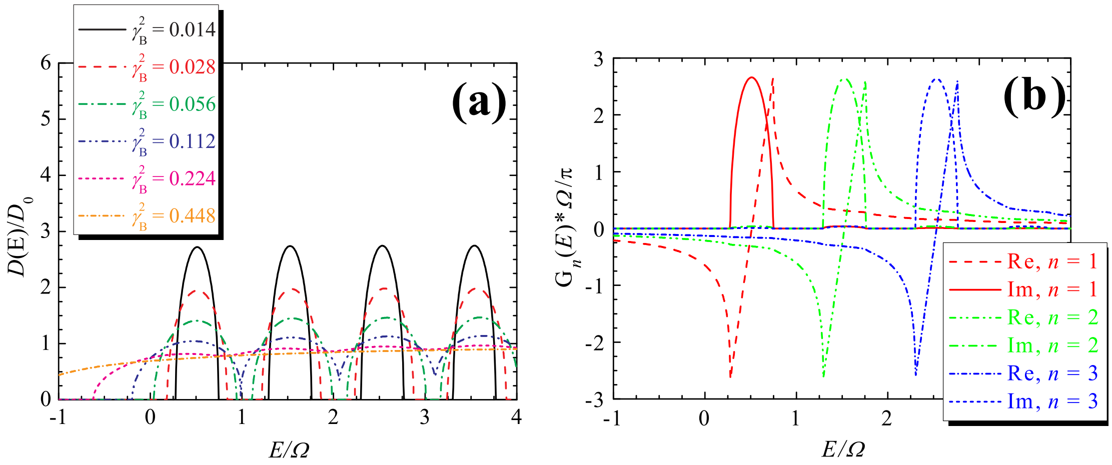

Figure 7.5: (a) DOS as the imaginary part of the self energy $\Sigma^-(E)$, determined for different values of the damping parameter γ_B^2. (b) Real and imaginary parts of the Green's function $G_n^-(E)$ for the first three LL's. The value of the damping parameter used in this calculation is $\gamma_B^2 = 0.014$.

Figure 7.5 (a) shows the determined density of states for different damping parameters γ_B^2. It shows also that at small damping parameter $\gamma_B^2 = 0.014$ the DOS shows high maxima and well separated LL's. By increasing the damping ($\gamma_B^2 = 0.028 - 0.056$), corresponding to lowering the mobility, the DOS starts to decrease in amplitude and the gap between LL's reduces. Increasing further the damping ($\gamma_B^2 = 0.112 - 0.224$), the LL's overlap and the gap between them vanishes. At even higher damping ($\gamma_B^2 = 0.448$) the DOS shows a nearly constant values without any quantum oscillations.
With the known self-energy the Green's function is deduced. The imaginary part of the Green's function is important since it defines the spectral function [54]:

$$A_n(E) = \frac{1}{\pi} \cdot \Im G_n^-(E) = \frac{1}{2\pi i} \cdot \left[G_n^-(E) - G_n^+(E)\right] . \tag{7.38}$$

Figure 7.5 (b) shows the spectral function for a fixed damping factor and for the first three LL's. It shows also that at each LL there are side peaks of the other LL, because the self-energy is independent of the quantum number n. However, at small damping these contributions are small.
To study the transport imposed by the laser, the laser-frequency-dependent *AC* conductivity $\sigma(\omega)$ has to be calculated. Within the SCBA, the Kubo formula of the *AC* conductivity [138] becomes simpler. Because of considering short-range scatterers, the vertex functions become small and negligible. The final form of the *AC* longitudinal conductivity $\sigma_1(\omega)$ is [54]:

$$\sigma_1(\omega) = \sigma_{xx}(\omega) = \sigma_{yy}(\omega) = \frac{1}{\omega} \cdot [\chi_1(\omega) - \chi_1(\omega = 0)] , \tag{7.39}$$

with the longitudinal susceptibility at finite laser frequency

$$\begin{aligned}\chi_{\mathrm{l}}(\omega) &= i \cdot \frac{e^2 g_s \omega_{\mathrm{c}}^2}{4\pi} \cdot \int_{-\infty}^{+\infty} dE \cdot f(E;\mu_{\mathrm{ch}},T) \\ &\cdot \sum_{n=0}^{+\infty} A_n(E)\cdot(n+1)\cdot\left[G_{n+1}^{+}(E+\hbar\omega)+G_{n+1}^{-}(E-\hbar\omega)\right] \\ &+ A_n(E)\cdot n\cdot\left[G_{n-1}^{+}(E+\hbar\omega)+G_{n-1}^{-}(E-\hbar\omega)\right] \qquad (7.40)\end{aligned}$$

and the longitudinal susceptibility at zero laser frequency

$$\begin{aligned}\chi_{\mathrm{l}}(\omega=0) &= i \cdot \frac{e^2 g_s \omega_{\mathrm{c}}^2}{4\pi} \cdot \int_{-\infty}^{+\infty} dE \cdot f(E;\mu_{\mathrm{ch}},T) \\ &\cdot \sum_{n=0}^{+\infty} A_n(E)\cdot(n+1)\cdot\left[G_{n+1}^{+}(E)+G_{n+1}^{-}(E)\right] \\ &+ A_n(E)\cdot n\cdot\left[G_{n-1}^{+}(E)+G_{n-1}^{-}(E)\right] \qquad (7.41)\end{aligned}$$

The *AC* Hall conductivity is obtained in a similar way

$$\sigma_{\mathrm{H}}(\omega) = -\sigma_{\mathrm{xy}}(\omega) = \sigma_{\mathrm{yx}}(\omega) = \frac{1}{\omega}\cdot\left[\chi_{\mathrm{H}}(\omega)-\chi_{\mathrm{H}}(\omega=0)\right]\,, \qquad (7.42)$$

with the longitudinal susceptibility at finite laser frequency

$$\begin{aligned}\chi_{\mathrm{H}}(\omega) &= \frac{e^2 g_s \omega_{\mathrm{c}}^2}{4\pi} \cdot \int_{-\infty}^{+\infty} dE \cdot f(E;\mu_{\mathrm{ch}},T) \\ &\cdot \sum_{n=0}^{+\infty} A_n(E)\cdot n\cdot\left[G_{n-1}^{+}(E+\hbar\omega)-G_{n-1}^{-}(E-\hbar\omega)\right] \\ &- A_n(E)\cdot(n+1)\cdot\left[G_{n+1}^{+}(E+\hbar\omega)-G_{n+1}^{-}(E-\hbar\omega)\right] \qquad (7.43)\end{aligned}$$

and the longitudinal susceptibility at zero laser frequency

$$\begin{aligned}\chi_{\mathrm{H}}(\omega=0) &= \frac{e^2 g_s \omega_{\mathrm{c}}^2}{4\pi} \cdot \int_{-\infty}^{+\infty} dE \cdot f(E;\mu_{\mathrm{ch}},T) \\ &\cdot \sum_{n=0}^{+\infty} A_n(E)\cdot n\cdot\left[G_{n-1}^{+}(E)-G_{n-1}^{-}(E)\right] \\ &- A_n(E)\cdot(n+1)\cdot\left[G_{n+1}^{+}(E)-G_{n+1}^{-}(E)\right] = 0 \qquad (7.44)\end{aligned}$$

where $g_s = 2$ is the degeneracy factor and $f(E;\mu_{\mathrm{ch}},T) = (\exp\left[(E-\mu_{\mathrm{ch}})/k_{\mathrm{B}}T\right]+1)^{-1}$ is the *Fermi-Dirac distribution function*[9] at a finite temperature T.

---

[9] The Fermi-Dirac distribution function was introduced in 1926 by Enrico Fermi and Paul Dirac but in fact this function was developed earlier by the German physicist Pascual Jordan in 1925 who called it *Pauli statistics*. The Fermi-Dirac function applies to fermions (spin $1/2, 3/2$), that obey the Pauli exclusion principle.

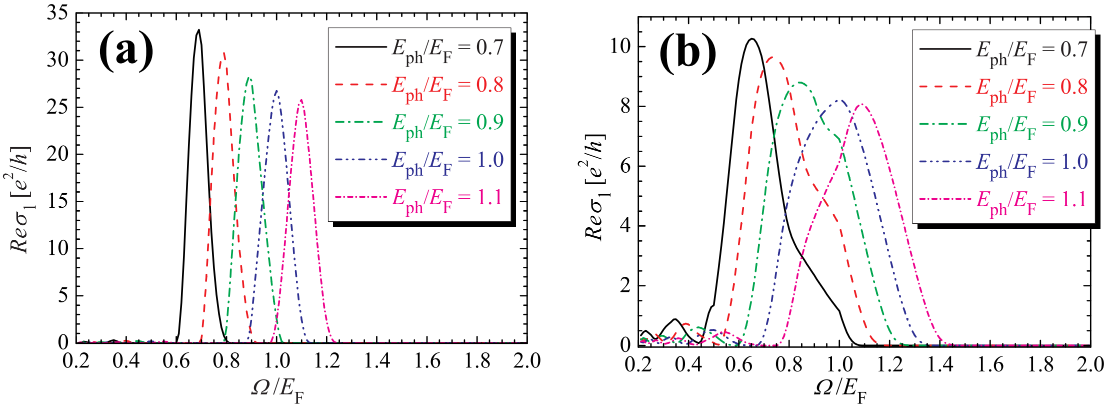

Figure 7.6: The real part of the *AC* longitudinal conductivity $\Re\sigma_1(\omega)$ as a function of the cyclotron energy Ω/E_F at various photon energies $E_\mathrm{ph}/E_\mathrm{F}$. The *AC* conductivity is calculated for a temperature corresponding to $k_\mathrm{B}T/E_\mathrm{F} = 0.02$ and for a damping parameter $\gamma_\mathrm{B}^2 = 0.001$ (a) and $\gamma_\mathrm{B}^2 = 0.01$ (b).

Calculated using SCBA, which in contrast to the Drude approximation describes correctly the quantum SdH-oscillations of the *DC* conductivity, the high-frequency (THz) conductivity shows structures mostly along the CR line. These structures (quantum oscillations) are due to the Landau quantization at high magnetic fields which quantizes the motion of the electrons in the 2DES plane. The *AC* conductivity is calculated at different damping parameters γ_B^2 (related to the mobility), different temperatures T (through the Fermi-Dirac function) and different photon energies $E_\mathrm{ph} = \hbar\omega$.

In the following we concentrate only on the real part of the *AC* longitudinal and the imaginary part of the *AC* Hall conductivities since these parts contribute to the transmission coefficient and absorption peaks. The behavior of the *AC* longitudinal conductivity depends on the damping because the damping influences the broadening Γ of the LL. With increasing the damping the broadening increases. At the same time the gap between adjacent LL's reduces. Therefore, in the case of the short-range scatterers, the broadening induces a strong dependence of the line shape of the *AC* conductivity on the position of the Fermi level (FL). By sweeping the magnetic field B, at constant electron density n_s, the FL passes through different LL successively. When the FL lies between two adjacent LL's, at the integer filling factor $\nu = 2$ ($\nu = 2E_\mathrm{F}/\Omega$), the line shape of the *AC* longitudinal conductivity is symmetric. If the FL lies within a LL, the line shape of the *AC* conductivity becomes asymmetric. The asymmetry is stronger on the high-B side of the *AC* conductivity (with a dip at $\omega_\mathrm{c} > \omega$). This asymmetry of the *AC* conductivity is due to the increasing broadening of the LL with the magnetic field ($\Gamma \propto \sqrt{B}$) [47, 121]. Thus, the asymmetry is stronger at higher damping parameters (see fig. 7.6 (b)). However, for $\gamma_\mathrm{B}^2 = 0.001$, corresponding to a sample of about $\mu_\mathrm{el} = 1.6 \times 10^6 \mathrm{cm}^2\mathrm{V}^{-1}\mathrm{s}^{-1}$ and

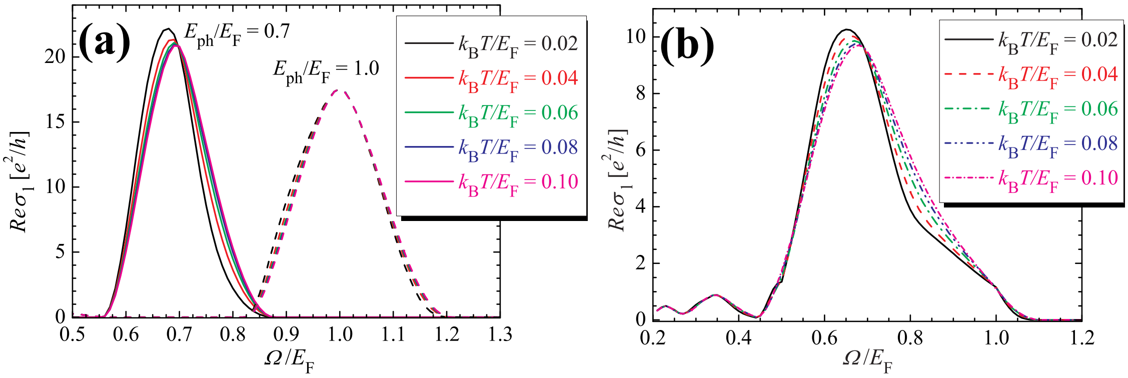

Figure 7.7: (a) The real part of the *AC* longitudinal conductivity $\Re\sigma_1(\omega)$ as a function of the cyclotron energy Ω/E_F at two photon energies E_{ph}/E_F. The *AC* conductivity is calculated for a temperature corresponding to $k_BT/E_F = 0.02$ and for a damping parameter $\gamma_B^2 = 0.001$. (b) As (a) but for $E_{ph}/E_F = 0.7$ and $\gamma_B^2 = 0.01$.

$n_s = 2 \times 10^{11}\text{cm}^{-2}$, the *AC* conductivity shows a very week asymmetry (see fig. 7.6 (b)).

At very high photon frequencies the quantum effects are smeared out. The temperature dependence of the longitudinal *AC* conductivity shows that the elevated temperature wash out this asymmetry, and the line shape becomes more symmetric (see fig. 7.7). When the laser is off ($\omega = 0$) the *AC* conductivity turns into the *DC* conductivity which shows the well-known SdH oscillations of the longitudinal conductivity going to zero or to small values at even integer filling factors (depending also on the temperature). The small oscillations at low magnetic fields of the *AC* longitudinal and Hall conductivities are due to the coupling of different LL's due to the scatterers. Thus, the shape of the spectral function of each LL gives contributions at the position of other LL's (see fig. 7.5 (b)). This gives rise to the subharmonic structure at $\Omega/E_F = 1/2, 1/3, \ldots$ in the 2DES (see fig. 7.8).
As we have already calculated the *AC* conductivity, we can also determine the transmission coefficient T (see eq. 7.19) and the power absorption W (see eq. 7.21). The calculated transmission coefficient and the power absorption are shown in fig. 7.9. The calculations reveal a strong signal along the CR line with quantum structures due to the Landau quantization, observed already in the *AC* conductivity behavior. When the incident THz radiation is absorbed by the 2DES, the equilibrium configuration of the electrons changes. This change concerns the rearrange of the electrons within the same LL, giving an oscillating distribution function [133, 134], or moves the electrons to the upper LL. The oscillating distribution function has not been included in the present work. Another effect of the THz absorption by the 2DES is the heating which increases the electron temperature T_{el} relative to the lattice (the bolometric effect), and reflects in the change of

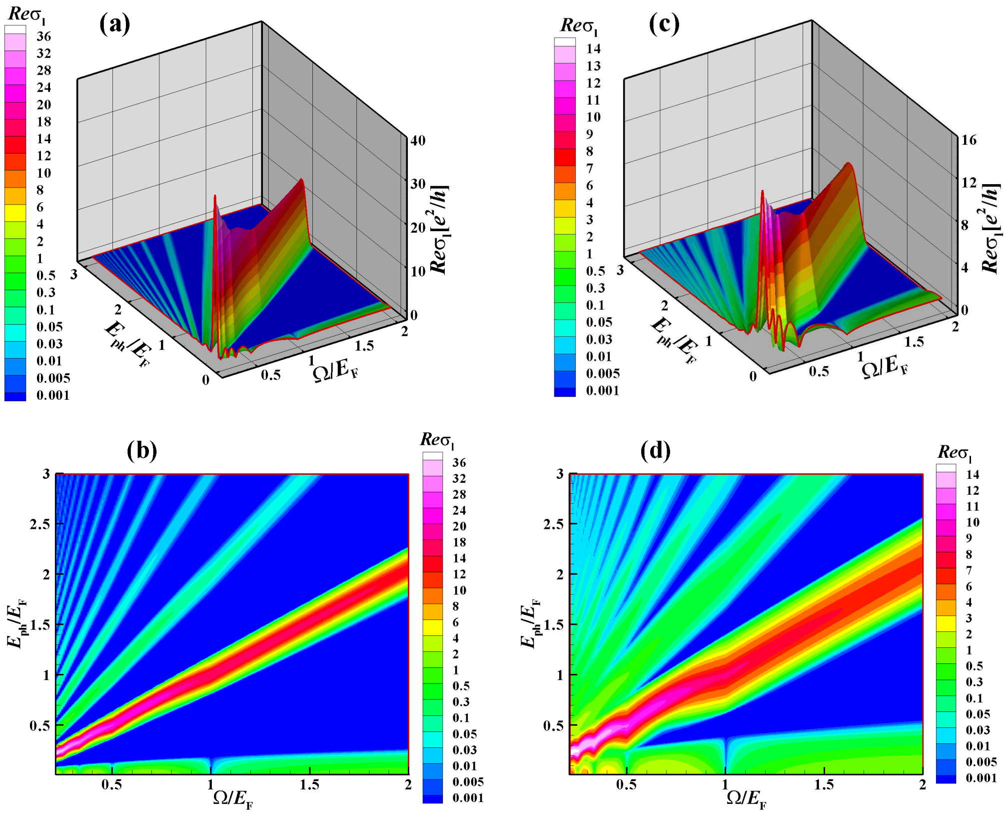

Figure 7.8: (a) and (b) The real part of the *AC* longitudinal conductivity $\Re\sigma_l(\omega)$, as a function of the cyclotron energy Ω/E_F and photon energy E_{ph}/E_F, is calculated for a temperature corresponding to $k_BT/E_F = 0.02$ and a damping parameter $\gamma_B^2 = 0.0023$. (c) and (d) As (a) and (b), respectively, but for $\gamma_B^2 = 0.01$.

the photoresponse (PR). The absorption of the THz by 2DES alters the equilibrium properties of the 2DES, like: the chemical potential μ_{ch}, the thermodynamic density of states (TDOS), the specific heat c_v and the *DC* longitudinal σ_l and Hall σ_H conductivities. A very sensitive equilibrium quantity is the specific heat. The investigation of this quantity could give interesting information about the bolometric response of the 2DES. In fact, the specific heat relates directly the change of the internal energy and the change of the electron temperature due to the Joule heating imposed by the THz radiation.

We have already observed that the DOS is very important in studying the electron properties of the 2DOS. Therefore, to describe the equilibrium properties (electron density, TDOS, specific heat) the DOS is used again. The electron density n_s could be defined as the sum of all filled eigenstates characterized by the eigenvalues $E(\vec{k})$ (see eq. 2.8) and the eigenfunctions $\Phi_{\vec{k}}(\vec{r}) = 1/\sqrt{L_xL_y}\exp(i\vec{k}\cdot\vec{r})$ (see eq. 2.6) according to the

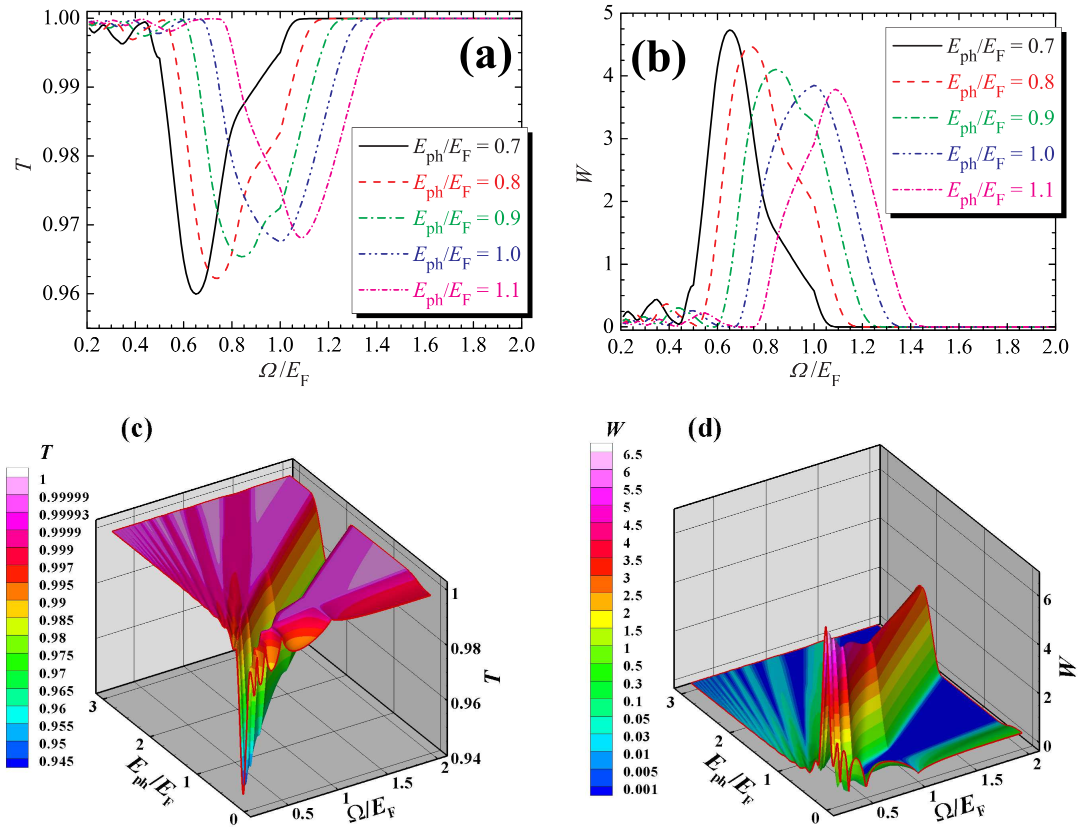

Figure 7.9: (a) Transmission coefficient T (a) and power absorption W (b) as function of the cyclotron energy Ω/E_{F} calculated for several photon energies $E_{\mathrm{ph}}/E_{\mathrm{F}}$ at $k_{\mathrm{B}}T/E_{\mathrm{F}} = 0.02$ and $\gamma_{\mathrm{B}}^2 = 0.01$. (c) and (d) show 3D plots of (a) and (b), respectively. The transmission coefficient T is defined by eq. 7.19 and the power absorption is plotted with the normalization introduced in eq. 7.21.

Fermi-Dirac distribution function $f(E;\mu_{\mathrm{ch}},T)$ [54]

$$n_{\mathrm{s}}(\vec{r}) = g_s \cdot \sum_{\vec{k}} f\left(E(\vec{k});\mu_{\mathrm{ch}},T\right) \cdot |\Phi_{\vec{\mathrm{k}}}(\vec{r})|^2 = \int dE \cdot f(E;\mu_{\mathrm{ch}},T) \cdot D(E)\,. \qquad (7.45)$$

Since, usually in the optically induced breakdown measurements [115–119], the electron density is kept constant, therefore the chemical potential μ_{ch} is calculated. By increasing the magnetic field $B \propto \omega_{\mathrm{c}}$, the chemical potential μ_{ch} follows the energy within one LL until the respective LL becomes depleted at an integer filling factor ν. Then, μ_{ch} jumps downward to the next LL. In the *zero temperature limit*, the chemical potential has an abrupt jump to the next LL but at finite temperature (also by the collision broadening), this jump is rounded off (see fig. 7.10).

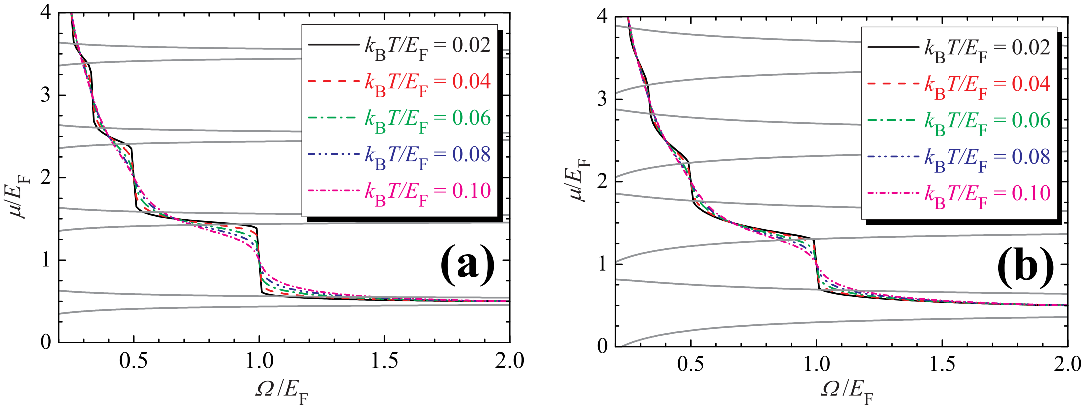

Figure 7.10: The chemical potential $\mu_{\mathrm{ch}}/E_{\mathrm{F}}$, as a function of the cyclotron energy Ω/E_{F}, is calculated for different values of $k_{\mathrm{B}}T/E_{\mathrm{F}}$ and for a damping parameter $\gamma_{\mathrm{B}}^2 = 0.001$ (a) and $\gamma_{\mathrm{B}}^2 = 0.01$ (b). The gray lines represent the edges of the LL's.

Another important equilibrium quantity that characterize the 2DES is the thermodynamic density of states TDOS. TDOS at finite magnetic field is given by

$$\begin{aligned} D_{\mathrm{T}}(\mu_{\mathrm{ch}}, T, B) &= \frac{dn_{\mathrm{s}}}{d\mu_{\mathrm{ch}}} = -\int_{-\infty}^{+\infty} dE \cdot \frac{df(E;\mu_{\mathrm{ch}},T)}{dE} \cdot D(E,B) \qquad (7.46) \\ &= \frac{1}{k_{\mathrm{B}}T} \cdot \int_{-\infty}^{+\infty} dE \cdot f(E;\mu_{\mathrm{ch}},T)[1 - f(E;\mu_{\mathrm{ch}},T)] \cdot D(E,B)\,, \end{aligned}$$

where $D(E,B)$ is the DOS at finite temperature and finite magnetic field (see eq. 7.37). Figure 7.11 shows the effect of the temperature on the TDOS for two damping parameters corresponding to low- and high-mobility sample. The DOS and TDOS show as functions of the magnetic field an oscillating behavior due to the Landau quantization. Thus, the DOS and TDOS develops deep minima (toward zero), like the SdH-oscillations, at values of B for which the filling factor ν takes even values ($\nu = 2i$, with i an integer number). However, by increasing the temperature, the minima of the TDOS are finite and at high enough temperature the oscillations are strongly reduced. The effect of the broadening is also observed. At low damping the broadening is small and there is a large gap between two-adjacent LL's. On the other hand, at high damping the broadening is large and the gap between LL's is small (see fig. 7.10). Therefore, an increase of temperature affects stronger in the case of low-damping than the case of high-damping (see fig. 7.11). Just to give some idea about the magnitude of temperatures, for the *GaAs* we have for $m^* = 0.067 \times m_{\mathrm{e}}$ with $m_{\mathrm{e}} = 9.11 \times 10^{-31}\mathrm{kg}$ the mass of electron and $n_{\mathrm{s}} = 2 \times 10^{11}\mathrm{cm}^{-2}$ we obtain the DOS $D_0 = m^*/\pi\hbar^2 = 2.8 \times 10^{10}\mathrm{cm}^{-2}\mathrm{meV}^{-1}$, the Fermi energy $E_{\mathrm{F}}^0 = n_{\mathrm{s}}/D_0 = 7.2\mathrm{meV}$. The ratio $k_{\mathrm{B}}T/E_{\mathrm{F}}^0 = 0.02$ corresponds the temperature $T = 1.7\mathrm{K}$. For

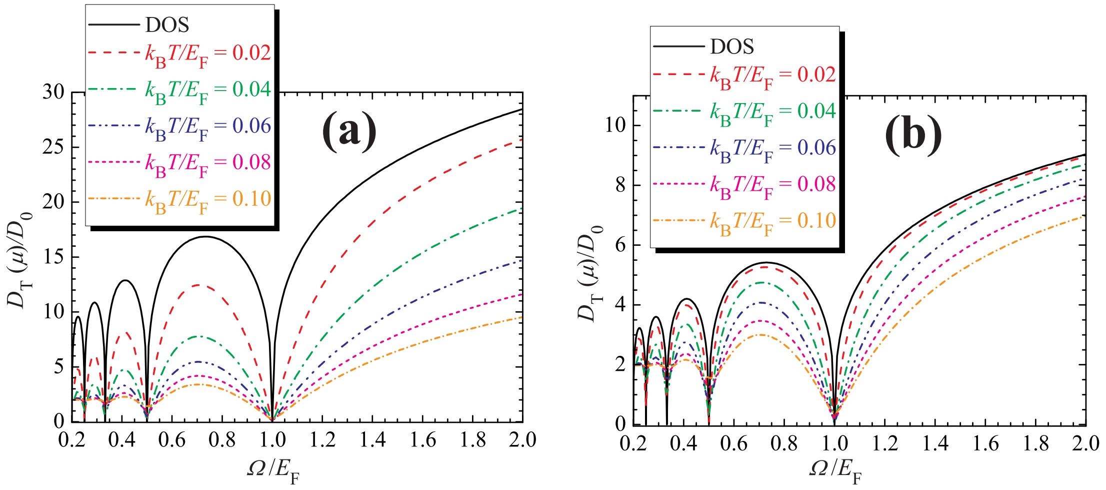

Figure 7.11: The DOS and TDOS, as a function of the cyclotron energy Ω/E_{F}, are calculated for different values of $k_{\mathrm{B}}T/E_{\mathrm{F}}$ and for a damping parameter $\gamma_{\mathrm{B}}^2 = 0.001$ (a) and $\gamma_{\mathrm{B}}^2 = 0.01$ (b).

$n_{\mathrm{s}} = 2.7\times10^{11}\mathrm{cm}^{-2}$ the Fermi energy is $E_{\mathrm{F}}^0 = n_{\mathrm{s}}/D_0 = 9.7\mathrm{meV}$ and for $k_{\mathrm{B}}T/E_{\mathrm{F}}^0 = 0.02$ corresponds the temperature $T = 2.3\mathrm{K}$.

As mentioned previously, the specific heat can give hints about the bolometric effect. This is because the specific heat of the 2DES might be defined as the rate of change of the electron temperature due to the heating of 2DES imposed by the THz radiation. The heat will change the internal energy density of the 2DES [54]

$$u(\mu_{\mathrm{ch}}, T, B) = \frac{U(\mu_{\mathrm{ch}}, T, B)}{A} = \int_{-\infty}^{+\infty} dE \cdot E \cdot f(E;\mu_{\mathrm{ch}}, T) \cdot D(E)\,, \tag{7.47}$$

where U is the internal energy and A is the unit area. Therefore, the specific heat at constant electron density n_{s} is given by

$$\begin{aligned} c_{\mathrm{v}} &= \left(\frac{\partial u}{\partial T}\right)_{n_{\mathrm{s}}=\mathrm{const.}} = \int_{-\infty}^{+\infty} dE \cdot E \cdot \left[\frac{\partial f(E;\mu_{\mathrm{ch}}, T)}{\partial T}\right]_{n_{\mathrm{s}}=\mathrm{const.}} \cdot D(E) \\ &= k_{\mathrm{B}}^2 \cdot T \cdot D_0 \left(L_2 - \frac{L_1^2}{L_0}\right)\,, \end{aligned} \tag{7.48}$$

with $L_m = \int_{-\infty}^{+\infty} dx \cdot [x^m/4\cosh^2(x/2)] \cdot [D(\mu_{\mathrm{ch}} + x \cdot k_{\mathrm{B}}T)/D_0]$ dimensionless coefficients [139, 140], $f(x) = [\exp(x)+1]^{-1}$ the Fermi-Dirac distribution function and $f'(x) = -f(x)[1-f(x)] = -[4\cosh^2(x/2)]^{-1}$. The following fig. 7.12 shows the calculated specific heat c_{v} as a function of the magnetic field B at different temperatures. These figures show a complicated structure of c_{v} near the integer filling factor. If $k_{\mathrm{B}}T << \hbar\omega_{\mathrm{c}}$, then no thermal excitation between two-adjacent LL's is possible, c_{v} has a small minimum

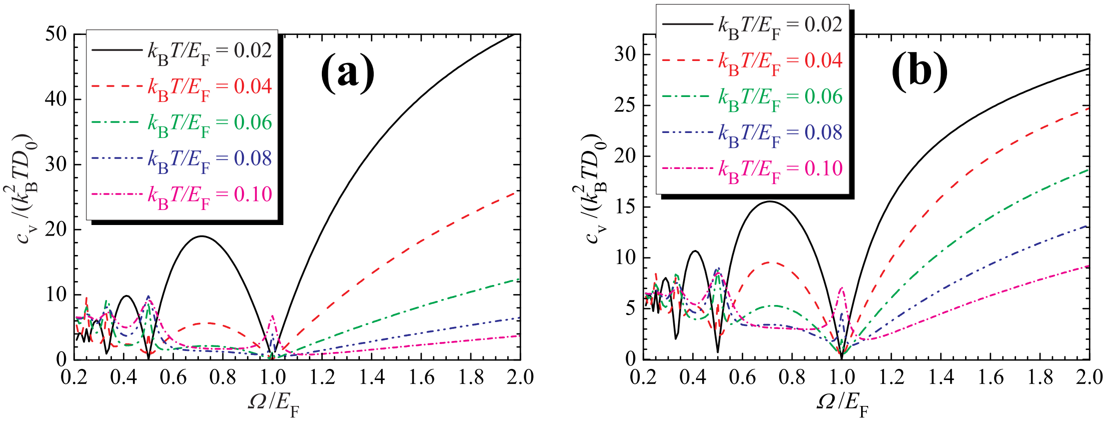

Figure 7.12: (a) The specific heat c_v, as a function of the cyclotron energy Ω/E_F, is calculated for different values of $k_\mathrm{B}T/E_\mathrm{F}$ and for a damping parameter $\gamma_\mathrm{B}^2 = 0.0023$ (a) and $\gamma_\mathrm{B}^2 = 0.01$ (b).

at the filling factor of the corresponding Landau gap. For this regime, an intra-LL contribution (due to excitation of electrons within one LL) to the specific heat is present. With increasing temperature, excitation between two-adjacent LL's becomes possible, and a narrow peak of c_v occurs in the center of the Landau gap, which increases with increasing T, and finally becomes dominant. This regime is characterized by the inter-LL contributions to the specific heat. At higher temperature (or for given T at higher LL) the specific heat c_v is dominated by the inter-LL excitations and not by the intra-LL excitations. However, at very high magnetic fields only the lowest LL is occupied. Therefore, the intra-LL level excitation dominates the specific heat. The transition from minima of c_v at low integer values of the filling factor to maxima at high filling factors has been observed in the measurements of the magnetic field dependent specific heat by Gornik *et al.* [141, 142]. The authors also observed that the sample temperature was higher for integer filling factors than for values in between, which reflects the variation of the electronic specific heat. The same trend was predicted by Zawadzki *et al.* [139, 140]. Because the specific heat is already determined, we can in principle find the change of the electron temperature due to the change of internal energy induced by the interaction between the THz radiation and the 2DES. The change of the internal energy can be described by the product between the power absorption (see eq. 7.21) and the duration of the pulse laser $t_\mathrm{p}^\mathrm{laser}$ which in the experiments was about $1\mu\mathrm{s}$. Therefore, the change of the electron temperature could be determined from

$$\Delta T = \frac{\Delta u}{c_\mathrm{v}} \propto \frac{W}{c_\mathrm{v}}, \tag{7.49}$$

and including eq. 7.21 and eq. 7.48 for the power absorption and the specific heat,

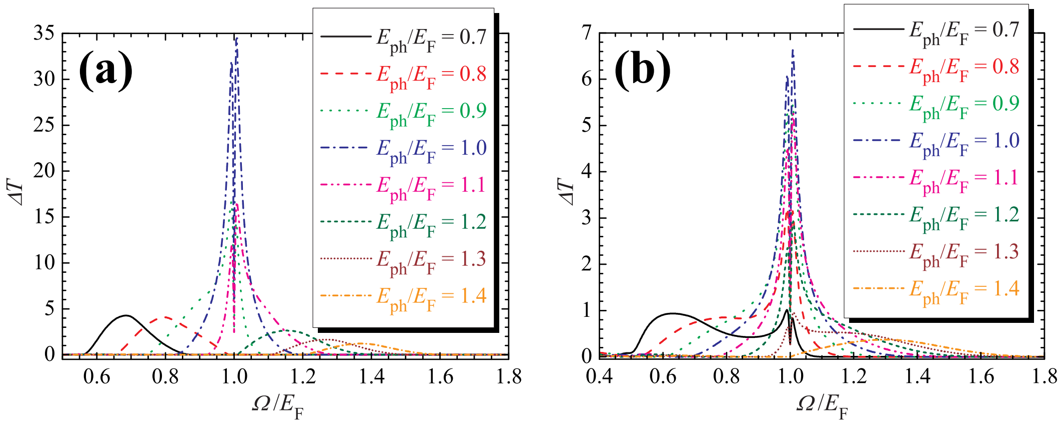

Figure 7.13: (a) The change of the electron temperature ΔT, as a function of the cyclotron energy Ω/E_{F}, is calculated for different photon energies $E_{\mathrm{ph}}/E_{\mathrm{F}}$ and for a temperature corresponding to $k_{\mathrm{B}}T/E_{\mathrm{F}} = 0.06$. The damping parameter is $\gamma_{\mathrm{B}}^2 = 0.0023$ (a) and $\gamma_{\mathrm{B}}^2 = 0.01$ (b). The change of electron temperature ΔT is plotted with the normalization introduced in eq. 7.50.

respectively, the change of the electron temperature is determined from

$$\Delta T \propto \frac{h}{e^2} \cdot \frac{W}{|E_{\mathrm{x}}^{\mathrm{e}}|^2} \cdot \frac{k_{\mathrm{B}}^2 \cdot T \cdot D_0}{c_{\mathrm{v}}} \,. \tag{7.50}$$

The numerical results of the change of electron temperature ΔT show for a certain temperature range, which depends on the level broadening, an interesting double peak structure. This double peak structure is observed around the even integer filling factors, as in the experiments (see Fig. 7.13 and Fig. 7.14). These peaks appear sharp, for a certain range of temperatures (lower temperatures), since for those temperatures the TDOS goes to zero at even integer filling factors. As the temperature increases further the nature of quantum oscillations of the specific heat c_{v} changes from looking like the TDOS, with minima at even integer filling factors, to anti-phase oscillations with maxima at these filling factors [139–142]. This behavior of the specific heat c_{v} affects also the change of the electron temperature ΔT. At a certain temperature the oscillations are washed out completely. We can also observe that by changing the photon energy, the function $\Delta T(\nu)$ shows a transition from single peak to a double peak structure by approaching the integer filling factor $\nu = 2 \Leftrightarrow \Omega/E_{\mathrm{F}} = 1$ [143, 144]. Due to the power absorption, the *DC* conductivity is changed and from a certain temperature range the minima of the SdH-oscillations of the *DC* longitudinal conductivity are finite and the plateaus of the vanishing longitudinal conductivity shrink. Therefore, the change of the electron temperature induced by the THz radiation alters the *DC* longitudinal and Hall conductivities. As already seen in fig. 7.8, for $\omega = 0$ the *AC* longitudinal $\sigma_{\mathrm{l}}(\omega)$ and Hall $\sigma_{\mathrm{H}}(\omega)$ conductivities turned into the *DC* longitudinal σ_{l} and Hall σ_{H} conductivities. The *DC* longitudinal

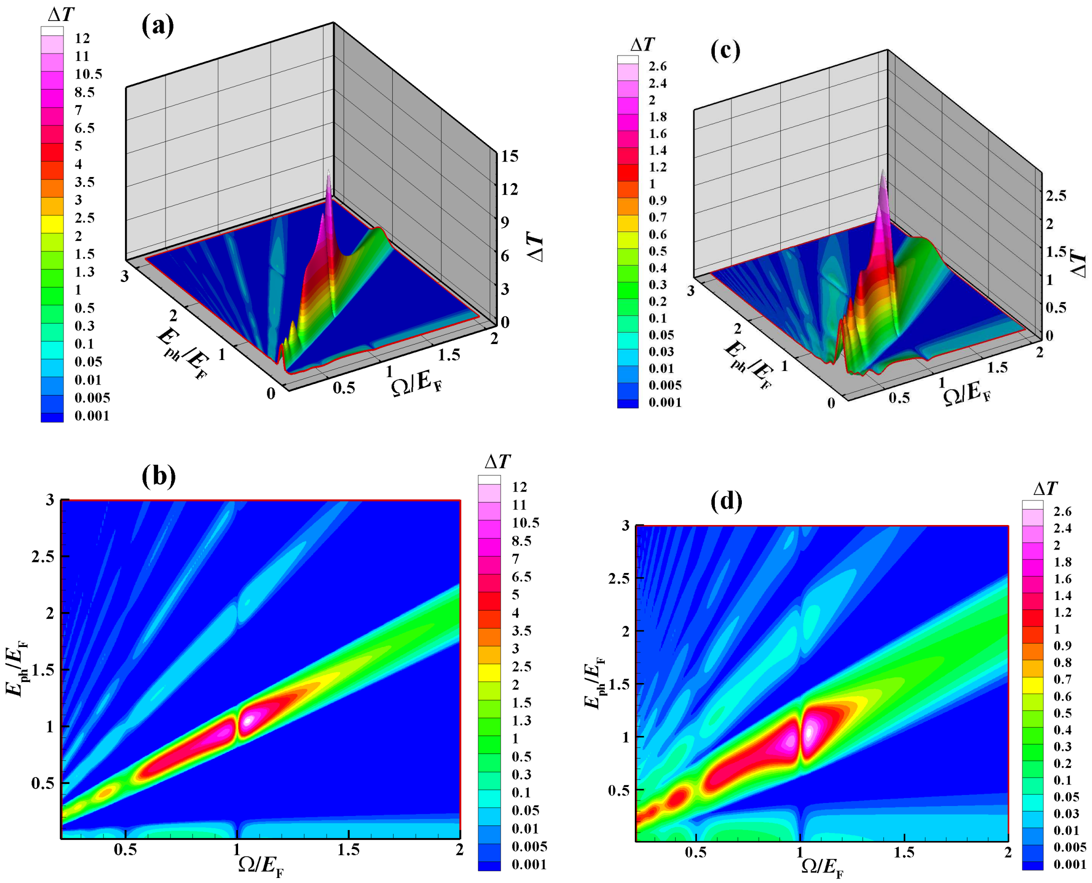

Figure 7.14: The change of the electron temperature ΔT, as a function of the cyclotron Ω/E_F and the photon $E_\mathrm{ph}/E_\mathrm{F}$ energies, is calculated for a temperature corresponding to $k_\mathrm{B}T/E_\mathrm{F} = 0.08$ and a damping parameter $\gamma_\mathrm{B}^2 = 0.0023$ (a) and $\gamma_\mathrm{B}^2 = 0.01$ (c). (b) and (d) show 2D plots of (a) and (c), respectively. The change of electron temperature ΔT is plotted with the normalization introduced in eq. 7.50.

conductivity σ_l is calculated according to [54]

$$\begin{aligned}
\sigma_\mathrm{l} &= -\frac{e^2}{m^*} \cdot \int_{-\infty}^{+\infty} dE \cdot \left[\frac{df(E;\mu_\mathrm{ch},T)}{dE}\right] \cdot \frac{\tau(E)\cdot\tilde{n}(E)}{1+[\omega_\mathrm{c}\cdot\tau(E)]^2} \\
&= \frac{e^2}{h} \cdot \frac{1}{k_\mathrm{B}T} \cdot \int_{-\infty}^{+\infty} dE \cdot f(E;\mu_\mathrm{ch},T)[1-f(E;\mu_\mathrm{ch},T)] \cdot \frac{\Gamma(E)/\hbar\omega_\mathrm{c}}{1+[\Gamma(E)/\hbar\omega_\mathrm{c}]^2} \\
&\cdot \left[\frac{E-\Delta(E)}{\hbar\omega_\mathrm{c}} + \gamma_\mathrm{B}^2\right] \cdot \frac{D(E,B)}{D_0} \qquad (7.51)
\end{aligned}$$

and the *DC* Hall conductivity σ_{H} is calculated according to [54]

$$\begin{aligned}\sigma_{\mathrm{H}} &= \nu - \frac{e^2}{h}\cdot\frac{1}{k_{\mathrm{B}}T}\cdot\int_{-\infty}^{+\infty} dE\cdot f(E;\mu_{\mathrm{ch}},T)[1-f(E;\mu_{\mathrm{ch}},T)]\cdot\frac{[\Gamma(E)/\hbar\omega_{\mathrm{c}}]^2}{1+[\Gamma(E)/\hbar\omega_{\mathrm{c}}]^2}\\ &\cdot \left[\frac{E-\Delta(E)}{\hbar\omega_{\mathrm{c}}}+\gamma_{\mathrm{B}}^2\right]\cdot\frac{D(E,B)}{D_0} \qquad (7.52)\end{aligned}$$

with $\tilde{n}(E) = [E-\Delta(E)]D(E) + D_0\Gamma(E)/2\pi$, $\tau(E) = \hbar/\Gamma(E)$ is the quantum relaxation time, $\Gamma(E)$ and $\Delta(E)$ are the real and imaginary parts of the self-energy $\Sigma^{\pm}(E) = \Delta(E) \mp (i/2)\Gamma(E)$. Figure 7.15 shows the calculated *DC* longitudinal σ_{l} and Hall σ_{H} conductivities as a function of the magnetic field B. At low temperatures, the longitudinal conductivity shows deep minima toward zero at magnetic fields for which the filling factor is integer. By increasing the temperature the SdH-oscillations of the longitudinal conductivity reduce in amplitude, and for high enough temperature the quantum effects vanish. The Hall conductivity shows a garland-like structure with deep minima at low temperature and magnetic fields corresponding to integer filling factor. By increasing the temperature, the garland-like structure reduces its magnitude, whereas at high temperatures it approaches the linear free-electron Hall conductivity.

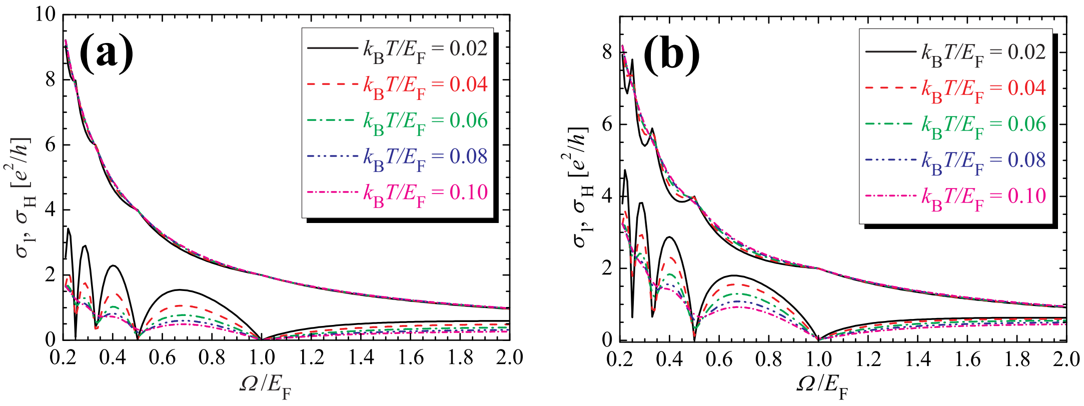

Figure 7.15: (a) *DC* longitudinal σ_{l} and Hall σ_{H} conductivities, as a function of the cyclotron energy Ω/E_{F}, are calculated for different values of $k_{\mathrm{B}}T/E_{\mathrm{F}}$ and for a damping parameter $\gamma_{\mathrm{B}}^2 = 0.0023$ (a) and $\gamma_{\mathrm{B}}^2 = 0.01$ (b).

7.4 Conclusions

To summarize, in this chapter we have described the interaction of the perpendicular incident THz radiation with the 2DES. The magnetic field applied perpendicular to the 2DES

couples the two components of the in-plane current density, and therefore the two field components (in this plane). For perpendicular incidence, the electric field of the THz radiation has no component perpendicular to the plane of the 2DES. We have started from Maxwell's equations and the boundary conditions at the 2DES plane and we ended up with a matrix equation which allows us to find the in-plane components of the transmitted field. Further, we have calculated the transmission coefficient T (defined in terms of the incident and transmitted fields) and the photocurrent absorption W as the average power dissipation induced by the current density as a result of the electric field application.
The calculations of transmission coefficient and the photocurrent absorption need the calculation of the dynamic (*AC*) longitudinal $\sigma_\mathrm{l}(\omega)$ and Hall $\sigma_\mathrm{H}(\omega)$ conductivities. The *AC* longitudinal and Hall conductivities are calculated applying the assumptions of the Drude and the self-consistent Born approximations. The Drude approximation assumes the scattering of electrons by a constant relaxation time, independent of the photon frequency and the magnetic field. Applying this approximation the *AC* conductivity reveals maxima without structure along the CR line. The CR line is the line calculated for the exact match between the cyclotron and the photon frequencies ($\omega = \omega_\mathrm{c}$). The SCBA considers that coherent scattering of an electron by more than one impurity is neglected, which results in half ellipses with sharp edges for the spectral function. Calculated under SCBA, which in contrast to the Drude approximation describes correctly the quantum SdH-oscillations of the *DC* conductivity, the high-frequency THz conductivity shows structures (quantum oscillations) mostly along the CR line due to the Landau quantization at high magnetic fields. However, at high photon frequencies the quantum effects are washed completely out. Since the transmission coefficient and the photocurrent absorption are proportional to the real part of the longitudinal and the imaginary part of the Hall conductivities [121, 136, 137], both reflect the quantum oscillations revealed by the *AC* longitudinal and Hall conductivities. One effect of the incidence of the THz radiation on the 2DES is the heating of the 2DES which leads to an increase of the electron temperature. To study the effect of the heating on the equilibrium properties of the 2DES, we calculated the chemical potential, the thermodynamic density of states, the specific heat and the *DC* conductivity as a function of the magnetic field at various temperatures. In principle all these equilibrium quantities show quantum oscillations due to the oscillating DOS that goes to zero at even filling factors. The specific heat shows transitions from minima of c_v at low integer values of the filling factor to maxima at high filling factors (also observed in the experiments by Gornik *et al.* [141, 142]). At high temperatures and low magnetic fields the inter-LL contributions on the specific heat are dominant while at low temperatures and high magnetic fields the intra-LL contributions are dominant. The authors also observed that the sample temperature was higher at magnetic field values corresponding to integer filling factors than for values in between, which reflects the variation of the electronic specific heat. This behavior was predicted by Zawadzki *et al.* [139, 140]. The calculation of the change of the electron temperature ΔT shows that the 2DES is sensitive to the THz radiation for certain range of temperatures at even integer filling factors. This sensitivity leads to a transition from a single to a double-peak structure of ΔT with the change of the photon energy, as observed in the experiments [115–119]. However, it

does not mean that this single- or double-peak structure of the change of the electron temperature at and near by the integer filling factor explains the experiments. A satisfactory explanation of the experiment [115–119] could be expected only by a quantitative model calculation. This quantitative model should explain why the CR signal, resulting from strong power absorption, uncritical specific heat and temperature-insensitive conductivity, and the BO signal, resulting from weak power absorption, peculiar B-dependence of the specific heat, and high temperature sensitivity of the conductivity, can lead to signals of comparable magnitude as observed in experiments. But this is far beyond the scope of this thesis. This quantitative model should include the oscillating Fermi distribution function, as an effect of the THz radiation, in the calculations of the *AC* conductivity and consequently in the calculation of the power absorption. Another ingredient might be the inclusion of the spin splitting which is important at high magnetic fields. The inclusion of the long-range potential fluctuation are important for wider samples; the experiments were done on sample with Hall bar (width $w = 200\mu\mathrm{m}$ and length $l = 300\mu\mathrm{m}$), meander (width $w = 100\mu\mathrm{m}$ and length of the meander path $l = 60\mathrm{mm}$) and Corbino (inner $r_1 = 500\mu\mathrm{m}$ and outer $r_2 = 1500\mu\mathrm{m}$ radii) geometries.

Chapter 8

Conclusions

In this thesis I present an experimental work concerning the real-time measurements of the electrical and optical excitation and relaxation of quantum Hall (QH) devices. Further, the thesis presents a theoretical work that proposes an explanation of the B-field dependent shape of the photoresponse (PR) around the QH plateau. The motivation of our real-time measurements was a deficiency of knowledge concerning the time evolution of electrical signals from QH samples as a response to individual electrical and optical excitation pulses.

To perform the real-time resolved measurements of the electrical and optical excitation and relaxation, we have used QH devices with Corbino geometry. The QH devices with Corbino geometry have been obtained from MBE grown *GaAs/AlGaAs* heterostructures with the electron density in the range of $1.9 \times 10^{11}\mathrm{cm}^{-2} \leq n_\mathrm{s} \leq 2.7 \times 10^{11}\mathrm{cm}^{-2}$ and different carrier mobilities $0.1 \times 10^6\mathrm{cm}^2/\mathrm{Vs} \leq \mu_\mathrm{el} \leq 1.6 \times 10^6\mathrm{cm}^2/\mathrm{Vs}$. After the preparation of the QH devices, these devices were placed on chip carriers and inserted in a magneto-cryostat system which provides temperatures down to $1.5\mathrm{K}$ and high magnetic fields up to $12\mathrm{T}$. However, during our measurements, we had not to exceed magnetic field values of $6\mathrm{T}$, due to the characteristic of our samples (the filling factor $\nu = 2$ is reached at about $5.6\mathrm{T}$ for the highest electron density).

The real-time measurements of the electrical excitation of the QH devices with Corbino geometry were performed by applying rectangular electrical pulses of constant pulse widths ($t_\mathrm{p} = 90\mathrm{ns}$ or $t_\mathrm{p} = 180\mathrm{ns}$, constant pulse period $T_\mathrm{p} = 300\mathrm{ns}$) to the sample, while the pulse amplitude is changed between $0.4\mathrm{V}$ and $1\mathrm{V}$ at fixed magnetic field B (filling factors around $\nu = 2$). During these electrical excitation measurements we have investigated the dependence of the excitation time (the time required by the electron system for the QH-breakdown) on the applied pulse amplitude A, on the perpendicular applied magnetic field B, on the electron mobility of the sample μ_el and on the lattice temperature T.

These investigations have shown that there is a direct relation between the excitation time and the applied pulse amplitude, electron mobility and magnetic field. The temperature dependence is week, possibly due to small contribution of the phonons at $T = 4\mathrm{K}$. We try to explain these dependences on the basis of a quasi-classical Drude model, a two-Landau levels model and a quasi-local transport model. However, the results of these approximations, could only describe satisfactorily the observations qualitatively.

The time scale of excitation ($3\mathrm{ns} \leq \tau_{\mathrm{exc}} \leq 30\mathrm{ns}$) determined with our real-time measurements of the electrical excitation agrees with an estimation given in a previous study [28] and agrees well with the results of the previous time-integrating measurements of the electrical excitation [35, 36, 44]. Due to the possibility to investigate the single pulse response of the sample our method gives a more conclusive insight into the electronic properties.

The real-time measurements of the optical excitation and relaxation of the QH devices with Corbino geometry were performed by applying to the sample rectangular electrical pulses of different pulse widths $1\mu\mathrm{s} \leq t_{\mathrm{p}}^{\mathrm{elec}} \leq 4\mu\mathrm{s}$ and a constant pulse period $T_{\mathrm{p}}^{\mathrm{elec}} = 1\mathrm{s}$, while the electrical pulse amplitude is changed $1\mathrm{V} \leq A_{\mathrm{p}}^{\mathrm{elec}} \leq 4\mathrm{V}$ at fixed magnetic field B (filling factors around $\nu = 2$). At the same time the QH devices were illuminated by THz radiation produced by a pulsed *p*-Ge laser (laser pulse widths $1\mu\mathrm{s} \leq t_{\mathrm{p}}^{\mathrm{laser}} \leq 4\mu\mathrm{s}$, constant laser pulse period $T_{\mathrm{p}}^{\mathrm{laser}} = 1\mathrm{s}$ and photon energy $7\mathrm{meV} \leq E_{\mathrm{photon}} \leq 10\mathrm{meV}$, corresponding $1.7\mathrm{THz} \leq f_{\mathrm{laser}} \leq 2.5\mathrm{THz}$).

The breakdown of the QHE starts only after a certain excitation time ($40\mathrm{ns} \leq \tau_{\mathrm{exc}} \leq 120\mathrm{ns},\ \tau_{\mathrm{exc}} << t_{\mathrm{p}}^{\mathrm{elec}},\ t_{\mathrm{p}}^{\mathrm{laser}}$), depending weekly on the applied electrical pulse amplitude $A_{\mathrm{p}}^{\mathrm{elec}}$, on the carrier mobility μ_{el} of the sample and on the strength of the perpendicular applied magnetic field B (filling factors around $\nu = 2$). This could be expected due to high rate of available photons to excite each electron in the 2DES. This high rate can principally drive the electron system into a saturation regime. However, this situation does not affect the relaxation of the electrons via inter-LL-scattering processes. The relaxation of electrons back to a QH state occurs only after a certain relaxation time ($30\mathrm{ns} \leq \tau_{\mathrm{rel}} \leq 170\mathrm{ns},\ \tau_{\mathrm{rel}} << t_{\mathrm{p}}^{\mathrm{elec}},\ t_{\mathrm{p}}^{\mathrm{laser}}$), depending on the applied electrical pulse amplitude $A_{\mathrm{p}}^{\mathrm{elec}}$, on the carrier mobility μ_{el} of the sample and on the strength of the perpendicular applied magnetic field B. The time scale of relaxation ($30\mathrm{ns} \leq \tau_{\mathrm{rel}} \leq 170\mathrm{ns}$) determined with our real-time measurements of the optical excitation and relaxation agrees well with the findings presented in a previous study [100]. We generally found shorter relaxation times than the excitation times for the corresponding values of the electrical pulse amplitudes. These findings agree well with the thermodynamical arguments given in Ref. [40]. However, we found that $\tau_{\mathrm{rel}} \leq \tau_{\mathrm{exc}}$ holds for the low- and medium- mobility samples. Further, $\tau_{\mathrm{rel}} \geq \tau_{\mathrm{exc}}$ holds for the high-mobility sample. We explain our results by a heating picture based on a two-Landau levels model.

The theoretical part of the thesis consists of the presentation of a two-Landau levels model and an electron heating model imposed by the THz radiation incident to the electron system. The two-Landau levels model [58] combines several ideas (the avalanche-like electron heating, the quasi-elastic-inter-Landau-level scattering (QUILLS) and the presence of the incompressible and compressible regions) in order to explain the space-resolved measurements [33]. To adapt the model to the experiments it is assumed that the Hall potential drops only across the incompressible strips, and that the effective width of the incompressible strips is much smaller than the geometrical width of the sample due to the random inhomogeneities in the sample. In another study the authors investigated the variation of the current density and of the Hall potential across a Hall sample [58]. Further, the authors found in agreement with the experiment [72] that the Hall potential effectively drops only across the incompressible strips, which have usually a width much smaller than the width of the sample. These findings provide an alternative justification of the investigated model. The model shows a qualitative agreement with the experimental observation, an avalanche-like excitation. The best agreement with the experiments has been obtained also considering equal excitation and relaxation times ($\widetilde{\tau} = \tau_{\mathrm{exc}}/\tau_{\mathrm{rel}} = 1$) and a circular shape of the compressible islands. These facts indicate that the basic ideas of this Landau levels model are correct.

The electron heating model describes the interaction between a THz radiation normal incident onto the plane of the electron system (2DES). We consider that the main effect of the THz radiation is the heating of the 2DES which leads to an increase of the electron temperature. The change of temperature affects the conductivity and therefore the photoresponse.

The first step to calculate the increase of temperature is to calculate the power absorption from the incident radiation. The power absorption W is defined as the average power dissipation induced by the current density as a result of the electric field. The numerical investigations are performed starting with the Drude approximation. Since the Drude model does not explain the quantum effects due to the Landau quantization, we further consider the Self-Consistent Born Approximation (SCBA). The SCBA includes these effects and describes correctly the quantum SdH-oscillations of the *DC* conductivity. It shows that the incident radiation is most effective under cyclotron resonance conditions, and it is by order of magnitude smaller far away from the resonance (at least if the damping is small). The second step is to convert the absorbed power into a temperature increase. This is achieved by calculating the specific heat, which shows some interesting peculiarities, e.g., a kind of double-peak structure near integer filling factor due to the inter-LL excitations [139,140]. Finally, the temperature dependence of the longitudinal conductivity is considered since the increase of temperature washes out the zero SdH-oscillations of the conductivity at integer filling factors.

Bibliography

[1] E. H. Hall, Amer. J. Math. **2**, 287 (1879).

[2] A. B. Fowler, F. F. Fang, W. E. Howard, and P. J. Stiles, Phys. Rev. Lett. **16**, 901 (1966).

[3] K. F. Komatsubara, K. Narita, Y. Katayama, N. Kotera, and M. Kobayashi, J. Phys. Chem. Solids **35**, 723 (1974).

[4] S. Kawaji and J. Wakabayashi, Surf. Sci. **58**, 238 (1976).

[5] T. Ando and Y. Uemura, J. Phys. Soc. Jpn. **36**, 959 (1974).

[6] T. Ando, J. Phys. Soc. Jpn. **36**, 1521 (1974).

[7] T. Ando, J. Phys. Soc. Jpn. **37**, 622 (1974).

[8] T. Ando, J. Phys. Soc. Jpn. **37**, 1233 (1974).

[9] T. Ando, Y. Matsumoto, and Y. Uemura, J. Phys. Soc. Jpn. **39**, 279 (1975).

[10] K. von Klitzing, G. Dorda, and M. Pepper, Phys. Rev. Lett. **45**, 494 (1980).

[11] B. N. Taylor, Phys. Today **42**, 23 (1989).

[12] K. von Klitzing, Rev. Mod. Phys. **58**, 519 (1986).

[13] R. E. Prange, Phys. Rev. B **23**, 4802 (1981).

[14] R. B. Laughlin, Phys. Rev. B **23**, 5632 (1981).

[15] D. C. Tsui, H. Störmer, and A. Gossard, Phys. Rev. Lett. **48**, 1559 (1982).

[16] R. B. Laughlin, Phys. Rev. Lett. **50**, 1395 (1983).

[17] R. B. Laughlin, Rev. Mod. Phys. **71**, 863 (1999).

[18] H. L. Störmer, Rev. Mod. Phys. **71**, 875 (1999).

[19] D. C. Tsui, Rev. Mod. Phys. **71**, 891 (1999).

[20] R. Landauer, Z. Phys. B-Cond. Matter **68**, 217 (1987).

[21] M. Büttiker, Phys. Rev. B **38**, 9375 (1988).

[22] B. I. Halperin, Phys. Rev. B **25**, 2185 (1982).

[23] P. Středa and L. Smrčka, J. Phys. C **16**, L895 (1983).

[24] O. Heinonen and P. L. Taylor, Phys. Rev. B **28**, R6119 (1983).

[25] A. Siddiki and R. R. Gerhardts, Phys. Rev. B **70**, 195335 (2004).

[26] G. Nachtwei, Physica E **4**, 79 (1999).

[27] S. Kawaji, K. Hirakawa, M. Nagata, T. Okamoto, T. Fukase, and T. Gotoh, J. Phys. Soc. Jpn. **63**, 2303 (1994).

[28] Y. Kawaguchi, F. Hayashi, S. Komiyama, T. Osada, Y. Shiraki, and R. Itoh, Jpn. J. Appl. Phys. **34**, 1881 (1995).

[29] Y. Kawaguchi, F. Hayashi, S. Komiyama, T. Osada, Y. Shiraki, and R. Itoh, Jpn. J. Appl. Phys. **34**, 4309 (1995).

[30] S. Komiyama, Y. Kawaguchi, T. Osada, and Y. Shiraki, Phys. Rev. Lett. **77**, 558 (1996).

[31] I. I. Kaya, G. Nachtwei, K. von Klitzing, and K. Eberl, Phys. Rev. B **58**, R7536 (1998).

[32] I. I. Kaya, G. Nachtwei, K. von Klitzing, and K. Eberl, Europhys. Lett. **46**, 62 (1999).

[33] I. I. Kaya, G. Nachtwei, B. E. Sağol, K. von Klitzing, and K. Eberl, Physica E **6**, 128 (2000).

[34] S. Komiyama and Y. Kawaguchi, Phys. Rev. B **61**, 2014 (2000).

[35] B. E. Sağol, G. Nachtwei, N. G. Kalugin, G. Hein, and K. Eberl, in *Proc. 15th Int. Conf. on High Magnetic Fields in Semiconductors Physics (SemiMag-15), Oxford-Great Britain*, edited by A. R. Long and J. H. Davies (Institute of Physics Conference Series 171, IOP (Bristol-Philadelphia), 2002).

[36] B. E. Sağol, Ph. D. thesis, *Space and Time-Resolved Measurements at the Breakdown of the Quantum Hall Effect*, Technische Universität - Braunschweig, 2003.

[37] I. I. Kaya, G. Nachtwei, K. von Klitzing, and K. Eberl, Physica B **256-258**, 8 (1998).

[38] G. Ebert, K. von Klitzing, K. Ploog, and G. Weimann, J. Phys. C **16**, 5441 (1983).

[39] S. Komiyama, T. Takamasu, S. Hiyamizu, and S. Sasa, Solid State Commun. **54**, 479 (1985).

[40] K. Güven, R. R. Gerhardts, I. I. Kaya, B. E. Sağol, and G. Nachtwei, Phys. Rev. B **65**, 155316 (2002).

[41] P. Středa and K. von Klitzing, J. Phys. C **17**, L483 (1984).

[42] L. Eaves and F. W. Sheard, Semicond. Sci. Technol. **1**, 346 (1986).

[43] V. Tsemekhman, K. Tsemekhman, C. Wexler, J. H. Han, and D. J. Thouless, Phys. Rev. B **55**, R10201 (1997).

[44] B. E. Sağol, G. Nachtwei, K. von Klitzing, G. Hein, and K. Eberl, Phys. Rev. B **66**, 075305 (2002).

[45] O. M. Corbino, Phys. Zeits. **12**, 561 (1911).

[46] K. von Klitzing, in *Commemorazione di Orso Mario Corbino-The ideal Corbino effect*, edited by P. E. Giua (Centro Stampa de Vittoria, Roma, 1987), p. 43.

[47] T. Ando, A. Fowler, and F. Stern, Rev. Mod. Phys. **54**, 437 (1982).

[48] M. S. Erukhimov and B. A. Tavger, Zh. Eksp. Teor. Fiz. **53**, 926 (1967).

[49] M. W. Cole, Rev. Mod. Phys. **46**, 451 (1974).

[50] D. C. Tsui and R. A. Logan, Appl. Phys. Lett. **35**, 99 (1979).

[51] J. H. Davies, *The Physics of Low-Dimensional Semiconductors* (Press Syndicate of the University of Cambridge, Pitt Building, Trumpington Street, Cambridge, United Kingdom, 1998).

[52] M. Abramowitz and I. A. Stegun, *Handbook of Mathematical* (Dover Publications Inc., New York, USA, 1968).

[53] G. Nachtwei, *Quanteneffekte in niederdimensionalen Systemen*, Technische Universität - Braunschweig, 2003.

[54] R. R. Gerhardts, *Low-Dimensional Electron Systems in Semiconductors*, unpublished, Max Planck Institut für Festkörperforschung - Stuttgart.

[55] C. Kittel, *Introduction to Solid State Physics* (John Wiley & Sons, New York, 1996).

[56] L. Shubnikov and W. J. de Haas, Leiden Commun. **207a**, (1930).

[57] T. Ando, J. Phys. Soc. Jpn. **53**, 3101 (1984).

[58] K. Güven and R. R. Gerhardts, Phys. Rev. B **67**, 115327 (2003).

[59] A. Siddiki and R. R. Gerhardts, Phys. Rev. B **68**, 125315 (2003).

[60] A. Siddiki, S. Kraus, and R. R. Gerhardts, Physica E **34**, 136 (2006).

[61] A. Siddiki and R. R. Gerhardts, Int. J. Mod. Phys. B **21**, 1362 (2007).

[62] J. K. Jain, Phys. Rev. B **40**, 8079 (1989).

[63] J. J. Harris, J. A. Pals, and R. Woltjer, Rep. Prog. Phys. **52**, 1217 (1989).

[64] H. L. Störmer, Surf. Sci. **142**, 133 (1984).

[65] M. Hatzakis, *Nanolithography*, 1994.

[66] B. E. Sağol, LabVIEW Codes, 2001.

[67] Oxford Instruments, *High Field Magnet System - Operator's Handbook*, Old Station Way, Eynsham, Witney, Oxon, OX8 1TL, England, 1994.

[68] Oxford Instruments, *Superconducting Magnet - Operator's Handbook*, Tubney Woods, Abingdon, Oxon, OX13 5QX, England, 2003.

[69] D. B. Chklovskii, B. I. Shklovskii, and L. I. Glazman, Phys. Rev. B **46**, 4026 (1992).

[70] D. B. Chklovskii, K. A. Matveev, and B. I. Shklovskii, Phys. Rev. B **47**, 12605 (1993).

[71] K. Lier and R. R. Gerhardts, Phys. Rev. B **50**, 7757 (1994).

[72] E. Ahlswede, P. Weitz, J. Weis, K. von Klitzing, and K. Eberl, Physica B **298**, 562 (2001).

[73] G. Vasile, C. Stellmach, G. Hein, and G. Nachtwei, in *Proc. 14th Int. Conf. on Nonequilibrum Carrier Dynamics in Semiconductors (HCIS-14), Chicago-U.S.A.*, edited by M. Saraniti and U. Ravaioli (Springer Proceedings in Physics (SPP) 110, 95, Springer-Verlag (Berlin-Heidelberg), 2006).

[74] G. Vasile, C. Stellmach, G. Hein, and G. Nachtwei, Semicond. Sci. Technol. **21**, 1714 (2006).

[75] R. J. Smith, *Circuits, Devices and Systems* (John Wiley & Sons, New York, 1984).

[76] T. Martin and S. Feng, Phys. Rev. Lett. **64**, 1971 (1990).

[77] N. Q. Balaban, U. Meirav, and H. Shtrikman, Phys. Rev. B **52**, R5503 (1995).

[78] G. Nachtwei, G. Lütjering, D. Weiss, Z. H. Liu, K. von Klitzing, and C. T. Foxon, Phys. Rev. B **55**, 6731 (1997).

[79] G. Nachtwei, Z. H. Liu, G. Lütjering, R. R. Gerhardts, D. Weiss, K. von Klitzing, and K. Eberl, Phys. Rev. B **57**, 9937 (1998).

[80] N. Q. Balaban, U. Meirav, H. Shtrikman, and Y. Levinson, Phys. Rev. Lett. **71**, 1443 (1993).

[81] R. R. Gerhardts and J. Gross, Phys. Rev. B **60**, 2561 (1999).

[82] S. Kawaji, H. Hirakawa, M. Nagata, T. Okamoto, T. Fukase, and T. Gotoh, Surf. Sci. **305**, 161 (1994).

[83] V. G. Burnett, A. L. Efros, and F. G. Pikus, Phys. Rev. B **48**, 14365 (1993).

[84] G. Nachtwei, S. Heide, C. Breitlow, P. Svoboda, and M. Cukr, Phys. Rev. B **50**, 8488 (1994).

[85] T. Kurosawa and H. Maeda, J. Phys. Soc. Jpn. **31**, 668 (1971).

[86] P. Pfeffer, W. Zawadzki, K. Unterrainer, C. Kremser, C. Wurzer, E. Gornik, B. Murdin, and C. R. Pidgeon, Phys. Rev. B **47**, 4522 (1993).

[87] Y. L. Ivanov and Y. B. Vasil'ev, Sov. Tech. Phys. Lett. **9**, 264 (1983).

[88] Y. B. Vasil'ev and Y. L. Ivanov, Sov. Tech. Phys. Lett. **10**, 104 (1984).

[89] K. Unterrainer, C. Kremser, E. Gornik, and Y. L. Ivanov, Solid- State Electronics **32**, 1527 (1989).

[90] V. I. Gavrilenko, Z. F. Krasil'nik, and V. V. Nikanorov, in *Proc. 20th Int. Conf. on Physics of Semiconductors (ICPS-20), Thessaloniki-Greece* (World Scientific, Vol. 3, 2483, Singapore, 1990).

[91] Y. L. Ivanov, Optical and Quantum Electronics **23**, 253 (1991).

[92] Y. L. Ivanov, Y. B. Vasil'ev, and S. D. Suchalkin, Fiz. Tekh. Poluprovodn. **27**, 1097 (1993).

[93] A. A. Andronov, I. V. Zverev, V. A. Kozlov, Y. N. Nozdrin, S. A. Pavlov, and V. N. Shastin, JETP Lett. **40**, 804 (1984).

[94] E. Gornik, K. Unterrainer, and C. Kremser, Optical and Quantum Electronics **23**, 267 (1991).

[95] A. A. Andronov, A. M. Belyantsev, V. I. Gavrilenko, E. P. Dodin, Z. F. Krasil'nik, V. V. Nikonorov, and S. A. Pavlov, JETP Lett. **40**, 989 (1984).

[96] A. A. Andronov, A. M. Belyantsev, E. P. Dodin, V. I. Gavrilenko, Y. L. Ivanov, V. A. Kozlov, Z. F. Krasil’nik, L. S. Mazov, A. V. Muravjov, I. M. Nefedov, V. V. Nikonorov, Y. N. Nozdrin, S. A. Pavlov, V. N. Shastin, V. A. Valov, and Y. B. Vasil’ev, Physica B **134**, 210 (1985).

[97] E. Gornik, V. Rosskopf, and W. Heiss, Infrared Phys. Technol. **36**, 113 (1995).

[98] M. E. Cage, R. F. Dziuba, B. F. Field, E. R. Williams, S. M. Girvin, A. C. Gossard, D. C. Tsui, and R. J. Wagner, Phys. Rev. Lett. **51**, 1374 (1983).

[99] T. Takamasu, S. Komiyama, S. Hiyamizu, and S. Sasa, Surf. Sci. **170**, 202 (1986).

[100] C. Stellmach, A. Hirsch, G. Nachtwei, Y. B. Vasil’ev, N. G. Kalugin, and G. Hein, Appl. Phys. Lett. **87**, 133504 (2005).

[101] V. Fal’ko and L. J. Challis, J. Phys. Condens. Matter **5**, 3945 (1993).

[102] G. Abstreiter, J. P. Kotthaus, J. F. Koch, and G. Dorda, Phys. Rev. B **14**, 2480 (1976).

[103] J. C. Maan, T. Englert, D. C. Tsui, and A. C. Gossard, Appl. Phys. Lett. **40**, 609 (1982).

[104] D. Stein, Diploma thesis, *Photoleitfähigkeitsmessungen an GaAs/AlGaAs-Heterostrukturen*, Technische Universität - München, 1983.

[105] R. E. Horstman, E. J. van der Broek, J. Wolter, R. W. van der Heijden, G. L. J. A. Rikken, H. Sigg, P. M. Frijlink, J. Maluenda, and J. Hallais, Solid State Commun. **50**, 753 (1984).

[106] D. Stein, G. Ebert, K. von Klitzing, and G. Weimann, Surf. Sci. **142**, 406 (1984).

[107] F. Neppl, J. P. Kotthaus, and J. F. Koch, Phys. Rev. B **19**, 5240 (1979).

[108] R. G. Mani, J. H. Smet, K. von Klitzing, V. Narayanamurti, W. B. Johnson, and V. Umansky, Nature **420**, 646 (2002).

[109] M. A. Zudov, R. R. Du, L. N. Pfeiffer, and K. W. West, Phys. Rev. Lett. **90**, 046807 (2003).

[110] M. A. Zudov, R. R. Du, L. N. Pfeiffer, and K. W. West, Phys. Rev. Lett. **96**, 236804 (2006).

[111] K. Hirakawa, K. Yamanaka, M. Saeki, and Y. Kawaguchi, in *Proc. 4th Int. Symposium on Advanced Physical Fields: Quantum Phenomena in Advanced Materials at High Magnetic Fields (APF-4), Tsukuba-Japan*, edited by G. Kida (PUBLISHER, ADDRESS, 1999).

[112] Y. Kawano, Y. Hisanaga, H. Takenouchi, and S. Komiyama, J. Appl. Phys. **89**, 4037 (2001).

[113] K. Hirakawa, K. Yamanaka, Y. Kawaguchi, M. Endo, M. Saeki, and S. Komiyama, Phys. Rev. B **63**, 085320 (2001).

[114] Y. Kawaguchi, K. Hirakawa, M. Saeki, K. Yamanaka, and S. Komiyama , Appl. Phys. Lett. **80**, 136 (2002).

[115] N. G. Kalugin, Y. B. Vasil'ev, S. D. Suchalkin, G. Nachtwei, B. E. Sağol, and K. Eberl, Physica B **314**, 166 (2002).

[116] N. G. Kalugin, Y. B. Vasil'ev, S. D. Suchalkin, G. Nachtwei, B. E. Sağol, and K. Eberl, Physica E **12**, 144 (2002).

[117] N. G. Kalugin, Y. B. Vasil'ev, S. D. Suchalkin, G. Nachtwei, B. E. Sağol, and K. Eberl, Phys. Rev. B **66**, 085308 (2002).

[118] C. Stellmach, A. Hirsch, N. G. Kalugin, G. Hein, B. E. Sağol, and G. Nachtwei, Semicond. Sci. Technol. **19**, S454 (2004).

[119] C. Stellmach, Y. B. Vasil'ev, R. Bonk, A. Hirsch, N. G. Kalugin, G. Hein, C. R. Becker, and G. Nachtwei, in *Proc. 14th Int. Conf. on Nonequilibrum Carrier Dynamics in Semiconductors (HCIS-14), Chicago-U.S.A.*, edited by M. Saraniti and U. Ravaioli (Springer Proceedings in Physics (SPP) 110, 95, Springer-Verlag (Berlin-Heidelberg), 2006).

[120] C. Stellmach, Ph. D. thesis, *Terahertz-Photoleitung von Quanten-Hall-Systemen*, Technische Universität - Braunschweig, 2006.

[121] A. Ando, J. Phys. Soc. Jpn. **38**, 989 (1975).

[122] E. Stahl, D. Weiss, G. Weimann, K. von Kitzing, and K. Ploog, J. Phys. C **18**, L783 (1985).

[123] H. Sakaki, K. Hirakawa, J. Yoshino, S. P. Svensson, Y. Sekiguchi, T. Hotta, and S. Nishii, Surf. Sci. **142**, 306 (1984).

[124] A. Wixforth, J. P. Kotthaus, and G. Weimann, Phys. Rev. Lett. **56**, 2104 (1986).

[125] A. Wixforth, J. Scriba, M. Wassermeier, J. P. Kotthaus, G. Weimann, and W. Schlapp, Phys. Rev. B **40**, 7874 (1989).

[126] A. Esslinger, A. Wixforth, R. W. Winkler, J. P. Kotthaus, H. Nickel, W. Schlapp, and R. Lösch, Solid State Commun. **84**, 939 (1992).

[127] A. L. Efros and Y. M. Galperin, Phys. Rev. Lett. **64**, 1959 (1990).

[128] V. Fal'ko, S. V. Meshkov, and S. V. Iordanskii, Phys. Rev. B **47**, 9910 (1993).

[129] M. A. Zudov, R. R. Du, J. A. Simmons, and J. L. Reno, Phys. Rev. B **64**, 201311 (2001).

[130] I. A. Dmitriev, A. D. Mirlin, and D. G. Polyakov, Phys. Rev. Lett. **91**, 226802 (2003).

[131] I. A. Dmitriev, A. D. Mirlin, and D. G. Polyakov, Phys. Rev. B **70**, 165305 (2004).

[132] M. G. Vavilov, I. A. Dmitriev, I. L. Aleiner, A. D. Mirlin, and D. G. Polyakov, Phys. Rev. B **70**, 161306 (2004).

[133] I. A. Dmitriev, M. G. Vavilov, I. L. Aleiner, A. D. Mirlin, and D. G. Polyakov, Physica E **25**, 205 (2004).

[134] I. A. Dmitriev, M. G. Vavilov, I. L. Aleiner, A. D. Mirlin, and D. G. Polyakov, Phys. Rev. B **71**, 115316 (2005).

[135] J. D. Jackson, *Classical Electrodynamics* (John Wiley & Sons, USA, 1975).

[136] C. S. Ting, S. C. Ying, and J. J. Quinn, Phys. Rev. B **14**, 4439 (1976).

[137] M. M. Fogler and B. I. Shklovskii, Phys. Rev. Lett. **80**, 4749 (1998).

[138] R. Kubo, J. Phys. Soc. Jpn. **12**, 570 (1957).

[139] W. Zawadzki and R. Lassnig, Solid State Commun. **56**, 537 (1984).

[140] W. Zawadzki and R. Lassnig, Surf. Sci. **142**, 225 (1984).

[141] E. Gornik, R. Lassnig, G. Strasser, H. L. Störmer, A. C. Gossard, and W. Wiegmann, Phys. Rev. Lett. **54**, 1820 (1985).

[142] E. Gornik, R. Lassnig, G. Strasser, H. L. Störmer, and A. C. Gossard, Surf. Sci. **170**, 277 (1986).

[143] G. Vasile, C. Stellmach, R. R. Gerhardts, and G. Nachtwei, in *Proc. 28th Int. Conf. on the Physics on Semiconductors (ICPS-28), Vienna-Austria*, edited by W. Jantsch and F. Schäffler (American Institute of Physics 893, 649, 2 Huntington Quadrangle, Suite 1NO1 Melville, NY 11747-4502, 2007).

[144] C. Stellmach, G. Vasile, A. Hirsch, R. Bonk, Y. B. Vasil'ev, G. Hein, C. R. Becker, and G. Nachtwei, Phys. Rev. B **76**, 035341 (2007).

Acknowledgments

The work performed to accomplish my Ph. D. project was carried out in Braunschweig in the Institut für Angewandte Physik and Physikalisch-Technische Bundesanstalt and in Stuttgart in the Max Planck Institut für Festkörperforschung. The financial support which made possible my stay in Germany was provided by the Deutsche Forschungsgemeinschaft (DFG), the Deutscher Akademischer Austausch Dienst (DAAD) and Max Planck Gesellschaft (MPG). I take the opportunity to express my thanks and gratitude to

- Prof. Dr. G. Nachtwei for giving me the opportunity to work in this field and in his group. I would like to thank him for his valuable experimental suggestions and hints, for his excellent pedagogy to explain different issues. Not at last, I thank him for his patience during the writing of my thesis and also for his jokes and stories that made me laughing;

- Prof. Dr. R. R. Gerhardts for his patience and support to perform the calculations during my stay in Max Planck Institute-Stuttgart. I thank him for sharing with me his Fortran codes and his unpublished notes. I also thank him for accepting to be one of the referee of my thesis and especially for his patience and criticism to overview my thesis, which helped me to improve it a lot;

- Prof. Dr. A. Hangleiter and Prof. Dr. A. Eichler for their kindness and support to overcome different situations, especially for the support of obtaining the DAAD scholarship;

- Prof. Dr. K. von Klitzing for the opportunity to work in his group in MPI-Stuttgart;

- Dr. G. Hein for his support and introduction in the clean room facilities during the preparation of my samples;

- Dr. C. Stellmach for his friendship, for his help and ideas about the experiments. I also thank him for all our discussions and for the time shared together;

- Dr. A. Siddiki for his readiness to help and explain me different issues about the screening of the 2DES;

- My former officemates A. Hirsch, A. Buss, F. Vogt, K. Knese and R. Bonk for their kindness at the beginning and during my work;
- Mrs. D. Schummacher for his permanent good mood and support to overcome different bureaucratic problems during my work;
- Mr. F. Werner and all the members of the technical department for their constant supply of enough helium necessary for my measurements;
- My family and my friends for their support during all these four years.

Curriculum Vitae

03.06.1975	born in Livezi-Romania
01.10.2006 - 01.10.2007	Scientific assistant at Technical University Carolo Wilhelmina Braunschweig, Institute of Applied Physics, Group of Prof. Dr. G. Nachtwei
01.12.2005 - 01.10.2006	Scholarship from the German Academic Exchange Service (DAAD), Technical University Carolo Wilhelmina Braunschweig, Institute of Applied Physics, Group of Prof. Dr. G. Nachtwei
01.03.2005 - 01.12.2005	Scholarship from the Max Planck Society, Max Planck Institute for Solid State Research, Department of Prof. Dr. K. von Klitzing
01.09.2003 - 01.03.2005	Scientific assistant at Technical University Carolo Wilhelmina Braunschweig, Institute of Applied Physics, Group of Prof. Dr. G. Nachtwei
2000 - 2002	Master of Science in Physics, University of Iceland, Reykjavik-Iceland, Thesis: *Magnetization of interacting confined* *two-dimensional electron systems,* Supervisors: Prof. Dr. V. Gudmundsson and Dr. A. Manolescu
1995 - 2000	Bachelor of Science in Physics, University of Bucharest, Bucharest-Romania, Thesis: *Laser Telemetry,* Supervisor: Prof. Dr. I. Iova
1989 - 1993	Air Force High-School "Tudor Vladimirescu", Craiova-Romania
1981 - 1989	"Scoala cu Clasele I-VIII Nr. 2" Elementary School, Ramnicu Valcea-Romania